Computational Design of Iron(II) Complexes with Tuneable Spin-State Energetics

James David Mattock

Submitted for the degree of Doctor of Philosophy

University of Sussex

June 2018

Declaration

I hereby declare that this thesis has not been and will not be, submitted in whole or in part to another University for the award of any other degree.

Signature:

Having established and studied some of the unique properties of boron, these were applied to homoaromatic systems in order to acquire a measure of control over the strength of the through-space interaction. It became evident that the structural isomerism made possible by inserting boron centres in place of the more traditional carbocations results in significantly varied properties in similar and closely-related compounds. The variation of the strength of aromaticity allows for a perturbation in the immediate electronic environment of donor atoms to metal centres thus leading to the modulation of the relative electronic energy difference of the different spin-states of the resulting complexes. The results suggest a possible application to controlled spin-state switching technologies, for instance in the design of spin-switchable materials including stable fully controllable room-temperature spin-crossover compounds.

Chapter 1 includes a discussion of relevant literature setting the context. Chapter 2 comprises a concise summary of work undertaken with multiple experimental groups to identify and characterise properties of boron compounds, this using DFT methodologies to provide a rationale for experimentally observed phenomena. Chapter 3 describes the design of a set of homoaromatic candidates stabilised with NHCs and Chapter 4 focuses on functionalising these compounds with a view towards increased exploitability. Chapter 5 assesses the viability of using an electron localisation method to identify through-space interactions. Chapter 6 documents the optimisation of the singlet excited state of [Fe(Phen)2(NCS)2] via a novel method that circumvents the usual complications of optimising these complex excited states for SCO complexes with the [Fe(bipy)3]2+ complex being included as a control. The methodologies and compound design from the preceding Chapters are collated in Chapter 7 where a homoaromatic ligand set based on a boron derivative of the homotropylium cation is designed and characterised and then applied to create a perturbation to control the spin-state energetics of a defined system. This is followed by a brief description of the possible directions of future work.

Table of Contents

Acknowledgements

I would like to thank Dr Alfredo Vargas for his teaching. I am grateful to the Braunschweig group at the University of Wuerzburg, the Kostakis group at the University of Sussex and the Chaplin group at the University of Warwick for successful collaboration. In particular, thanks to Dr Rian D. Dewhurst. Also thanks to Mr Alhamdu Umaru Bello, Mr Jeremy Maris and Mr Luke Ingerson at the University of Sussex for their assistance with the HPC and the multiple fault fixes. I am also thankful to the late Dr Mike Malone without whom I may well have chosen physics. Most importantly, I would like to thank my family and friends, especially my parents, for their unwavering support.

Glossary of Abbreviations

ω-B97X-D	A long-range corrected version of Grimme's functional
ADF	Amsterdam Density Functional
AIM	Atoms in Molecules
ALDA	Adiabatic Local-Density Approximation
Anth	Anthryl
AoC	Average of Configuration
B3LYP	Becke exchange with Lee-Yang-Parr correlation (20% exact-exchange)
B3LYP*	Becke exchange with Lee-Yang-Parr correlation (15% exact-exchange)
BA	Bent Allene
Bipy	Bipyridene
BJ	Becke-Johnson
Bpp	2,6-di(pyrazol-1-yl)pyridine
Bpym	2-2'-bipyrimidine
Bt	2,2'-bithiazoline
Btz	2,2'-bi-4,5-dihydrothiazine
CAAC	Cyclic (Alkyl)(Amino)carbene
CAM-B3LYP	Coulomb-Attenuating Method B3LYP
Carb	Carbene (See NHC)
Cat	Catechol
Cy	Cyclohexyl
DCD	Dewar-Chatt-Duncanson
Dep	2,6-diethylphenyl
DFT	Density Functional Theory

Dip	2,6-diisopropylphenyl
DMPE	1,2-Bis(dimethylphosphino)ethane
DMPM	1,2-Bis(dimethylphosphino)methane
DPA	2,2'-dipyridylamine
DPPM	1,2-Bis(diphenylphosphino)methane
EDA	Energy Decomposition Analysis
ELF	Electron Localisation Function
Elstat.	Electrostatic
Et	Ethyl
EPR	Electron Paramagnetic Resonance
ETS-NOCV	Extended Transition State Natural Orbitals for Chemical Valence
eV	Electron Volt
G09	Gaussian 09
GGA	Generalised Gradient Approximation
GIAO	Gauge Independent Atomic Orbital
GS	Ground State
GTO	Gaussian Type Orbital
GUI	Graphical User Interface
HFS	Hartree-Fock-Slater
HOMO	Highest Occupied Molecular Orbital
HS	High-Spin
ICH_2Cy	1,3-$(CH_2Cy)_2$-imidazole-2-ylidene
IDep	1,3-$(Dep)_2$-imidazole-2-ylidene
IDip	1,3-$(Dip)_2$-imidazole-2-ylidene
IiPr	1,3-$(iPr)_2$-imidazole-2-ylidene
IiPrDip	1,3-$(iPrDip)_2$-imidazole-2-ylidene

IMe	1,3-dimethylimidazole-2-ylidene
IMeMe	1,3,4,5-tetramethylimidazole-2-ylidene
IMes	1,3-dimesitylimidazole-2-ylidene
Int.	Interaction
iPr	iso-Propyl
I^{t}Bu	1,3-di-*tert*-butylimidazole-2-ylidene
ITol	1,3-(toluene)$_2$-imidazole-2-ylidene
kcal	Kilocalorie
kJ	Kilojoule
KS-DFT	Kohn-Sham Density Functional Theory
LA	Lewis Acid
LB	Lewis Base
LCAO	Linear Combination of Atomic Orbitals
LHS	Left-Hand Side
LIESST	Light Induced Excited Spin State Trapping
LFT	Ligand Field Theory
LS	Low-Spin
LUMO	Lowest Unoccupied Molecular Orbital
M06-L	A local Minnesota functional
Me	Methyl
MEP	Molecular Electrostatic Potential
Mes	Mesityl
MLCT	Metal to Ligand Charge Transfer
MO	Molecular Orbital
Mol	Mole
NBO	Natural Bond Orbital

Neut	Neutral
NHC	N-Heterocyclic Carbene
NICS	Nucleus-Independent Chemical Shift
NMR	Nuclear Magnetic Resonance
OLYP	Handy's exchange with Lee-Yang-Parr correlation
Orb. Int.	Orbital Interaction
PAoC	Polarised Average of Configuration
Pauli	Pauli Repulsion
PBE	Perdew-Burke-Ernzerhof
PBE0	Hybrid form of PBE
PBEKCIS	Perdew-Burke-Ernzerhof Krieger-Chen-Iafrate-Savin
PES	Potential Energy Surface
Phen	Phenanthroline
Py	Pyridyl
Pz	Pyrazine
QZ4P	Quadruple-ζ basis set with four polarisation functions
RHS	Right-Hand Side
RPBE	Revised PBE by Hammer-Hansen-Norskov
SCF	Self-Consistent Field
SCO	Spin-Crossover
SEDD	Single-Exponential Decay Detector
SF	Spin-Flip
SIDep	1,3-$(Dep)_2$-2,4-dihydroimidazole-2-ylidene
SIDip	1,3-$(Dip)_2$-2,4-dihydroimidazole-2-ylidene
SIMesDip	1,3-$(MesDip)_2$-2,4-dihydroimidazole-2-ylidene
SOMO	Singly Occupied Molecular Orbital

SQUID	Superconducting Quantum Interference Device
STO	Slater Type Orbital
TDDFT	Time-Dependent Density Functional Theory
TMS	Trimethylsilane
TP	Trispyrazolylborate
TPA	Tris(2-pyridylmethyl)amine
Tz	Triazolyl
TZ2P	Triple-ζ basis set with two polarisation functions
TZP	Triple-ζ basis set with a single polarisation function
WBI	Wiberg Bond Index
ZORA	Zeroth Order Regular Approximation

Chapter 1 – Introduction

The Broad Applications of Boron

Known since antiquity and unique in its bonding patterns and its position as being the only non-metal in group 13, boron has been said to yield a more diverse and intricate array of inorganic chemistry than any other element.[1] Since the separation of the two isotopes became commercially viable boron has found a wide range of valuable uses from the use of ^{10}B as a neutron suppressant in nuclear reactors,[2] to the use of ^{11}B in synthetic chemistry such as cross-coupling reactions and selective reductions among many others.[3–7] Boron based compounds have also been shown to be capable of activating H_2 molecules.[8,9] Boron possesses a $2s^2\ 2p^1$ valence electron structure with these electrons being tightly held with high ionisation energies, thus is common for it to adopt a trivalent structure however, it is by no means limited to this. The empty p_z orbital left by forming three two-centre two-electron bonds is available for a range of bonding applications and it is this which allows for boron's many unique applications. Whilst generally described as being "electron deficient", this is not an accurate description of the wide range of properties this empty orbital allows for. Firstly, "electron deficiency" would suggest a high electronegativity and this is certainly not the case as the electronegativity of boron is 2.0 which is significantly lower than that of carbon at 2.5.[1] Thus the standard bonding of boron tends to occur through a predominantly covalent interaction as evidenced in boranes and trihalides amongst many others.

When bonding in a trivalent pattern boron acts as a strong Lewis acid able to accept a pair of electrons into the vacant p_z orbital. However the utility of the vacant p_z orbital is not limited to purely electron donation. The presence of boron within a molecular system can allow for increased electron movement with boron acting as a charge redirecting node able to facilitate

the movement of charge in a transient manner. The application of boron to creating π-systems, is made possible due to its unique capability to act as a charge harnessing and redirection node, this is showcased by Braunschweig *et al.* in a communication documenting the synthesis of a borirene, a system isoelectronic to cyclopropenylium cation.[10] In this system, the boron atom not only accepts π-electron density in a delocalised 3-centre 2-electron interaction in order to facilitate ring-current, but it then participates in an η^3 complexation to a chromium metal centre. However, boron is not restricted to merely being a π-acceptor and directing node, through the expansion of the borirene systems into borylborirene, it was shown that the boron atom within the system was acting as a multisymmetry charge flux bridging element.[11] That is, Braunschweig *et al.* showed that the boron atom could simultaneously both accept and redirect charge from both σ- and π-systems. This was identified by measuring the effects of various substituents and calculating the impact on the bonding in the molecular core via an energy decomposition analysis.

It is these properties that, in recent years, has allowed for the formation of B-B multiple bonds. Upon first glance, the isolobality of boron with a carbocation would appear to suggest that multiple homoatomic bonding should be a logical progression but these compounds are rare. Indeed, initial forays into group 13 homoatomic multiple bonding revolved around tricoordinate systems. The first of these were radical anionic systems of boron,[12–15] aluminium,[16] and gallium.[17] Similarly dianionic boron systems were also developed that possessed a more classical π-bond.[18–20] However, when strong two-electron donation is applied into the vacant p_z orbital, neutral compounds become, not only viable, but stable under standard conditions. This was first shown by Robinson et al. using the bulky N-heterocyclic carbene (NHC), IDip, to stabilise a dihydrodiborene.[21] The communication included DFT calculations at the B3LYP/6-311+G** and displayed what have become the expected HOMO and HOMO-1 orbitals centred upon the B-B

π-bond. The creation of these diborenes usually requires, with some recent exceptions, symmetric ancillary groups and two-electron donors with N-heterocyclic carbenes being prevalent; additionally phosphorus donors are uncommon but not unknown.[21] This is shown by the capability of boron to form stable, homonuclear, triple bonds.[22] In order to stabilise a boryne species, a large amount of electron density needs to be donated into the vacant p_z orbital. In the initial paper the Braunschweig group achieve this by utilising the strongly donating N-heterocyclic carbenes to create an electron rich system. The unusual nature of these systems has made them the subject of multiple reviews.[23,24] Given these properties, boron is particularly useful in stabilise neutral radical species.[25–27]

These compounds have shown interesting similarities to alkenes in their properties and their ligation to metal species, although mainly limited to coinage metals. This type of multisymmetry charge flux is also seen with a manganese based borylene complex where the boron centre mediates charge transfer between two Mn centres and will then facilitate the binding of the anion to a coinage metal centre.[28] DFT calculations upon a B-C σ-coordination via the η^2 complexation of a C-B bond of a borirene showed a strong M→B dative interaction, thus showing the boron accepting large amounts of charge without reporting the population of a B-C anti-bonding orbital.[29] This is a prime example of one of boron's most applicable properties, the ability to act as a strong electron sink, which, along with its ability to mediate charge flow, allows it to yield direct control over the flow of charge within molecular systems.

The position of boron in the first row of group 13 would suggest that it displays fully non-metal character, however this is not completely accurate. For example, the vacant p_z orbital and the subsequent ability to accept a pair of electrons allows boron centres to coordinate with compounds more often considered as L-type ligands under the MLX counting scheme. This can

be seen in reactions such as the co-catenation of a diboron moiety and CO ligands to a Fe metal centre where DFT calculations showed the formation of a σ-system within the C-B-B-C unit.[30] It has also been shown that it is possible to bind multiple carbonyl moieties to a borylene system in a manner analogous to transition metal complexes.[31] In addition to this particularly metallic behaviour, it has been shown in the literature that it is possible to bind, and even couple, multiple moieties of CO across a B-B triple bond in a manner reminiscent of uranium systems.[32] The length of the C-O bonds in this paper are attributed to a strong back-bonding interaction from the diboron unit suggesting that boron can act to amplify a DCD-type back-bonding interaction. This property is likely a result of boron's formidable electron accepting capability.

There are also multiple examples of boron participating in aromatic bonding in a further analogy to carbon. It is particularly suited to this form of bonding with the vacant orbital in phase with the aromatic plane to facilitate charge flow. The field of boron-containing compounds exhibiting aromatic behaviour has recently been covered by an authoritative review by Su and Kinjo.[33] These often include multiple atoms with lone pairs in order to obey the 2n+1 rule such as with one or more B-O and B-N pairs. The first reported example of a B-N moiety being used in an aromatic system was borazine, a $B_3N_3H_6$ benzene analogue, which was reported as early as 1926.[34] There has been some discussion over the nature of the bonding in borazine and it has been analysed via numerous computational methods, with AIM, ELF and NICS all being commonly utilised.[35–39] It would appear to possess aromaticity albeit somewhat weaker than that observed in classical benzene. Borazine is by no means an isolated case, with there being many examples in the literature of aromatic compounds including B-N pairs. There are multiple reviews that cover the use B-N pairings within aromatic systems.[40–43] These B-N moieties are isoelectronic, isolobal and isosteric with C=C units making them ideal for insertion into aromatic systems. These aromatic compounds can bind to metals not only as the usual side on, η^x

aromatic ring binding, but also as an L-type ligand via the nitrogen centre giving them a range of functionality.[44,45]

In rare cases, particularly strong donation into the vacant p_z orbital can result in the formation of a borylene moiety, which result in a boron atom utilising two of its three valence electrons in a manner analogous to a carbene. When used as ligands these compounds are isolobal to CO and N_2. These systems have an interesting array of properties and have been well reviewed.[46,47]

The properties that boron has been shown to display make it a useful tool for compound design where there is a requirement for the transfer of charge. This ability to accept and support charge can be strong enough to support and mediate through-space interactions.

Spin-State Switching Behaviour

The selectable control of spin-switching in molecular systems has been a target for synthetic and computational chemists for decades. The field of spin-crossover (SCO) is now large and is covered by many authoritative reviews.[48–54] SCO materials have many desirable applications to computing such as large, high density memory in addition to switching devices where on/off control is applicable.[55,56] This spin-transition can be induced via light through Light-Induced Excited Spin State Trapping (LIESST) or pressure however it is most common for a transition to proceed thermally. This thermal transition is entropically driven, both through the increase of entropy gained via the change in electronic configuration and through vibronic entropy gained from the increase in metal to ligand bond lengths. Whilst the effect is observed from d^4 to d^7 transition metal compounds the most common complexes remain based around the d^6 Fe(II) ion, although complexes including the d^5 Fe(III) are also numerous and the are several important

examples including the d^7 Co(II) ion. The strength of the ligand sphere of these compounds must be tightly controlled to ensure a high-spin low-spin gap suitable for facilitating a transition. Hence these complexes tend to be 6-coordinate of octahedral symmetry with a first sphere of coordination of six nitrogen centres.

The initial discoveries of Cambi and Szego in 1931 demonstrated the magnetic phenomena associated with SCO behaviour.[57] However, following this discovery, the field was dormant until multiple re-investigations of the initial work in the 1960s.[58,59] This lead to a daunting range of systems being designed such as the $[Fe(NCS_2(phen)_2)]$ system and its selenocyanate analogue of Konig *et al.* in 1967,[60] from which an entire range of $[FeL_2(NCS)_2]$ compounds has been synthesised. With the NCS group being a mid-field X-type ligand it has found use across several SCO complexes such as; $[Fe(bt)_2(NCS)_2]$,[61] $[Fe(py)_2phen(NCS)_2]$,[62] $[Fe(py)_2bpym(NCS)_2]$,[62] $[Fe(DPA)_2(NCS)_2]$,[63] and $[Fe(TPA)_2(NCS)_2]$.[64] As can be seen, a mid-field X-type ligand is particularly useful as it allows for the design of neutral SCO compounds. This is useful from a computational perspective as highly charged systems can add a layer of complexity to already convoluted theoretical systems. At the same time Trofimenko *et al.* detailed SCO compounds including the tridentate L_3-type ligand, tris-(1-pyrazolyl)-hydridoborate, the so called "scorpionate" ligand.[65] These ligands are anionic with a negative charge centred upon the boron atom, the pair of these ligands yield a neutral complex again suggesting it is another computationally useful ligand set.

More common than the neutral complexes, there exists a vast array of dicationic Fe(II) and Fe(III) based SCO complexes. Many of these result from the replacement of six-member heterocyles in a low-spin Fe(II) system with five-member heterocyles with the aim of reducing σ-donation and π-acceptance. A discussion of these compounds was the basis for an informative review by

Brooker *et al.* in 2011.[66] Additional charged SCO complexes have been designed via the inclusion of cationic scorpionate ligands.[67,68] For a further example of cationic SCO complexes, a 2009 review by Halcrow discusses the effect of a large number of varying substitutions upon the 2,6-di(pyrazol-1-yl)pyridenes within the $[Fe(1\text{-}bpp)_2]^{2+}$ complex.[48] This was followed by an additional review providing a rationale for the structural changes in SCO compounds upon transition to the high-spin state.[49] As an aside, the importance of structural distortion that these reviews show suggests that it may be a prudent idea to run computational calculations upon SCO systems without forcing symmetry within the systems.

Many of the recent advances in the field of SCO systems have been related to multinuclear systems i.e. more than one transition metal ion capable of undergoing a spin-transition in an interlinked system. Initial forays into this field concerned the formation of covalent bridges between SCO metal centres to test for effects on physical properties.[69,70] This has ultimately led to the design of SCO nanoparticles in an attempt to create functional materials. These are largely based around the triazole and pyrazine ligands.[50,71,72] Whilst these systems display promising properties they are largely unsuitable as a test bed for the computational design in this work due to the complex spin-transition pathways created by the impact of cooperative effects.

Due to the nature of the relative energetics of the spin-states required for SCO behaviour to be induced thermally, SCO compounds possess multiple low-lying states of distinct symmetry. This, in addition to the issues already caused by a compact d-space, can make simulating these compounds at various spin-states particularly complex. There exists a staggering array of literature focused on finding a catch all approach to calculating the various properties of the complex spin-transition pathways using DFT.[73–87] Whilst it is evident that varying systems often require different methods hence placing importance upon a method assessment, several points

can be stated with some degree of confidence. Firstly, despite the improvement in results for calculations involving compact d-space generally acquired via the inclusion of exact-exchange into the exchange correlation functional, i.e. a hybrid functional, the same is not true for calculations pertaining to SCO systems. Instead, the use of a hybrid functional will often yield a significant underestimation of the high-spin low-spin gap, even to the extent of producing an incorrect ordering of states. Secondly, the impact of the inclusion of parameters to simulate dispersion interactions will be highly system dependent. These methods should also be used with caution as they will often cause an artificial shortening of pertinent bond lengths and thus an over-estimation of stability. Additionally, GGA-type functionals may provide the most accurate relative spin-state energies but are highly system specific.

Applying Computational Methods

Given the varied and complex bonding common to boron containing compounds, they can be convoluted to probe computationally. Due to a reliance solely on the electron density term, $\rho(r)$, Density Functional Theory (DFT) has rapidly gained popularity in the last two decades due to its favourable compromise between accuracy and computational cost. There are many programmes with differing algorithms capable of conducting DFT calculations each with their own advantages and disadvantages, of particular importance to this work are the Gaussian and Amsterdam Density Functional (ADF) programmes.[101] Gaussian relies on Gaussian Type Orbitals (GTOs) and is suited to a rapid screening of large number of calculations, especially if those calculations include hybrid orbitals that require a portion of exact exchange due to its more rapid calculation and smaller scaling.[137] ADF excels in situations with more complex electronic situations due to its basis around Slater Type Orbitals (STOs) and its tolerance of fractional occupations of molecular orbitals (MOs).[88] Of particular import is the facility of ADF to be used to conduct ETS-NOCV calculations and to then display the resultant decomposition of energy

terms (EDA) for specific bonding interactions. This is crucial when analysing boron containing compounds as the bonding situation may not necessarily follow standard models. The facility for the input of fractional occupations also opens a range of possibilities to states that may not be accessible through standard methods or with the use of Time-Dependent Density Functional Theory (TDDFT).

In order to conduct a full characterisation of SCO behaviour it is necessary to find the energy of the singlet excited state, to do this computationally that state must therefore be optimised. It is commonly held that, in order to optimise a system, the forces on each nucleus must be minimised such that the system approaches an equilibrium.[89]

$$F_A = -\nabla_A E = -\frac{\delta E}{\delta R_A}$$

Equation 1: Calculation the total energy at force equilibrium.[89]

R_A is the description of the coordinates of nucleus A as shown below in Equation 2.

$$R_A = \begin{pmatrix} X_A \\ Y_A \\ Z_A \end{pmatrix}$$

Equation 2: Nuclear coordinate matrix.[89]

The method of analytically evaluating analytical energy variants using STO basis functions was initially conceived by Versluis and Ziegler in 1987.[90] This was originally derived under the

Hartree-Flock-Slater method (HFS). This requires the statement of the total energy with respect to a normalised single Slater determinant. This is given in Equation 3 below.

$$E_{HFS} = -\frac{1}{2}\sum_{i}^{n} \Psi_i(1)\,\nabla_1^2 \Psi_i(1)\delta\tau_1 + \frac{1}{2}\sum\sum_{A\neq B} \frac{Z_A Z_B}{|\overrightarrow{R_A} - \overrightarrow{R_B}|} - \sum_{i}^{n}\sum_{A}^{N} \int \Psi_i(1)\frac{Z_A}{|\overrightarrow{R_A} - \overrightarrow{r_1}|}\Psi_i(1)\delta\tau_1$$
$$+ \frac{1}{2}\sum_{i}^{n}\sum_{j}^{n} \int \Psi_i(1)\Psi_i(1)\frac{1}{|\overrightarrow{r_1} - \overrightarrow{r_2}|}\Psi_j(2)\Psi_j(2)\,\delta\tau_1\delta\tau_2$$
$$- \frac{9}{4}a_0\left(\frac{3}{4\pi}\right)^{\frac{1}{3}} \int \left[\sum_{i(\alpha)}^{n_\alpha} \Psi_i(1)\Psi_i(1)\right]^{\frac{4}{3}} \delta\tau_1 - \frac{9}{4}a_0\left(\frac{3}{4\pi}\right)^{\frac{1}{3}} \int \left[\sum_{i(\beta)}^{n_\beta} \Psi_i(1)\Psi_i(1)\right]^{\frac{4}{3}} \delta\tau_1$$

Equation 3: The calculation of the total energy within the Hartree-Fock-Slater method.[90]

where $\Psi_i(1)$ and $\Psi_j(2)$ represent spin-orbitals. When the derivative of the E_{HFS} in Equation 5 with respect to some molecular coordinate, X_A.

$$\frac{dE_{HFS}}{dX_A} = 2\sum_{\gamma}^{\alpha,\beta}\sum_{i(\gamma)}^{n_\gamma} \int \frac{\delta\Psi_i(1)}{\delta X_A}[h^\gamma(1) - \varepsilon_i]\Psi_i(1)\delta\tau_1 + \sum_{B\neq A}^{N} \frac{Z_B(X_B - X_A)}{|\overrightarrow{R_B} - \overrightarrow{R_A}|^3}$$
$$- \int \rho(1)\frac{x_1 - X_A}{|\overrightarrow{r_1} - \overrightarrow{R_A}|^3}\delta\tau_1$$

Equation 4: The calculation of the energy gradient with the HFS method. [90]

where:

$$h^{\gamma}(1) = -\frac{1}{2}\nabla^2 - \sum_{A}^{N}\frac{Z_A}{|\overrightarrow{R_A} - \overrightarrow{r_1}|} + \sum_{i}^{n}\int \Psi_i(2)\Psi_i(2)\frac{1}{|\overrightarrow{r_1} - \overrightarrow{r_2}|}\delta\tau_2$$

$$- 3a_0\left(\frac{3}{4\pi}\right)^{\frac{1}{3}}\left[\sum_{i(\gamma)}^{n(\gamma)}\Psi_i(1)\Psi_i(1)\right]^{\frac{1}{3}}$$

Equation 5: The expansion of h^{γ}.[90]

where $\gamma = \alpha, \beta$, $\overrightarrow{r_1}$ pertains to the position of electron 1 and $\overrightarrow{R_A}$ pertains to the position of nucleus A. The variable a_0 represents a global molecular parameter and has the value 0.7. The set of one-electron spin orbitals is expanded in terms of a linear combination of slater type orbitals as shown below in Equation 6:

$$\frac{\delta\Psi_i(1)}{\delta X_A} = \sum_{\nu}^{2M}\frac{C_{\nu i}\delta\omega_{\nu}(1)}{\delta X_A}$$

Equation 6: The expansion of the one-electron spin orbitals via LCAO.[90]

Therefore, in order to apply this method of calculating gradients to DFT it becomes necessary to elucidate the method of calculating the energy of the system within DFT.

$$E[\rho(\overrightarrow{r_1})] = T_S[\rho] + J[\rho] + E_{XC}[\rho] + E_{NE}[\rho]$$

Equation 7: The total energy of a non-interacting system within Kohn-Sham DFT.[91,92]

where $T_S[\rho]$ is the non-interacting kinetic energy term, $J[\rho]$ is the electrostatic interaction term and where $E_{NE}[\rho]$ is the external potential energy (also often labelled $V[\rho]$). The most important divergence from the HFS method described above is the presence of the $E_{XC}[\rho]$ term. This term represents the exchange-correlation energy and is the only part of Equation 7 that cannot be solved precisely.

$$E[\rho(\overrightarrow{r_1})] = T_S[\rho] + \frac{1}{2}\iint \frac{\rho(\overrightarrow{r_1})\rho(\overrightarrow{r_2})}{r_{12}} d(\overrightarrow{r_1})d(\overrightarrow{r_2}) + E_{XC}[\rho] + \int V_{Ne}\rho(\vec{r})d\vec{r}$$

Equation 8: The expansion of the total energy of a non-interacting system within KS-DFT.[92]

Equation 8 represents an expansion of Equation 7 including position vectors.

$$E[\rho(\overrightarrow{r_1})] = -\frac{1}{2}\sum_{i}^{N}\langle\varphi_i|\nabla^2|\varphi_i\rangle + \frac{1}{2}\sum_{i}^{N}\sum_{j}^{N}\iint |\varphi_i(\overrightarrow{r_1})|^2 \frac{1}{r_{12}} \left|\varphi_j(\overrightarrow{r_2})\right|^2 d(\overrightarrow{r_1})d(\overrightarrow{r_2}) + E_{XC}[\rho(\vec{r})]$$
$$-\sum_{i}^{N}\int \sum_{A}^{M}\frac{Z_A}{r_{1A}}|\varphi_i(\overrightarrow{r_1})|^2 d(\overrightarrow{r_1})$$

Equation 9: A more detailed expansion of the total energy of a non-interacting system within KS-DFT.[92]

Equation 9 represents a further expansion of Equation 8 including the one-electron spin-orbitals, φ_i and φ_j. With the total energy of the system defined, the method of calculating analytical energy gradients shown by Versluis and Ziegler, and described above, can be applied.[90] This is displayed below in Equation 10.

$$\frac{dE_{DFT}}{dX_A} = 2\sum_{R_\sigma}\int \frac{\delta\Psi_{R_\sigma}}{\delta X_A}\left[h^\sigma(1) - \varepsilon_{R_\sigma}\right]\Psi_{R_\sigma}\delta\tau_1 - \sum_{B\neq A}^{N}\frac{Z_A Z_B(X_A - X_B)}{R_{AB}^3} - \int \rho(1)\frac{x_1 - X_A}{R_{A1}^3}\delta\tau_1$$

Equation 10: The expression for the calculation of the energy gradients within KS-DFT.[89]

The variable, $h^\sigma(1)$, is the one-electron Kohn-Sham operator and is expanded below in Equation 11.

$$h^\sigma(1) = -\frac{1}{2}\nabla_1^2 - \sum_A \frac{Z_A}{r_{A1}} + \int \frac{\rho(2)}{r_{12}}\delta\tau_2 + V_x + V_C$$

Equation 11: The definition of the one-electron Kohn-Sham operator.[89]

Here the exact form of V_x and V_C is determined by the exchange-correlation functional used. The energy gradients expressed in Equation 10 are accurate for the ground-state of the system. In order to optimise the structures of excited states it is necessary to consider the excitation energies calculated via Time-Dependent DFT (TDDFT). The calculation of molecular excitation energies with TDDFT can be expressed as follows:

$$\omega\begin{pmatrix}1 & 0\\ 0 & -1\end{pmatrix}\begin{pmatrix}X\\ Y\end{pmatrix} = \begin{pmatrix}A & B\\ B* & A*\end{pmatrix}\begin{pmatrix}X\\ Y\end{pmatrix}$$

Equation 12: Molecular excitation energies.[93]

Here, ω corresponds as the energy difference between the ground state and an excited state, where X and Y describe the transition densities between the specified states. Where all the STOs are elements of the set of real numbers, Equation 12 can be rearranged into Equation 13.

$$\omega = \frac{1}{2}\Big(\big(X^\dagger + Y^\dagger\big)(A+B)(X+Y) + \big(X^\dagger - Y^\dagger\big)(A-B)(X-Y)\Big)$$

Equation 13: The expansion of the equation describing the molecular excitation energies.[93]

Through the use of the adiabatic local-density approximation (ALDA), the method for the calculation of molecular excitation energies within ADF can be displayed.

$$\begin{aligned}\omega = \frac{1}{2}\Bigg(&\sum_{ai\sigma}((X+Y)_{ai\sigma}(X+Y)_{ai\sigma} + (X-Y)_{ai\sigma}(X-Y)_{ai\sigma})(\varepsilon_{a\sigma} - \varepsilon_{i\sigma}) \\ &+ 2\sum_{\sigma}\int \rho_\sigma^{X+Y} V_C^{X+Y} + 2(1-c_X)\sum_{\sigma\tau}\rho_\sigma^{X+Y} f_{\sigma\tau}^{xc,ALDA}\rho_\tau^{X+Y} \\ &- c_X \sum_{ai\sigma,bj\sigma}\Big((X+Y)_{ai\sigma}(X+Y)_{ai\sigma}\big((ab\sigma|ij\tau) + (aj\sigma|bi\tau)\big) \\ &+ (X-Y)_{ai\sigma}(X-Y)_{ai\sigma}\big((ab\sigma|ij\tau) - (aj\sigma|bi\tau)\big)\Big)\Bigg)\end{aligned}$$

Equation 14: The implementation of Equation 13 with the ADF program.[93]

Here, Ziegler *et al.* define the molecular orbital subscripts a, b, c… as unoccupied MOs in the ground state, i,j,k… as occupied orbitals in the ground state, p,q,r… indicates any orbital and Greek subscripts indicate spin indices.[93] The term, ρ_σ^{X+Y}, is described in Equation 15.

$$\rho_\sigma^{X+Y} = \sum_{\mu\nu}(X+Y)_{\mu\nu\sigma}X_\mu X_\nu$$

Equation 15: The density of the vector (X+Y) corresponding to spin σ.[93]

The derivative of this energy with respect to a perturbation to the coordinate system will then allow for the calculation of the energy gradients to allow for the optimisation of an excited state. This is shown below in Equation 16.

$$\omega^{\zeta} = \sum_{\sigma} \int \rho_{\sigma}^{P(\zeta)} (T + V_{ext} + V_C + V_{\sigma}^{xc}) + \sum_{\sigma} \int \left(V_C^P \rho_{\sigma}^{P(\zeta)} + V_{ext}^{\zeta} \rho_{\sigma}^P \right)$$
$$+ \sum_{\sigma\tau} \int \rho_{\sigma}^P f_{\sigma,\tau}^{xc,FULL} \rho_{\tau}^{P(\zeta)} + \sum_{\sigma\tau} \int \rho_{\sigma}^{(X+Y)(\zeta)} \left(V_C^{(X+Y)} + f_{SS,\sigma\tau}^{xc,ALDA} \rho_{\tau}^{(X+Y)} \right)$$
$$+ \sum_{\sigma\tau\nu} \int \rho_{\sigma}^{(X+Y)} \rho_{\tau}^{(X+Y)} \rho_{\nu}^{(\zeta)} g_{\sigma\tau\nu}^{xc,ALDA} + \sum_{\mu\nu K\lambda\sigma\tau} (\mu\nu|K\lambda)^{\zeta} \Gamma_{\mu\nu\sigma K\lambda\tau}^{X} - \sum_{\mu\nu\sigma} S_{\mu\nu}^{(\zeta)} W_{\mu\nu\sigma}$$

Equation 16: The equation defining TDDFT energy gradients.[93]

In Equation 16, Ziegler *et al.* define a superscripted ζ as denoting differentiation with respect to a real perturbation.[93] It is also noted that they have neglected terms in the two-electron integrals to simplify the notation. Although not repeated here due to the targets for calculations in this work being Singlet-Singlet transitions, a spin- flip version of TDDFT (SF-TDDFT) can be used to calculate Singlet-Triplet transitions.

Thus it should be possible to optimise the singlet excited state of an SCO compound and thus allow for the analysis of multiple Potential Energy Surfaces. However these calculations present significant difficulties.

Ligand Field Theory

Given the great importance of the size of the HOMO-LUMO gap in determining whether or not a compound will exhibit SCO behaviour, it is necessary to briefly reflect on the core points of

Ligand-Field Theory (LFT). Initially developed as crystal field theory by Bethe and Van Vleck nearly 90 years ago,[94,95] LFT yields a rationale for the population of the valence orbitals in a transition metal complex and is the subject of multiple reviews.[96–98] In such a complex, the valence electrons are usually placed in metal-based d-orbitals. In spherical symmetry the five d-orbitals are energetically degenerate, in an octahedral field these orbitals split into the triply degenerate t_{2g} orbitals and the doubly degenerate e_g orbitals. In order to bind to a metal centre, the majority of ligands either possess a formal negative charge or an available lone pair of electrons. Thus, the first sphere of coordination consists entirely of the negative ends of lone pair dipoles directed towards the metal centre. Due to the relative positions of the d-orbitals with respect to the ligands the d_{z^2} and $d_{x^2-y^2}$ orbitals are subject to a significant degree of repulsion by the ligand sphere whilst the d_{xy}, d_{yz} and the d_{xz} orbitals remain relatively unperturbed. The t_{2g} and e_g states can each be proven to be degenerate via group theory.[99]

The occupation of these orbitals is controlled by the size of energetic stabilisation acquired through pairing and thus occupying lower energy orbitals against the entropic stability acquired by maximising the number of unpaired electrons and also a lower repulsive electrostatic energy. Whilst the latter two energies remain relatively static, the HOMO-LUMO gap between the t_{2g} and e_g orbitals, known in octahedral complexes as Δ_O, can be dramatically impacted by the ligand field.

Ligands which are π-donating are weak field ligands and lead to a small Δ_O, thus meaning that the reduction of coulombic repulsion and the increase in entropy will result in a high-spin compound. Ligands which are π-accepting are known as strong-field ligands and result in a large Δ_O. Here, the stabilisation incurred by spin-pairing within the lower energy t_{2g} state is greater

than the stabilisation incurred via the spreading of the electrons thus resulting in a low-spin compound.[100]

Ligand Field Theory Within DFT

The impact of the ligand charge density at the metal centre can be accounted for within DFT by the addition of an electrostatic potential to the Hamiltonian as per Equation 17.

$$h = h_0 + v_{LF}$$

Equation 17: The addition of the electrostatic potential of ligand charge at the metal centre (v_{LF}) to the Hamiltonian.[97]

where the electrostatic potential can be described as;

$$v_{LF}(\vec{r}) = -e \int \frac{\rho(\vec{R})}{|\vec{R} - \vec{r}|} d\vec{R}$$

Equation 18: The expansion of the electrostatic potential of ligand charge at the metal centre.[97]

Through the expansion of $1/|\vec{R} - \vec{r}|$ within Equation 18, the term v_{LF} can be expressed as follows in Equation 19.

$$v_{LF}(\vec{r}, \theta, \varphi) = \sum_{k=0}^{2l} \sum_{q=-k}^{+k} h_{kq}(\vec{r}) Y_{kq}(\theta, \varphi)$$

Equation 19: The full expansion of the electrostatic potential of ligand charge at the metal centre.[97]

The parameters represented by h_{kq} within Equation 19 can be adjusted to describe the particular ligand field based on the Tanabe-Sugano diagrams acting upon the orbitals, $Y_{kq}(\theta, \varphi)$.

The Structure of This Work

The remainder of this work will organised as follows. Chapter 2 contains a discussion of a pertinent selection of collaborative works undertaken by the author. Chapter 3 introduces homoaromatic compounds and discusses the attempted stabilisation of these compounds via the utilisation of N-heterocyclic carbenes. Chapter 4 expands on Chapter 3; detailing the design of homoaromatic compounds intended to be more easily incorporated into functional materials. Chapter 5 assesses the practicality of using an electron localisation method for a rapid identification of the presence of a homoaromatic interaction. Chapter 6 documents the benchmarking of a methodology for the documentation of the spin-transition pathways for a selection of Spin-Crossover candidates. Chapter 7 is the culmination of this work and brings together the previous chapters in the design of transition-metal systems utilising homoaromatic candidate ligands with a view to investigating the impact of homoaromaticity on SCO properties. Concluding remarks are presented in Chapter 8.

Chapter 2 – Investigating the Varied Properties of Boron Containing Compounds and Elucidating upon Through-Space Interactions

Introduction

The unique properties of boron allow access to many varied compounds that offer utility impossible with any other element. Given this varied properties, a rationale for compound behaviour can often be elusive, DFT offers an attractive route to elucidate upon these properties. DFT can also be used to analyse through-space interactions which can occur due to a complex array of reasons. Thus this chapter documents a wide range of calculations that have been performed in collaboration with multiple experimental groups upon a variety of compounds. The work presented herein will be based purely upon the computational work upon these compounds performed by the author. It should be noted that, in order to retain the ability to directly compare the properties of compounds between multiple projects, any calculations conducted on diborene based systems were performed with the ADF program at the OLYP/TZ2P level of theory as this methodology represents an efficient balance between accuracy and computational cost for ground state calculations. The only deviation from this is where relativistic corrections were rendered necessary by the inclusion of heavy elements.

Some Particular Features of Boron

DFT calculations are well suited to provide rationales for the experimental phenomena made possible by the unique properties of boron. The ETS-NOCV function of the ADF program allows for the description of the interaction between fragments of the molecule, thus, with the strategic choice of fragments, individual bonding interactions can be described.[101,102] It has been used in a collaboration with the Braunschweig group where boron was shown to enhance DCD-

type backbonding in a coinage metal based complex through DFT calculations.[103] This provided a rationale for the observed differences in structure across multiple complexes. A representative example of this is given below as Figure 1 and Figure 2.

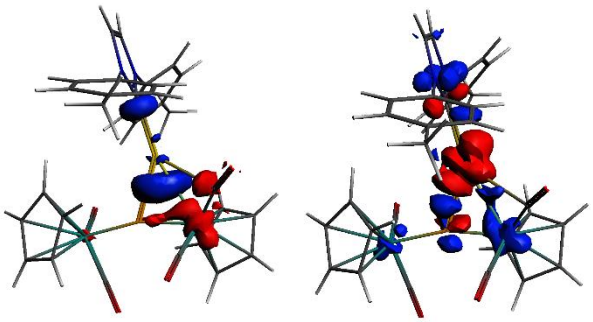

Figure 1: The first (left) and second (right) deformation densities for AuITol. Charge flow is from red to blue.

The first deformation density for the asymmetric AuITol shows the expected donation from the anionic dimanganoborylene onto the metal centre. However the second deformation density shows a back-donation from the AU centre into the anionic ligand mediated by the central boron atom. Note that deformation densities are listed in order of decreasing magnitude of the associated eigenvalue.

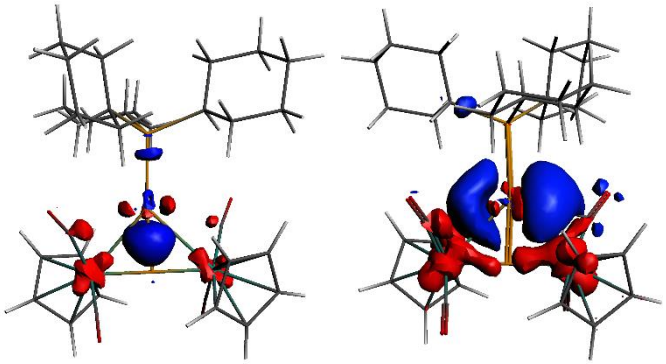

Figure 2: The first (left) and second (right) deformation densities for $CuPCy_3$. Charge flow is from red to blue.

The deformation densities in Figure 2 show that the symmetric PCy_3 based Cu complex does not undergo DCD type back-bonding between the $CuPCy_3$ moiety and the dimanganoborylene. This suggests that the presence of DCD-type back-bonding resulted in the asymmetric structure of some of the coinage metal complexes whilst those without tended to present with more symmetric binding. The aforementioned article also included a full EDA thus adding a quantitative argument.

The anionic dimanganoborylene has additional applications to the binding of coinage metals. The use of two dimanganoborylene moieties by the Braunschweig group allowed for the binding of two coinage metals with an unusually small inter-atomic separation.[104] This unusual separation distance suggested that additional investigation should be conducted computationally. The utilisation of Grimme's D3 dispersion with additional BJ damping suggested that the shortened inter-metal distance was as a result of closed shell, d^{10}-d^{10} interactions.[153-155]

DFT is not limited to purely discussing bonding. In support of experimental results, a rationale was provided for unusual optical data in a diboraferrocenophane system.[105] The smaller optical band width of the diboraferrocenophane appeared to be divergent from that generally expected of trans-acyclic diborenes and was postulated to be due to the strained cis configuration of the B=B bond. The simulation of UV-Vis spectra requires the use of TDDFT. Note this project was an exception to the other boron based projects in this section with the calculations having been conducted at the B3LYP*/TZ2P level of theory due to the inaccuracies incurred by performing TDDFT calculations without the inclusion of exact exchange.

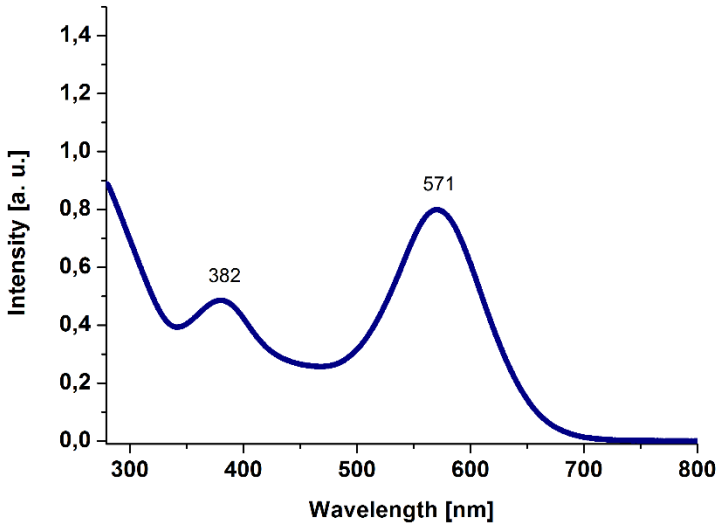

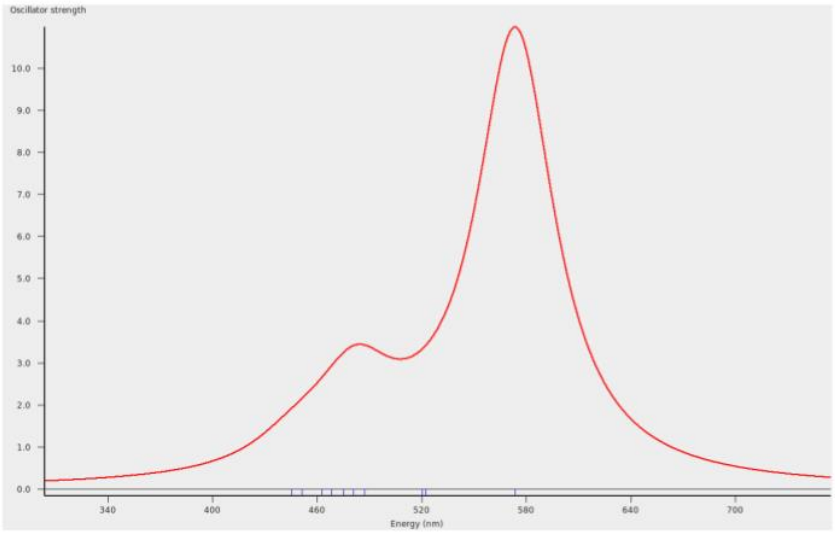

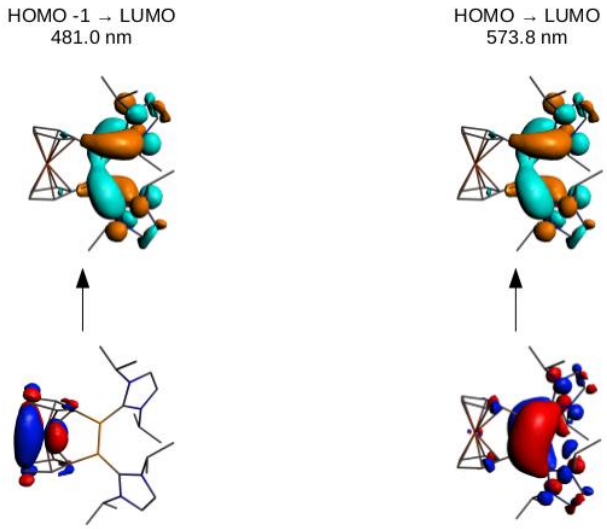

Figure 3: The simulation of UV-Vis spectra for a diboraferrocenephane. Calculate at the B3LYP/TZ2P level of theory.*

The simulated spectrum displayed in Figure 3 displayed a good match to that attained experimentally. Thus the orbital transitions could be assigned to each peak and these have been shown below the simulated spectra. Inspection of the orbitals shows that the LUMO is not anti-bonding in character and is significantly stabilised resulting in a small HOMO-LUMO gap. This small HOMO-LUMO gap provided reasoning for the small optical band gap observed experimentally.

Whilst TDDFT is a powerful and valuable technique, it can be highly dependent on the exchange-correlation functional. This became apparent during the evaluation of the excitations of the metal π-complexes of diborynes.[106] Initially the nature of the binding of the metal centres to the B-B triple bond was investigated via ETS-NOCV and the Energy Decomposition Analysis (EDA) is presented below in Table 1.[101,102] Note a full explanation of ETS-NOCV will be given later in this chapter.

	ΔE_{Pauli}	$\Delta E_{Orb.\ Int.}$	$\Delta E_{Elsta.}$
$BBIDip_2(CuCl)_3$	1878.66	-889.73	-1808.16
$BBIDip_2(CuCl)_2$ (linear)	1136.88	-533.71	-1185.41
$BBIDip_2(CuCl)_2$ (orthogonal)	1184.66	-545.26	-1212.02

Table 1: The energy decomposition analysis for $BBIDip_2(CuCl)_3$ and two conformations of $BBIDip_2(CuCl)_2$ calculated via ETS-NOCV at the B3LYP/TZP level. All energies in kJ mol^{-1}.*

The EDA in Table 1 shows that, whilst the bonding in all three systems is dominated by an attractive electrostatic component and a repulsive Pauli component, there is a significant stabilisation incurred through orbital interaction.

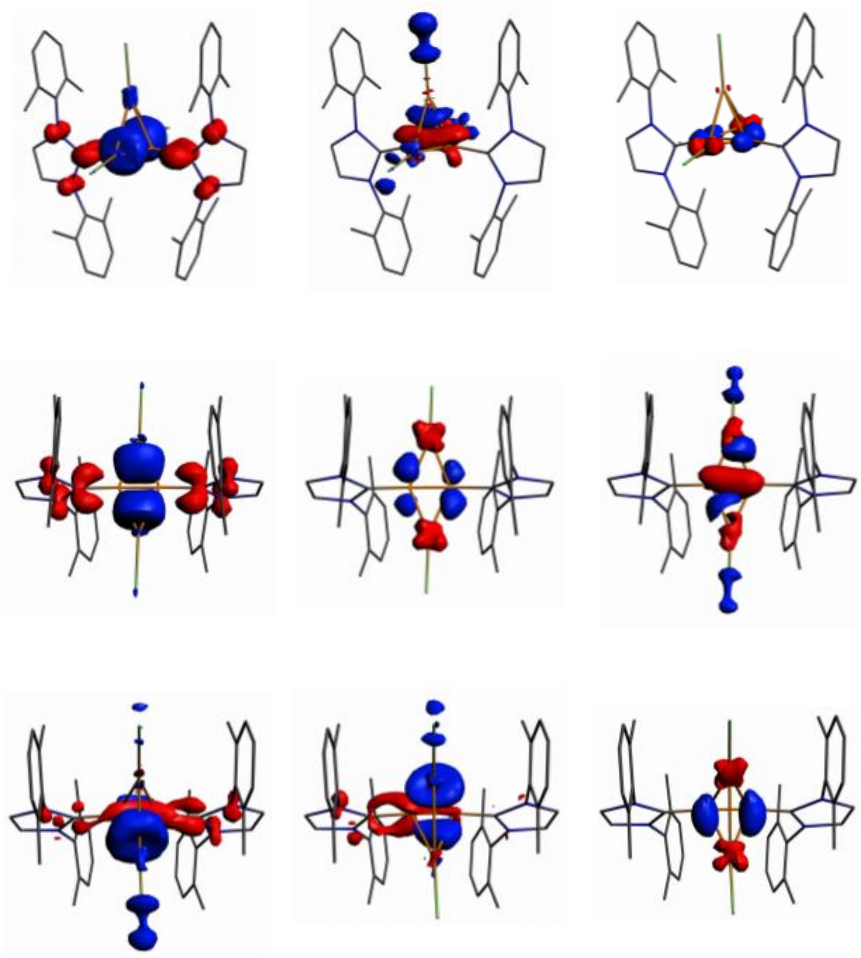

Figure 4: The first 3 deformation densities of $BBIDip_2(CuCl)_3$ (top), the linear conformation of $BBIDip_2(CuCl)_2$ (middle) and orthogonal conformation of $BBIDip_2(CuCl)_2$ (bottom) calculated at the B3LYP/TZP level. All isovalue cutoffs were set to 0.003 except the far right, middle deformation density where it was set to 0.002. It should be noted that charge flow is from red to blue.*

When combined with the large orbital interaction energies observed from the EDA in Table 1, the deformation densities from Figure 4 suggest that there is a degree of DCD-type back-bonding from the CuCl moieties to the diboryne. The presence of back-bonding implies a degree of covalency to the metal-boron π-interaction.

Given that the alkene analogues of these systems are nonemissive and that the systems displayed strong luminescent character, an investigation via TDDFT was attempted. Despite the

assignment of orbital transitions to the simulated UV-Vis spectra, the TDDFT data were not used due to a strong functional dependence of the higher spin states.

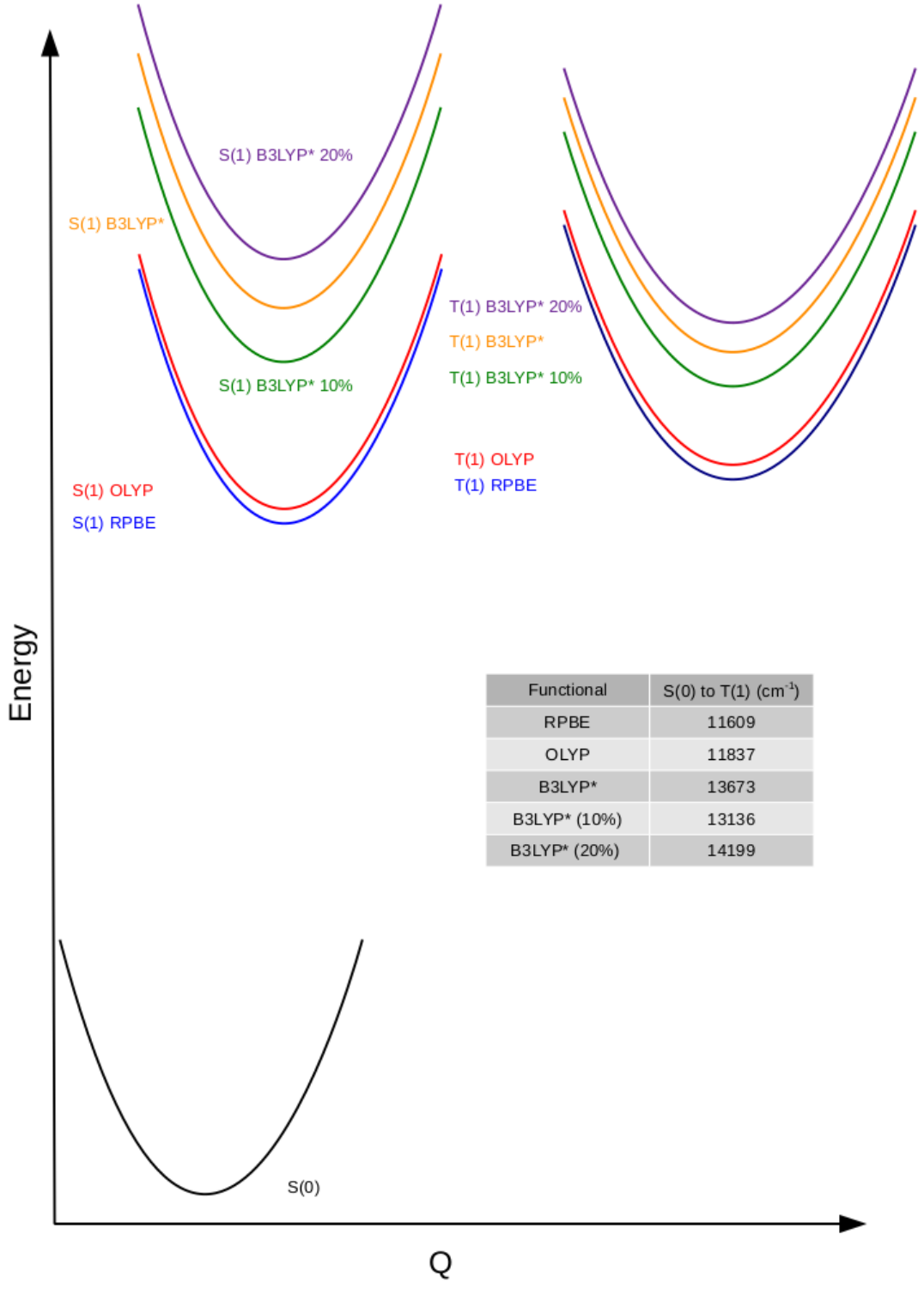

Functional	S(0) to T(1) (cm^{-1})
RPBE	11609
OLYP	11837
B3LYP*	13673
B3LYP* (10%)	13136
B3LYP* (20%)	14199

Figure 5: The spin-transition pathway from ground-state singlet to triplet for $BBIDip_2(CuCl)_3$.

As can be seen from Figure 5, there is a substantial dependence on the exchange-correlation functional when calculating states above the ground state. The presence of a functional dependence within DFT is not uncommon, the unusual property of this particular dependence is its apparent systematic relation to the proportion of exact-exchange included within the functional. As a result of this, OLYP and RPBE, both GGA-type functionals, result in an incorrect ordering of states. Additionally, the increase of exact exchange within the B3LYP* hybrid-type functional leads to an increase in the magnitude of the relative energies of the spin-states.

Further work within the Braunschweig group resulted in a stable diborene with electron-pair donation from PMe_3 groups with ancillary anthracene groups.[107] This compound possessed a remarkably small HOMO-LUMO gap in comparison to other similar diborenes. Computational analysis of the MOs revealed that this was due to the innocent intercalation of the anthryl π* orbitals between the expected boron centred π-bonding HOMO and the boron centred π* orbital. This is displayed within Figure 6 below.

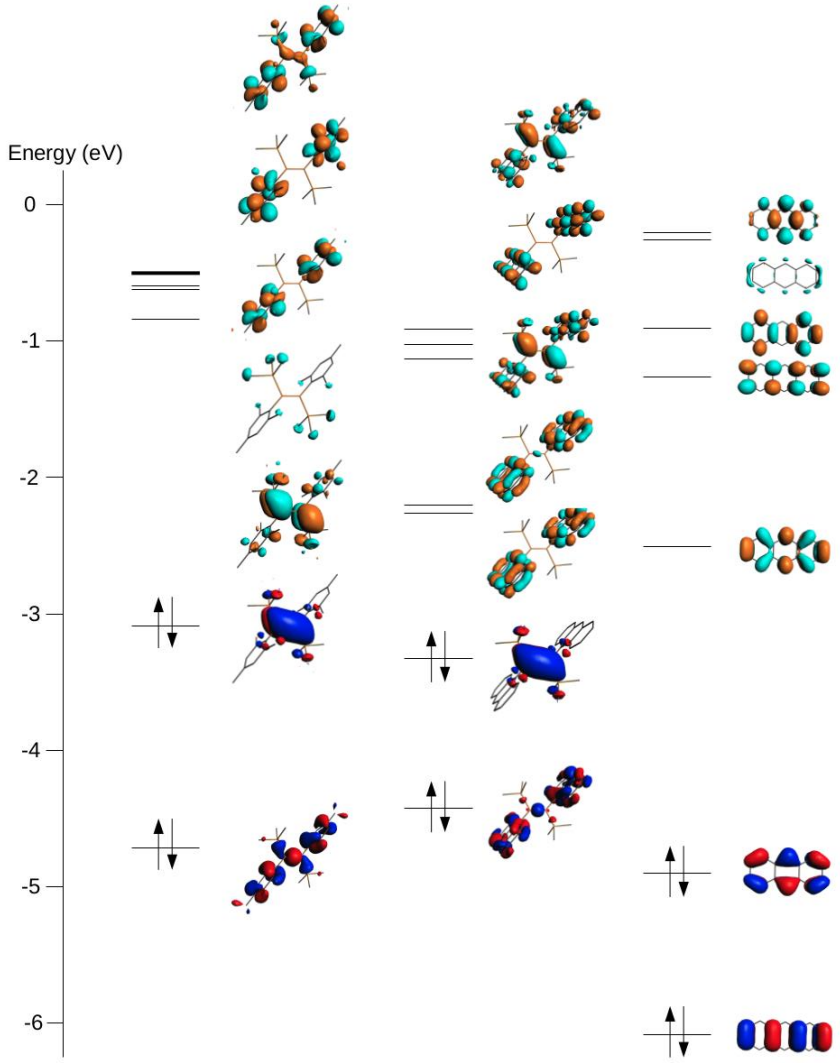

Figure 6: The valence MOs of $BB(PMe_3)_2Mes_2$ (left), $BB(PMe_3)_2Anth_2$ (middle) and anthracene (right). The orbital levels are scaled with respect to the energy in eV.

Figure 6 shows that the HOMO-LUMO gap is calculated to be small with respect to a similar diborene. It also shows the innocent nature of the intercalation with the relative energy of the anthracene based MOs being largely conserved and these MOs within the diborenes showing only negligible density upon the boron centres.

ETS-NOCV was again employed to elucidate upon the bonding motif within the π-diborene complexes of Zn(II) and Cd(II) of this diborene in a later publication.[108] The MCl2 moiety and the diborenes were taken as fragments. The resulting EDA is shown below in Table 2.

EDA	$ZnCl_2$	$CdCl_2$
E_{Pauli}	131.17	128.76
$E_{Orb.\ Int.}$	-75.28	-68.12
$E_{Elsta.}$	-103.92	-104.13
E_{Total}	-48.02	-43.49

Table 2: The EDA of two π-diborene complexes of Zn(II) and Cd(II). All energies in kcal mol^{-1}.

This EDA shows that the strongest contribution to the binding arrives from the electrostatic component however the orbital interaction component is of a significant size. This would usually suggest back-bonding however the relative absence of this from the deformation densities would suggest in this case the back-bonding is present but only weakly so. The EDA also suggests that there is no appreciable difference in bonding motif between M=Zn and M=Cd bar a slight reduction in the bonding contribution from orbital interaction as expected from a larger atom causing less overlap. The domination of the electrostatic character would render the angle of the MCl_2 plane sensitive to the sterics of the substituents on the diborene. Given the nature of the bonding it would seem the unusual d^{10} binding to a π-bond is due to the unique nature of boron allowing the diborene to act as an electron sink. Therefore the B=B bond can acquire a greater concentration of electron density than would be seen in the π-bond of an olefin. This allows for a more substantial electrostatic contribution.

The Determination of the Spin-State of a Bis(boratabenzene) Co(I) Complex

The neutral bis(boratabenzene) complex synthesised within the Braunschweig group was investigated at a number of charges and spin states in order to provide an understanding of the associated oxidation and reduction products. The resultant calculations provided strong corroborating evidence to the experimental data obtained via EPR and solid-state SQUID magnetic measurements obtained within the Braunschweig group, which suggests that the

triplet state is populated at 20 K. Figure 7 shows this corroboration by presenting the various spin-states of the neutral complex.

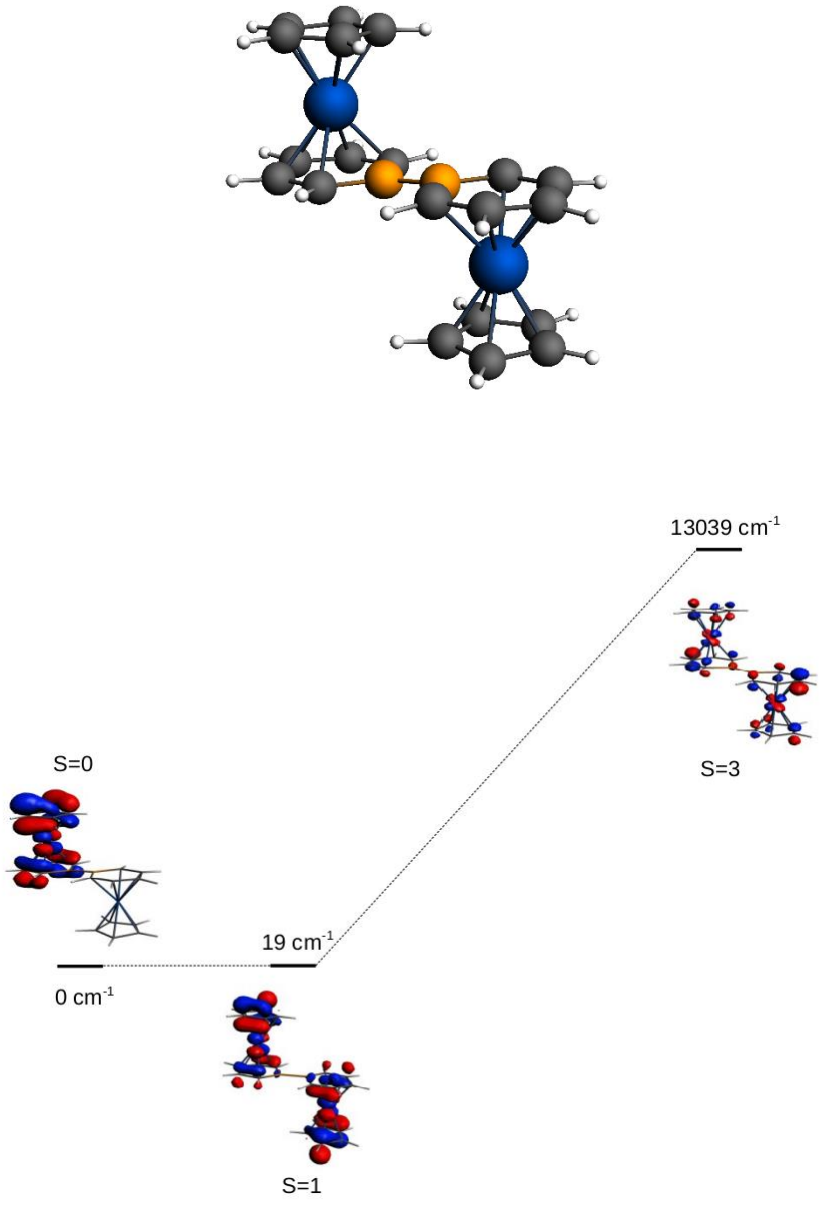

Figure 7: The relative energies between the spin states of the neutral species with the structure displayed (top).

The relative energy diagram above shows that the S = 1 state is less stable than the S = 0 ground state by a marginal 19 cm^{-1} and is therefore likely to be favourable when vibrational and entropic stabilisations are considered. This concurs with the S = 1 state being appreciably populated at

temperatures above 10 K. The S = 3 state energy is larger than 13000 cm^{-1} and is therefore unlikely to be populated thermally. Due to the unrestricted nature of the calculation, the inspection of the MOs of the S=1 state yields a pair of single electron MOs as the HOMO-2 that suggest communication between the two metal centres.

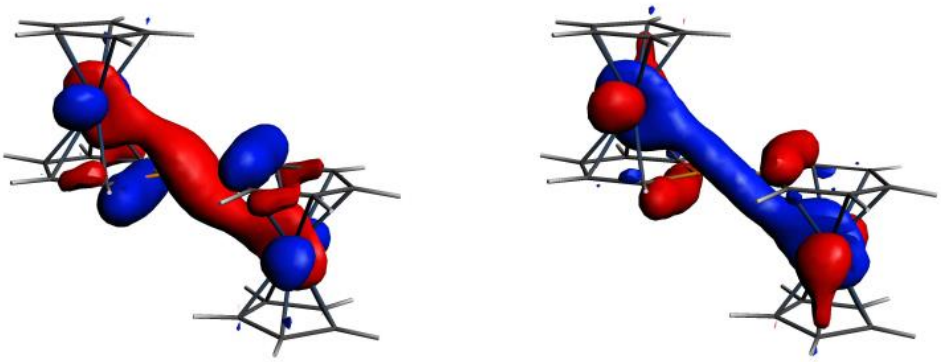

Figure 8: The HOMO-2 of the S = 1 state of the neutral system, for both the α (left) and β (right) electrons.

Figure 8 clearly shows that there exists the significant possibility of communication between the two Co centres through a heavily conjugated bridging ligand system.

Characterising the B-B bond

Given the wide range of behaviours and properties exhibited by the diborene species so far a characterisation of the B=B bonds was undertaken. Characterising the strength and nature of individual inter-atomic bonds is a complex exercise. The descriptions of bond strength shown earlier in this chapter have resulted from either the assessment of the Mayer-type bond orders or the implementation of ETS-NOCV. Mayer-type bond orders are generally a good approximation of bond strength calculated via the exchange-component of the inter-atomic electrostatic term which itself results from the Linear Combination of Atomic Orbitals (LCAO)

Hamiltonian, however, there are drawbacks to the method.[109] Bond order methods are often relative to the bonding structure within the compound in question as they may not match classical Lewis structures and they are generally based on the overlap resulting from an orbital interaction and tend to rather poorly treat coulombic and long-range interactions.

These drawbacks can be alleviated via the application of ETS-NOCV.[110,111] This method yields quantitative information via the Energy Decomposition Analysis (EDA) (also known as "the fragment approach") according to the methods of Morokuma and Ziegler and Rauk. Using the EDA scheme, the energy E_{Int} associated to the interaction between the fragments can be decomposed into three components: $E_{Int} = E_{Elstat} + E_{Pauli} + E_{orb.\ int}$ The first term, $E_{Elstat.}$, corresponds to the classical electrostatic interaction between the unperturbed charge distributions of the fragments (the overall density being the superposition of the fragment densities). The second term, E_{Pauli}, expresses the energy change that arises upon going from the simple superposition of the fragment densities to the wavefunction that obeys the Pauli principle through antisymmetrization and normalization of the product of the fragment wavefunctions. In the last term, $E_{Orb.\ Int.}$, the energy that originates from the contributions from stabilizing orbital interactions (electron pair bonding, charge transfer, polarization) is given. To quantify the contributions of the σ and π interactions between the TM and the B-B core, we employed the techniques based on the ETS-NOCV formalism. The Natural Orbitals for Chemical Valence (NOCV) component of the ETS-NOCV description provides visual qualitative information via deformation densities which display the flow of electron density. It is based on the NOCV wavefunction as an eigenvector of the deformation density matrix in the basis of fragment orbitals, the deformation density (Δρ) is then decomposed in the NOCV representation, as a sum of pairs of complimentary eigenfunctions.

Thus ETS-NOCV would appear to be the ideal solution for conducting a computational investigation of bonding, however it possess one considerable drawback. When specifying the fragments for bonding it is only possible to specify a spin-restricted fragment i.e. the fragment must contain no unpaired electrons. Therefore it is not possible to investigate the nature of bonding in a bond such as a two-centre two-electron bond split heterolytically. This is obviously problematic for characterising a BB π-bond as the most statistically likely outcome of the heterolytic fission of the π-bond is two boron moieties each with two singly occupied valence MOs centred upon the boron atom.

In order to bypass this problem, a technique based on the Average of Configuration (AoC) needs to be applied in order for multiplet fragments to be constructed whilst retaining a spin-restricted orbital occupation. This requires the 'smearing' of unpaired electrons equally across α and β orbitals being careful to ensure any degeneracy is accounted for, such as with the d orbitals within transition metal species. A spin-unrestricted single-point energy calculation with the number of SCF iterations set to zero in order to conserve the electron configuration is conducted using this 'smeared' electron configuration in order to create a density from an averaged potential. The resulting restart file is then used for a spin-restricted single-point energy calculation with the desired multiplicity in order to generate a restricted fragment file, which is required for an ETS-NOCV calculation. An example of this is shown below for a triplet fragment.

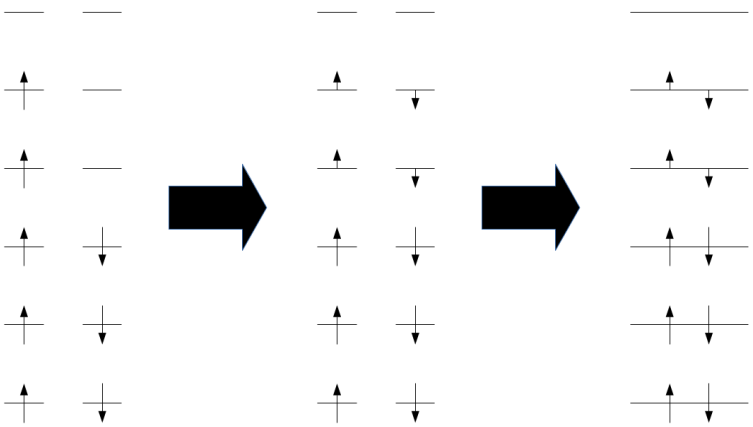

Figure 9: An example of the electron smearing of a triplet fragment in order to generate a restricted fragment.

For small, simple systems with a clear orbital structure this lack of polarisation is an accurate method of calculation as the bonding energy of the fragment should not incur large errors compared to the same fragment which is self-consistent as suggested within the H_2 example within the ADF manual. However, for larger systems with multiple unoccupied orbitals close in energy, or even degenerate, the retention of the specified electronic configuration can result in massive errors in interaction energy. This is due to the electrons specified assigned to orbitals that may not accurately represent the ground state electronic structure of the fragment. The full SCF required in the ETS-NOCV calculation then results in the relaxation of the electron density into the bonding orbitals thus convoluting the interaction energy therefore significantly over-estimating the energetics of the system. Hence larger systems require polarisation of the fragment files and thus a Polarised Average of Configuration (PAoC) calculation.

This was showcased during the computational analysis of a large number of diborenes with various ancillary groups synthesised by the synthetic chemists of the Braunschweig group. Here, the calculations to investigate the B-B π-bond required triplet fragments thus would be unsuitable for standard ETS-NOCV and therefore required PAoC to generate the fragment files.

Compound	B-B bond length (Å)	B-B Mayer bond order	$E_{Orb.\ Int.}$	$E_{Elstat.}$	E_{Pauli}	$E_{Int.}$
BB(aminothienyl)$_2$(IiPr)$_2$	1.6264	1.4067	-163.05	-140.88	187.23	-116.70
BB(anthryl)$_2$(PMe$_3$)$_2$	1.6012	1.6522	-187.94	-153.42	219.94	-121.43
BB(BCat)$_2$(IMeMe)$_2$	1.6152	1.4804	-170.90	-131.51	188.81	-113.61
BB(borylthienyl)$_2$(IiPr)$_2$	1.6357	1.3558	-160.58	-139.76	185.17	-115.18
BB(duryl)$_2$(ICH$_2$Cy)$_2$	1.6518	1.4222	-166.16	-151.59	215.27	-102.49
BB(duryl)$_2$(IMe)$_2$	1.6391	1.4343	-166.93	-155.59	215.54	-106.98
BB(duryl)$_2$(IMeMe)$_2$	1.6391	1.4425	-168.18	-157.56	219.33	-106.41
BB(ferrocenyl)(IiPr)$_2$	1.6445	1.3498	-	-	-	-
BB(fluorenylthienyl)$_2$(IMe)$_2$	1.6230	1.3900	-163.28	-148.20	194.08	-117.40
BB(isopropyl)$_2$(IiPr)$_2$	1.6155	1.6320	-166.18	-138.90	191.57	-113.51
BB(mesityl)$_2$(DMPE)	1.6087	1.5592	-	-	-	-
BB(mesityl)$_2$(DMPM)	1.6104	1.4350	-	-	-	-
BB(mesityl)$_2$(DPPM)	1.6234	1.4247	-	-	-	-
BB(mesityl)$_2$(IMe)$_2$	1.6387	1.4301	-166.63	-154.73	213.77	-107.58
BB(methylthienyl)$_2$(IMe)$_2$	1.6239	1.3330	-161.50	-150.71	200.65	-111.55
BB(phenyl)$_2$(ICH$_2$Cy)$_2$	1.6307	1.4122	-161.35	-150.04	200.12	-111.26
BB(thienyl)$_2$(IiPr)$_2$	1.6217	1.4237	-167.23	-152.25	204.84	-114.65
BB(thienyl)$_2$(IMe)$_2$	1.6265	1.3747	-162.99	-153.66	202.36	-114.30
BB(thienyl)$_2$(IMeMe)$_2$	1.6244	1.4158	-165.69	-150.62	201.98	-114.33
BB(trimethylsilylthienyl)$_2$(IiPr)$_2$	1.6233	1.4319	-167.87	-145.07	199.43	-113.50
BB(trimethylsilylthienyl)$_2$(IMe)$_2$	1.6253	1.3952	-165.06	-148.39	199.15	-114.30
BB(trimethylsilylthienyl)$_2$(IMeMe)$_2$	1.6244	1.4355	-161.45	-135.74	181.93	-115.26
BB(mesityl)$_2$(PEt$_3$)$_2$	1.6113	1.6747	-176.13	-151.72	211.10	-116.75
BB(mesityl)$_2$(PMe$_3$)$_2$	1.6052	1.6465	-176.24	-156.24	214.33	-118.15
BB(propanone)$_2$(SIMesDip)$_2$	1.6408	1.3332	-146.08	-149.41	190.60	-104.90
BB(Br)$_2$(IDep)$_2$	1.6012	1.4216	-168.78	-153.91	206.62	-116.07
BB(Br)$_2$(IDip)$_2$	1.6149	1.4126	-169.28	-156.22	214.04	-111.47
BB(Br)$_2$(IiPrDip)$_2$	1.5893	1.5221	-175.99	-161.92	214.05	-123.85
BB(Br)$_2$(IMes)$_2$	1.6012	1.4397	-168.19	-153.58	205.12	-116.65
BB(Br)$_2$(SIDep)$_2$	1.6101	1.3762	-163.65	-154.27	205.90	-112.02
BB(Br)$_2$(SIDip)$_2$	1.6186	1.3444	-160.82	-153.50	208.73	-105.59
BB(CO)$_2$(CAAC)$_2$	1.7660	0.7699	-	-	-	-

$BB(CN)_2(CAAC)_2$	1.6546	1.3084	-163.32	-124.00	182.81	-104.51
$BBH_2(CAAC)_2$	1.6411	1.2816	-137.47	-147.44	181.66	-103.25
$BBH_2(SIDep)_2$	1.6154	1.3664	-142.10	-146.94	176.73	-112.31
$BBH_2(SIMesDip)_2$	1.6245	1.3722	-140.57	-144.34	175.77	-109.14
$BB(HSiPr)_2(IDip)_2$	1.6477	1.2983	-154.77	-146.56	199.19	-102.14
$BB(HSiPr)_2(SIDep)_2$	1.6315	1.3086	-158.87	-153.34	204.39	-107.83
$BB(BCat)_2(IiPr)_2$	1.6158	1.4792	-170.05	-131.31	188.06	-113.30
$BB(BCat)_2(IMe)_2$	1.6151	1.4766	-168.41	-130.44	183.59	-115.26

Table 3: Bond lengths, Mayer type bond orders and the EDA for a range of diborene compounds. All energies are listed in kcal mol^{-1}.

The data in Table 3 represent a comprehensive assessment of the bonding contributions between the π-bonded boron centres for a number of diborene systems synthesised by collaborators (a comparison between calculated and experimental bond lengths is available in the appendix). This is accompanied by the calculation of the HOMO-LUMO gap of each calculated by both a difference in the associated eigenvalues of the valence orbitals and via inspection of the appropriate transition from TDDFT (this data is presented in the appendix). Whilst a global trend is not immediately identifiable, there is certainly an impact from the modification of the two-electron donor and ancillary groups upon the nature of the B=B π-bond. It should be noted that a number of values for the EDA are missing, this occurs where the fragments cannot be easily separated due to groups that span both of the boron atoms. This issue can be circumvented by solving multi-fragment calculations simultaneously but this makes several assumptions regarding the nature of the electronic environment that reduce the accuracy of the calculated EDA for these compounds. These data not only provides a proof of method, it also provides useful reference material for future work in the field.

Investigating a Through-Space Interaction

One of the most applicable uses of computational chemistry is providing rationales for phenomena that are difficult or impossible to probe experimentally. ETS-NOCV has been shown

above, albeit with some modification, can be a powerful tool in describing bonding interactions. Through-space interactions are particularly difficult to characterise, however, ETS-NOCV can still be applied. A collaboration with the Chaplin group at the University of Warwick typifies this. The computations within this paper revolved around determining the nature of the binding of a potassium ion within a calix arene, ligated to an iridium metal centre.[112] The interaction energies between closed shell moieties can be probed using standard ETS-NOCV.

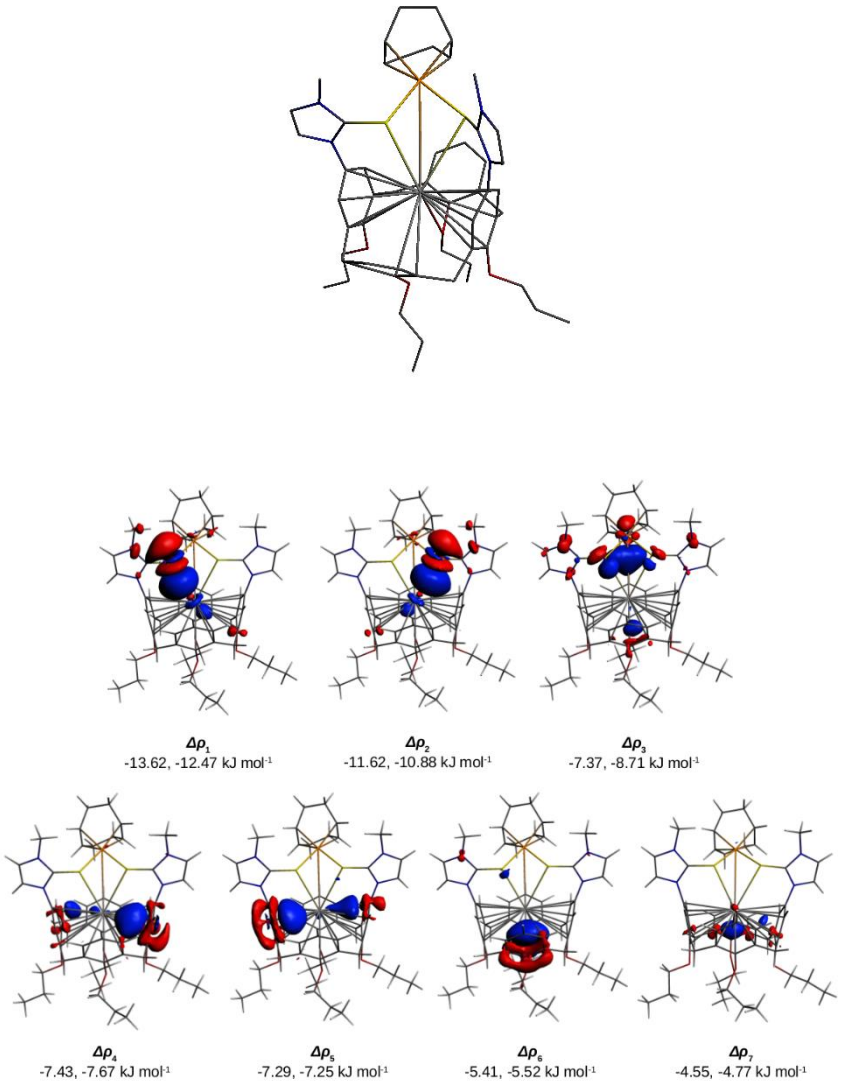

Figure 10: The structure of the calix arene system (top) with the deformation desities (Δρ) with the largest associated eigenvalues for the interaction between K^+ and a ligated calix arene. Charge flow is from red to blue.

The deformation densities displayed in Figure 10 above elucidate the binding of the K^+ ion. The interaction was shown to be dominated by electrostatic interactions with the thione groups acting as the strongest donors but with a significant donation from the surrounding aryl system. ETS-NOCV is not limited to graphical representations and quantitative data can be attained via inspection of the EDA.

OLYP/TZP	1, M=Ir	1, M=Rh	2	3
E_{Pauli}	56.09	58.46	78.00	91.04
$E_{Electro.}$	54.00	46.65	-215.79	-151.76
$E_{orb.\ Int.}$	-125.41	-125.37	-122.70	-128.93
E_{Total}	-15.32	-20.26	-260.50	-189.65

Table 4: EDA of a calix arene complex optimised at the OLYP/TZP level of theory with scalar ZORA with K^+ as a fragment. All energies listed in kcal mol^{-1}.

Table 4 gives the EDA where **1** refers to the complete complex (as shown in Figure 10), **2** refers to the removal of the metal complex and **3** refers to the removal of the thione donors leaving merely the cyclic aryl system with the aim of isolating each of the binding interactions. The analysis of the EDA showed that the addition of the metal centre introduced a destabilising effect, confirmed that the orbital overlap originated from the aryl system and the strong electrostatic interaction is due to the presence of the thione donors.

Summary

The capability of DFT to provide rationales for complex chemical phenomena makes it a valuable tool in the chemist's arsenal. A number of collaborative projects have been undertaken and allowed for the utilisation of a wide range of computational methodologies. In particular, the use of PAoC-ETS-NOCV to describe the nature of previously inaccessible bonds suggests this method may have wide potential applications.

Chapter 3 – The Definition and Application of Metrics to Assess the Viability of Carbene-Stabilized Homoaromatics

Foreword

This chapter is based upon the article "Identification of a Lead Candidate in the Search for Carbene-Stabilised Homoaromatics" published in Chemistry: A European Journal, in which the author is first author.[116]

Introduction

Homoaromaticity is generally defined as the presence of an aromatic π bond system without a contiguous σ bond system.[117] This requires stabilizing aromatic interactions can exist between unconnected atoms thus creating homoconjugative gaps. While exceedingly rare, most known homoaromatic systems are based on σ-interrupted analogues of known aromatic cations, prominent examples being those based on the cyclopropenyl (e.g. the norbornen-7-yl cation; **I**) or tropylium cations (e.g. the homotropylium cation; **II**). Neutral and anionic examples of homoaromatic systems are even rarer still, semibullvalene being an exception that is a subject of much discussion within past literature.[118–123] One conceivable way to expand the range of synthetically-accessible homoaromatic compounds is to exploit the extraordinary stabilizing ability of strong Lewis donors, such as NHCs.

A thriving field of synthetic chemistry has recently built up around the use of Lewis donors, such as NHCs and others, to stabilize otherwise unstable low-valent species, radicals or elemental allotropes.[124–133] While descriptions of such main group-based molecules as Lewis acid (LA) Lewis

base (LB) adducts has recently spurred heated debate,[134–136] the binding of Lewis basic fragments such as singlet carbenes to main group elements falls on a continuum of bonding possibilities, and it is clear that in many cases a LB→LA model is the most accurate description.

The Lewis-donor stabilization concept is based on the filling of one orbital of a molecular fragment with two electrons exclusively from a LB group (i.e. formation of a dative bond), forcing the electrons that would otherwise be in this orbital to be accommodated by other orbitals. Thus, base-stabilization allows synthetic and computational chemists to play with the amount of electrons that a carbon (or any other) atom is able to contribute to a delocalized π system. Taking a neutral divalent sp^2 carbon atom as an example relevant to homoaromatics, formal LB donation would "force" two electrons into the carbon's π system, allowing us to simulate the π-electron contribution of a carbanion without making the system negatively charged – a clearly unfavoured situation for homoaromatics. When the Lewis base is a heterocyclic carbene, it should be noted that such a system presumably exists as a mixture of the Lewis adduct resonance form NHC→CR_2 and the zwitterionic form. However, this assumes that the heterocyclic Lewis base remains perpendicular to the plane of the sp^2 carbon atom. If the two are allowed to become coplanar or near-coplanar, π electron acceptance by the carbene carbon atom will result in domination of the bonding situation by a quinoidal form. Therefore, enforcing the desired perpendicular adduct form requires disfavouring the coplanar structure either sterically (using large blocking groups) or electronically (use of poorly π-accepting donors).

Computational Details

Geometry optimization was carried out using the Gaussian09[137] program at the B3LYP/6-311G* level.[138–144] To obtain the singlet state, spin-restricted calculations were performed constraining the projection of the total electronic spin along a reference axis to 0. Frequency calculations

were conducted to determine if each stationary point corresponds to a minimum. The Wiberg bond indexes (WBI)[145] were determined in Natural Bond Orbital (NBO) basis.[146,147] Nucleus-independent chemical shift (NICS)[148,149] values were determined at the B3LYP/6-311G* level of theory using the gauge independent atomic orbital (GIAO) method as implemented in Gaussian09.[150,151] ^{13}C-NMR shifts were calculated with the GIAO method using the corresponding TMS shielding calculated at the same level of theory as reference. The Jmol program was used for visualisation purposes.[152] The effect of dispersion was assessed by inclusion of the D3 version of Grimme's dispersion both with and without the Becke-Johnson damping in addition to using a diffuse function into the Pople basis set.[153–155]

Results and Discussion

Criteria for homoaromaticity. Our criteria for judging the homoaromaticity of a molecule are for the most part based on those set out by Williams in his authoritative review on the subject.[117] However, as with so many concepts in chemistry, homoaromaticity is a continuum. In general, decisive classification into homoaromatic and non-homoaromatic is unwise, and no quantitative measure of the phenomenon exists. Nevertheless, the criteria for homoaromaticity considered herein are: (A) Homoconjugation as determined by visible conjugated (or near-conjugated) π orbitals across the no-bond portion(s) of the molecule. This is found by analysis of the highest occupied molecular orbitals and gives a first indication that homoaromaticity might be present. (B) Significant through-space interactions in the no-bond portion(s) of the molecule as measured by Wiberg Bond Indices and relatively small "homoconjugative gap(s)". The review by Williams[117] states that "the homoconjugative gap should range between 1.8 and 2.2 Å and is ideally approximately 2 Å". (C) Bond length equalization in the σ-bonded system as determined by the calculated geometry. (D) Equalization of the ^{13}C NMR shifts of the carbon nuclei in the homoaromatic system, as determined by GIAO NMR calculations. (E) Aromatic magnetic effects,

as determined by calculated $NICS_0$ values ($NICS_1$ values, usually a better gauge of aromaticity, are of limited utility here due to the highly non-planar nature of homoaromatic systems). (F) Positive homoaromatic stabilization energies, i.e. the relative stability of the homoaromatic molecule over analogous molecules with isolated π-systems. These are obtained using homodesmotic equations, as described by Freeman.[156] Here we add two further criteria particular to Lewis donor-stabilized systems: (G) The donor groups must bind such that they remain near-perpendicular to the plane of the carbon atom to which it is attached, in order to rule out inter-ring (quinoidal) π-bond formation and to ensure that the necessary two electrons are provided to the homoaromatic ring. The inter-ring C_{carb}-C distances and WBIs should also be examined in order to rule out extensive quinoidal character. (H) Given the need for the heterocyclic carbenoids to act as Lewis donors in this study, the heterocyclic ring should remain planar. Strong deviations from planarity would indicate that the heterocyclic unit is acting less like a Lewis donor and more like (half of) a quinoidal alkene unit.

An illustrative experimental demonstration of the effect of a Lewis donor inducing (conventional) aromaticity can be found in a study by Kunz et al.,[157] wherein neutral molecules [NHC→C_5H_3R] showed very little C-C bond length alternation in the homocyclic ring and very long inter-ring C_{carb}-C distances (1.430(3) and 1.436(7) Å), with only modest inter-ring angles (32.0 and 23.8°). The compounds were thus described as having high ylidic character, despite these small angles. The norbornen-7-yl (I) and homotropylium (II) cations were chosen as benchmark homoaromatic models.

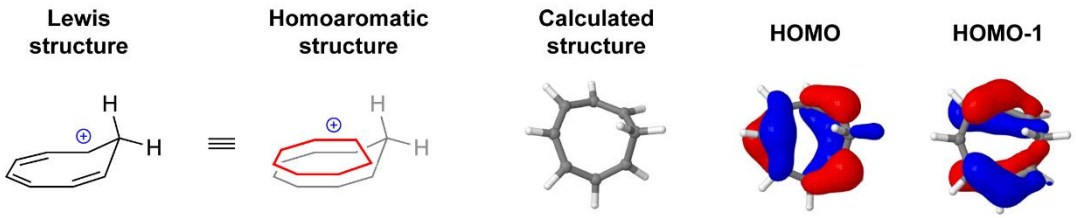

Figure 11: Lewis structure, proposed homoaromatic structure, calculated structure and highest occupied molecular orbitals of the homotropylium cation (II) as a homoaromatic benchmark.

The norbornen-7-yl cation I was found to rearrange to a non-homoaromatic structure. In contrast, II optimized to an apparently homoaromatic structure, in which the carbon atoms astride the homoconjugative gap appeared to approach each other, with a C-C distance within the range stipulated by Williams[117] (*d*(C-C) = 2.15 Å; Figure 2 and Table 1) and a significant WBI between these atoms (0.24). Further indicators of homoaromaticity are all in order: the HOMO of II showed clear homoconjugation (π orbital overlap spanning the no-bond portion), bond length equalization in the π system (*d*(C-C) = 1.38-1.40 Å), equalization of ^{13}C NMR shifts (δ 140-157), a large negative $NICS_0$ value (–10.13), and a significant positive homoaromatic stabilization energy (19.38 kcal mol^{-1}). Thus, II fulfils the applicable criteria A-F, providing a useful positive control for comparison with our donor-stabilized examples.

	WBIs in the π-system	WBI(s) of C_{carb}-C bonds	Inter-ring torsion angles	C-C distances in π⍰system	C_{carb}-C distances	δ(^{13}C) in π$_{system}$	δ(^{13}C) of C_{carb}	$NICS_0$
II	1.53, 1.36, 1.43, 1.43, 1.36, 1.52, **0.24**	n/a	n/a	**2.15**, 1.38, 1.40, 1.40, 1.40, 1.40, 1.38	n/a	140, 152, 157, 146, 157, 152, 140	n/a	–10.13
1	1.18, 1.78, **0.08**, 1.66, 1.20, 1.67	1.06	56.9 / 55.9	**2.45**, 1.44, 1.35, 1.36, 1.44, 1.36	1.46	149, 137, 126, **106**, 146, 134	154	–3.67
2	**0.02**, 1.15, 1.76, **0.01**	1.64, 1.47	–21.8 / –25.6 20.4 / 9.8	**2.45**, **2.48**, 1.45, 1.35	1.35, 1.38	**100**, **97**, 122, 107	147, 151	–1.18
3	1.30, **0.13**, **0.21**, 1.45, 1.49	1.26, 1.16	30.6 / 54.9 30.6 / 30.2	**2.40**, **2.25**, 1.42, 1.39, 1.38	1.41, 1.44	**78**, **54**, 97, 125, 107	154, 158	–11.49
4	1.72, **0.02**, 1.72, 1.11, 1.11	1.26	–66.2 / –59.3	**2.49**, 1.35, 1.35, 1.46, 1.46	1.42	143, 110, **86**, 143, 111	160	+2.78
5	1.77, **0.06**, 1.20, 1.57, 1.16	1.29	54.2 / 62.0	**2.46**, 1.35, 1.45, 1.37, 1.44	1.43	130, 127, 114, 146, **78**	157	–1.35
6	1.17, 1.78, **0.07**, 1.67, 1.14, 1.70	1.01	–95.9 / –87.0	**2.48**, 1.44, 1.35, 1.36, 1.45, 1.36	1.49	143, 134, 144, **125**, 153, 138	156	–2.24
7	1.18, 1.77, **0.08**, 1.70, 1.18, 1.68	1.01	–69.7 / –64.6	**2.46**, 1.44, 1.35, 1.36, 1.44, 1.36	1.48	143, 136, 125, **113**, 141, 134	100	–4.01
8	1.17, 1.78, **0.09**, 1.71, 1.13, 1.69	0.99	80.2 / 79.5	**2.43**, 1.44, 1.35, 1.36, 1.45, 1.36	1.49	142, 134, 127, 132, **131**, 139	98	–3.94
9	1.18, 1.77, **0.08**, 1.77, 1.14, 1.63	0.99	–97.0 / –103.2	**2.43**, 1.44, 1.35, 1.35, 1.45, 1.37	1.49	149, 131, 131, 126, 137, **132**	101	–3.74

Table 5: Calculated indicators of homoaromaticity for benchmark molecules I and II and promising candidates 1-9 (figure 12).

For Table 5 Wiberg bond indices for interactions spanning the homoconjugative gap are shown in bold. Inter-ring N-C-C-C (NHC) or C-C-C-C (bent allene) torsion angles (in °). Distances between carbon atoms spanning the homoconjugative gap are shown in bold (in Å). Chemical shifts of carbene-bound carbon nuclei are shown in bold (shifts shown in ppm).

A number of Lewis-donor-bound candidate molecules were calculated based on their predicted homoaromaticity, however, only a cursory qualitative analysis was required in order to exclude most of these. These rejected molecules included mono- and bicyclic structures, with up to three Lewis donor groups, both 2π and 6π homoaromatic systems, and with net charges ranging from +2 to –2. The rejected candidates were rejected for a variety of reasons which include lack of

visible homoconjugation, coplanarization of the Lewis donor units with the attached rings, deviation from planarity of the Lewis donor unit, and in most cases combinations thereof. A number of anionic candidates were found to rearrange during optimization and formed non-classical cluster structures.

The first round of candidate molecules included the small NHC IMe (1,3-dimethylimidazole-2-ylidene), and in general suffered from unacceptable coplanarization of the Lewis donor and its attached ring. In order to prevent this, and the resulting quinoidization, the Lewis donors were replaced with the much more bulky NHC I^{t}Bu (1,3-di-*tert*-butylimidazole-2-ylidene); carbon atoms adjacent to these carbene connections were also methylated where possible to further disfavour coplanarity. In almost all cases, the increased bulk of the donor groups led to pyramidalization of the NHC nitrogen atoms, presumably due to the extreme steric bulk.

A second strategy for reducing quinoidization was envisaged based on reducing the π-accepting ability of the Lewis donor, reasoning that this would minimize the likelihood of π bond formation between the rings. Here we turned to the so called “bent allenes”, persistent, neutral molecules developed by Bertrand and coworkers.[158–161] Despite their description as allenes, these species possess a carbene-like carbon atom with stronger σ-donor ability and weaker π acceptance. Replacing the IMe donors with BA units led to similar quinoidization in most cases and in general these molecules were only slightly superior to the previous models. It should be noted also that in one molecule in which two BA donors were bound to two adjacent carbon atoms, the BA units were found to undergo C-C bond formation between their C_β atoms.

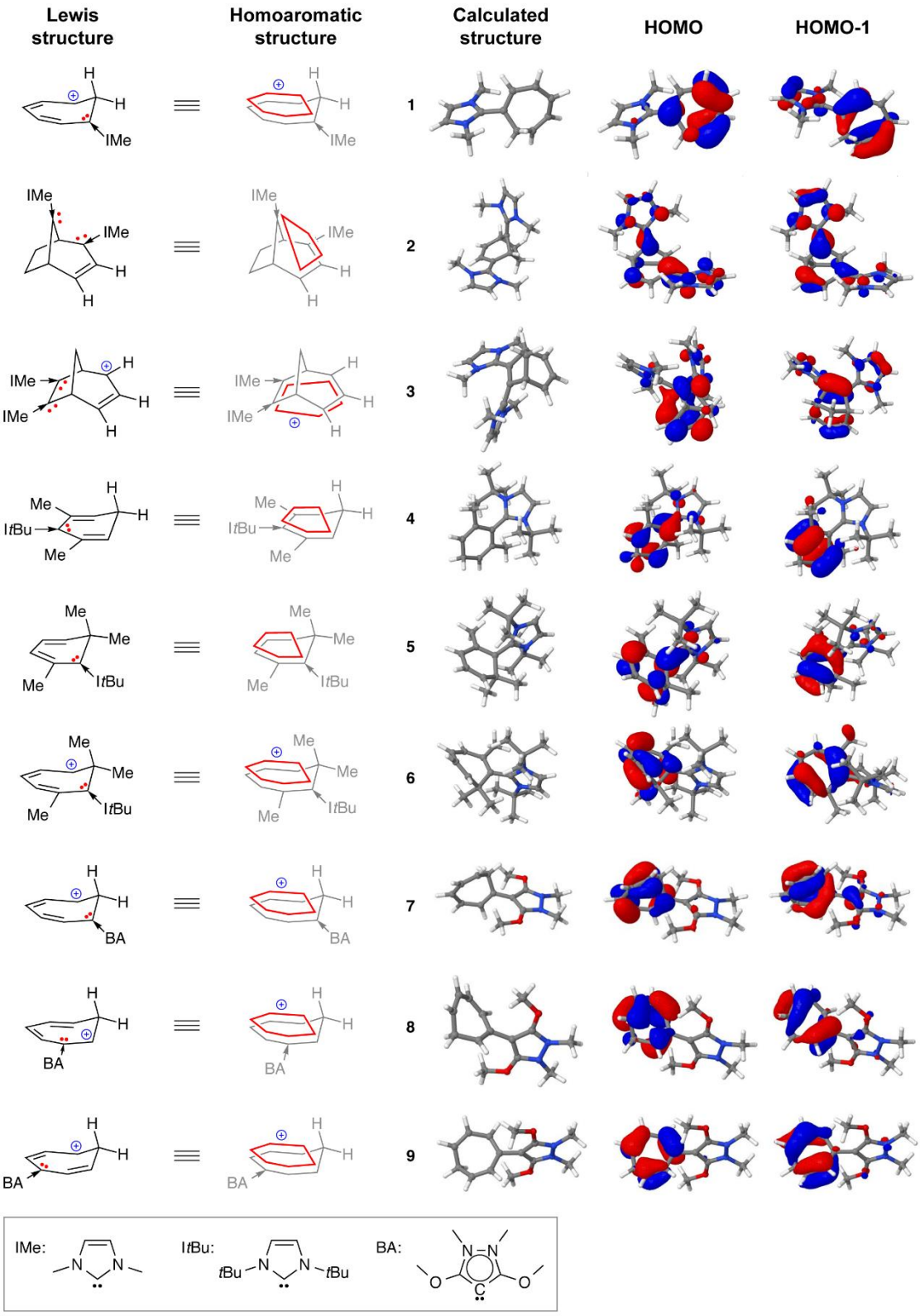

Figure 12: Lewis structures, proposed homoaromatic structures, calculated structures and highest occupied molecular orbitals of base-stabilized compounds

Promising candidates **1-9** were chosen on the basis of either possible homoconjugation (by visual analysis of HOMOs), non-coplanarity of donor and attached rings, and planar donor heterocycles, except molecule **2**, which has visibly pyramidalized nitrogen atoms (Figure 12). All of these (except molecule **2**) are 6π-electron systems based on five or six atoms, and all have net charges of either 0 or +1. It is noteworthy that candidates with negative charges or high positive charges (greater than +1), 2π-electron systems, or fewer than five sp^2 conjugated C atoms (apart from **2**) were all rejected. It was also found that carbene stabilization in these molecules causes perturbations in the ^{13}C NMR shifts around the rings that could not be rationalised. These effects, in addition to the three different NHCs present in **1-9**, mean that ^{13}C NMR data do not provide meaningful information for the analysis below. Candidates **1** and **6-9** are all based on the same seven-membered monocyclic ring, with six sp^2 carbon atoms, and are essentially ring-contracted analogues of the homotropylium cation, where the loss of one carbon atom from the latter is compensated by the extra electron provided by the Lewis donor. While **1** is the basic IMe-containing model, **6** is the bulky and methylated I*t*Bu analogue, and **7-9** are the three constitutional isomers of the BA analogue. Cations **1** and **6-9** were all found to have small but non-negligible bonding interactions across the homoconjugative gap (WBIs: 0.07 to 0.08), long inter-ring C-C distances and small but negative $NICS_0$ values (–2.24 to –4.01). From all of these measures, modest homoaromaticity can be inferred in cations **1** and **6-9**.

As alluded to above, homoaromaticity in bicyclic bis(NHC) compound **2** can be ruled out based on the non-planarity of the donor units, but also its negligible bonding over the homoconjugative gaps (WBIs: 0.01, 0.02), significant inter-ring multiple bonding (WBIs: 1.47, 1.64; $d(C_{carb}\text{-}C)$: 1.35, 1.38) and nominal bond distance equalization. It can be assumed that homoaromaticity in such a molecule is at least partly avoided due to the unfavoured situation in which six electrons occupy a four-atom π-system.

Neutral molecules **4** and **5** are both based on a six-membered monocyclic framework, with six electrons in a five-atom π-system, with the bulky I^{t}Bu group bound γ and α to the sp^3 carbon atom, respectively. These two compounds were classified as promising based on HOMO lobes that show possible bonding overlap. Due to geometrical constraints, the carbon atoms astride the homoconjugative gap in **4** appear unable to bend towards each other, preventing homoconjugation, while those of **5** appear to bend slightly, creating modest homoconjugation. This is borne out by the metrics in Table 1, which show a negligible bonding interaction across the homoconjugative gap of **4** but a small amount in **5**. The homoaromaticity of **4** is therefore judged to be negligible, while that of **5** is comparable to that seen in **1** and **6-9**.

By far the standout of the candidates **1-9** is cation **3**. Like neutral **2**, cation **3** is based on a bicyclic, bis(NHC) framework, but has one extra sp^2 carbon atom in its π-system. Cation **3** is selected as lead candidate as it was the only model that showed explicit π-bonding lobes spanning its homoconjugative gap. In line with this observation, **3** shows significant bonding between these carbon atoms (WBIs: 0.13, 0.21) of comparable strength to that seen in benchmark **II**. Other metrics also indicate a level of homoaromaticity that is clearly stronger than the other candidates but slightly weaker than that of **II**, including relatively short no-bond C-C distances (2.25 and 2.40 Å) and significant bond length equalization. That cation **3** also has a more negative NICS value than **II** is another compelling argument for homoaromaticity in the former. However, weak quinoidization can also be also inferred from the greater-than-unity inter-ring WBIs and relatively low inter-ring torsion angles. This suggests that there is a very small amount of interaction between two of the hydrogen-bearing sp^2 carbons across the homoconjugative gap to the corresponding carbene carbon atom, a conclusion that is borne out by visual inspection of the HOMO of the cation.

Stabilization energy calculations were carried out according to a modification of those established by Freeman.[156] This method differs due to the additional π-electron density provided by the NHC. Thus the right-hand side (RHS), consisting of the separated π-terms, was modified to consist of 3 terms where each term is a 2 π-electron system. This requires an additional alkane term on the left-hand side (LHS), which consists of the parent molecule and an alkane, in order to chemically balance both sides of the equation i.e. both sides of the equation must pertain to an equal number of atoms. The alkane molecules allow this as each acts as a 'blank' molecule, thus allowing for the contribution of the π-system to be assessed in isolation. Each term was geometry optimized at the same level of theory as above and the zero-point energy correction was applied individually to each term by taking the sum of the electronic and zero-point energies from the frequency calculation output. The calculation of the stabilisation energies is displayed below.

$$SE = E_{\pi-term1} + E_{\pi-term2} + E_{\pi-term3} - E_{Parent} - 2E_{Alkane}$$

Equation 20: A modified homodesmotic equation to calculate the stabilization due to aromatic behaviour.

The stabilization energy calculated for benchmark **II** is 19.38 kcal mol^{-1}, while those calculated for **1-9** are considerably lower (3-11 kcal mol^{-1}), with the exception of that of **3** (72.90 kcal mol^{-1}). This apparently anomalous value is at odds with the other metrics presented here, which suggest that the homoaromaticity of **3** is significant but slightly weaker than that of **II**. We feel that this result highlights a limitation of the stabilization energy technique in cases where the bonding to external groups is variable, i.e. the base-stabilized/quinoid continuum of the carbene-bound systems herein. The stabilization energy technique is presumably only reliable in cases where the bonding to the substituents remains constant; in other words, comparing the

energy of a model with pure σ-donor carbene bonding with a model with quinoidal (multiple) bonding will lead to anomalous results. The full results are shown below in tables 2 and 3.

Compound	Stabilisation Energy (Kcal mol^{-1})		
	Standard	**GD3**	**GD3BJ**
Homotropylium	21.0	20.2	20.4
1	9.4	8.9	9.2
2	10.9	11.1	11.2
3	74.3	76.5	76.8
4	3.9	9.7	5.8
5	11.6	14.2	14.5
6	10.7	10.8	10.9
7	7.2	6.3	7.3
8	7.8	6.8	7.6
9	7.1	5.9	6.6

Table 6: Stabilisation energies for promising homoaromatic candidates including an assessment of the impact of dispersion.

Compound	Zero-Point Energy Corrected Stabilisation Energy (Kcal mol^{-1})		
	Standard	**GD3**	**GD3BJ**
Homotropylium	19.4	18.6	18.8
1	8.6	8.2	8.6
2	10.8	10.9	11.1
3	72.9	75.0	75.5
4	3.0	8.4	5.4
5	11.1	13.0	13.6
6	10.3	-	-
7	6.4	5.8	6.5
8	7.1	6.5	7.1
9	6.4	5.6	6.1

Table 7: Zero-point energy corrected stabilisation energies for promising homoaromatic candidates including an assessment of the impact of dispersion.

To confirm whether the carbene units are indeed instrumental in producing the homoaromaticity of cation 3, isoelectronic analogues of 3 with the same [3.2.1] bicyclic structure and 6-electron π systems were modelled by sequential replacement of the neutral [NHC]0 fragments with [H]–units, resulting in the neutral mono(NHC) molecules 3_{neutA} and 3_{neutB} and the

anionic compound 3_{minus} (Figure 3, top). Upon geometry optimization, the neutral molecules 3_{neutA} and 3_{neutB} were both observed to rearrange to geometries that rule out homoaromaticity, one to a monocyclic structure with a quinoidal C=C_{carb} bond, the other to an unusual tricyclic structure. The anionic NHC-free analogue 3_{minus} did not rearrange; however, no frontier orbitals suggestive of homoconjugation were found (Figure S5). In addition, the C(sp^2)-C(sp^2) distances spanning the insulating C(sp^3) groups (2.41 Å) are approximately equivalent to the longest analogous bond of 3. The homoaromaticity in 3_{minus}, while seemingly non-negligible, appears to be weak. However, it should be kept in mind that neutral and anionic homoaromatics are in general much rarer, presumably due to their relative instability. Thus the favourable homoaromaticity of 3 in this case may be partly due to the inherently more favourable homoaromaticity of cationic compounds.

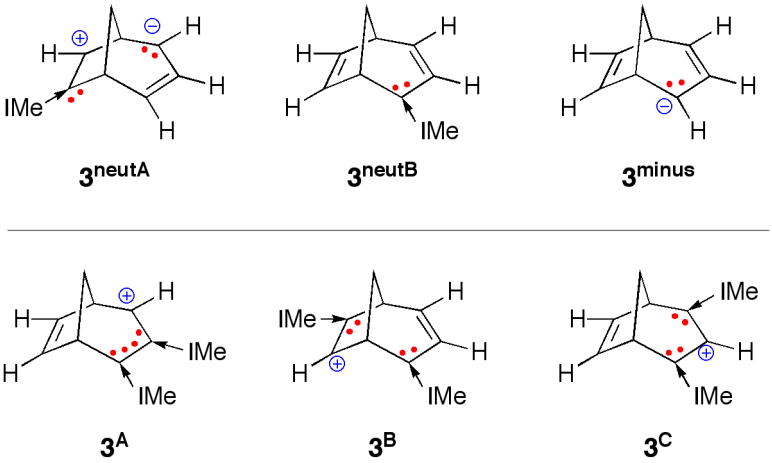

*Figure 13: Top: neutral and anionic isoelectronic analogues of 3. Bottom: constitutional isomers of **3**.*

Given the promising observation of homoaromaticity in cation 3, we were naturally interested in screening its constitutional isomers for compounds with superior homoaromaticity. Isomers 3A-C (Figure 13, bottom) were envisaged based on moving the NHC units around the sp^2 system. Upon geometry optimization, cation 3A rearranged to a non-classical structure, while 3B ring-

opened to a monocyclic cation. Cation 3C did not rearrange, however, a distinct quinoidal C=C_{carb} bond was present and no homoconjugation could be observed. Therefore, the homoaromaticity in candidate 3 appears to be unique among its isomers. One possible rationalization could be due to the favourable combination of the electron-rich NHC-C(sp^2)-C(sp^2)-NHC unit with the electron-poor allyl cation moiety on the other side of the insulating C(sp^3) bridges.

Conclusion

These calculations, while uncovering a number of promising specific leads for future exploration, also suggested a few structural features that appear to have detrimental effects on homoaromaticity, such as: (a) 2π-electron systems, (b) having too many electrons in too small a π-system, (c) negative or strongly positive net charges, (d) too much or too little steric congestion, and (e) adjacent placement of Lewis bases that can undergo C-C bond coupling (e.g. BAs). Isoelectronic and constitutional isomers of lead candidate **3** were explored, however, the homoaromaticity in these models was found to be either non-existent or vastly inferior. These results suggest that (a) the carbene units are beneficial for, and possibly the key determinant of, homoaromatic stabilization in **3**; and (b) the bicyclic cage geometry and placement of the carbenes is critical to the homoaromaticity of the system.

Chapter 4 - Boron centres allow design, control and systematic tuning of neutral homoaromatics for functionalization purposes

Foreword

The data and conclusions from Chapters 4 and 5 were published in ChemPhysChem as “Boron Centres Allow Design, Control and Systematic Tuning of Neutral Homoaromatics for Functionalization Purposes” with the author as first author.

Introduction

Homoaromatic compounds, i.e. compounds that feature a contiguous π-system with a non-contiguous σ-system, have been known for decades.[156] However such compounds are limited in scope and are generally highly charged. Density functional theory (DFT),[91,162] which has proven to be a versatile and convenient computational method offers an opportunity to screen large numbers of candidates in order to assess the basic principles of the construction of these compounds without the high (manpower and material) costs and with far easier control over structural isomerism and ultimately molecular design than traditional chemical synthesis. It was shown in previous work that computationally stable homoaromatic molecules can be designed via the use of carbenes[124–133] as two-electron donors within homotropylium and norbornyl analogues and a set of metrics for assessing the strength of homoaromaticity was proposed.[163] However, in order to maintain a significant delocalized π-cloud in the majority of the homoaromatic candidates it was found that a carbocation was required to act as an electron acceptor. This requirement for the carbocation renders it impossible to design neutral homoaromatic systems. It was also found that due to the transient nature of a positive charge within a conjugated system the carbocation would migrate to the position adjacent to the

carbene. The element boron is an ideal tool to combat these issues due to its unique properties which allow it to act as an electron 'sink'. Its ability to accept and donate charge and the fact that a tricoordinate boron atom is isolobal with a carbocation should allow for the acceptance of electron density from the carbene and its subsequent incorporation into the delocalized π-system. The ability of tricoordinate boron to mimic a carbocation and facilitate a homoconjugative interaction has previously appeared in literature.[164] The use of boron allows for control over the structural isomers thus allowing for a broader scope of design. The following sets of molecules are based on homotropylium analogues using either an N-heterocyclic carbene or bent allene[158–161] as the two-electron donor. Here, the objective is not necessarily to obtain the best example of a homoaromatic system, rather it is to acquire a measure of control over the strength of aromaticity within a molecule via the use of the structural isomers resulting from the relative arrangement of the two-electron donor, the electron acceptor, the sp^3 centre and the conjugated system.

The unique features of boron of its electron deficiency and its ability to act as an electron 'reservoir'[165,166] may also open up other avenues for the design of homoaromatic systems. Whilst it has been shown that carbenes offer a strong enough source of electron donation to stabilize a homoaromatic interaction, they are also a source of significant additional steric bulk thus incurring further complexity in attempts to functionalize homoaromatic compounds. Therefore sets of molecules have also been investigated that simply use a nitrogen atom within the ring as a two-electron donor in conjunction with a boron atom with the aim of generating a homoaromatic system with a greater utility for functionalization. A similar set of structural isomers has been characterized in order to again assess whether these compounds offer a route to the controllable modulation of the strength of aromaticity. The set of metrics for homoaromaticity as defined in a previous work will be applied in order to assess trends in the

set of designed candidates. However, given that the aim of this work is to achieve a significant amount of electron donation into the vacant p_z orbital on a boron atom an additional metric for homoaromaticity is required; the boron centres should adhere to sp^2 geometry as the vacant p_z orbital should be aligned with the delocalized π-system. Additionally, calculations have been performed to assess additional routes towards the functionalization of the systems via the addition of hetero atoms within the homoaromatic ring.

Computational Methods

Geometry optimisations were performed using the Gaussian G09 software at the B3LYP/6-311G* level of theory.[137–144,155] To obtain the singlet state, spin-restricted calculations were performed constraining the projection of the total electronic spin along a reference axis to 0, and for the triplet in the unrestricted formalism and setting the projection to 1. Frequency calculations were used to confirm a minimum.[137–144,155] Nucleus-independent chemical shift (NICS) values were determined at the same level of theory using the gauge-independent atomic orbital (GIAO) method as implemented in Gaussian09.[150,151] For ^{13}C NMR shifts the isotropic shielding was compared to the corresponding TMS values, along with ammonia for ^{15}N NMR shifts and $BF_3{\cdot}OEt_3$ for ^{11}B NMR shifts. The Wiberg bond indexes (WBI),[145] the so-called Natural charge and the second-order perturbative analysis of donor-acceptor interactions were determined in Natural Bond Orbital (NBO) basis.[146,147] It should be noted that, despite the through-space interaction being investigated, it was found that the use of additive dispersion term Grimme-D3 with BJ damping was found to be unnecessary in previous work and hence has not been included here. The Jmol program was used for visualisation purposes.[152]

Results and Discussion

Relying on a carbocation to provide the properties of a base building block can significantly convolute compound design given its large concentration of electron density and its attendant steric bulk. Given the isolobality of boron with a carbocation, and boron's documented ability to act as an electron 'sink', this element would seem the obvious choice to allow for the removal of carbocations. However the insertion of a heteroatom within a ring system increases the number of possible structural isomers which may well exhibit differing properties. Thus, a range of structural isomers have been evaluated.

The assessment of structural isomerism across multiple variations obviously requires the analysis of large numbers of compound variations; thus the schematic shown in Figure 1 will be used as the basis for a naming convention, 7-N(#)B(#)I(#)A(#) where the first number denotes ring size and the positions of two-electron (i.e. amine-type) nitrogen donors (N), boron atoms (B), carbons with an attached carbene (I) and one-electron (i.e. imine-type) nitrogen donors (A) are denoted by the number following in parentheses.

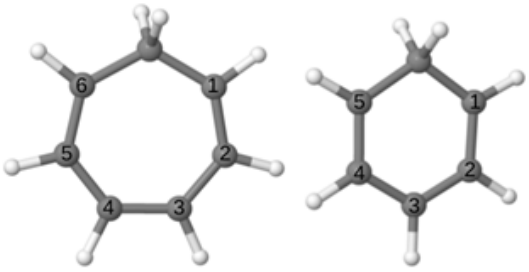

Figure 14: Schematic of the numbering system used to enable the specification of the positioning of heteroatoms.

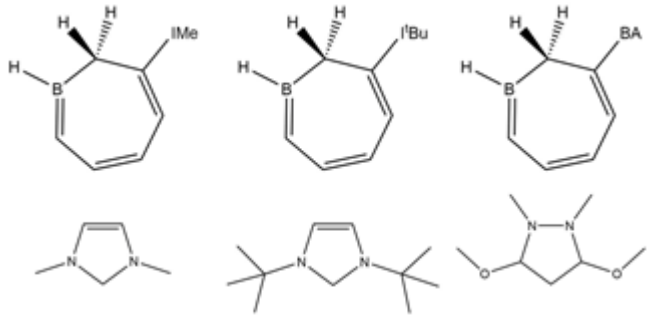

Figure 15: The homoaromatic compound 7-B(6)I(1) is shown here with the two-electron donors used, left to right; the N-heterocyclic carbenes IMe and ItBu along with a bent allene (BA).

The resultant evaluation of the properties of boron and carbene including homoaromatic candidates is shown below in Tables 8-10.

Compound identifier	WBI of the homo-conjugative gap	Inter-ring torsion angles	Homoconjugative gap distance	δ(^{13}C) in the π-system	δ(^{13}C) of C_{carb}	δ(^{11}B)	$NICS_0$
7-B(4)I(3)	0.04	42.6 / 52.6	2.50	105, 134, 111, 140, 141	170	39	-1.22
7-B(6)I(1)	0.14	-37.3 / -38.0	2.36	62, 136, 120, 147, 137	156	26	-5.28
7-B(2)I(1)	0.09	35.1 / 40.0	2.46	137, 124, 128, 119, 102	168	34	-4.26
7-B(1)I(2)	0.04	-39.1 / -36.5	2.55	151, 144, 135, 131, 100	167	37	-1.20
7-B(2)I(3)	Rearranged						
7-B(4)I(1)	0.04	-34.8 / -37.6	2.55	154, 125, 149, 135, 87	159	43	-1.22

Table 8: Calculated indicators of aromaticity for seven-membered, boron-substituted, structural isomers with a carbene donor. Inter-ring torsion angles are between Ncarb-Ccarb-C-C (in °). Chemical shifts of carbene-bound carbon nuclei are shown in ppm.

Compound identifier	WBI of the homo-conjugative gap	Inter-ring torsion angles	Homoconjugative gap distance	δ(^{13}C) in the π-system	δ(^{13}C) of C_{carb}	δ(^{11}B)	$NICS_0$
7-B(4)I(3)	0.05	96.3 / 102.0	2.48	102, 147, 107, 135, 143	175	40	-1.77
7-B(6)I(1)	0.13	-82.7 / -87.1	2.49	92, 141, 113, 148, 121	164	32	-5.61
7-B(2)I(1)	0.09	80.8 / 75.3	2.46	147, 120, 128, 119, 100	175	35	-4.50
7-B(1)I(2)	0.06	-89.4 / -93.0	2.53	154, 140, 132, 145, 102	174	34	0.02
7-B(2)I(3)	0.13	100.3 / 88.3	2.39	146, 124, 118, 106, 144	173	29	-4.92
7-B(4)I(1)	0.06	-95.1 / -86.3	2.52	157, 120, 147, 141, 81	165	36	-1.96

Table 9: Calculated indicators of aromaticity for seven-membered, boron-substituted, structural isomers with a carbene donor including additional steric bulk. Ordered as per Table 8.

Compound identifier	WBI of the homo-conjugative gap	Inter-ring torsion angles	Homoconjugative gap distance	δ(^{13}C) in the π-system	δ(^{13}C) of C_{carb}	δ(^{11}B)	$NICS_0$
7-B(4)I(3)	0.06	-91.4 / -74.2	2.49	100, 144, 101, 128, 142	117	35	-2.66
7-B(6)I(1)	0.16	-66.4 / -77.3	2.39	64, 133, 109, 144, 128	109	18	-8.03
7-B(2)I(1)	0.13	-108.7 / -99.7	2.42	142, 117, 126, 108, 100	116	21	-6.70
7-B(1)I(2)	0.07	-118.6 / -119.3	2.49	153, 138, 132, 121, 83	117	29	-2.36
7-B(2)I(3)	0.12	92.0 / 78.9	2.43	141, 124, 115, 111, 144	116	25	-4.67
7-B(4)I(1)	0.07	65.2 / 65.2	2.50	152, 120, 149, 120, 63	109	35	-3.26

Table 10: Calculated indicators of aromaticity for 7-membered, boron substituted structural isomers with a bent allene donor. Ordered as per Table 8.

As in previous work the addition of steric bulk, i.e. exchanging IMe for I^{t}Bu (as shown in Figure 15) and adding methyl groups to the adjacent carbon atoms, in order to prevent the quinoidization of the carbine, tends to provide stronger homoaromatic interactions among the candidates, as does the replacement of the carbene with a bent allene to decrease π-donation back onto the donating group. The data shown in Tables 8, 9 and 10 correspond to the candidates IMe, I^{t}Bu and a bent allene respectively. Note that Table 1 shows the rearrangement of 7-B(2)I(3), this is most likely due to high quinoidization of the IMe creating a severe lack of electron density within the ring system as reducing the risk of quinoidization allows for a retention of the homoaromatic ring structure. It is immediately evident that there exists a significant range of the strength of the homoaromatic interaction across the differing structural isomers. Despite the increase in degree of aromaticity, the trend among the structural isomers is largely maintained. That is, the homoaromaticity seems at its strongest when the boron-carbene interaction bridges the homoconjugative gap. Unsurprisingly, bond length deviation between structural isomers is slight, but some decrease in the size of the homoconjugative gap can be seen with an increase in homoaromatic character. The presence of appreciable bond orders across the homoconjugative gap and negative $NICS_0$ values suggests the majority of the structural isomers show homoaromatic character. However, the equalisation of bond orders, bond length and ^{13}C shifts is lacking. This is likely due to the introduction of the heteroatom into

the ring. It should be noted that the torsion angles indicate only slight quinoidization of the carbine, however, quinoidization is heavily present in the IMe candidates.

Compound identifier	WBI of the homo-conjugative gap	Inter-ring torsion angles	Homoconjugative gap distance	δ(^{13}C) in the π-system	δ(^{13}C) of C_{carb}	δ(^{11}B)	$NICS_0$
6-B(2)I(3)	0.01	-7.8 / 2.8	2.58	131, 125, 48, 77	144	82	-3.49
6-B(1)I(3)	0.09	28.9 / 23.8	2.24	132, 124, 66, 76	152	119	-6.11
6-B(2)I(1)	0.01	2.0 / 21.8	2.56	112, 144, 54, 72	151	82	-6.24
6-B(4)I(1)	0.01	26.6 / 25.9	2.60	49, 96, 154, 84	156	87	-1.89
6-B(3)I(1)	0.01	-19.3 / -27.7	2.58	158, 125, 76, 77	157	99	-2.66
6-B(5)I(1)	0.09	28.2 / 20.4	2.32	113, 117, 58, 82	151	94	-6.10
6-B(1)I(2)	0.19	12.6 / 21	2.45	76, 135, 97, 98	150	70	-9.41

Table 11: Calculated indicators of aromaticity for 6-membered, boron substituted structural isomers with a carbene donor. Ordered as per Table 8.

Compound identifier	WBI of the homo-conjugative gap	Inter-ring torsion angles	Homoconjugative gap distance	δ(^{13}C) in the π-system	δ(^{13}C) of C_{carb}	δ(^{11}B)	$NICS_0$
6-B(2)I(3)	0.01	22.8 / 35.3	2.58	152, 130, 58, 93	152	71	-3.50
6-B(1)I(3)	0.09	56.7 / 53.4	2.24	143, 125, 93, 84	152	127	-4.16
6-B(2)I(1)	0.02	51.7 / 72.9	2.56	128, 140, 57, 65	155	76	-6.00
6-B(4)I(1)	0.04	87.6 / 88.6	2.58	61, 65, 163, 89	160	92	-7.21
6-B(3)I(1)	0.02	-47.3 / -56.3	2.54	168, 118, 84, 98	152	104	-3.54
6-B(5)I(1)	Rearranged						
6-B(1)I(2)	0.19	54.4 / 57.0	2.47	91, 138, 98, 105	165	67	-9.30

Table 12: Calculated indicators of aromaticity for 6-membered, boron substituted structural isomers with a carbene donor with additional steric bulk. Ordered as per Table 8.

Compound identifier	WBI of the homo-conjugative gap	Inter-ring torsion angles	Homoconjugative gap distance	δ(^{13}C) in the π-system	δ(^{13}C) of C_{carb}	δ(^{11}B)	$NICS_0$
6-B(2)I(3)	0.01	-41.4 / -17.5	2.57	137, 124, 56, 60	115	75	-4.72
6-B(1)I(3)	0.14	-81.4 / -97.0	2.40	137, 115, 87, 42	111	109	-8.44
6-B(2)I(1)	0.02	-63.0 / -34.2	2.57	113, 148, 52, 58	120	77	-7.00
6-B(4)I(1)	0.03	-108.5, -100.8	2.56	44, 61, 157, 75	109	84	-4.78
6-B(3)I(1)	0.02	49.5 / 61.7	2.53	84, 142, 135, 43	120	163	-6.48
6-B(5)I(1)	0.21	-57.9 / -54.1	2.26	119, 94, 66, 52	112	85	-10.36
6-B(1)I(2)	0.17	-61.9 / -81.3	2.50	95, 132, 118, 90	108	102	-6.51

Table 13: Calculated indicators of aromaticity for six-membered, boron-substituted structural isomers with a bent allene donor. Ordered as per Table 8.

Tables 11-13 show data for the six-membered rings where the boron atom acts to both donate an electron to the π-system and to partially accept the pair of electrons provided by the carbene. This should be possible as a result of boron's apparent capability to act as a charge redirection

node. In this case the set of data using bent allenes in place of the carbene is shown due to the rearrangement of some of the candidates with the other data sets, likely due to an excessive acceptance of electron density by the boron centre. Here, the six-membered rings seem to show a greater magnitude of interaction across the homoconjugative gap than that of similar seven-membered compounds. However, in cases such as 6-B(2)I(3) and 6-B(3)(1), where the majority of the metrics of homoaromaticity suggest the likelihood of only a weak homoaromatic system there is still a significant $NICS_0$ value suggesting that some perturbation of the $NICS_0$ value is incurred due to the reduced size of the surrounding sigma-bond system. Thus $NICS_0$ may be insufficient as a metric by its own merits. A highly conjugated system appears to be exhibiting a large $NICS_0$ value without necessarily possessing aromaticity. Whilst this appears to be contrary to previous literature, it seems possible that a non-continuous sigma system may reduce the $NICS_\sigma$ component resulting in an artificially negative NICS value.[148,149] Thus it is necessary to examine the bond order across the gap in the sigma system as well as the symmetry around the individual atoms as a system where the boron accepts more electron density may not result in a stronger homoaromatic interaction.

Compound identifier	WBI of the homo-conjugative gap	Homoconjugative gap distance	$\delta(^{13}C)$ in the π-system	$\delta(^{13}C)$ of C_{carb}	$\delta(^{11}B)$	$NICS_0$
7-N(2)B(1)	0.02	2.57	124, 143, 131, 141	114	40	-3.41
7-N(1)B(2)	0.03	2.47	133, 138, 148, 147	140	32	-0.98
7-N(3)B(4)	0.04	2.51	136, 111, 150, 137	168	35	-0.84
7-N(1)B(6)	0.08	2.49	143, 107, 156, 137	104	39	-2.70
7-N(1)B(4)	0.04	2.47	156, 114, 152, 136	120	47	-0.80
7-N(3)B(6)	0.11	2.38	101, 129, 142, 119	162	37	-6.78

Table 14: Calculated indicators of aromaticity for seven-membered, boron-substituted, structural isomers where two-electron donation occurs from a [N-H] fragment within the ring. Chemical shifts are shown in ppm.

Compound identifier	WBI of the homo-conjugative gap	Homoconjugative gap distance	δ(^{13}C) in the π-system	δ(^{15}N) of N	δ(^{11}B)	$NICS_0$
7-N(2)B(1)	0.09	2.43	138, 121, 128, 125	206	26	-5.10
7-N(1)B(2)	0.04	2.47	134, 138, 146, 148	188	32	-1.83
7-N(3)B(4)	0.03	2.47	138, 114, 150, 139	207	34	-1.28
7-N(1)B(6)	0.09	2.49	142, 107, 155, 136	145	37	-3.97
7-N(1)B(4)	0.04	2.48	155, 114, 152, 137	163	45	-1.43
7-N(3)B(6)	0.12	2.31	100, 130, 143, 120	193	35	-7.52

Table 15: Calculated indicators of aromaticity for seven-membered, boron-substituted, structural isomers where two-electron donation occurs from a [N-H] fragment within the ring with additional steric bulk to form a [N-^{t}Bu} fragment. Chemical shifts are shown in ppm.

Despite their synthetic accessibility, there are experimental difficulties inherent in incorporating carbenes, and thus instances of homoaromaticity, into larger systems. This is made more difficult by the need for additional bulk to prevent quinoidization. Thus, in order to allow for additional functionality the [C-carbene] fragments were substituted with isoelectronic [N-H] fragments within the ring. Here the greater propensity of boron to accept electron density should compensate for the decrease of donor strength.

Table 15 shows data with a [N-^{t}Bu] fragment as the donor as these compounds tend to show a greater degree of homoaromatic character. Whilst the increased steric bulk of this fragment is of less consequence as there is obviously no need to prevent quinoidization, the positive inductive effect should increase the electron density upon the nitrogen donor and thus aid in the donation of the electron pair into the homoaromatic system. They again show significant bond orders and $NICS_0$ values across the homoconjugative gap and similar geometric trends. There is a slight decrease in the strength of the homoaromatic interaction. However, contrary to the carbene-stabilized compounds, the strongest interactions appear to occur when only the boron atom is adjacent to the homoconjugative gap. This suggests that the unique electron acceptor properties of boron can allow for the formation of homoaromatic compounds using nitrogen as a two-electron donor whilst remaining a neutral compound.

Compound identifier	WBI of the homo-conjugative gap	Homoconjugative gap distance	δ(^{13}C) in the π-system	δ(^{15}N) of N	δ(^{11}B)	$NICS_0$
6-N(1)B(5)	0.06	2.27	122, 81, 50	130	124	-6.93
6-N(1)B(4)	0.03	2.50	156, 82, 87	119	52	-4.78
6-N(1)B(3)	0.03	2.52	85, 125, 168	79	79	-4.34
6-N(1)B(2)	0.02	2.51	40, 145, 114	89	75	-7.64
6-N(3)B(5)	0.12	2.22	117, 136, 89	85	132	-8.05
6-N(3)B(4)	0.01	2.56	130, 139, 44	107	67	-5.28
6-N(2)B(1)	0.37	2.47	121,127,68	161	61	-10.18

Table 16: Calculated indicators of aromaticity for six-membered, boron-substituted, structural isomers where two-electron donation occurs from a [N-H] fragment within the ring. Chemical shifts are shown in ppm.

Compound identifier	WBI of the homo-conjugative gap	Homoconjugative gap distance	δ(^{13}C) in the π-system	δ(^{15}N) of N	δ(^{11}B)	$NICS_0$
6-N(1)B(5)	0.12	2.36	124, 103, 63	118	71	-10.22
6-N(1)B(4)	0.04	2.54	156, 76, 48	153	86	-5.97
6-N(1)B(3)	Rearranged					
6-N(1)B(2)	0.02	2.51	44, 146, 113	131	69	-8.27
6-N(3)B(5)	0.13	2.19	113, 134, 126	117	87	-8.82
6-N(3)B(4)	0.01	2.56	131, 139, 44	149	64	-6.05
6-N(2)B(1)	0.29	2.45	104, 130, 82	214	48	-10.86

Table 17: Calculated indicators of aromaticity for six-membered, boron-substituted, structural isomers where two-electron donation occurs from a [N-H] fragment within the ring with additional steric bulk to form a [N-^{t}Bu} fragment. Chemical shifts are shown in ppm.

Tables 16 and 17 show data for the six-membered rings in order to again evaluate boron both donating an electron to the π-system and to partially accept the pair of electrons and pertains to the unsubstituted nitrogen data despite showing a lesser degree of homoaromaticity, due to the rearrangement of one of the ^{t}Bu substituted nitrogen structural isomers. These show a similar general increase in interaction across the homoconjugative gap as seen in the carbene-based compounds upon the reduction of the ring size and a similar broad increase in $NICS_0$ values. They again show significant interactions across the homoconjugative gap but to a lesser extent than the comparable carbene-based analogues. They also possess similar positional trends to the seven-membered variants. Given the increased potential for functionality gained from the replacement of carbenes and the inclusion of boron centres this was expanded by introducing an additional unsubstituted nitrogen atom into the ring system as a single electron donor to the homoaromatic system and thus leaving its lone pair available for chemical applications i.e. the creation of pyridine-like analogues.

Compound identifier	WBI of the homo-conjugative gap	Inter-ring torsion angles	Homo-conjugative gap distance	δ(^{13}C) in the π-system	δ(^{13}C) of C_{carb}	δ(^{15}N) of A	δ(^{11}B)	$NICS_0$
7-B(6)I(1)A(4)	0.45	34.6 / 50.0	1.86	193, 143, 113, 34	160	392	-14	-4.24
7-B(6)I(1)A(5)	0.09	39.3 / 37.3	2.37	156, 109, 139, 71	156	364	14	-4.62
7-B(6)I(1)A(3)	0.09	135.1 / 139.3	2.50	126, 167, 153, 86	164	316	34	-3.59
7-B(6)I(1)A(2)	0.14	149.0 / 158.6	2.42	140, 140, 135, 90	156	342	20	-7.38
7-B(6)I(5)A(1)	0.08	-128.4 / -134.8	2.47	159, 121, 141, 107	166	372	38	-2.72
7-B(6)I(3)A(1)	0.08	132.8 / 140.8	2.47	149, 129, 150, 102	165	348	42	-3.37
7-B(6)I(2)A(1)	0.16	127.5 / 132.9	2.34	110, 143, 139, 143	166	293	23	-8.44
7-B(2)I(1)A(6)	0.04	-140.5 / 1.39.5	2.46	163, 141, 157, 100	165	399	37	-0.88
7-B(2)I(1)A(3)	0.04	-144.1 / 143.2	2.49	141, 133, 165, 91	162	431	36	0.33
7-B(4)I(1)A(2)	0.06	28.1 / 26.2	2.47	127, 146, 158, 100	151	425	36	-2.26
7-B(4)I(3)A(1)	0.04	43.9 / 36.5	2.47	165, 145, 143, 105	168	357	39	-0.90
7-B(4)I(3)A(2)	0.05	150.6 / 135.3	2.47	131, 133, 144, 129	164	361	34	-2.32
7-B(3)I(2)A(4)	0.12	-126.6 / -107.1	2.37	133, 88, 158, 120	166	348	23	-5.35
7-B(3)I(1)A(4)	0.07	59.2 / 50.6	2.42	88, 156, 148, 102	159	368	28	-4.02

Table 18: Calculated indicators of aromaticity for 7-membered, boron substituted, structural isomers with a carbene donor and a nitrogen one-electron donor (unsubstituted N atom) introduced into the ring. Ordered as per Table 8.

Compound identifier	WBI of the homo-conjugative gap	Inter-ring torsion angles	Homo-conjugative gap distance	δ(^{13}C) in the π-system	δ(^{13}C) of C_{carb}	δ(^{15}N) of A	δ(^{11}B)	$NICS_0$
7-B(6)I(1)A(4)	Rearranged							
7-B(6)I(1)A(5)	0.10	82.3 / 88.9	2.44	157, 104, 143, 93	164	318	18	-5.93
7-B(6)I(1)A(3)	0.11	84.8 / 91.3	2.48	116, 166, 156, 99	164	307	38	-3.46
7-B(6)I(1)A(2)	0.17	87.0 / 97.1	2.41	128, 137, 126, 104	164	358	24	-8.11
7-B(6)I(5)A(1)	0.09	-79.0 / -79.3	2.44	158, 118, 151, 108	174	363	35	-4.35
7-B(6)I(3)A(1)	0.09	76.3 / 86.3	2.43	158, 126, 155, 98	168	344	34	-4.00
7-B(6)I(2)A(1)	0.12	73.6 / 76.1	2.40	114, 152, 130, 147	163	313	25	-7.05
7-B(2)I(1)A(6)	0.06	-86.8 / -90.8	2.47	158, 139, 162, 102	173	406	34	-1.09
7-B(2)I(1)A(3)	0.07	-88.4 / -91.2	2.49	151, 126, 163, 92	172	439	33	-0.17
7-B(4)I(1)A(2)	0.08	102.2 / 104.7	2.49	138, 147, 145, 100	162	401	31	-2.77
7-B(4)I(3)A(1)	0.02	-4.8 / -8.7	2.48	179, 161, 144, 130	164	374	55	0.42
7-B(4)I(3)A(2)	0.06	117.9 / 96.0	2.46	124, 128, 145, 126	171	370	36	-2.97
7-B(3)I(2)A(4)	0.08	-86.7 / -75.1	2.43	145, 88, 155, 130	166	314	30	-3.37
7-B(3)I(1)A(4)	0.06	90.0 / 91.7	2.49	105, 157, 161, 124	160	320	31	0.93

Table 19: Calculated indicators of aromaticity for 7-membered, boron substituted, structural isomers with a carbene donor with additional steric bulk and a nitrogen one-electron donor (unsubstituted N atom) introduced into the ring. Ordered as per Table 8.

Compound identifier	WBI of the homo-conjugative gap	Inter-ring torsion angles	Homo-conjugative gap distance	δ(^{13}C) in the π-system	δ(^{13}C) of C_{carb}	δ(^{15}N) of A	δ(^{11}B)	$NICS_0$
7-B(6)I(1)A(4)	0.55	30.7 / 56.0	1.78	192, 142, 123, 54	161	394	-11	-5.59
7-B(6)I(1)A(5)	0.12	63.3 / -114.9	2.39	152, 103, 134, 70	110	321	10	-7.26
7-B(6)I(1)A(3)	0.14	104.7 / 109.0	2.39	121, 164, 150, 72	108	310	24	-6.14
7-B(6)I(1)A(2)	0.20	108.7 / 109.5	2.30	132, 130, 129, 80	109	340	10	-10.18
7-B(6)I(5)A(1)	0.10	-91.1 / -95.8	2.46	156, 116, 146, 104	114	356	30	-4.76
7-B(6)I(3)A(1)	0.10	-114.4 / -98.5	2.45	151, 123, 157, 92	110	335	31	-5.19
7-B(6)I(2)A(1)	0.12	-106.6 / -101.7	2.44	114, 147, 129, 146	110	318	27	-5.64
7-B(2)I(1)A(6)	0.06	80.6 / 73.5	2.47	162, 137, 160, 95	115	380	29	-2.27
7-B(2)I(1)A(3)	0.05	119.9 / 121.7	2.52	140, 132, 162, 81	120	440	31	-0.03
7-B(4)I(1)A(2)	0.09	-113.9 / -119.9	2.45	113, 148, 149, 83	108	405	26	-4.94
7-B(4)I(3)A(1)	0.05	75.3 / 57.7	2,47	169, 135, 143, 103	115	330	37	-2.20
7-B(4)I(3)A(2)	0.07	-76.3 / -84.6	2.45	118, 120, 143, 123	116	382	29	-3.57
7-B(3)I(2)A(4)	0.08	-103.6 / -90.5	2.43	134, 88, 155, 128	108	325	29	-3.84
7-B(3)I(1)A(4)	0.07	71.6 / 70.5	2.46	83, 159, 153, 110	106	339	27	-3.07

Table 20: Calculated indicators of aromaticity for 7-membered, boron substituted, structural isomers with a bent allene donor and a nitrogen one-electron donor (unsubstituted N atom) introduced into the ring. Ordered as per Table 8.

Tables 18, 19 and 20 displays the results of the inclusion of an unsubstituted nitrogen atom into the seven-membered homoaromatic rings with IMe, I^{t}Bu and bent allene two-electron donors respectively. Again a large range of the relative strength of aromaticity is evident across a range of the structural isomers. It is also evident that the prevention of quinoidization results in a strengthening of the through-space interaction evidenced through the numerical metrics. It is apparent that a homoaromatic interaction is maintained despite the inclusion of the unsubstituted nitrogen atom within the homoaromatic system. It should be noted that 7-B(6)I(1)A(4) shows more of a formal covalent interaction over a through-space interaction, the simulated ^{11}B NMR shift suggests four-coordinate boron, the WBI is large and the gap distance is particularly short, this would suggest that the rearrangement of this candidate when utilising the I^{t}Bu two-electron donor is due to the lack of quinoidization resulting is an excess of electron density across the homoconjugative gap allowing for the formation of formal bonding.

Compound identifier	WBI of the homo-conjugative gap	Inter-ring torsion angles	Homo-conjugative gap distance	δ(^{13}C) in the π-system	δ(^{13}C) of C_{carb}	δ(^{15}N) of A	δ(^{11}B)	$NICS_0$
6-B(5)I(1)A(2)	0.10	15.3 / 18.8	2.31	119, 136, 59	152	330	106	-6.89
6-B(5)I(1)A(3)	0.08	-155.1 / -150.9	2.29	103, 137, 80	154	328	116	-6.13
6-B(5)I(1)A(4)	0.06	20.2 / 28.9	2.29	135, 117, 87	155	221	63	-3.61
6-B(4)I(1)A(2)	0.02	-16.9 / -17.0	2.59	57, 120, 102	153	430	91	-0.36
6-B(4)I(1)A(3)	0.01	-147.1 / -150.9	2.61	31, 170, 90	159	286	72	-2.28
6-B(4)I(1)A(5)	0.03	-155.1 / -150.5	2.52	79, 162, 91	156	189	53	-1.96
6-B(3)I(1)A(2)	0.01	-9.0 / -8.0	2.59	152, 118, 92	145	225	57	-4.96
6-B(3)I(1)A(4)	0.01	-0.1 / 10.6	2.61	166, 62, 109	152	367	88	-3.26
6-B(3)I(1)A(5)	Rearranged							
6-B(2)I(1)A(3)	0.01	-5.3 / -14.6	2.59	106, 156, 55	151	198	60	-5.16
6-B(2)I(1)A(4)	0.01	177 / 163.4	2.53	132, 73, 72	150	412	93	-8.08
6-B(2)I(1)A(5)	0.03	2.3 / -24.4	2.57	171, 54, 79	152	328	82	-8.15
6-B(5)I(3)A(1)	0.22	25.4 / 32.4	2.25	153, 65, 93	150	360	114	-3.31
6-B(5)I(3)A(2)	0.08	-21.3 / -26.0	2.37	140, 70, 95	154	365	99	-10.04
6-B(5)I(3)A(4)	0.07	15.7 / 17.7	2.25	134, 115, 97	146	197	59	-5.20
6-B(4)I(3)A(1)	0.03	19.4 / 8.4	2.58	155, 59, 81	152	378	78	-6.02
6-B(4)I(3)A(2)	0.01	-2.1 / -6.8	2.55	150, 52, 94	147	374	79	-4.28
6-B(4)I(3)A(5)	0.02	-175.6 / -175.2	2.49	130, 129, 63	145	130	49	-3.03
6-B(5)I(4)A(1)	Rearranged							
6-B(5)I(4)A(2)	0.24	163.3 / 153.4	2.49	94, 116, 100	154	355	72	-11.71
6-B(5)I(4)A(3)	0.21	16.8 / 2.8	2.32	149, 105, 107	150	173	91	-9.59
6-B(1)I(4)A(5)	Rearranged							
6-B(2)I(4)A(5)	0.05	129.5 / 126.0	2.55	68, 63, 156	165	326	83	-8.04
6-B(3)I(4)A(5)	0.04	9.9 / 20.2	2.53	135, 110, 163	155	204	127	-1.66

Table 21: Calculated indicators of aromaticity for 6-membered, boron substituted, structural isomers with a carbene donor and a nitrogen one-electron donor (unsubstituted N atom) introduced into the ring. Ordered as per Table 8.

Compound identifier	WBI of the homo-conjugative gap	Inter-ring torsion angles	Homo-conjugative gap distance	δ(^{13}C) in the π-system	δ(^{13}C) of C_{carb}	δ(^{15}N) of A	δ(^{11}B)	$NICS_0$
6-B(5)I(1)A(2)	Rearranged							
6-B(5)I(1)A(3)	Rearranged							
6-B(5)I(1)A(4)	0.15	53.6 / 58.3	2.16	132, 129, 93, 93	157	239	66	-5.25
6-B(4)I(1)A(2)	0.04	-59.2/ -59.8	2.55	64, 102, 110	160	408	90	-7.07
6-B(4)I(1)A(3)	0.04	-94.5 / -81.7	2.58	32, 170, 70	163	231	66	-8.29
6-B(4)I(1)A(5)	0.05	-104.5/ -90.7	2.51	48, 170, 80	163	210	61	-5.51
6-B(3)I(1)A(2)	0.03	-41.0 / -38.7	2.57	158, 112, 110	153	241	57	-8.41
6-B(3)I(1)A(4)	Rearranged							
6-B(3)I(1)A(5)	0.05	-78.7 / -71.4	2.52	161, 144, 75	164	278	151	-10.08
6-B(2)I(1)A(3)	0.02	-146.3 / -110.0	2.56	123, 152, 52	160	207	54	-6.23
6-B(2)I(1)A(4)	0.02	-123.8 / -129.2	2.55	139, 73, 94	161	392	90	-10.00
6-B(2)I(1)A(5)	0.04	-60.4 / -87.2	2.58	170, 56, 66	160	351	79	-7.11
6-B(5)I(3)A(1)	0.07	9.6 / -8.3	2.40	182, 84, 131	169	371	66	-6.94
6-B(5)I(3)A(2)	0.10	-51.4 / -54.3	2.41	134, 94, 102	159	369	83	-10.02
6-B(5)I(3)A(4)	0.07	41.1 / 33.3	2.24	151, 123, 102	151	212	60	-3.97
6-B(4)I(3)A(1)	0.03	46.1 / 34.1	2.58	172, 60, 87	158	373	70	-4.64
6-B(4)I(3)A(2)	0.01	10.1 / 10.8	2.54	142, 57, 94	149	383	74	-1.92
6-B(4)I(3)A(5)	0.02	-146.6 / -144.2	2.52	151, 133, 75	152	192	48	-2.23
6-B(5)I(4)A(1)	Rearranged							
6-B(5)I(4)A(2)	0.24	124.7 / 119.5	2.49	103, 120, 106	166	362	66	-11.43
6-B(5)I(4)A(3)	0.21	-47.3 / -34.1	2.28	148, 102, 104	157	182	87	-9.22
6-B(1)I(4)A(5)	Rearranged							
6-B(2)I(4)A(5)	0.04	78.6 / 78.3	2.55	78, 65, 167	166	353	78	-6.91
6-B(3)I(4)A(5)	0.05	-123.1 / -116.2	2.51	136, 82, 166	168	193	158	-8.53

Table 22: Calculated indicators of aromaticity for 6-membered, boron substituted, structural isomers with a carbene donor with additional steric bulk and a nitrogen one-electron donor (unsubstituted N atom) introduced into the ring. Ordered as per Table 8.

Compound identifier	WBI of the homo-conjugative gap	Inter-ring torsion angles	Homo-conjugative gap distance	δ(^{13}C) in the π-system	δ(^{13}C) of C_{carb}	δ(^{15}N) of A	δ(^{11}B)	$NICS_0$
6-B(5)I(1)A(2)	0.24	-42.8 / -36.0	2.34	96, 114, 68	119	343	83	-11.67
6-B(5)I(1)A(3)	Rearranged							
6-B(5)I(1)A(4)	0.11	-34.9 / -39.7	2.25	111, 122, 65	118	216	62	-5.75
6-B(4)I(1)A(2)	0.04	-58.8 / -59.1	2.53	46, 86, 90	111	437	84	-5.17
6-B(4)I(1)A(3)	Rearranged							
6-B(4)I(1)A(5)	0.03	-103.2 / -100.9	2.50	48, 161, 71	107	181	54	-2.99
6-B(3)I(1)A(2)	0.03	-6.0 / -7.5	2.51	115, 127, 63	116	292	73	-9.02
6-B(3)I(1)A(4)	0.04	-123.1 / -108.9	2.48	87, 126, 63	116	371	92	-11.42
6-B(3)I(1)A(5)	0.05	-125.0 / -120.3	2.50	166, 128, 47	115	237	152	-11.90
6-B(2)I(1)A(3)	0.01	-15.8 / -39.7	2.57	105, 157, 25	116	209	54	-7.03
6-B(2)I(1)A(4)	0.02	-23.3 / -59.0	2.53	136, 74, 50	115	406	85	-9.17
6-B(2)I(1)A(5)	0.04	-56.5 / -18.7	2.57	174, 54, 72	119	323	80	-9.18
6-B(5)I(3)A(1)	0.30	-103.5 / -99.2	2.21	147, 76, 55	105	344	118	-3.66
6-B(5)I(3)A(2)	0.15	-31.2 / -35.2	2.42	130, 79, 77	120	368	95	-11.10
6-B(5)I(3)A(4)	0.10	-22.2 / -19.5	2.23	133, 108, 74	116	202	64	-5.39
6-B(4)I(3)A(1)	0.04	-123.8 / -101.5	2.57	165, 71, 54	106	361	76	-7.29
6-B(4)I(3)A(2)	0.02	-0.1 / 8.6	2.53	145, 58, 81	117	378	74	-6.18
6-B(4)I(3)A(5)	0.02	-26.7 / -19.5	2.50	136, 117, 39	113	177	49	-3.75
6-B(5)I(4)A(1)	0.18	106.2 / 106.8	2.51	97, 156, 86	107	345	87	-6.57
6-B(5)I(4)A(2)	0.22	-54.8 / -36.2	2.50	98, 132, 93	117	362	76	-10.11
6-B(5)I(4)A(3)	Rearranged							
6-B(1)I(4)A(5)	Rearranged							
6-B(2)I(4)A(5)	0.04	-104.7 / -101.1	2.57	78, 61, 162	111	347	78	-5.19
6-B(3)I(4)A(5)	0.03	-23.5 / -22.5	2.53	138, 111, 175	112	294	92	-2.68

Table 23: Calculated indicators of aromaticity for 6-membered, boron substituted, structural isomers with a bent allene donor and a nitrogen one-electron donor (unsubstituted N atom) introduced into the ring. Ordered as per Table 8.

A similar conservation of numerical trends within the metrics upon addition of an unsubstituted nitrogen atom to the homoaromatic system across structural isomers is seen in the six-membered homoaromatic analogues with the carbene and bent allene two electron donors as displayed in Table 21, 22 and 23. An increased number of poor candidates due to rearrangement can be seen across these three sets of compounds, this is likely due to a large amount of electron density destabilising the homoaromatic structure and causing an overly strong interaction across the homoconjugative gap, hence the lower number of rearrangements in the set of compounds utilising an IMe two-electron donor as partial quinoidization reduces the strength of donation into the homoaromatic system.

Compound identifier	WBI of the homo-conjugative gap	Homoconjugative gap distance	δ(^{13}C) in the π-system	δ(^{15}N) of N	δ(^{15}N) of A	δ(^{11}B)	$NICS_0$
7-N(1)B(6)A(4)	0.15	2.32	180, 130, 125	90	458	23	-5.61
7-N(1)B(6)A(5)	0.03	2.54	160, 141, 160	82	401	41	-0.44
7-N(1)B(6)A(3)	0.03	2.63	123, 176, 154	144	259	59	7.26
7-N(1)B(6)A(2)	0.02	2.57	149, 148, 168	149	457	70	1.71
7-N(5)B(6)A(1)	0.04	2.60	128, 146, 162	113	437	36	-3.84
7-N(3)B(6)A(1)	0.07	2.47	120, 147, 141	141	315	48	-3.38
7-N(2)B(6)A(1)	Rearranged						
7-N(1)B(2)A(6)	0.03	2.43	153, 145, 168	151	413	32	-0.78
7-N(1)B(2)A(3)	0.03	2.46	171, 139, 145	125	427	29	0.41
7-N(1)B(4)A(2)	0.05	2.45	150, 151, 136	170	454	43	-1.08
7-N(3)B(4)A(2)	0.04	2.48	142, 139, 144	222	389	32	-1.49
7-N(3)B(4)A(1)	0.03	2.49	150, 139, 156	184	324	36	-0.50
7-N(2)B(3)A(4)	Rearranged						
7-N(1)B(3)A(4)	0.07	2.39	161, 160, 91	178	373	24	-6.55

Table 24: Calculated indicators of aromaticity for seven-membered, boron-substituted, structural isomers where two-electron donation occurs from a [N-H] fragment within the ring with a nitrogen one-electron donor (unsubstituted N atom) introduced into the ring. Chemical shifts are shown in ppm.

Compound identifier	WBI of the homo-conjugative gap	Homoconjugative gap distance	δ(^{13}C) in the π-system	δ(^{15}N) of N	δ(^{15}N) of A	δ(^{11}B)	$NICS_0$
7-N(1)B(6)A(4)	0.15	2.34	177, 130, 126	136	453	24	-5.78
7-N(1)B(6)A(5)	0.06	2.43	142, 103, 160	153	362	17	-5.21
7-N(1)B(6)A(3)	0.07	2.49	131, 170, 151	177	289	42	-2.70
7-N(1)B(6)A(2)	0.16	2.31	147, 138, 135	181	395	25	-7.39
7-N(5)B(6)A(1)	0.07	2.47	142, 119, 159	214	394	32	-3.12
7-N(3)B(6)A(1)	0.06	2.43	119, 149, 144	208	326	48	-3.66
7-N(2)B(6)A(1)	Rearranged						
7-N(1)B(2)A(6)	0.03	2.44	155, 142, 168	206	409	30	-1.32
7-N(1)B(2)A(3)	0.03	2.48	167, 138, 145	180	428	27	-0.84
7-N(1)B(4)A(2)	0.06	2.45	148, 151, 136	213	453	40	-2.12
7-N(3)B(4)A(2)	0.04	2.45	143, 140, 141	264	393	30	-1.97
7-N(3)B(4)A(1)	0.03	2.45	153, 139, 155	222	329	34	-1.29
7-N(2)B(3)A(4)	0.21	2.26	121, 160, 78	229	314	18	-9.63
7-N(1)B(3)A(4)	0.07	2.42	165, 160, 93	237	367	25	-5.65

Table 25: Calculated indicators of aromaticity for seven-membered, boron-substituted, structural isomers where two-electron donation occurs from a [N-H] fragment with additional steric bulk to form a [N-^{t}Bu} fragment within the ring with a nitrogen one-electron donor (unsubstituted N atom) introduced into the ring. Chemical shifts are shown in ppm.

Tables 24 and 25 show the numerical metrics pertaining to candidates with the addition of an unsubstituted N atom into a 7-membered system where a [N-H] fragment is acting as a two-electron donor to the homoaromatic system. The data set constitutes a significantly larger analysis of structural isomers due to the larger number of distinct combinations possible. Thus there is an even greater range in the strength of the homoaromatic interaction across the isomers, however, upon assessment of the homoconjugative gap it can be seen that a number

of the isomers show a significant bond order and a concurrent reduction in distance. Here, in most case, the modification of the [N-H] fragment to a [N-^{t}Bu] does not result in a uniform strengthening of the through-space interaction, although the inductive effect and relative size in the group does increase the strength of the homoaromatic interaction in several cases and does seem to increase the stability of the homoaromatic system with respect to rearrangement.

Compound identifier	WBI of the homo-conjugative gap	Homoconjugative gap distance	δ(^{13}C) in the π-system	δ(^{15}N) of N	δ(^{15}N) of A	δ(^{11}B)	$NICS_0$
6-N(1)B(5)A(2)	0.18	2.31	145, 58	167	365	92	-10.62
6-N(1)B(5)A(3)	0.06	2.27	129,74	153	244	113	-10.64
6-N(1)B(5)A(4)	0.06	2.31	121, 131	89	215	57	-6.25
6-N(1)B(4)A(2)	0.12	2.49	126, 57	159	470	86	-3.10
6-N(1)B(4)A(3)	0.02	2.52	156, 30	132	249	75	-4.88
6-N(1)B(4)A(5)	0.04	2.43	156, 61	126	183	49	-3.99
6-N(1)B(3)A(2)	0.04	2.57	118, 154	268	268	73	-5.17
6-N(1)B(3)A(4)	0.04	2.53	78, 179	57	378	74	-6.61
6-N(1)B(3)A(5)	0.06	2.43	126, 160	70	255	141	-12.10
6-N(1)B(2)A(3)	0.02	2.52	159, 105	50	200	51	-7.26
6-N(1)B(2)A(4)	0.02	2.48	58, 135	94	410	88	-10.66
6-N(1)B(2)A(5)	0.04	2.52	42, 170	108	328	75	-10.80
6-N(3)B(5)A(1)	0.30	2.15	136, 88	120	308	109	-7.16
6-N(3)B(5)A(2)	0.14	2.15	152, 89	129	384	140	-9.60
6-N(3)B(5)A(4)	0.10	2.21	106, 141,	131	231	69	-6.53
6-N(3)B(4)A(1)	0.03	2.55	144, 61	130	346	62	-7.68
6-N(3)B(4)A(2)	0.02	2.52	157, 57	156	392	56	-7.44
6-N(3)B(4)A(5)	0.02	2.50	123, 139	69	167	45	-3.78
6-N(4)B(5)A(1)	0.32	2.45	152, 67	150	382	60	-9.98
6-N(4)B(5)A(2)	0.38	2.45	132, 75	157	339	54	-13.52
6-N(4)B(5)A(3)	Rearranged						

Table 26: Calculated indicators of aromaticity for six-membered, boron-substituted, structural isomers where two-electron donation occurs from a [N-H] fragment within the ring with a nitrogen one-electron donor (unsubstituted N atom) introduced into the ring. Chemical shifts are shown in ppm.

Compound identifier	WBI of the homo-conjugative gap	Homoconjugative gap distance	δ(^{13}C) in the π-system	δ(^{15}N) of N	δ(^{15}N) of A	δ(^{11}B)	$NICS_0$
6-N(1)B(5)A(2)	0.16	2.34	130, 58	197	364	87	-11.03
6-N(1)B(5)A(3)	0.07	2.31	129, 74	182	250	98	-11.84
6-N(1)B(5)A(4)	0.11	2.33	118, 126	112	220	52	-7.61
6-N(1)B(4)A(2)	0.04	2.51	122, 54	186	471	85	-3.41
6-N(1)B(4)A(3)	0.02	2.56	159, 24	166	248	69	-6.11
6-N(1)B(4)A(5)	0.04	2.48	159, 61	152	179	51	-3.93
6-N(1)B(3)A(2)	0.05	2.58	120, 134	143	280	64	-8.60
6-N(1)B(3)A(4)	0.03	2.55	77, 181	81	381	78	-7.11
6-N(1)B(3)A(5)	Rearranged						
6-N(1)B(2)A(3)	0.01	2.51	160, 103	94	198	46	-8.04
6-N(1)B(2)A(4)	0.02	2.49	63, 134	135	408	82	-10.86
6-N(1)B(2)A(5)	0.04	2.51	46, 171	154	326	70	-10.90
6-N(3)B(5)A(1)	0.34	2.07	134, 87	172	289	94	-6.72
6-N(3)B(5)A(2)	0.15	2.21	147, 87	160	383	136	-9.89
6-N(3)B(5)A(4)	0.11	2.19	104, 137	160	227	66	-7.22
6-N(3)B(4)A(1)	0.03	2.55	146, 59	175	354	61	-7.90
6-N(3)B(4)A(2)	0.02	2.52	156, 50	198	396	56	-7.50
6-N(3)B(4)A(5)	0.02	2.50	123, 138	112	167	43	-4.46
6-N(4)B(5)A(1)	0.25	2.45	155, 90	205	331	44	-9.29
6-N(4)B(5)A(2)	0.33	2.45	120, 86	214	338	45	-13.52
6-N(4)B(5)A(3)	Rearranged						

Table 27: Calculated indicators of aromaticity for six-membered, boron-substituted, structural isomers where two-electron donation occurs from a [N-H] fragment with additional steric bulk within the ring with a nitrogen one-electron donor (unsubstituted N atom) introduced into the ring. Chemical shifts are shown in ppm.

The numerical metrics related to the strength of homoaromaticity upon the addition of an ancillary nitrogen atom to the six-membered, [N-H] fragment donor based homoaromatic systems are displayed in Tables 26 and 27.

Conclusion

Through the incremental modification of a set of previously identified homoaromatic candidates, made possible by the use of DFT, it has been shown that boron can stabilize the homoaromatic interaction to a greater extent and with more control than the isolobal carbocation and that this stabilization is sufficient to allow the use of two-electron nitrogen donors to achieve a strong interaction across the homoconjugative gap. With this additional control it is then possible to introduce functionalization without compromising stability. The functionalization of neutral homoaromatic compounds theoretically allows for their insertion

into useful systems in place of any other aromatic system when a perturbation to the strength of aromaticity would allow for a subtle modification towards desirable properties.

Chapter 5 - Single-Exponential Decay Detector (SEDD) as a Non-Standard Interactions Metric and Shell Descriptor: Application to the Design of Boron-Stabilized Homoaromatic Compounds

Introduction

Homoaromaticity is defined as the presence of an aromatic π-system without a contiguous σ-system.[156] The field of homoaromatic compounds is currently sparse with very few known compounds. Those that are known tend to be positively charged such as the homotropylium cation and the norbornen-7-yl cation. As presented above in Chapter 3, a group of nine compounds were identified as being good candidates to display a degree of homoaromaticity (a sample of which are shown below in Figure 16) and seven metrics were given, these have been further applied to the design of functionalised homoaromatic compounds.

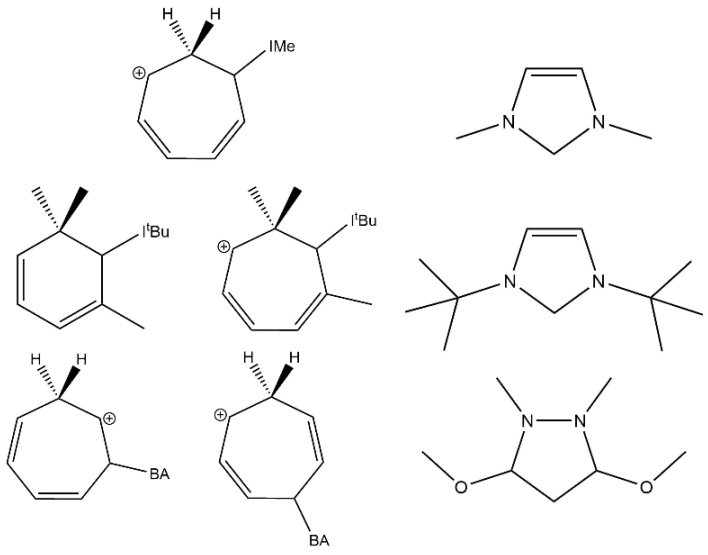

Figure 16: Schematic representation of previous compounds, from left to right 1 (top), 2 and 5 (middle) and 8 and 9 (bottom), the N-heterocyclic carbenes IMe and ItBu and the bent allene are displayed on the right hand side (top to bottom).

Despite these metrics, the nature of the through-space π-interaction is complex to portray accurately. In particular, as discussed earlier, the use of $NICS_0$ as a measure of aromaticity is a feature of much discussion.[167–169] It is generally agreed that a greater degree of accuracy and additional detail can be provided by the use of $NICS_{zz}$ values,[170–173] however, this exact positioning of individual tensors is convoluted, in much the same way as the difficulty in positioning a ghost atom for $NICS_1$, with homoaromatic molecules which often do not possess exact planarity. NICS values in any form are not a perfect measure of aromatic. Additionally the main flaw with $NICS_0$ values is the convolution of the isotropic shielding originating from the surrounding σ-system. Thus, when used as a relative measure comparing the strength of aromaticity with a set of structural isomers this error should remain relatively constant. When used in conjunction with an electron localization method, $NICS_0$ can provide a useful indication as to the relative strength of aromaticity at a slight computational cost. Applying an electron localisation method to display the location of the bonding interactions, more specifically the delocalized ring system implicit in aromatic compounds, is a powerful method to elucidate the nature of the homoconjugative gap. What is thus needed is a rigorous method of mapping electron density. Previously this would have been achieved using the Electron Localisation Function (ELF).[174] However this method, whilst useful, possesses several flaws.[175] The Single Exponential Decay Detector (SEDD), a more recent method designed by de Silva et al. is based solely on the density, is relatively computationally inexpensive and gives an accurate, qualitative image of the bonding interactions within molecules.[176] The relationship between SEDD at each point of a defined grid and the electron density ($\rho(\boldsymbol{r})$) is shown below in Equation 21:

$$SEDD(\boldsymbol{r}) = \ln\left[1 + \left(\frac{\nabla\left(\frac{\nabla\rho(\boldsymbol{r})}{\rho(\boldsymbol{r})}\right)^2}{\rho(\boldsymbol{r})}\right)^2\right]$$

Equation 21: The definition of SEDD describing its relation to the electron density, ρ(r).[177]

The current literature utilising SEDD applies the method to small, planar molecules and reproduces atomic shell structure with a good degree of accuracy, these are then applied, alongside isosurfaces, to define a 'fingerprint' of aromaticity.[178] Whilst the homoaromatic candidates are more complex, and often deviate significantly from planarity, by concentrating on the homoaromatic ring structure SEDD should provide a useful additional metric in the identification and classification of homoaromatic compounds. Whilst an SEDD analysis would be purely a qualitative analysis, it is a powerful tool in the identification of homoaromatic compounds which adds a strong additional metric to those previously established.

Computational Details

All calculations were performed within the ADF programme.[101] All compounds were initially optimised at both the B3LYP/TZ2P and B3LYP/ZORA-QZ4P levels.[88,179–182] These were then used to perform SEDD calculations with a fine grid which were visualised within the ADF-GUI. Minima were confirmed by performing analytical frequency calculations.[183–185] As suggested within existing literature, as the SEDD values can take any real value, they have been limited such that values below 2 are dark blue and those above 15 are red. The isosurfaces in this paper were generated using an isovalue of 5.0.[178] Using a QZ4P basis set also requires the use of a Zeroth Order Regular Approximation (ZORA) Relativistic Hamiltonian.[186,187]

Results and discussion

In this work the SEDD diagrams display the values of the SEDD as a colour scale on a cut plane showing the largest degree of homoaromaticity. This should be a fully valid approach as aromatic orbitals should be planar. However, due to the strain introduced in the system by the addition of a sp^3 centre into the sp^2 system the homoaromatic rings tend to show a significant deviation away from planarity. In order to determine whether or not SEDD is useful as a metric in designing homoaromatics it is important to assess whether this deviation away from planarity affects the capability of a cut plane to assess the bonding pattern in a non-planar structure. To alleviate the impact of the non-planarity the cut contour has been placed such that it includes the plane through which a through-space interaction across the homoconjugative gap i.e. in the area in which some evidence of a bonding interaction would be expected.

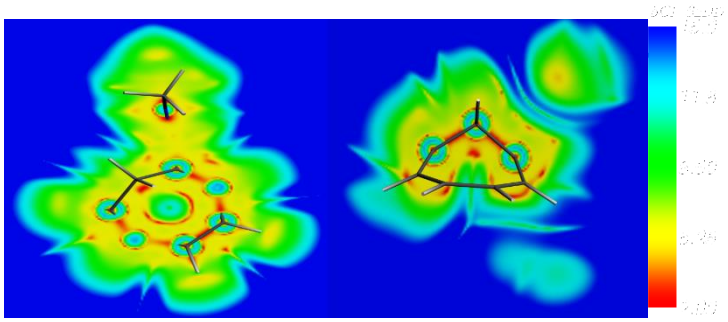

Figure 17: A contour plane showcasing the homoaromatic interaction in compound 1.

Figure 17 shows a pair of cut planes where the left hand plane was chosen to assess the presence of a through-space interaction. Note, the colour scale to the left shows the gradient of the colour change from areas of low electron density (blue) to areas of high electron density (red), this scale is used henceforth. This plane clearly shows the atomic shell structure of those carbon atoms which it bisects. Also evident is the presence of the σ-system, it should be noted that the areas of seemingly low electron density in these bonds are caused by the deviation of these

bonds away from the chosen cut plane. Literature states that the confirmation of aromaticity is the presence of a continuous ring of electron density within the centre of a molecule. Figure 17 shows that this is not fully present within **1**. This is not unexpected as homoaromaticity is known to be a weaker interaction than that of classical aromaticity. In **1** there is a continuous crescent of electron density where the σ-framework coincides with the π-system. The continuity of this crescent suggests aromaticity over mere conjugation. The difference arises in the area of the postulated through-space interaction. Here, instead of a section of continuous electron density there appears a single bead of electron density equidistant between the bridgehead carbon atoms of the π-system. The cut plane on the right hand side of the figure is near perpendicular to the original cut plane and suggests that the bead of electron density is due to the presence of a through-space interaction and not an artefact generated by the proximity of the sp^3 centre. This analysis of the through-space interaction was expanded to cover all nine of the original homoaromatic candidates.

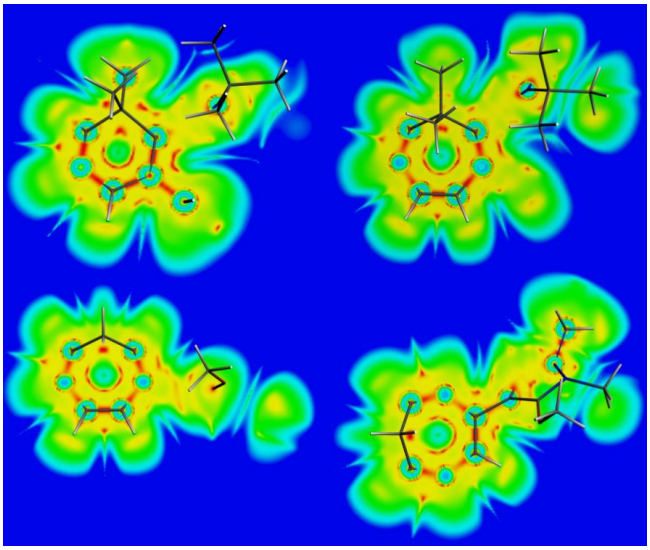

Figure 18: Cut contour planes set to investigate the homoaromatic interactions in compounds 5 (top left), 6 (top right), 8 (bottom left) and 9 (bottom right).

Figure 18 shows the cut planes for compounds 5 and 6 from the bulky candidates and compounds **8** and **9** from the bent allene candidates where the cut plane was chosen in a manner analogous to that of compound 1. All four compounds show the same crescent and bead pattern of interior electron density as compound **1**. It is apparent that whilst the crescents are continuous they are not homogeneous, this disparity is likely caused by the deviation of the homoaromatic molecule away from planarity. This variation within the crescent also yields an approximation of the relative strength of the homoaromaticity between the compounds upon direct comparison although not with a degree of accuracy sufficient to replace the previously discussed metrics. To ensure that the perceived indicators of aromatic character are not a fortuitous representation of a heavily conjugated system, the other 'fingerprint of aromaticity' suggested by de Silva *et al.* was also investigated. It is also important to recognise that, as stated in previous literature, the appearance of the continuous ring of electron density is also heavily dependent upon the geometry of the aromatic system. This is likely to be a particularly prevalent issue in homoaromatic compounds given the tendency of the homoaromatic interaction to deviate away from planarity due to the presence of the tetrahedral sp^3 centre. This perturbation to the geometry could cause the central ring of density to fragment and appear non-aromatic in nature, the same previous literature also suggests the isosurfaces as a way to mitigate this issue.

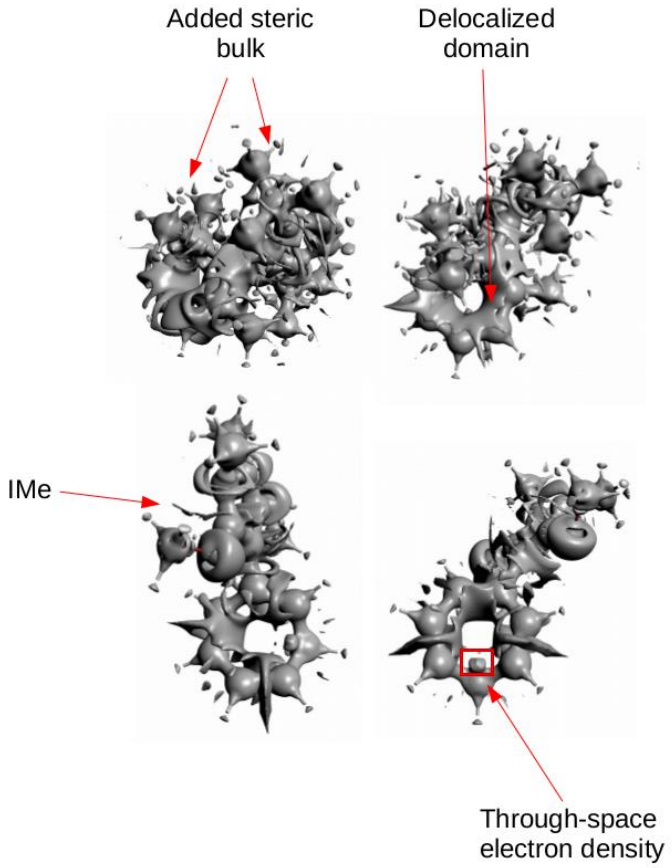

Figure 19: Isosurfaces for compounds 5 (top left), 6 (top right), 8 (bottom left) and 9 (bottom right).

The investigation of the 'fingerprint of aromaticity' requires the generation of isosurfaces such as that shown above in Figure 19 containing compounds **5**, **6**, **8** and **9**. These isosurfaces show the single localisation domain that has been associated with aromaticity but, in a similar manner to the cut planes, it only appears where the σ-framework and the π-system coincide. Crucially, a portion of electron density is observed in the exact position where the bead of electron density is observed in the cut plane. This rules out a false positive being caused by the proximity of the sp^3 centre and thus confirms that there is some through-space interaction between the terminal carbon atoms. It should be noted that the generation of clear isosurfaces becomes increasingly

difficult as the size and complexity of the compound increases as it becomes more difficult to prevent pertinent detail from being obscured. The contour planes and isosurfaces shown here were calculated using a ZORA-QZ4P STO basis set as these calculations provide a more precise image for both representations. The images generated from calculations utilising a TZ2P STO basis set do still yield useful information and may be worth considering for larger systems. It should be noted that although literature shows that basis sets larger than QZ4P provide more precise mapping, the computational cost becomes prohibitive with larger molecules thus making using a larger basis set would render the method less attractive for use as a metric.

Given that calculations on previously considered homoaromatic candidates show that SEDD has the potential to act as a valuable and easy-to-use metric for homoaromaticity the limits of the metric should be assessed. The variable strength of homoaromatic interaction across the geometric isomers in boron and carbene-based homotropylium analogues offers an opportunity to assess whether the SEDD plots vary with respect to the strength of the through-space interaction. Figure 20 displays contour planes and isosurfaces generated for a number of structural isomers of a neutral seven-membered ring system with a single interrupting centre utilising a simple NHC as a two-electron donor and a [B-H] fragment as a acceptor (due to it being isolobal to a carbocation).

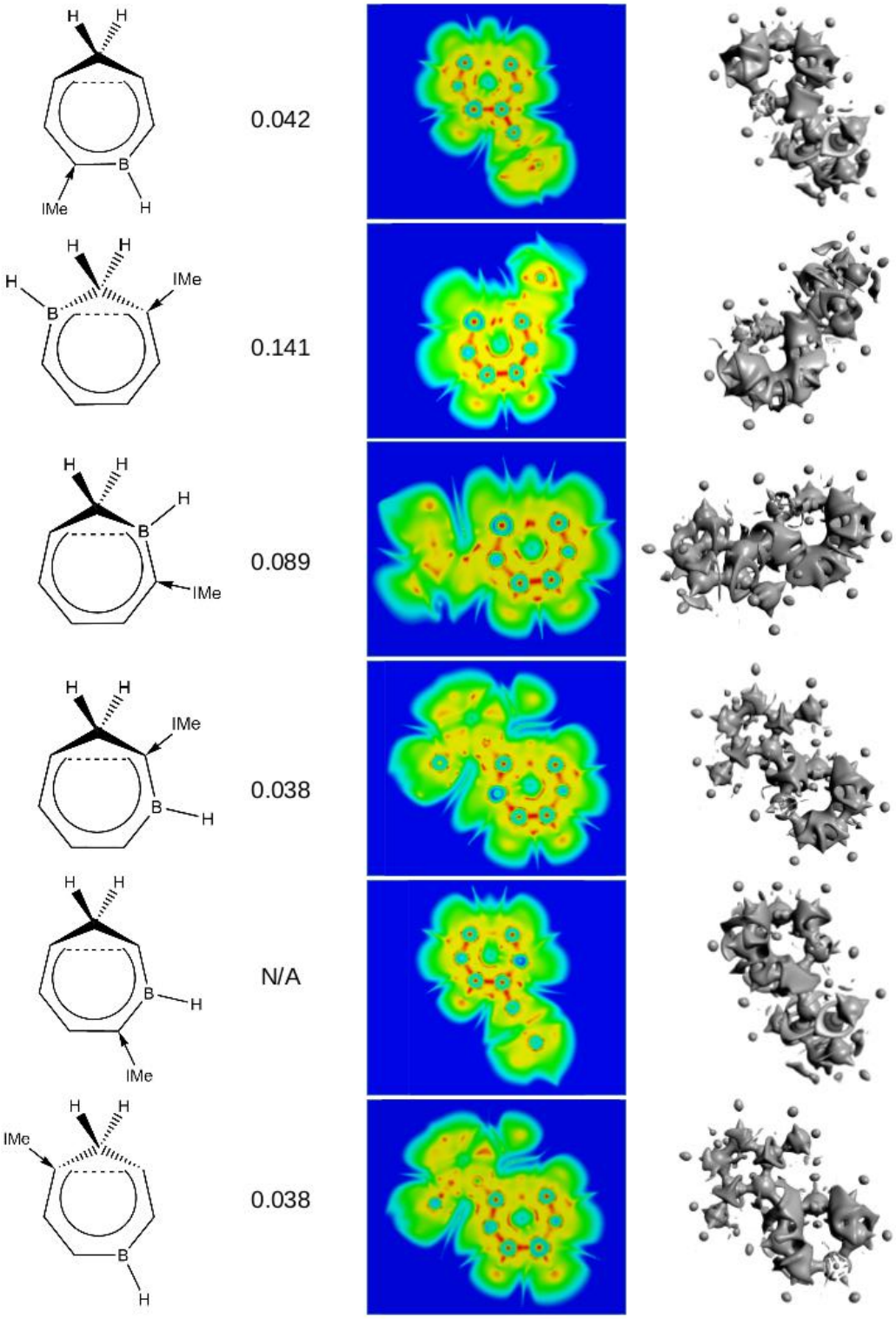

Figure 20: Contour planes and isosurfaces for a set of structural isomers of seven-membered homoaromatic candidates with IMe as a two-electron donor calculated with a TZ2P STO basis set. All isomers listed with their associated WBI bond orders.

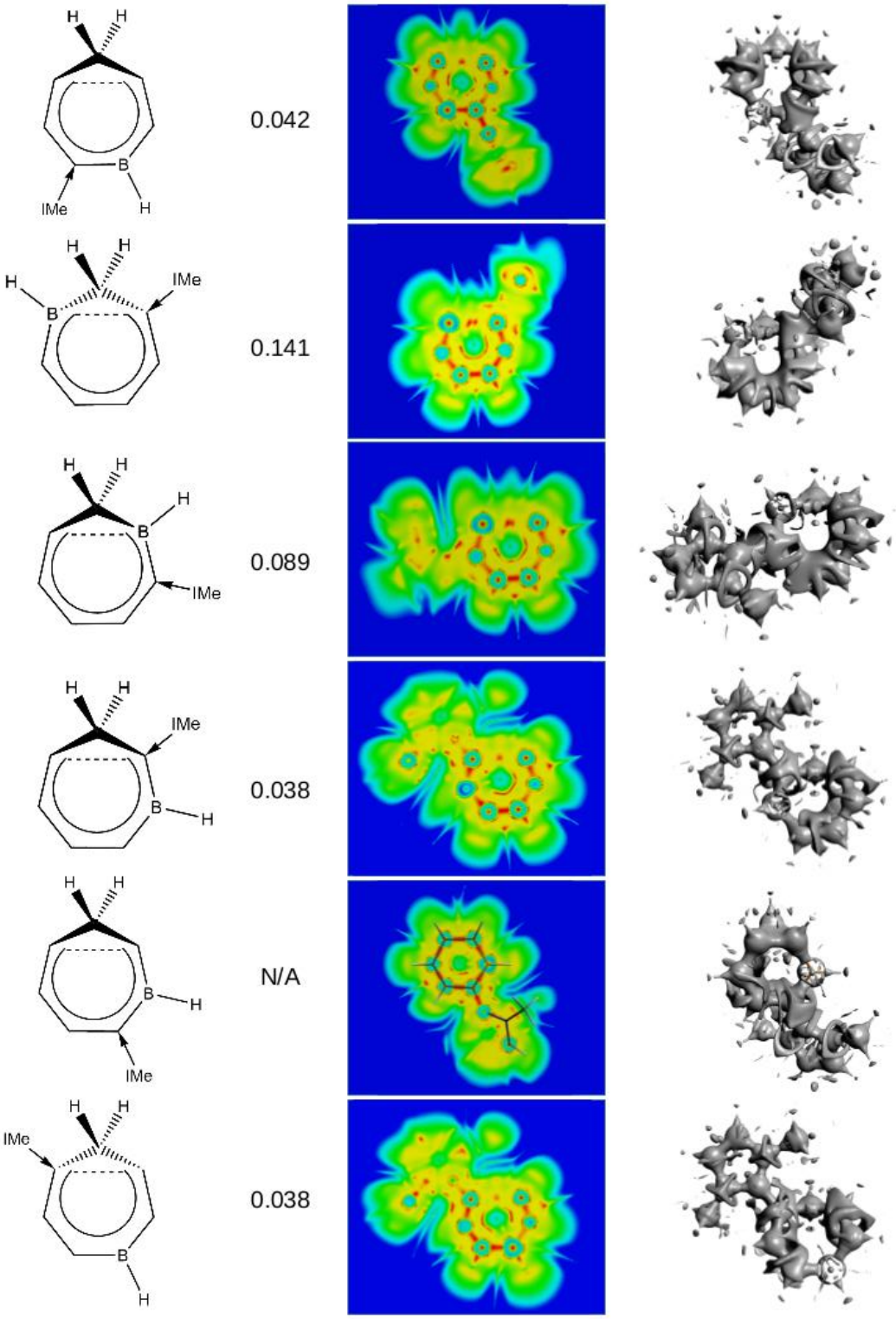

Figure 21: Contour planes and isosurfaces for a set of structural isomers of seven-membered homoaromatic candidates with IMe as a two-electron donor calculated with a ZORA-QZ4P STO basis set. All isomers listed with their associated WBI bond orders. Note the rearrangement of the 5th compound to a 6-membered ring.

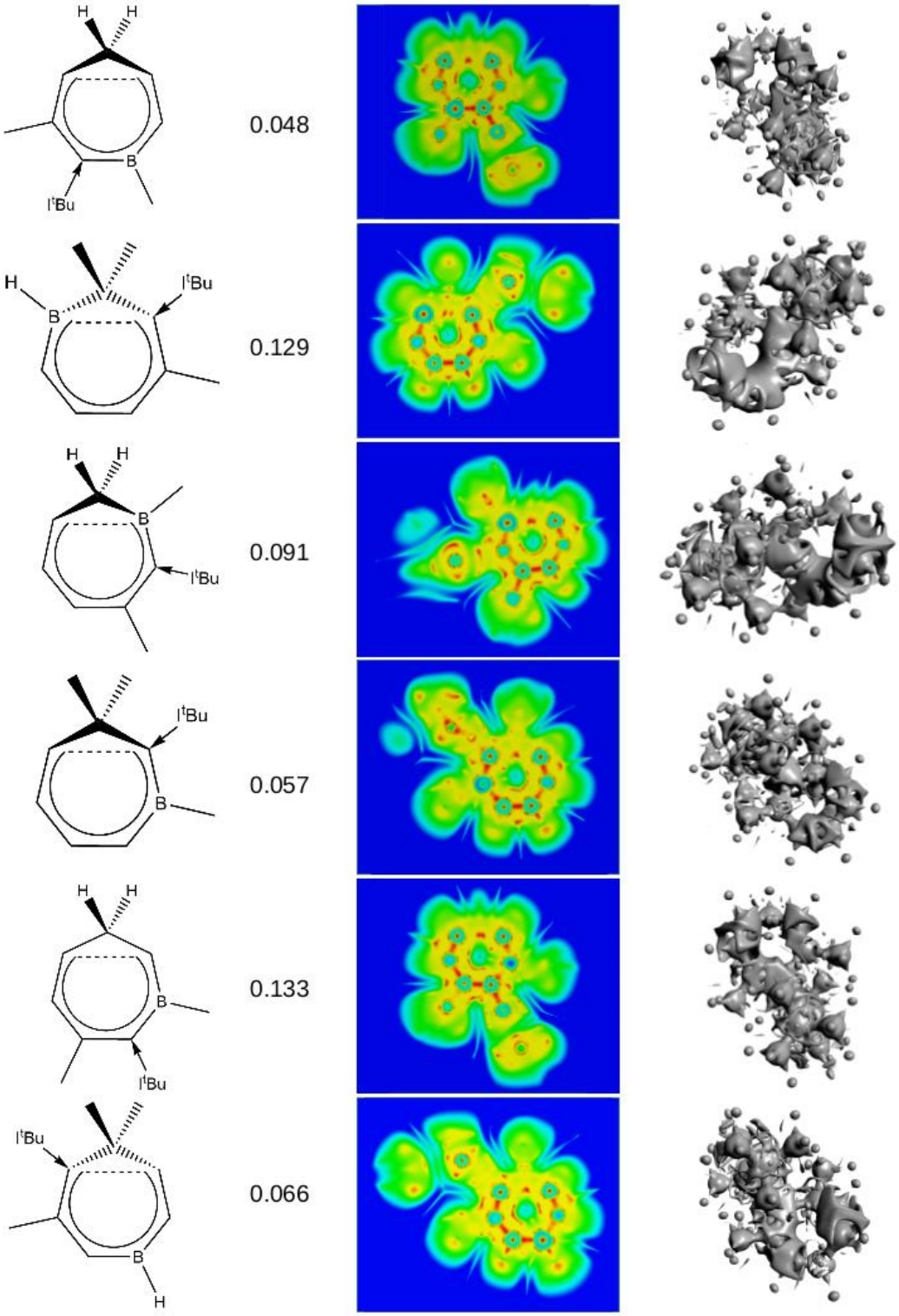

Figure 22: Contour planes and isosurfaces for a set of structural isomers of seven-membered homoaromatic candidates with I^{t}Bu as a two-electron donor calculated with a TZ2P STO basis set. All isomers listed with their associated WBI bond orders.

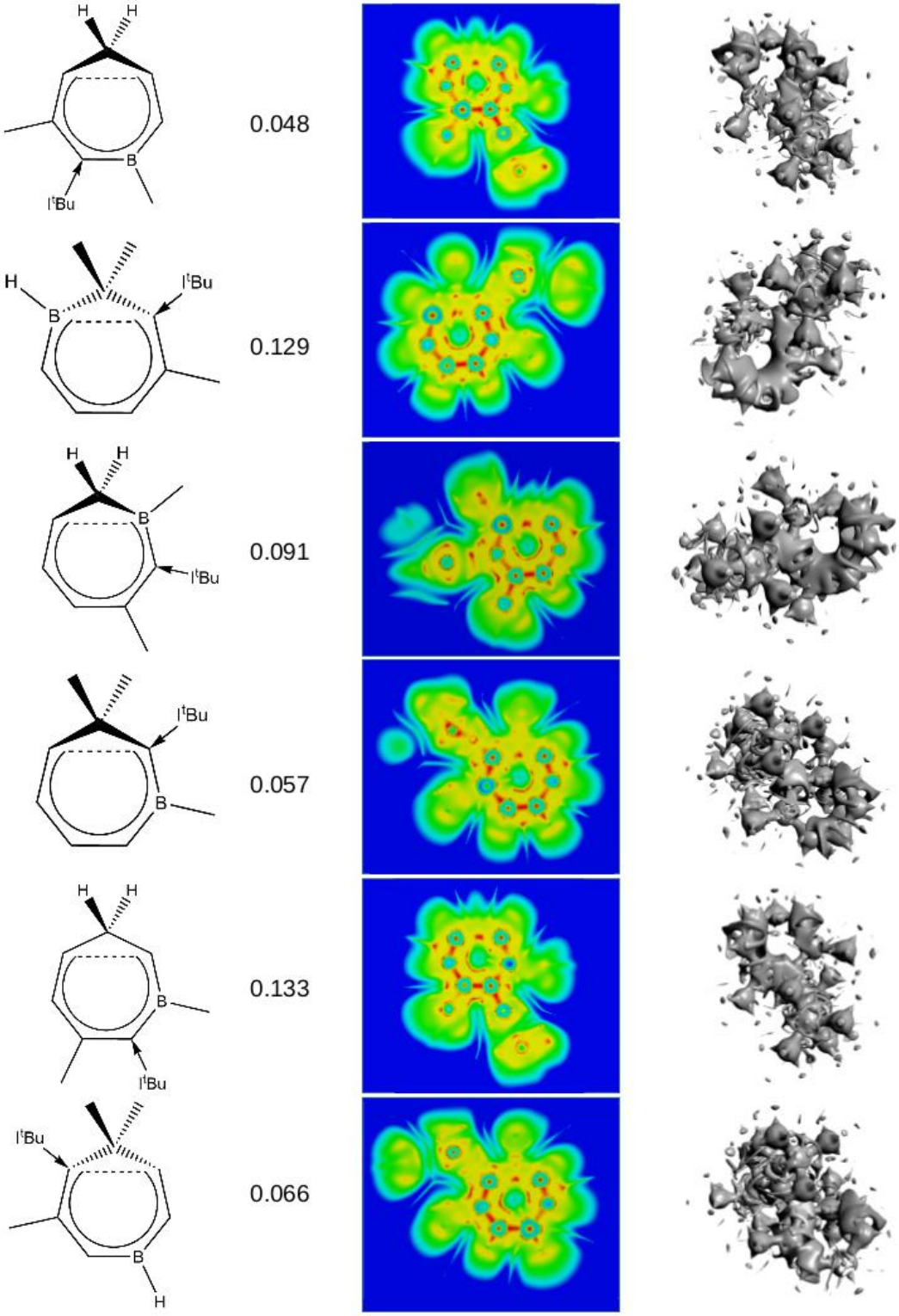

Figure 23: Contour planes and isosurfaces for a set of structural isomers of seven-membered homoaromatic candidates with I^{t}Bu as a two-electron donor calculated with a ZORA-QZ4P STO basis set. All isomers listed with their associated WBI bond orders.

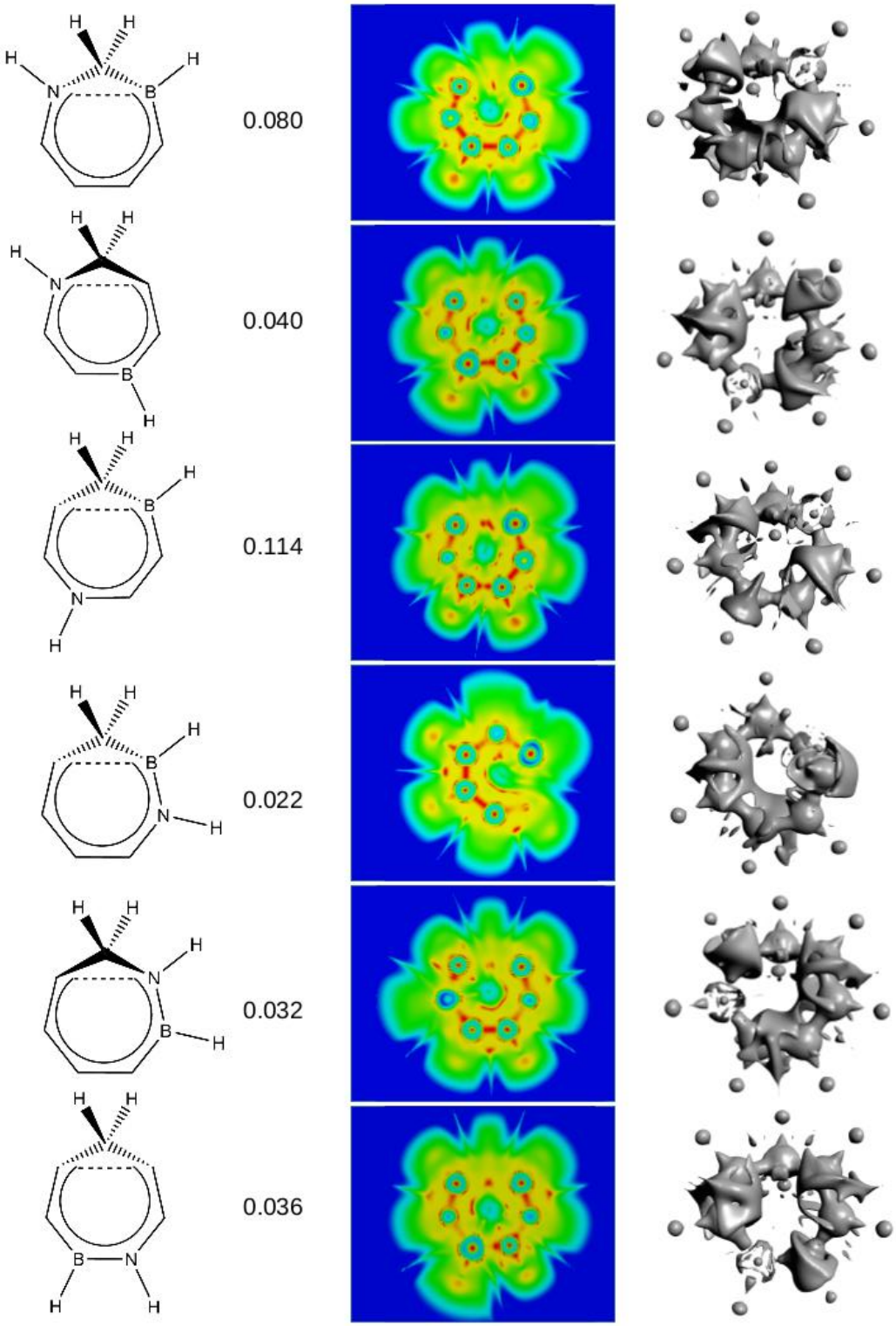

Figure 24: Contour planes and isosurfaces for a set of structural isomers of seven-membered homoaromatic candidates with a [N-H] fragment replacing the NHC as a two-electron donor calculated with a TZ2P STO basis set. All isomers listed with their associated WBI bond orders.

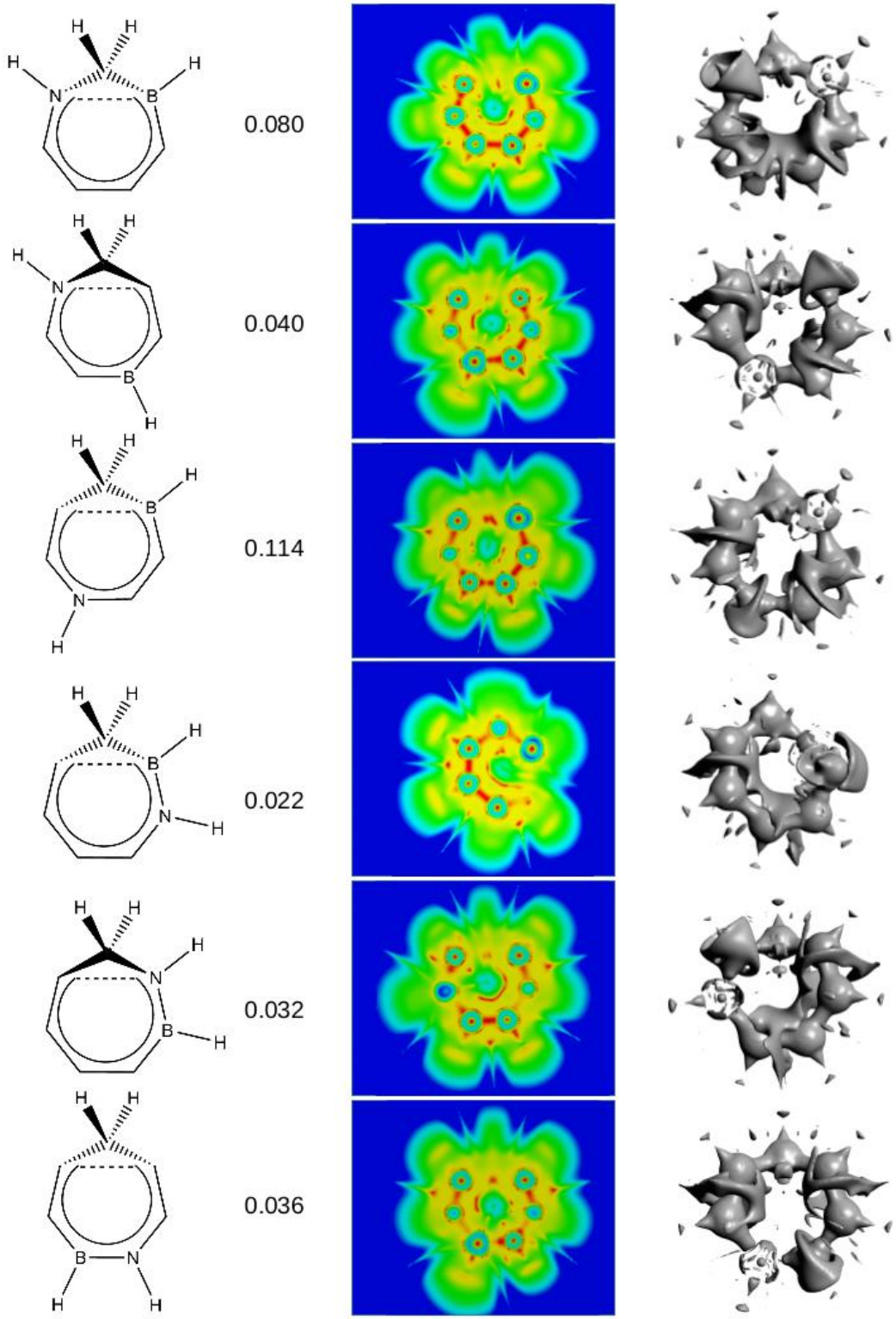

Figure 25: Contour planes and isosurfaces for a set of structural isomers of seven-membered homoaromatic candidates with a [N-H] fragment replacing the NHC as a two-electron donor calculated with a ZORA-QZ4P STO basis set. All isomers listed with their associated WBI bond orders.

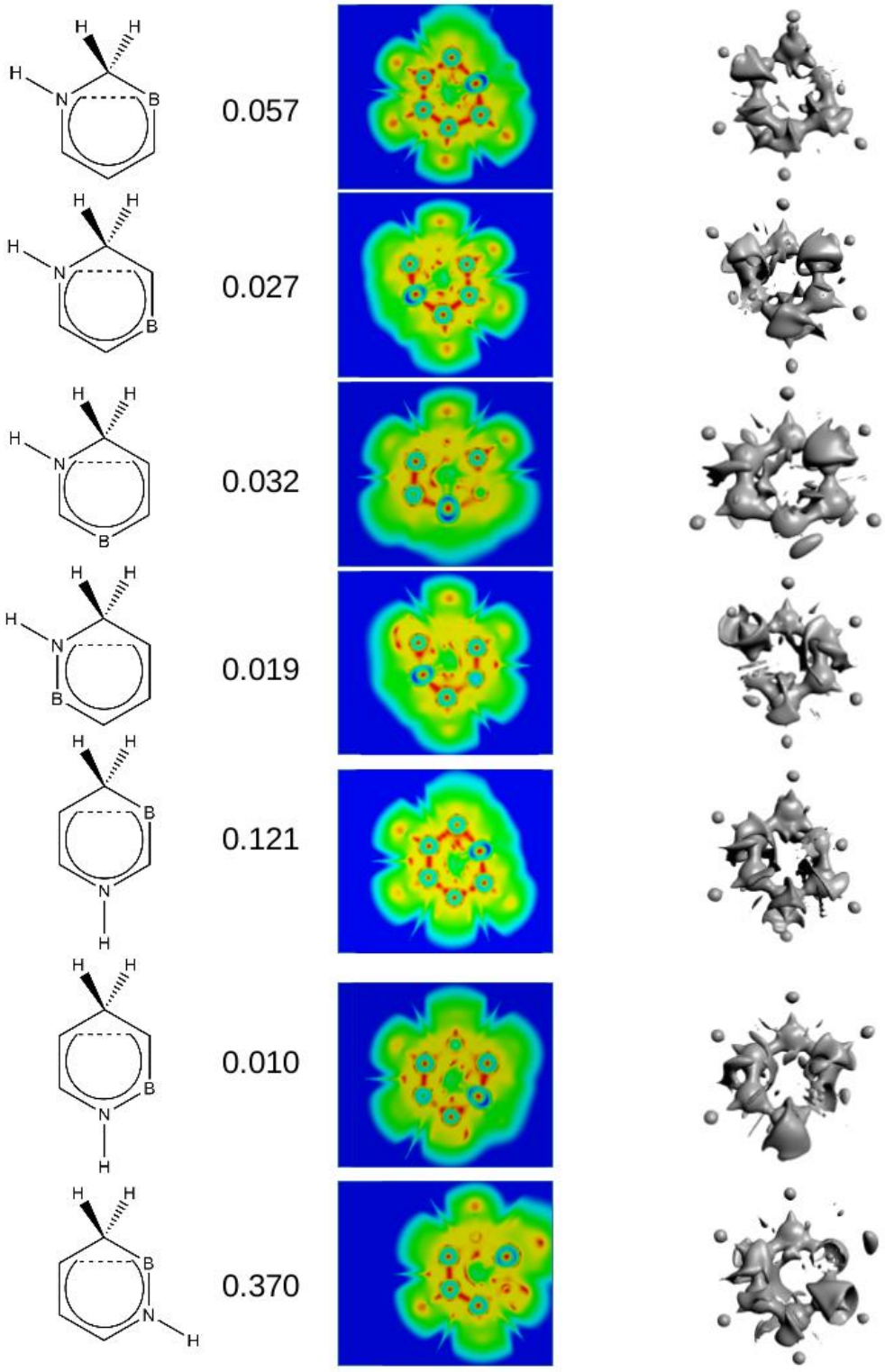

Figure 26: Contour planes and isosurfaces for a set of structural isomers of six-membered homoaromatic candidates with a [N-H] fragment replacing the NHC as a two-electron donor calculated with a TZ2P STO basis set. All isomers listed with their associated WBI bond orders.

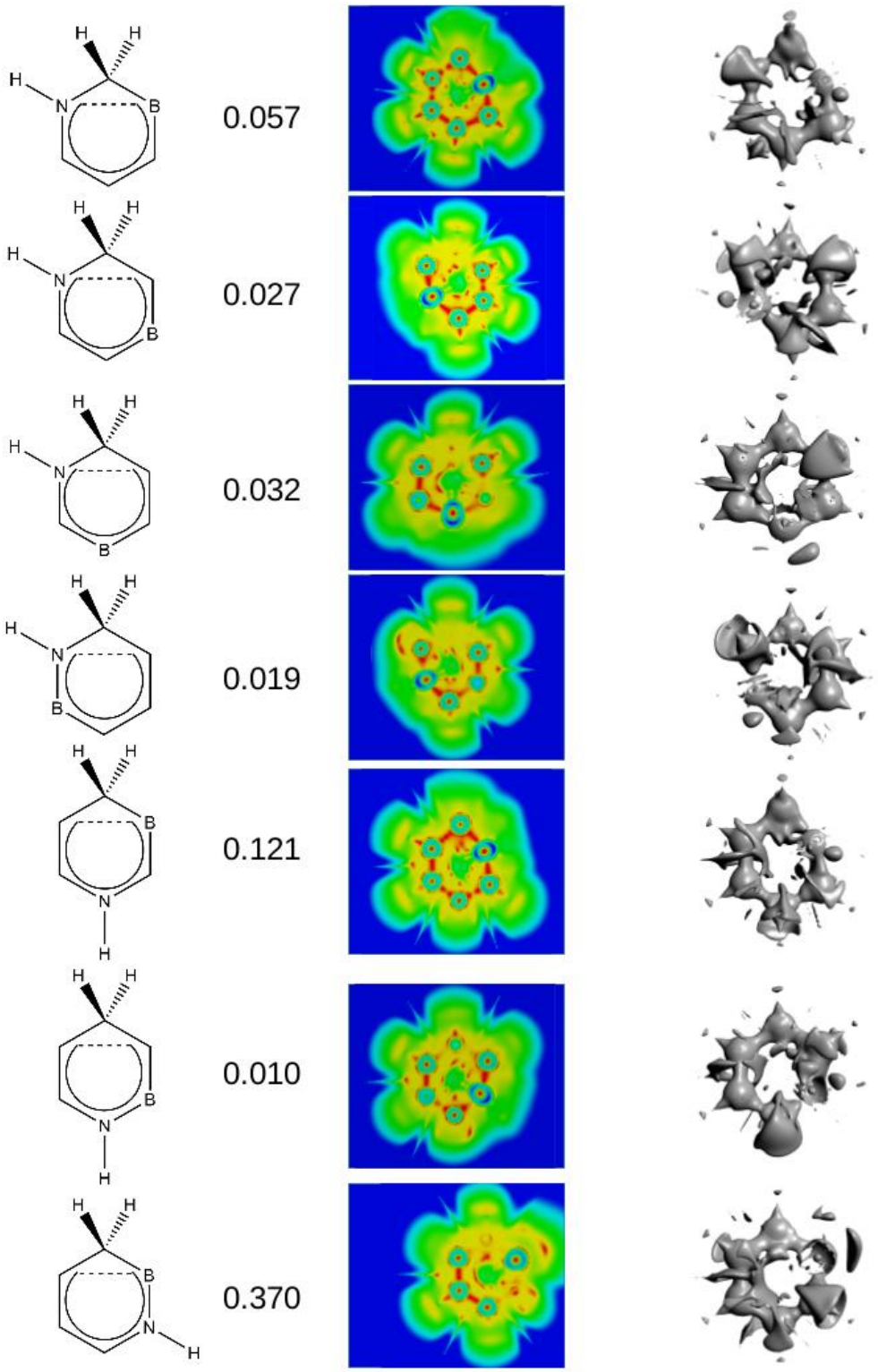

Figure 27: Contour planes and isosurfaces for a set of structural isomers of six-membered homoaromatic candidates with a [N-H] fragment replacing the NHC as a two-electron donor calculated with a ZORA-QZ4P STO basis set. All isomers listed with their associated WBI bond orders.

Although immediately obvious when viewing the geometry, Figure 20 clearly shows that the fifth isomer has rearranged, here the σ-bonding system can be seen to extend between all atoms in addition to the lack of any internal structure between the areas of electron density thus showing no evidence of aromaticity. This adds to the utility of the use of SEDD as a metric where through-space interactions of a large magnitude can cause significant bond-shortening, the lack of σ-bonding character could help confirm the presence of a homoaromatic interaction. Inspection of the contour planes for the remaining isomers reveals similar structures of near continuous arcs of electron density within the centre of the postulated homoaromatic systems to those displayed by compounds **1**, **5**, **7**, **8** and **9**. From the contour planes alone it is difficult to assess whether the variation of continuity results from a weakening or even the absence of the homoaromatic interaction or from a deviation away from planarity as discussed previously. Therefore the isosurfaces again prove more reliable in showing the homoaromatic interaction via the presence of the delocalized domains. The domains spread over all connected donor atoms in the system suggesting aromatic behaviour, furthermore, some part of the fragmentation of the delocalised isosurface is likely to be due to the deviation away from planarity that is common across the isomers. This behaviour of the isosurface could suggest that the variation of the homoaromatic interaction between geometric isomers could be attributed to the variation in planarity of the compounds as much as the differing electronics caused by the spatial arrangement of the donor atoms. These effects should be expected to be co-dependent i.e. the incremental removal of electron density from the ring via a distortion away from the plane of the π-interaction will result in a weaker interaction. Both the contour planes and the isosurfaces show the correlated 'lobe' of electron density in the centre of the predicted through space interaction. The degree of fragmentation of the delocalized domain may allow for a relative assessment of the strength of the interaction but this assessment obviously remains qualitative in nature.

It is also evident from both the contour planes and the isosurfaces that SEDD displays the 'electron deficient' nature of boron. This appears as areas of low electron density in the contour planes and as an absence of isosurface covering the core of the atom. Such behaviour is not observed with the carbocation centres in the early compounds. As both the [B-H] fragment and the carbocation should be isolobal this suggests significant delocalisation of the charge around the homoaromatic system. Whilst there is no delocalized domain present in the vicinity of the boron, the majority of the isomers still show some degree of homoaromatic interaction suggesting evidence for the electron 'sink' behaviour of boron allowing it to act as a charge redirection node.

Figure 26 displays the contour planes and isosurfaces for a set of structural isomers for a 7-membered ring including a boron centre and a [N-H] fragment acting as a two-electron donor in place of an NHC. Across this set of isomers there is generally an increase in the degree of fragmentation of the localization domain suggesting that the interaction is more likely to be more the result of conjugation rather than aromaticity in some of the isomers. However, most of the structural isomers display a significant amount of through-space interaction suggesting that the addition of the boron atom is sufficient to maintain the homoaromatic interaction despite the introduction of a weaker donor. Figure 27 again shows the increased clarity obtained via the use of a larger basis set.

For all compounds, figures pertaining to both the TZ2P and ZORA-QZ4P levels have been presented. These clearly show that the contour planes generated from optimisations at the ZORA-QZ4P level of theory are significantly sharper and are thus more useful for analysis.

Conclusions

Given the complexity in determining the properties inherent to homoaromatic compounds caused by the problems of ring current and a deviation away from planarity, a powerful and relatively computationally inexpensive method of electron localization is a useful method for the rapid identification of the presence of aromatic behaviour. SEDD identifies the presence of a through space interaction and the homoaromatic candidates identified previously display the 'fingerprints of aromaticity' as determined by Silva *et al.* in literature and, more importantly, can clearly show a distinction between a homoaromatic interaction and mere conjugation. It is also apparent that SEDD will identify electron deficiency within a system and account for charge transferal across a boron node and thus would be of use showing a visible distinction between 6- and 8-electron boron.

Chapter 6 – Optimising an Fe(II) Complex in the Excited State via a Polarised Average of Configuration Method

Introduction

SCO compounds are notoriously complex to model computationally. [73–87] This is largely due to having multiple, easily accessible low-lying states of distinct symmetry. There are many existing examples in the literature of wide-ranging method analyses trying to isolate a single all-encompassing method. The importance of this excited state is conveyed below in Figure 28.

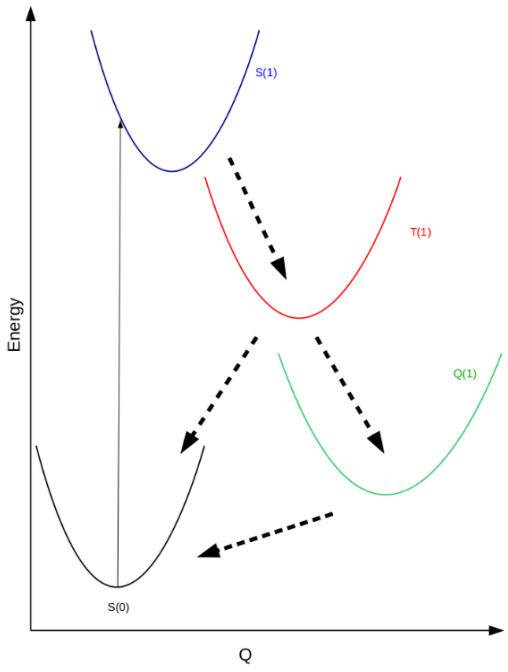

Figure 28: A general example of an SCO spin-transition from a low-spin to high-spin state.

Figure 28 shows a simplified spin-transition pathway describing the mechanism of the spin – transition when populating excited states. Initial excitation occurs to the first excited singlet state (often via MLCT), before relaxation brings the system to the minimum via vibronic coupling

before a mixture of intersystem crossing and quantum tunnelling leads to the high-spin quintet state. [48–54] The HS-LS gap must be of a magnitude that it is low enough for the quintet state to have an appreciable lifetime but large enough that the compound retains a low-spin singlet ground state. Thus the ability to finely tune this energy gap would be a useful tool in the search for a viable SCO material.

Assessment of Functionals

Although there are many authoritative and comprehensive assessments of various levels of theory applied to SCO compounds in the literature, the difficulty of applying DFT to SCO energetics calls for a more specific approach in terms of systems and properties considered. This assessment is limited in scope as it is not intended to repeat existing work, it has been included to ensure no perturbation due to system differences or changes in algorithm.

Initial calculations were performed on three known SCO compounds: $[Fe(Phen)_2(NCS)_2]$, $[Fe\{HB(pz)_3\}_2]$ and $[Fe\{HB(tz)_3\}_2]$. Optimisations were conducted utilising a range of exchange-correlation functionals with some variation of basis set in both the ADF and Gaussian09 programs. It should be noted that, in order to acquire smooth convergence, many of the calculations within this assessment required a tightened integration grid, where this has been used a single-point energy calculation was then conducted upon the converged calculation to maintain complete consistency.

Level of Theory		$[Fe(Phen)_2(NCS)_2]$		$[Fe\{HB(pz)_3\}_2]$		$[Fe\{HB(tz)_3\}_2]$	
Program	XC Functional/basis set	S(0)→T(1)	S(0)→Q(1)	S(0)→T(1)	S(0)→Q(1)	S(0)→T(1)	S(0)→Q(1)
ADF	OLYP/TZP	9.94	-4.01	14.57	1.84	14.36	1.41
ADF	OLYP/TZP - frozen core	-	-	14.43	1.72	14.26	1.38
ADF	RPBE/TZP	12.54	6.63	18.12	11.98	17.86	11.92
ADF	B3LYP/TZP	-	-	-	-	20.01	-1.86
ADF	PBE/TZP	-	10.90	18.12	11.94	24.33	23.61
ADF	PBE0/TZP	6.17	-11.93	19.46	-6.00	18.84	-6.85
ADF	D3-RPBE/TZP	1.6	-	-	-	33.81	26.36
ADF	D3-OLYP/TZP	1.26	4.80	-	-	31.31	17.94
ADF	D3BJ-OLYP/TZP	-5.03	-12.62	-	-	25.29	11.84
G09	OLYP/6-311G*	-	-	15.62	3.40	15.47	3.00
G09	OLYP/TZVP	-	-	14.79	2.66	14.88	2.65
G09	B3LYP/TZVP	-	-	12.59	-0.28	18.09	-1.20
G09	B3LYP*/6-311G*	-	-	19.08	14.52	20.37	13.68
G09	PBEKCIS/6-311G*	-	-	12.64	-2.22	13.90	-3.40
G09	ω-B97XD/6-311G*	42.02	-6.06	-	-	27.35	7.09
G09	M06-L/6-311G*	22.10	-5.40	-	-	22.87	-

Table 28: An assessment of various levels of theory for the known SCO compounds: $[Fe(Phen)_2(NCS)_2]$, $[Fe\{HB(pz)_3\}_2]$ and $[Fe\{HB(tz)_3\}_2]$ with the normalised spin-state energetics as a metric. All energies are in kcal mol^{-1}.

Table 28 gives the results of the initial method assessment, note there are multiple levels of theory for which further calculation was deemed a poor use of resources or where multiple attempts at optimisation failed to yield convergence. The ADF program is particularly adapted for calculations upon systems with high degeneracy such as Fe(II) based SCO spin-states. It is also apparent that hybrid-type functionals, that is, functionals that contain a portion of exact exchange, almost universally produce an incorrect ordering of states, giving the quintet as being more stable than the singlet. This is an obviously nonsensical result when working with known

SCO compounds. OLYP, a GGA-type functional also seems prone to yielding a substantially underestimate S(0) to Q(1) energy and is also prone to producing an incorrect ordering of states. Conversely, PBE, another GGA-type functional, tends to overestimate the HS-LS energy gap for each compound. In line with previous literature, the GGA-type functional RPBE was found to consistently provide the correct ordering of states with sensible spin-state energetics for SCO compounds. It should be noted that RPBE was not tested in Gaussian due to it not being available. The application of Grimme's-D3 dispersion both with and without BJ damping within the ADF program yields varied results depending on the system being considered and is therefore unlikely to yield reliable spin-state energetics.[153-155]

Varying the basis set across both programs and several exchange-correlation functionals seems to have only a limited impact upon the spin-state energetics. Introducing frozen cores appears to have little impact over using an all-electron basis set, however as the largest atom in the system is Fe additional computational cost is slight for the additional accuracy.

These observations were confirmed by the application of three GGA-type functionals to a further known SCO compounds, $[Fe(Btz)_2(NCS)_2]$, due to the intention of applying the NCS ligand in later design work. These results are displayed below in Table 29.

Level of Theory		$[Fe(Btz)_2(NCS)_2]$	
Program	Functional/basis set	S(0)→T(1)	S(0)→Q(1)
ADF	OLYP/TZP	6.91	-6.40
ADF	RPBE/TZP	10.66	4.41
ADF	PBE/TZP	15.62	16.45

Table 29: An assessment of various levels of theory for the known SCO compound $[Fe(Btz)_2(NCS)_2]$ with the normalised spin-state energetics as a metric. All energies are in kcal mol^{-1}.

Again the same trends across the GGA-type functionals are seen. In this case, PBE results in an incorrect ordering of states by suggesting the Q(1) state is less energetically favourable than the T(1) state, thus breaking the spin-transition pathway. It should be noted that optimisations for PBE0 were attempted upon this system but failed to attain convergence. In order to confirm the behaviour of a selection of the above levels of theory, a limited assessment of method was then conducted upon a known low-spin compound, $[Fe(BiPy)_3]^{2+}$.

Level of Theory		$[Fe(BiPy)_3]^{2+}$	
Program	XC Functional/basis set	S(0)→T(1)	S(0)→Q(1)
ADF	OLYP/TZP	16.28	7.05
ADF	RPBE/TZP	19.94	17.50
ADF	PBE/TZP	26.11	29.70
ADF	PBE0/TZP	12.37	-
ADF	D3-RPBE/TZP	25.00	23.56
ADF	D3-OLYP/TZP	32.84	38.69
ADF	D3BJ-OLYP/TZP	27.03	17.17

Table 30: An assessment of various levels of theory for the known low-spin compound $[Fe(BiPy)_3]^{2+}$ with the normalised spin-state energetics as a metric. All energies are in kcal mol^{-1}.

Table 30 shows similar trends as discussed for the SCO compounds above. Two Gaussian based methods, ω-B97XD/6-311G* and M06-L/6-311G* were attempted but failed to give convergence for any of the three spin-states. PBE0 failed to give convergence for the Q(1) state.

Computational details

Given the complexities of modelling SCOs with DFT and the above assessment of various levels of theory, optimisations were performed within the ADF programme at the RPBE/TZ2P level of theory.[101,102] All geometries have been confirmed as local minima via analytical frequency calculations.[183–185] ETS-NOCV was calculated taking the Fe(II) ion and the ligand system as separate fragments in a manner similar as to that described above in Chapter 2.[110,111] TDDFT calculations were performed upon the ground-state singlet geometry.[188] The Jmol program was used for visualisation purposes.[152] It should be noted that the following calculations were performed after a version update to the ADF program and hence were conducted using a Becke-type integration grid rather than the numerical integration grid used for the above assessment of functionals, this was adopted due to an increase in accuracy and a result increase in ease of convergence.

Results and Discussion

Given the aforementioned difficulties inherent to calculating spin-state energetics with DFT initial calculations were performed upon the well-known $[Fe(Phen)_2(NCS)_2]$ complex.[60] This complex is an ideal candidate for use as a benchmark due to its proliferation through literature where an assessment of exchange-correlation functionals has been performed and its previous identification as an SCO compound via experimental methods. Thus the following assessment focuses on known SCO compounds, with a single known low-spin compound as a control and assess the relative energies of the S(0), S(1), T(1) and Q(1) spin-states.

Excited state optimisation calculations are notoriously complex, hence current literature tends to focus on merely singlet and quintet states. This simplification leaves out a large portion of the pathway of the spin-transition. KS-DFT can often struggle with calculating states above that of

the ground state potential energy surface (GS-PES). Generally DFT programs will use TDDFT gradients in order to conduct an excited state optimisation. However these are complicated calculations which are often riddled with convergence issues both within the SCF procedure and within the geometry cycles themselves. The algorithmic implementation of the TDDFT gradients also often results in incompatibility with other important parts of the code, such as spin-orbit ZORA and analytical frequencies within the ADF program. Additionally, there is a significant exchange-correlation functional dependency apparent in the calculation of the properties of SCO compounds. Functionals incorporating a portion of exact exchange and long-range corrections, such as CAM-B3LYP, are far-superior at simulating excitation energies via TDDFT but are known to be poor at estimating the energy differences between spin-states in SCO compounds, even to the extent of resulting in an incorrect ordering of states. Conversely, GGA functionals are known to more accurately and reliably estimate the spin-state energetics of SCO compounds however, they are also known to significantly under-estimate the transition energies within TDDFT. These calculations also often optimise to an energy similar to that of the ground-state suggesting that the geometry merely pertains to a local minima upon the GS-PES. Fortunately, as demonstrated previously in Chapter 2, a subtle use of the occupations block can allow for usually inaccessible functionality due, in large part, to the possibility in ADF to treat partial occupations. This functionality allows for the manual specification of electron distribution in a two-step optimisation calculation where the first step is a manual smearing of the valence electrons across the d-space in a spin-unrestricted single-point energy calculation. The output file resulting from this single-point energy calculation is then used as a restart file for a spin-restricted geometry optimisation with specified electron occupation numbers for the excited singlet state. Given that this calculation is, in essence, a ground-state optimisation, it is plausible that it will apply in a range of situations which are impossible to achieve with TDDFT gradients. Also, given the removal of the reliance upon TDDFT gradients, this method should be accurate when used in conjunction with GGA functionals therefore allowing for the accurate calculation

of the energy differences between spin-states. It should be noted that this is not a procedure without faults. The SCF convergence for the initial geometry cycles can be problematic and often needs to be bypassed by lowering the secondary convergence threshold to achieve moderate convergence. Additionally, as with many other DFT calculations, an accurate starting geometry is of the utmost importance. Given that theoretically the electron density should occupy orbitals in a similar manner to the triplet; using the geometry from a converged triplet optimisation can aid in the optimisation of the first excited singlet state. Additionally, by further capitalising on the PAoC method of ETS-NOCV described in Chapter 2 it should be possible to elucidate upon the bonding interaction between the Fe(II) ion and the N6 ligand sphere that is intrinsic to SCO behaviour in Fe(II) based complexes. Applying these techniques allows for the full computational characterisation of the spin-transition pathway of the $[Fe(Phen)_2(NCS)_2]$ complex.

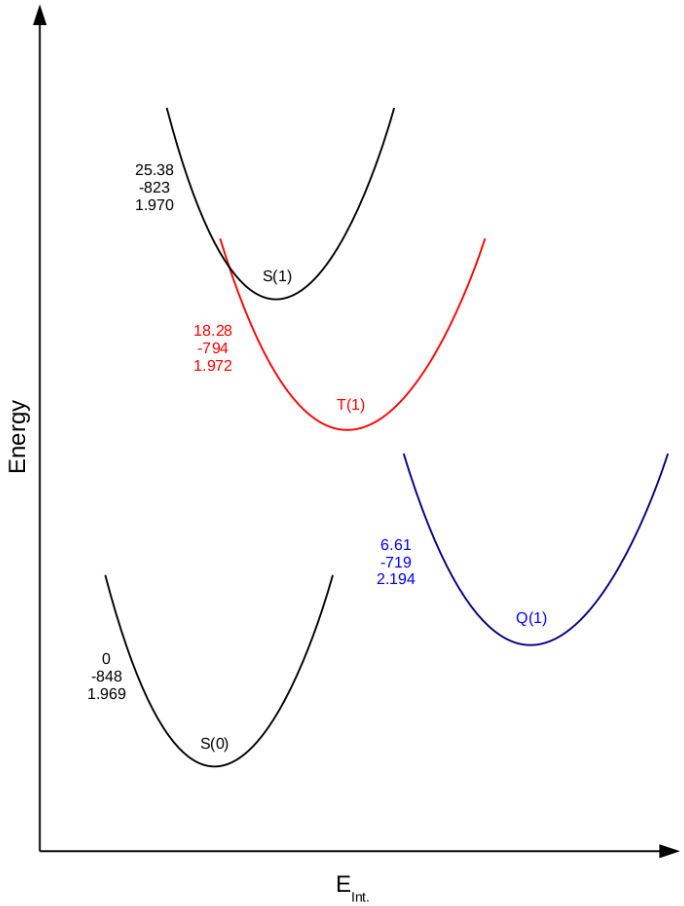

Figure 29: The scaled spin-transition pathway for the [Fe(Phen)2(NCS)2] complex with the values being the absolute energy (top), interaction energy (middle) and average Fe-N bond length (bottom). All energies are presented in kcal mol^{-1} with bond lengths presented in Å.

Figure 29 shows that the use of the RPBE GGA type functional with a TZ2P all-electron, STO type basis set provides the correct ordering of states and yields a high-spin to low-spin gap (ΔE_{HL}) of 6.61 kcal mol^{-1}. Furthermore the decrease in magnitude of $E_{Int.}$ towards higher spin-states correlates well with the bond weakening expected with removal of electrons from the typically non-bonding t_{2g} orbitals into the anti-bonding e_g orbitals. Hence this interaction energy between the Fe(II) ion and the ligand system appears to be a valid tool for the computational examination of SCO compounds in lieu of a generalised reaction coordinate.

	S(0)	S(1)	T(1)	Q(1)
Mean Fe-N bond length (Å)	1.969	1.970	1.972	2.194
Mean Fe-N bond order	0.586	0.587	0.599	0.419
Mean Fe-N_{Phen} bond length (Å)	1.981	2.012	2.012	2.2915
Mean Fe-N_{Phen} bond order	0.567	0.541	0.546	0.417

Table 31: A comparison of bond lengths and bond orders for the S(0), S(1), T(1) and Q(1) states of the $[Fe(Phen)_2(NCS)_2]$ complex both including and excluding the effects of the NCS ligands.

Table 31 shows that the mean bond lengths are affected by an unusual strengthening of the NCS bonds. Thus, whilst the mean Fe-N bond favoured in literature to yield the 0.2 Å HS-LS bond length difference indicative of an SCO compound can be seen to be replicated here, it can be a poor metric when the geometry of the S(1) and T(1) states are considered. Therefore $E_{Int.}$ was used as the reaction coordinate in Figure 29 above. The rationale for the effect of the NCS ligands can be further elucidated upon examination of the orbitals of $[Fe(Phen)_2(NCS)_2]$ as seen in Figure 30 below.

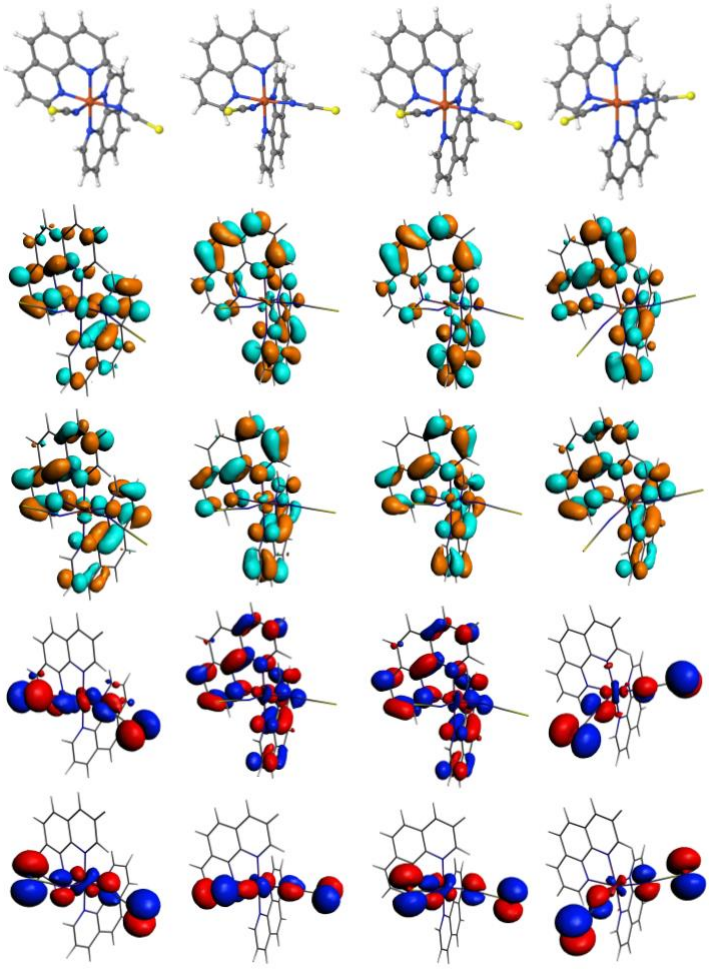

Figure 30: LUMO+1 to HOMO-1 (in descending order) for the S(0), S(1), T(1) and Q(1) states (from left to right) of the [Fe(Phen)$_2$(NCS)$_2$] complex.

Despite the usually non-bonding behaviour of the t_{2g} orbitals in SCO compounds, the valence MOs for the S(0) state displayed above show a significant degree of contribution from NCS-based anti-bonding orbitals. Figure 30 also demonstrates the similarity in the positioning of the electron density in the T(1) and S(1) states. This is not surprising because, as mentioned previously, both states should exhibit a $t_{2g}^5 e_g^1$ electron configuration merely differing in the relative spin of the unpaired electrons. Thus bond lengths remain the same across the system however, a small but significant difference is seen in the magnitude of $E_{Int.}$. The more surprising property of the orbitals of the T(1) and S(1) states is the presence of electron density on the aryl system and the subsequent lack of such density in the aryl system of the Q(1) state. This suggests

that a more favourable spin-transition to the quintet may be achieved with a better π-accepting aryl system around the coordinating N atoms stabilising the T(1) and S(1) states. Given that it proved to be possible to conduct PAoC-ETS-NOCV upon the usually inaccessible unrestricted states above the ground state singlet via the generation of pseudo-restricted fragments, there is the possibility of examining the deformation densities, these are displayed below.

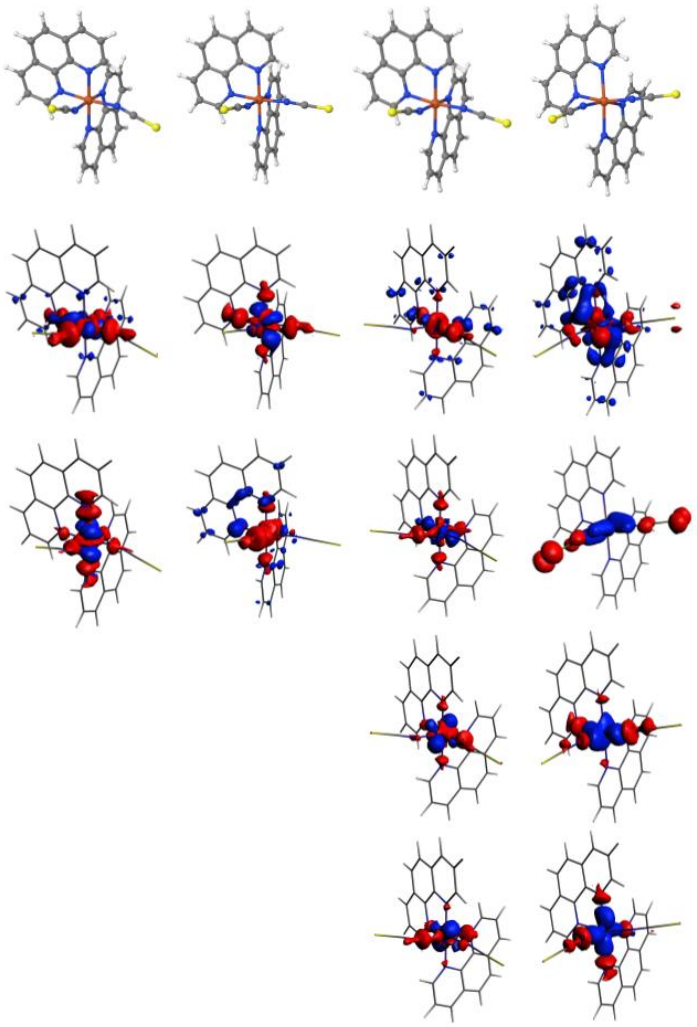

Figure 31: The deformation densities for the S(0), S(1), T(1) and Q(1) states (from left to right) of the [Fe(Phen)$_2$(NCS)$_2$] complex listed in descending order of magnitude of their respective eigenvalues. Charge flow is from red to blue.

As can be seen from Figure 31, the majority of charge flow, is, as expected, from the N6 donor sphere towards metal based d-orbitals as well as some charge flow indicative of d-d transitions. However, what is unexpected is signs of Dewar-Chatt-Duncanson (DCD) style back-bonding into the aryl system. Whilst this is only slight in the S(0), S(1) and T(1) states, it is significant in the Q(1) state. This suggests that back-bonding may be an integral factor in determining the stability of the Q(1) state in SCO compounds. A comparison to the deformation densities of the low-spin $[Fe(BiPy)_3]^{2+}$ complex as shown in Figure 32 is revealing.

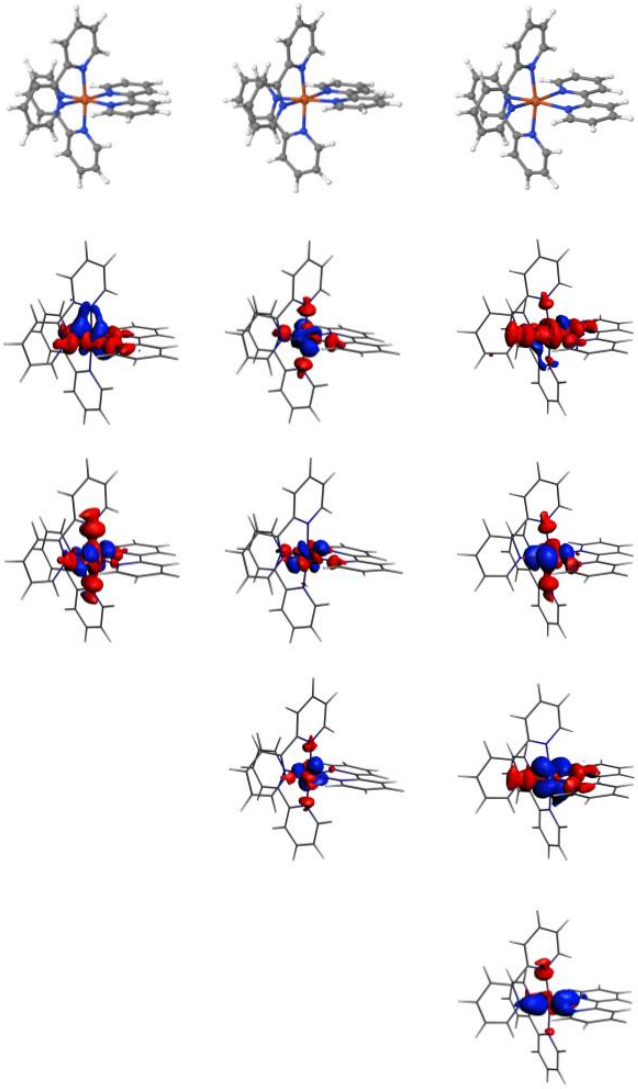

Figure 32: The deformation densities for the S(0), T(1) and Q(1) states (from left to right) of the $[Fe(BiPy)_3]^{2+}$ complex listed in descending order of magnitude of their respective eigenvalues. Charge flow is from red to blue.

These deformation densities are dominated by N to Fe donation and d to d transitions, any evidence of back-donation is negligible. Being a low-spin compound and given the difficulties with using DFT upon SCO compounds, it is useful to calculate the absolute energies of the states to benchmark the particular level of theory, this is shown below in Figure 33.

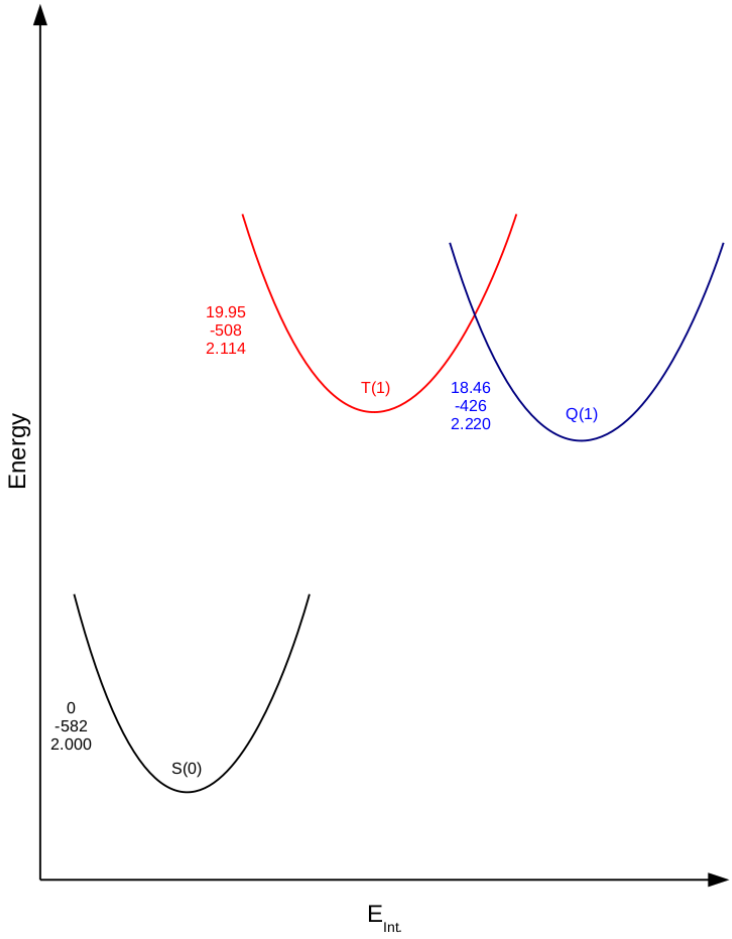

Figure 33: The scaled spin-transition pathway for the $[Fe(BiPy)_3]^{2+}$ complex with the values being the absolute energy (top), interaction energy (middle) and average Fe-N bond length (bottom). All energies are presented in kcal mol^{-1} with bond lengths presented in Å.

The HS-LS gap here is large ruling out any significant spin-transition behaviour thus confirming the RPBE/TZ2P level of theory is correctly replicating the relative energetics of the system. The lack of the S(1) state here is immediately apparent and highlights the limitations of using a

ground-state approach to acquiring excited-state electronic configurations. The rationale for this can be elucidated via the inspection of the TDDFT data for the HOMO-LUMO transition as displayed in Table 32 below.

System	HOMO-LUMO	TDDFT	Weight	Oscillator strength
$[Fe(Phen)_2(NCS)_2]$	18.449	19.872	75.22%	4.59E-03
$[Fe(BiPy)_3]^{2+}$	38.858	38.550	99.10%	5.98E-04

Table 32: The eigenvalue and TDDFT values for the HOMO-LUMO singlet transition from the S(0) state for $[Fe(Phen)_2(NCS)_2]$ and $[Fe(BiPy)_3]^{2+}$. All energies in kcal mol^{-1}.

It is evident that the value of the HOMO-LUMO singlet transition for $[Fe(Phen)_2(NCS)_2]$ is well below the relative energy of the minima of the optimisation of the S(1) state as shown above in Figure 29. This is not unexpected because, as discussed above, RPBE is known to underestimate the energetics of vertical excitations. Despite this, useful insight can still be gained from Table 32. That is, both systems display non-zero oscillator strengths suggesting that it is possible to populate the S(1) state. Additionally the energy associated with the HOMO-LUMO singlet transition in $[Fe(BiPy)_3]^{2+}$ complex is large even with an underestimation, suggesting that the difficulty in attaining the excited state through a ground state optimisation is due to this electron configuration being drastically more unstable than the S(0) state. The size of the underestimation in both systems would also suggest that the standard TDDFT spin-flip gradient based excited state optimisation is likely to fail due to the algorithm 'missing' the higher PES and hence producing results similar to the S(0) optimisation. The valence orbitals for the $[Fe(BiPy)_3]^{2+}$ complex are displayed below in Figure 34 for reference.

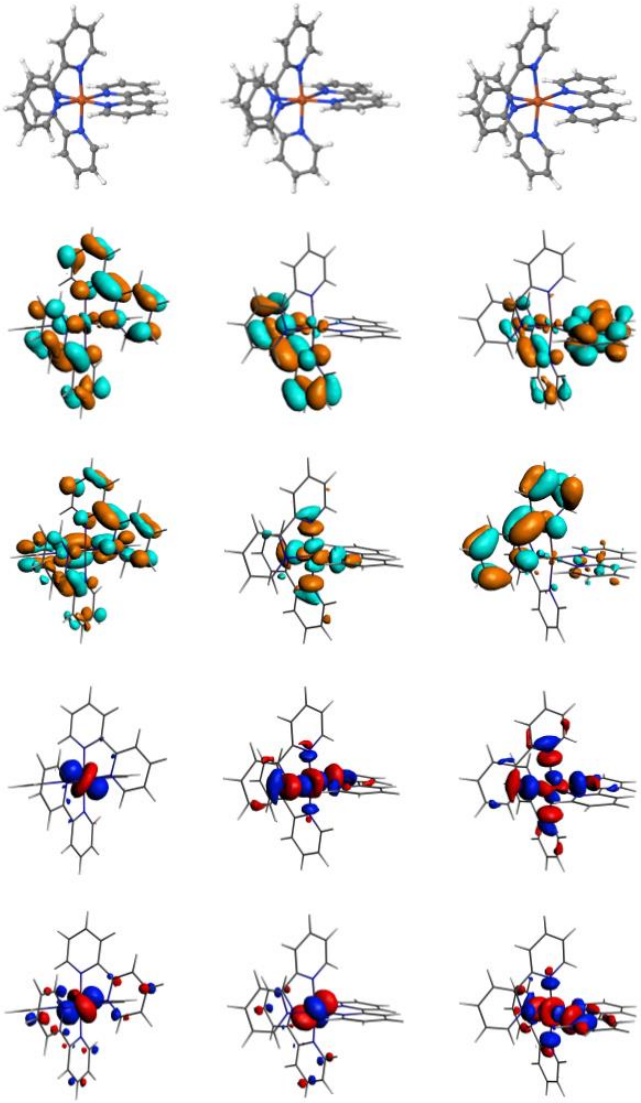

Figure 34: LUMO+1 to HOMO-1 (in descending order) for the S(0), T(1) and Q(1) states (from left to right) of the $[Fe(BiPy)_3]^{2+}$ complex.

Conclusion

Given previously mentioned reported literature and a method assessment, a RPBE/TZ2P level of theory in the ADF program has been adopted for further SCO calculations. It has also proven to be possible to fully model the spin-transition pathway of the known SCO compound, $[Fe(Phen)_2(NCS)_2]$ and fully describe the bonding interaction between the ligand sphere and the metal ion at all spin-states, thus providing a benchmark for the KS-DFT based design of SCO compounds. Additionally, whilst a PAoC based ground-state approach has its limitations, it

would appear to be an important tool in allowing a more complete description of the spin-transition pathways of SCO compounds without having to resort to the use of exact exchange which demonstrably fails to replicate the relative energetics of the spin states.

Chapter 7 - Boron Mediated Modulation of Spin-State Energetics Assessed with Density Functional Theory

Introduction

Given the advances in DFT in dealing with complex electronic configurations and the control over these electronic states granted by the unique properties of boron, both of these have been applied in this work to the intriguing problem of spin-state energetics, particularly to that which is inherent to the mechanics of spin-crossover. As mentioned previously in Chapter 1, these compounds are commonly based around one or more Fe(II) centres in an octahedral field to provide a d^6 electronic configuration across t_{2g} and e_g orbitals. Electron donation is usually provided to the metal centre through a N6 first sphere of coordination consisting of various combinations of both L- and X- type ligands. It should be eminently possible to modulate the donating power of the first sphere of coordination via the precise inclusion of boron centres into the ligands to affect a subtle modulation of the high-spin low-spin (HS-LS) energy gap.

The role aromaticity in a significant number of SCO ligand systems should allow for a novel manner of modulating the HS-LS gap. Previous chapters have focused upon the controlled tuning of aromaticity through the use of an interrupting sp^3 centre. These are bridged by a through-space homoaromatic interaction and the modification of these rarely encountered curiosities towards utility.[6] A neutral homoaromatic compound lacking strongly donating groups such as N-heterocyclic carbenes with suitably placed nitrogen centres should be susceptible to binding to a metal ion such as Fe(II). As previously shown in Chapter 4, the addition of boron into these homoaromatic compounds allows for control over the flow of charge within the ring system and thus opens up a range of strengths for the π-interaction across a set of structural isomers. Thus,

when a metal-binding nitrogen centre is included with a homoaromatic system as a one-electron donor it should be possible to affect a subtle perturbation to the electron density upon this nitrogen centre thus affecting its donor strength. The application of these to spin-switchable systems offers a route to the subtle modulation of the donating power of the N6 sphere and thus perturb the magnitude of the high-spin low-spin (HS-LS) gap with the aim of allowing for a more controlled spin-transition. Although showcased here with the well-known $[Fe(phen)_2(NCS)_2]$, the replacement of aromatic rings with comparable homoaromatic systems is theoretically applicable to a wide range of chemical situations.

Computational details

All optimisations upon transition metal complexes were performed within the ADF program at the RPBE/TZ2P level of theory.[101,102] Calculations regarding the homoaromatic metrics for the homoaromatic ligand candidates were performed in Gaussian at the B3LYP/6-311G* level of theory.[137–144,155] SEDD was performed in the ADF programme based on optimisation at the B3LYP/ZORA-QZ4P level of theory.[88,176,179–182] B3LYP has been used to characterise the homoaromatic ligand candidates due to its accurate treatment of small organics systems, however, it has not been used across all calculations in this work due to its tendency to result in an incorrect ordering of states upon application to SCOs.

Results and Discussion

Characterisation of a set of homoaromatic ligand candidates

The proposed homoaromatic ligand candidates are a set of structural isomers resulting from the inclusion of homoaromatic architecture into the aromatic phenanthroline (phen) ligand within the well-known $[Fe(Phen)_2(NCS)_2]$ complex.[60] This results in an increased number of possible

arrangements in space of the heteroatoms and thus the following naming system is proposed and displayed upon a key in Figure 35.

Figure 35: Schematic of the numbering system used to enable the specification of the positioning of heteroatoms

This system is similar to that as proposed previously in Chapter 4 but differs in that the one-electron (i.e. imine-type) nitrogen donors (A) are not specified as they are the N centres positioned to donate an electron pair to the metal and are therefore required to remain in the same position across all of the structural isomers. Thus the scheme proceeds as follows; 7(#)-N(#)B(#) where the first number denotes ring size with the number in parentheses specifying the position of the interrupting sp^3 centre. The positions of two-electron (i.e. amine-type) nitrogen donors (N) and boron atoms (B) are denoted by the number following in parentheses. Note that the two ring systems supporting the imine-type donors have been arranged symmetrically through a mirror plane.

The strength of the resultant homoaromatic interaction has been assessed according to a set of previously designed numerical metrics with the results displayed below in Table 33.

Compound identifier	WBI of the homoconjugative gap	Homoconjugative gap distance	δ(^{13}C) in the π-system	δ(^{15}N) of N	δ(^{15}N) of A	δ(^{11}B)	$NICS_0$
Phen	N/A	N/A		N/A		N/A	
7(6)-N(4)B(5)	0.07, 0.07	2.46, 2.46	139, 132, 161 161, 132, 139	174, 174	414, 414	32, 32	-2.86, -2.86
7(3)-N(4)B(5)	0.02, 0.02	2.46, 2.46	184, 138, 152 152, 138, 184	159, 159	456, 456	29, 29	1.59, 1.59
7(5)-N(4)B(6)	0.05, 0.05	2.41, 2.41	146, 118, 159 159, 118, 146	122, 122	357, 357	13, 13	-5.41, -5.40
7(5)-N(2)B(6)	0.08, 0.08	2.31, 2.31	112, 129, 138 137, 129, 112	194, 194	316, 316	18, 18	-7.19, -7.21
7(5)-N(2)B(1)	0.05, 0.05	2.41, 2.41	154, 107, 140 140, 107, 154	194, 194	389, 389	32, 32	-4.12, -4.12
7(5)-N(1)B(2)	0.04, 0.04	2.44, 2.44	141, 143, 141 141, 143, 141	274, 274	387, 387	26, 26	-2.85, -2.86
7(6)-N(2)B(5)	0.07, 0.07	2.42, 2.42	122, 149, 145 145, 149, 122	195, 195	344, 344	48, 48	-3.79, -3.78
7(5)-N(6)B(4)	0.16, 0.16	2.27, 2.27	150, 143, 144 144, 143, 150	141, 141	397, 397	21, 21	-7.93, -7.94
7(4)-N(3)B(2)	0.02, 0.02	2.45, 2.45	151, 116, 201 201, 116, 151	144, 144	432, 432	31, 31	1.36, 1.35
7(4)-N(2)B(3)	0.14, 0.14	2.28, 2.28	144, 107, 148 148, 107, 144	201, 201	324, 324	23, 23	-6.66, -6.56

Table 33: A collection of numerical metrics to assess the strength of the π-interaction in a set of homoaromatic ligand candidates.

The data displayed in Table 33 mirrors the conclusions attained from Chapter 4 and shows that massive differences in the strength of interaction across a homoconjugative gap can be accessed by the use of structural isomerism. This isomerism is achieved via the use of a boron centre acting as a charge transfer node in order to mediate the ring current through the system. This allows for a greater control of placement over the more classical carbocation based approach. It should be noted that compounds 7(3)-N(4)B(5) and 7(4)-N(3)B(2) show little to no homoaromatic behaviour. However these compounds will be included in the Fe(II) based SCO

compound test as a form of control, showcasing the impact of a highly conjugated system in place of aromaticity on the HS-LS gap.

Compound identifier	WBI of the homoconjugative gap	Homoconjugative gap distance	$\delta(^{13}C)$ in the π-system	$\delta(^{15}N)$ of N	$\delta(^{15}N)$ of A	$\delta(^{11}B)$	$NICS_0$
7(1)-N(4)B(5) Cis	0.03, 0.04	2.65, 2.44	178, 134, 125 135, 129, 182	165, 174	488, 479	29, 32	-1.18, 6.20
7(1)-N(4)B(5) Trans	0.04, 0.04	2.43, 2.43	182, 133, 131 131, 133, 182	176, 176	486, 486	31, 31	-1.25, -1.25
7(1)-N(3)B(2) Cis	0.04, 0.08	2.62, 2.36	157, 116, 140 137, 119, 156	166, 160	415, 414	40, 28	2.92, -4.12
7(1)-N(3)B(2) Trans	0.07, 0.07	2.44, 2.44	156, 118, 139 139, 118, 156	165, 165	410, 410	31, 31	-2.79, -2.79

Table 34: A collection of numerical metrics to assess the strength of the π-interaction in a pair of homoaromatic ligand candidates exhibiting stereochemistry.

Table 34 shows the homoaromatic metrics as applied to 7(1)-N(4)B(5) and 7(1)-N(3)B(2). These compounds differ from the previous candidates in the that positioning of the interrupting sp^3 centre within the central aromatic ring allows for the possibility of a pair of geometric isomers due to the positioning of H atoms either above or below the plane of the molecule. As can be seen from the cis isomers, this creates an asymmetric molecule with different behaviour across each homoconjugative gap. Conversely, inspection of the rapid metrics for the trans compounds show that both structural isomers are symmetric systems that display low to middling degrees of homoaromatic behaviour.

The recent advance in electron localisation methods represented by the Single Density Decay-Detector (SEDD) offers an opportunity to visualise the homoaromatic interaction via a computationally inexpensive manner. As shown above in Chapter 5, this electron localisation

technique can be used to add a powerful qualitative method for a rapid assessment as to whether a system displays aromatic character. These are displayed below in Figure 36 and Figure 37.

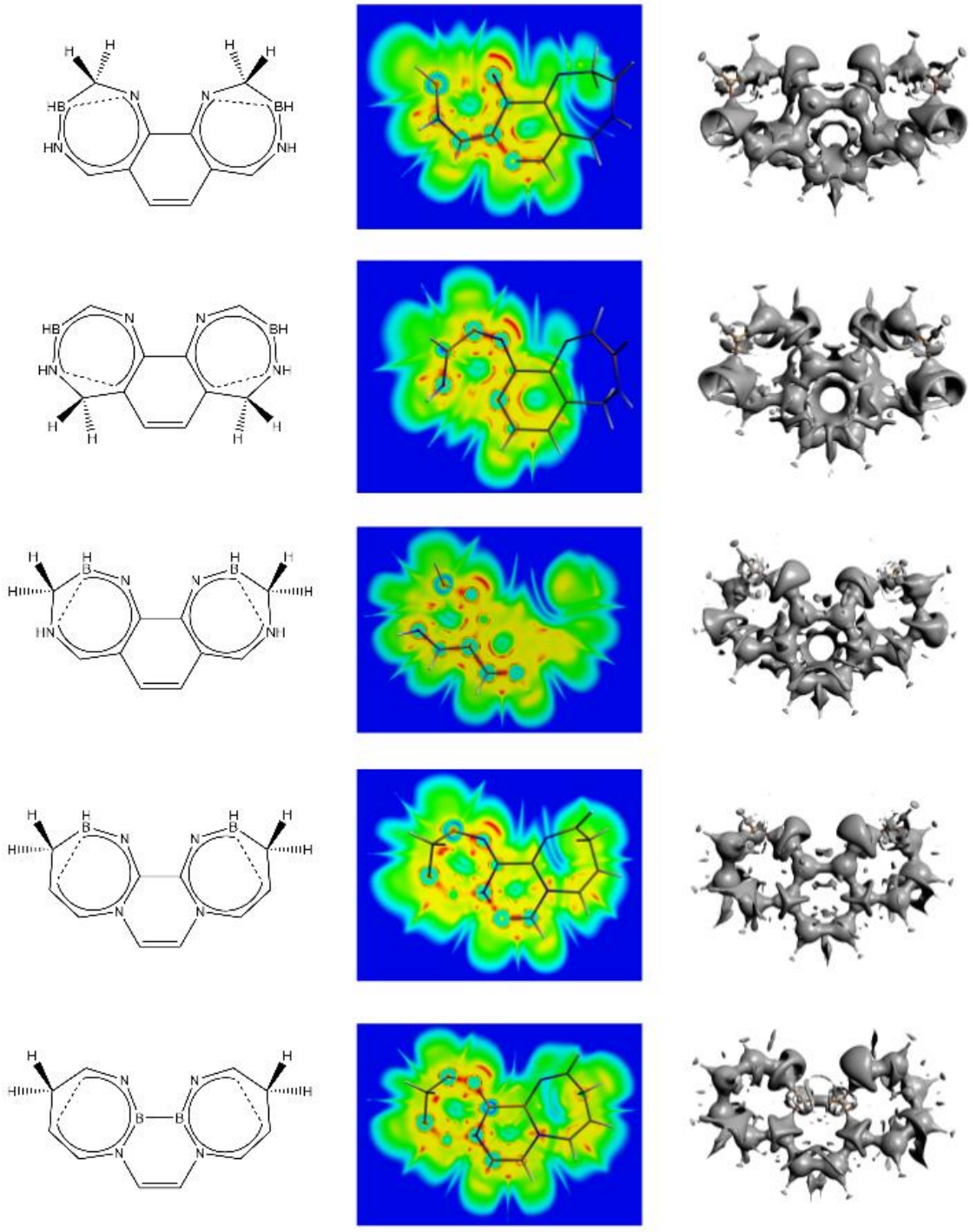

Figure 36: Contour planes and isosurfaces for a set of geometric isomers of seven-membered homoaromatic ligand candidates based on the well-known phen ligand with a [N-H] fragment as a two-electron donor calculated with a ZORA-QZ4P STO basis set.

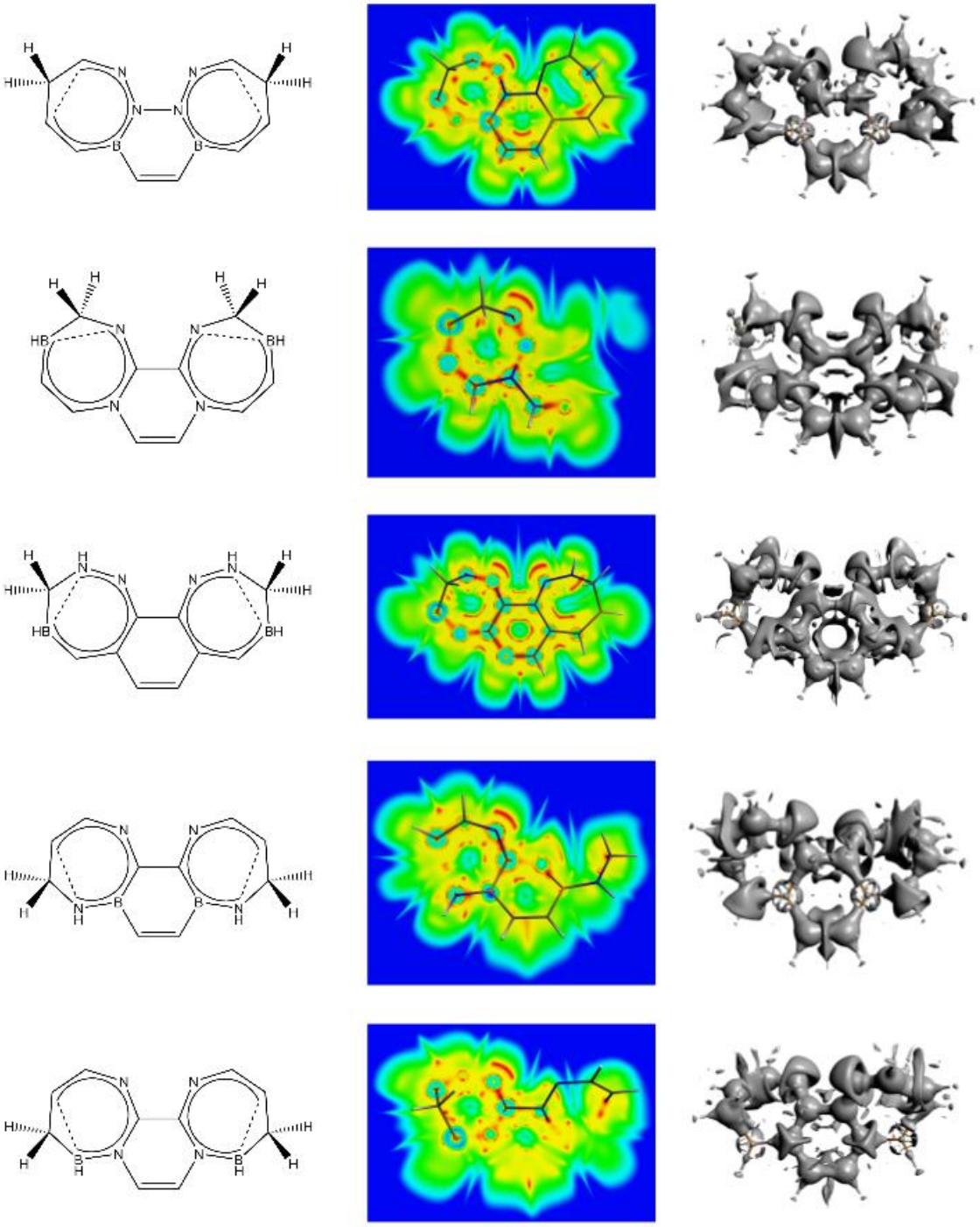

Figure 37: Contour planes and isosurfaces for a set of geometric isomers of seven-membered homoaromatic ligand candidates based on the well-known phen ligand with a [N-H] fragment as a two-electron donor calculated with a ZORA-QZ4P STO basis set.

It is immediately obvious that the directionality of the N lone pair towards the metal is largely conserved and a qualitative difference in electron density can be seen. As discussed previously,

homoaromatic interactions viewed via SEDD tend to show varying degree of fragmentation in both the interior ring of density in the contour planes and the localisation domains of electron density in the isosurfaces. In some cases, especially in areas of significant fragmentation, this may suggest a lack of aromatic character but the presence of any indicators suggests a degree of conjugation and a node of electron density across the homoconjugative gap shows the existence of ring current thus there is likely to be an impact on the strength of electron donation from the N centre to the metal.

Attenuating the HS-LS gap

Having been characterised with the rapid metrics developed in Chapter 3, the ligand candidates were applied in place of both phen ligands upon the $[Fe(phen)_2(NCS)_2]$ complex. These candidate compounds have been fully characterised with the methodology developed above in Chapter 6 to elucidate upon the spin-transition pathways and display both the valence orbitals and the deformation densities with the largest associated eigenvalues. Each candidate has been assessed individually and labelled as per the numbering system presented in Figure 35.

[Fe{7(6)-N(4)B(5)}$_2$(NCS)$_2$]

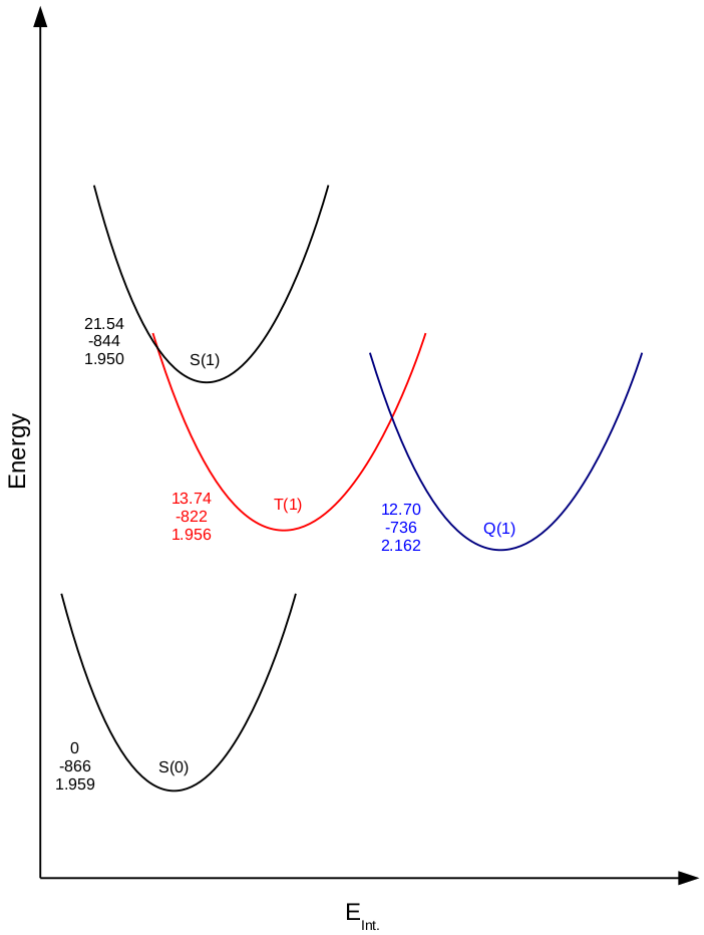

Figure 38: The scaled spin-transition pathway for the [Fe{7(6)-N(4)B(5)}$_2$(NCS)$_2$] SCO candidate with the values being the absolute energy (top), interaction energy (middle) and average Fe-N bond length (bottom). All energies are presented in kcal mol^{-1} with bond lengths presented in Å.

The homoaromatic ligand candidate, 7(6)-N(4)B(5), displays a relatively weak homoaromatic interaction although the Wiberg bond order values are considerable. The use of this ligand in a Fe(II) complex has significantly increased the HS-LS gap as can be seen above in Figure 38. The gap has increased to such an extent that the Q(1) state is close to the energy of the T(1) state that would result in a spin-transition pathway that is more reminiscent to that of the low-spin [Fe(BiPy)$_3$]$^{2+}$ complex although these states are much closer in energy to that of the S(0) state however the S(1) state is of a significantly lower energy and thus is likely to be easier to populate thermally. The increase in bond length between the S(0) and Q(1) states is 0.203Å and is thus

similar to the bond length expansion of 0.2 Å common to SCO compounds. However, the large HS-LS gap means that [Fe{7(6)-N(4)B(5)}$_2$(NCS)$_2$] is far more likely to act as a low-spin compound rather than exhibit spin-switchable behaviour. The T(1) and S(1) states exhibit a similar geometry and interaction energy.

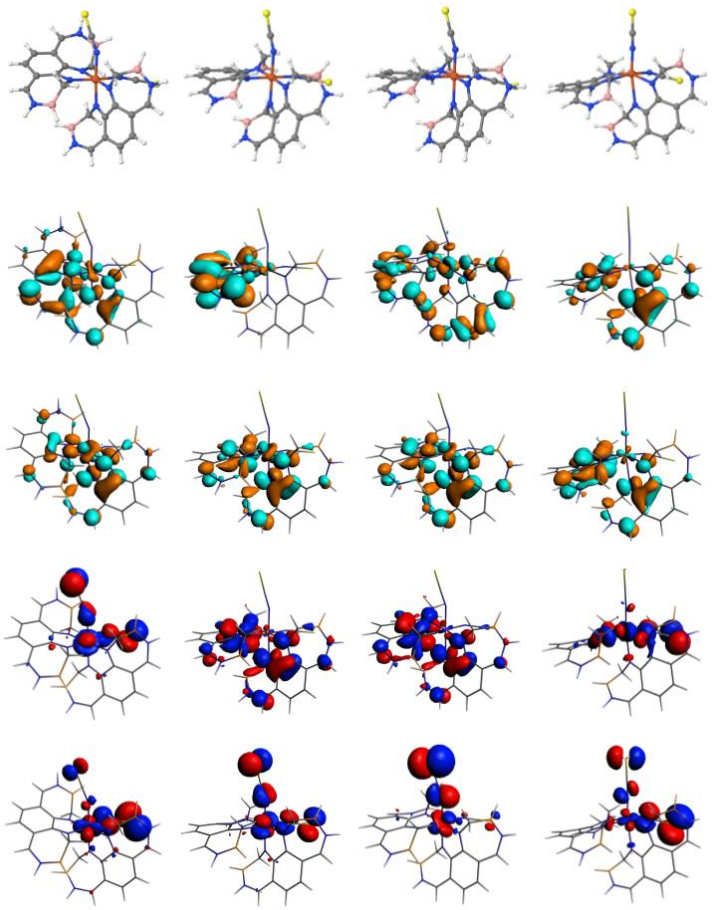

Figure 39: LUMO+1 to HOMO-1 (in descending order) for the S(0), S(1), T(1) and Q(1) states (from left to right) of the [Fe{7(6)-N(4)B(5)}2(NCS)2] SCO candidate

The orbitals displayed in Figure 39 are similar to those of [Fe(Phen)$_2$(NCS)$_2$] and also show similar positioning of the valence electrons in the S(1) and T(1) states thus providing a rationale for the similarities in their molecular geometries.

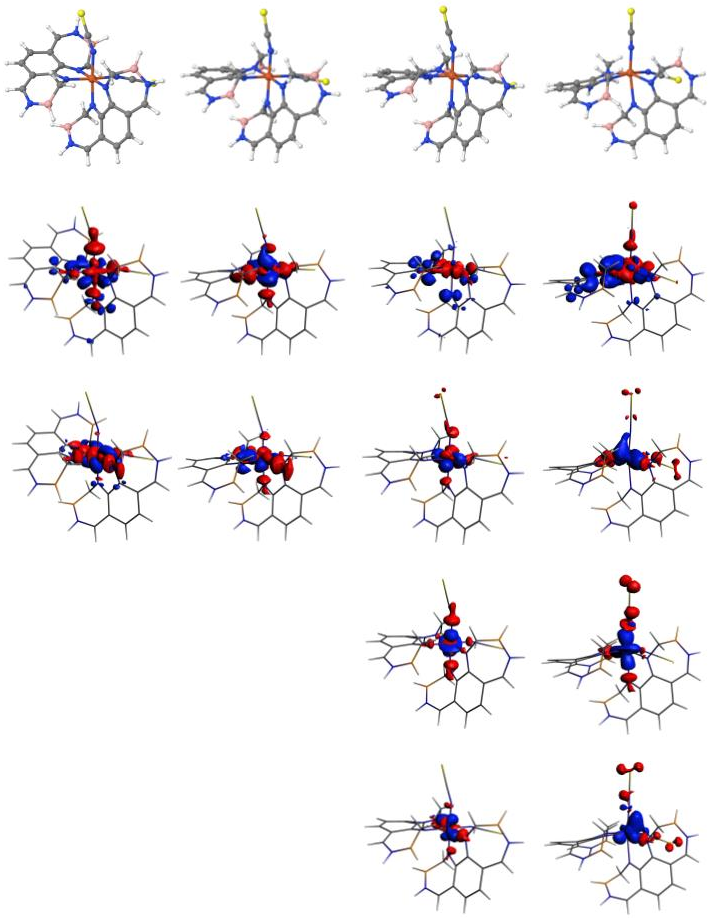

Figure 40: The deformation densities for the S(0), S(1), T(1) and Q(1) states (from left to right) of the [Fe{7(6)-N(4)B(5)}$_2$(NCS)$_2$] SCO candidate listed in descending order of magnitude of their respective eigenvalues. Charge flow is from red to blue.

The deformation densities are also similar thus suggesting that the differing HS-LS gap is due to the modulation of the donation strength of the aryl-based nitrogen centres rather than the direction of electron flow. This is supported by the $E_{Int.}$ values which are approximately 20 kcal mol^{-1} larger in each spin-state for the [Fe{7(6)-N(4)B(5)}$_2$(NCS)$_2$] candidate.

[Fe{7(1)-N(4)B(5)}$_2$(NCS)$_2$]

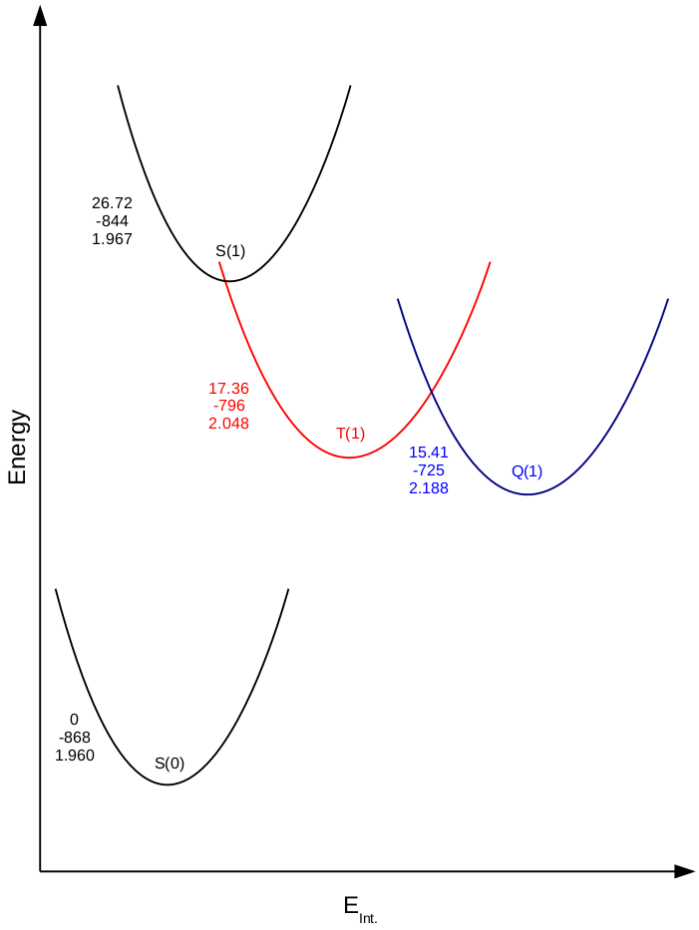

Figure 41: The scaled spin-transition pathway for the [Fe{7(1)-N(4)B(5)}$_2$(NCS)$_2$] SCO candidate with the values being the absolute energy (top), interaction energy (middle) and average Fe-N bond length (bottom). All energies are presented in kcal mol^{-1} with bond lengths presented in Å.

The homoaromatic ligand candidate, 7(1)-N(4)B(5), is an interesting case as presented in Table 34, it is subject to geometric isomerism due to the placement of the sp^3 centre within the central aromatic ring structure. The homoaromatic ligand candidates attached here are both of the cis geometry because this ligand may be more likely to bind to a metal centre due reduced strain in comparison to the trans ligand. Figure 41 shows that adding these candidates into the test complex yields a spin-transition even more similar to the low-spin [Fe(BiPy)$_3$]$^{2+}$ complex than that of [Fe{7(6)-N(4)B(5)}$_2$(NCS)$_2$] shown above, with a large HS-LS gap, suggesting that [Fe{7(1)-N(4)B(5)}$_2$(NCS)$_2$] will almost certainly be low-spin. The Fe-N bond length increase between the

S(0) and Q(1) of 0.228 Å is slightly larger than that expected of SCO behaviour but not substantially so. However, it is interesting to note that the S(1) state is not particularly high energetically.

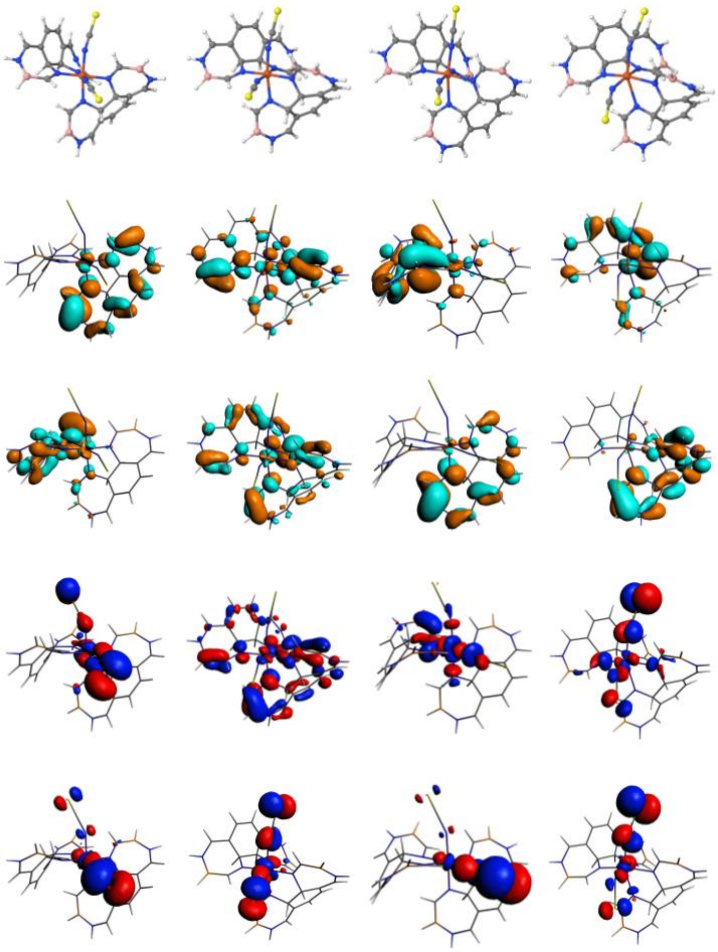

Figure 42: LUMO+1 to HOMO-1 (in descending order) for the S(0), S(1), T(1) and Q(1) states (from left to right) of the [Fe{7(1)-N(4)B(5)}$_2$(NCS)$_2$] SCO candidate.

The valence orbitals of [Fe{7(1)-N(4)B(5)}$_2$(NCS)$_2$] shown in Figure 42 offer a rationale for the relative stabilisation of S(1) state. They show that, unlike [Fe(Phen)$_2$(NCS)$_2$] and some of the other promising SCO candidates in this set, the HOMO of the T(1) state is less delocalised throughout the aryl system and is largely centred upon the Fe(II) centre and a single π-bonding orbital and even a reduction in delocalisation across the anti-bonding NCS orbitals is seen in the

HOMO-1, this is also seen in the Q(1) state. However, the S(1) state retains this delocalisation within the HOMO and HOMO-1 likely accounting for its relatively low absolute energy.

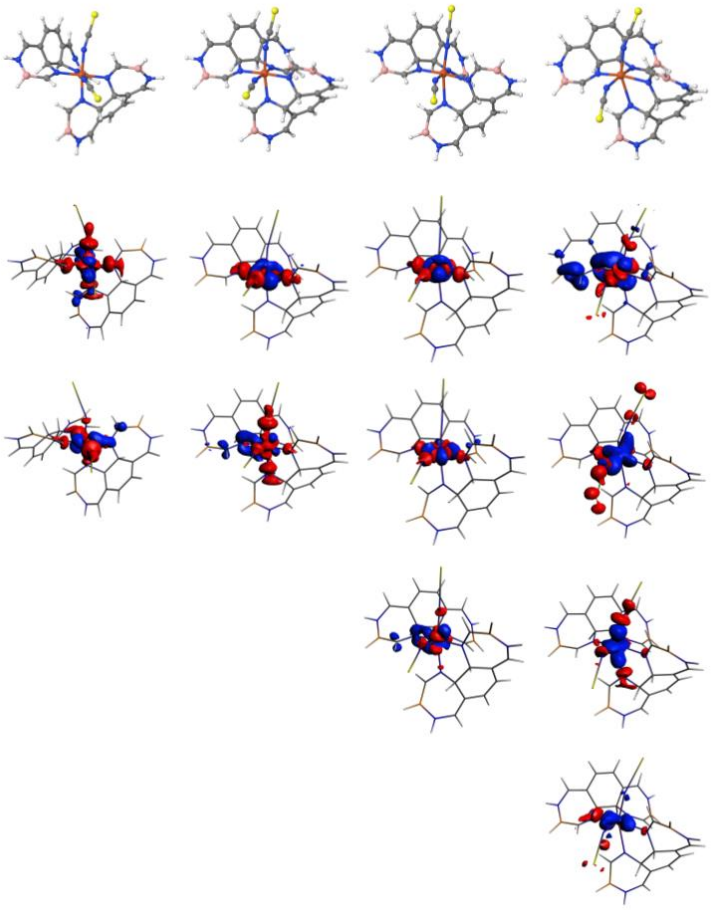

Figure 43: The deformation densities for the S(0), S(1), T(1) and Q(1) states (from left to right) of the [Fe{7(6)-N(4)B(5)}$_2$(NCS)$_2$] SCO candidate listed in descending order of magnitude of their respective eigenvalues. Charge flow is from red to blue.

It is interesting to note that there appears to be only limited back-bonding present in the deformation densities of [Fe{7(1)-N(4)B(5)}$_2$(NCS)$_2$] upon inspection of Figure 43 compared to [Fe(Phen)$_2$(NCS)$_2$]. This may be due to the heavy reduction of aromatic character in the homoaromatic ligand.

[Fe{7(3)-N(4)B(5)}$_2$(NCS)$_2$]

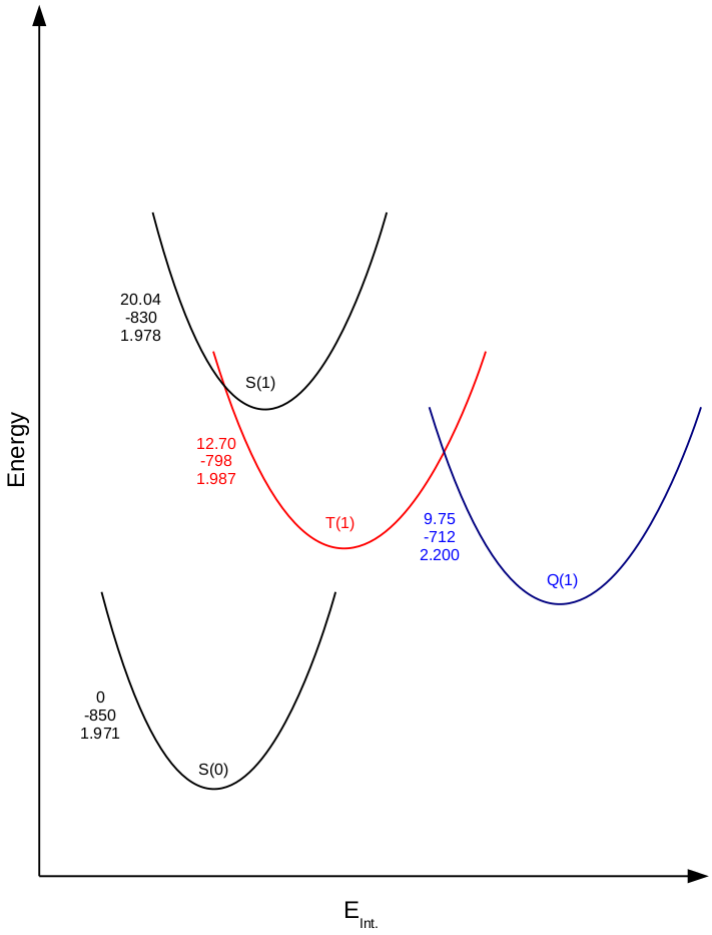

Figure 44: The scaled spin-transition pathway for the [Fe{7(3)-N(4)B(5)}$_2$(NCS)$_2$] SCO candidate with the values being the absolute energy (top), interaction energy (middle) and average Fe-N bond length (bottom). All energies are presented in kcal mol^{-1} with bond lengths presented in Å.

Figure 44 shows the scaled spin-transition pathway pertaining to [Fe{7(1)-N(4)B(5)}$_2$(NCS)$_2$] which includes two moieties of the bidentate homoaromatic ligand candidate, 7(1)-N(4)B(5). The numerical metrics for this ligand candidate suggest that there should be no substantial homoaromatic interaction although the SEDD does show strong delocalisation and a slight interaction across the homoconjugative gap suggesting there is some slight ring current. There is a S(0) to Q(1) average Fe-N bond length increase of 0.229Å is slightly above that expected of SCO behaviour however the interaction energies between the ligand sphere and the Fe(II) ion

are similar to that seen in $[Fe(Phen)_2(NCS)_2]$. Whilst the T(1) state energy is close to that of the Q(1) state, the HS-LS gap is approaching SCO range although it is still potentially too large.

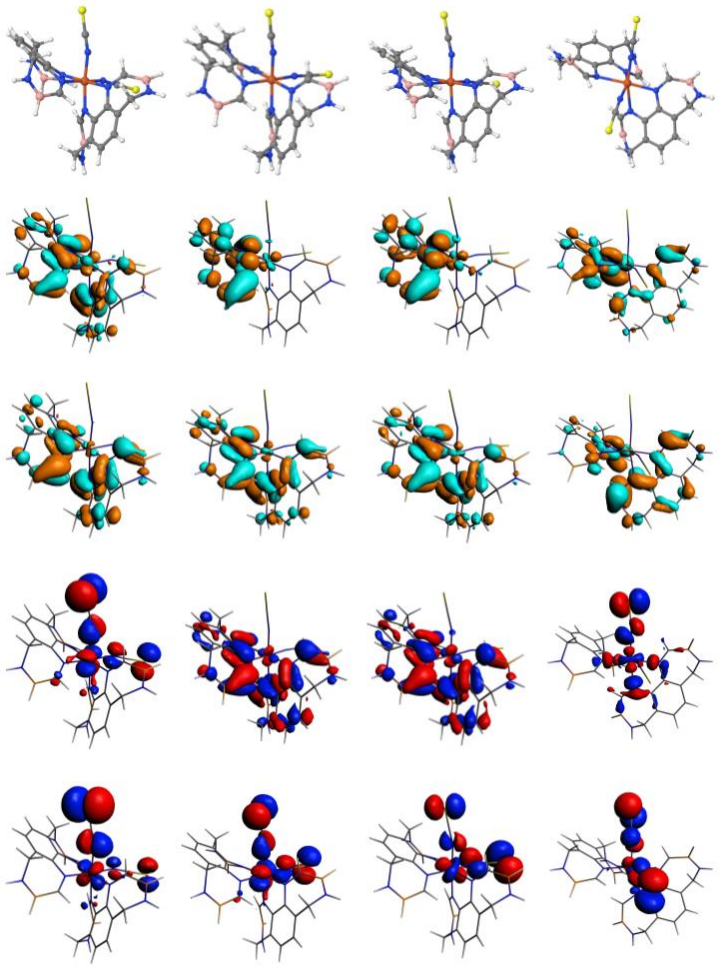

Figure 45: LUMO+1 to HOMO-1 (in descending order) for the S(0), S(1), T(1) and Q(1) states (from left to right) of the $[Fe\{7(3)\text{-}N(4)B(5)\}_2(NCS)_2]$ SCO candidate.

The valence orbitals displayed in Figure 45 suggest that the excitation of an electron to the S(1) or T(1) states results in the occupation of a delocalised π-bonding orbital including the vacant boron p_z orbital likely due to a lack of homoaromatic interaction.

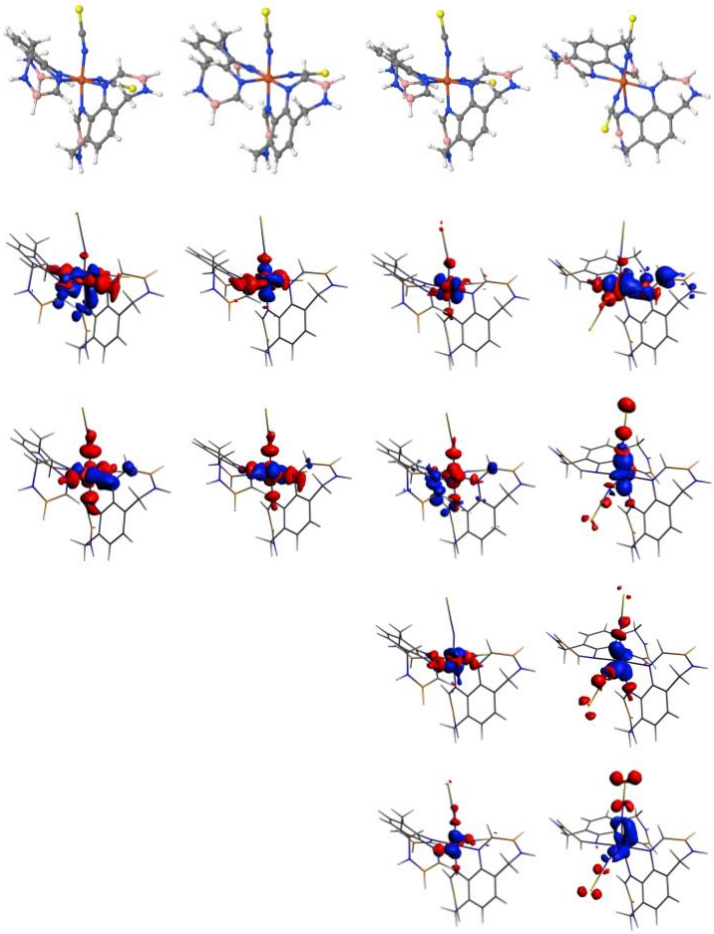

Figure 46: The deformation densities for the S(0), S(1), T(1) and Q(1) states (from left to right) of the [Fe{7(6)-N(4)B(5)}$_2$(NCS)$_2$] SCO candidate listed in descending order of magnitude of their respective eigenvalues. Charge flow is from red to blue.

Analysis of the deformation densities displayed in Figure 46 yields the usual N→Fe donation and d→d transitions. There is some slight evidence of DCD back-bonding to the aryl donating nitrogen and the adjacent carbon atoms, especially in the T(1) and Q(1) states.

[Fe{7(5)-N(4)B(6)}$_2$(NCS)$_2$]

The bidentate homoaromatic ligand candidate 7(5)-N(4)B(6) displays moderately strong homoaromatic interactions via the numerical metrics. It is also possible to see some evidence of delocalisation and a small interaction across the homoconjugative gap through the SEDD. This

makes it an interesting prospect for addition into the test complex however the positioning of the boron centre next to the nitrogen centre designed to donate an electron pair to the Fe(II) ion resulted in undesirable rearrangement. The subsequent availability of the empty boron p_z orbital, designed to facilitate the flow of charge around the homoaromatic system, allowed for the migration of the NCS ligands through the available lone pair on the nitrogen centre. This occurred at all spin-states bar the S(1), which likely failed due a poor starting geometry.

$[Fe\{7(5)\text{-}N(2)B(6)\}_2(NCS)_2]$

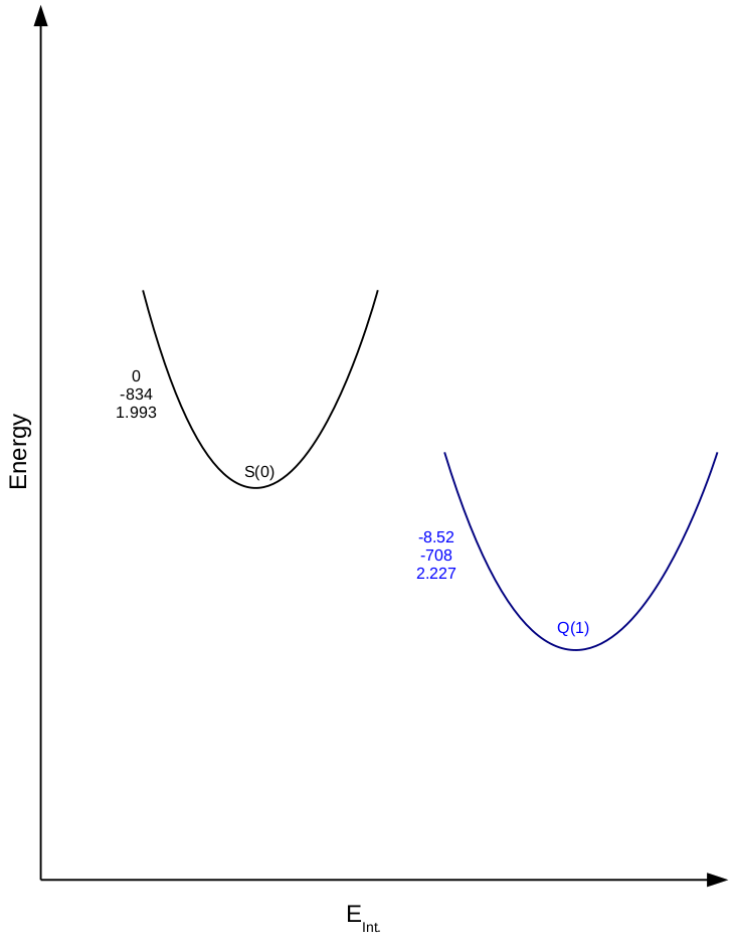

Figure 47: The scaled partial spin-transition pathway for the $[Fe\{7(5)\text{-}N(2)B(6)\}_2(NCS)_2]$ SCO candidate with the values being the absolute energy (top), interaction energy (middle) and average Fe-N bond length (bottom). All energies are presented in kcal mol^{-1} with bond lengths presented in Å.

The homoaromatic ligand candidate 7(5)-N(2)B(6) displays some of the strongest homoaromatic interactions of the structural isomers via the numerical metrics. Although the localisation domain in the SEDD is particularly fragmented, this is due to the presence of heteroatoms with the ring system. What is visible and useful is the node of electron density across the homoconjugative gap suggesting a through-space interaction. This strength of homoaromatic interaction appears to have had a concurrent effect on the relative energies of the spin states and these are displayed in Figure 47. Both the T(1) and S(1) states are absent, due to a theoretically similar positioning of electron density within these two spin-states they are likely to share a similar geometry which appears to be unstable in this case. This instability is likely due to [Fe{7(5)-N(2)B(6)}$_2$(NCS)$_2$] being a high-spin ligand due to the Q(1) state being substantially lower in energy, and hence more stable. Average Fe-N bond length increase is 0.234Å and the interaction energy between the ligand sphere and the Fe(II) ions is particularly weak at each of the shown spin-states.

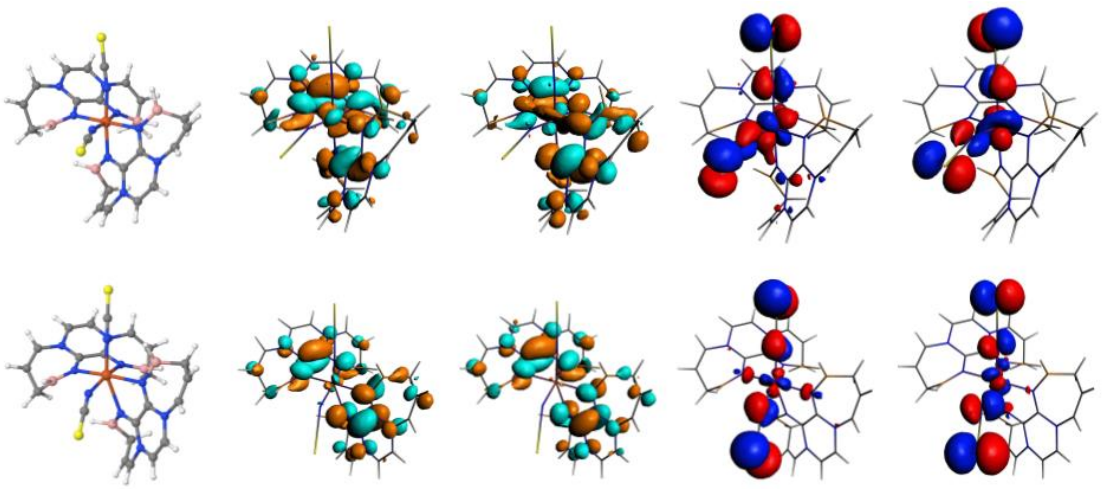

Figure 48: LUMO+1 to HOMO-1 (left to right) for the S(0) (top) and Q(1) states (bottom) of the [Fe{7(5)-N(2)B(6)}$_2$(NCS)$_2$] SCO candidate.

The valence atomic orbitals displayed in Figure 48 show no unusual deviations away from the valence orbitals of $[Fe(Phen)_2(NCS)_2]$ suggesting the change in the ordering of states is due to the modulation of the donating power of the nitrogen centres.

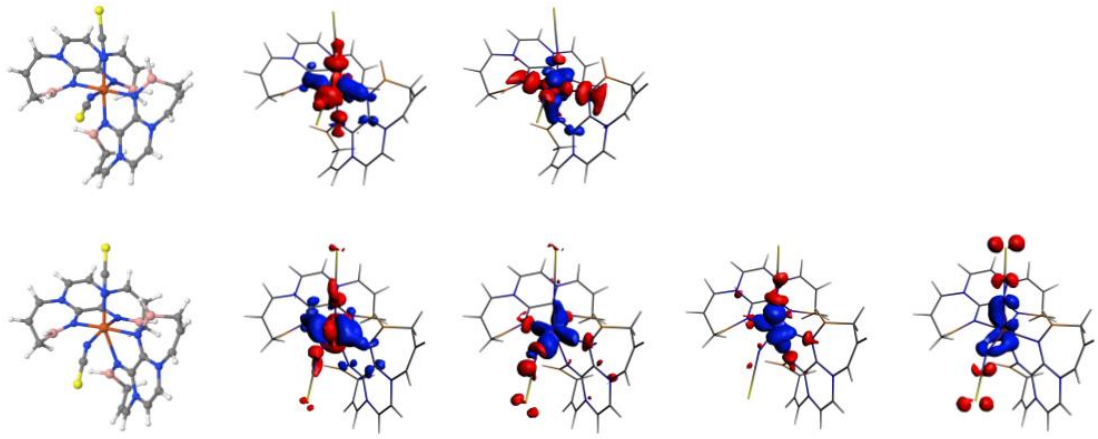

Figure 49: The deformation densities for the S(0) (top) and Q(1) states (bottom) of the $[Fe\{7(5)\text{-}N(2)B(6)\}_2(NCS)_2]$ SCO candidate listed in descending order of magnitude of their respective eigenvalues from left to right. Charge flow is from red to blue.

The deformation densities documented in Figure 49 further suggest that the change in ordering of states is due to a perturbation of the strength of donation of the homoaromatic nitrogen centres. The one difference to note is that there only appears to be minimal back-bonding suggesting that the presence of a moderate amount back-bonding interaction may be necessary for SCO behaviour.

$[Fe\{7(1)\text{-}N(3)B(2)\}_2(NCS)_2]$

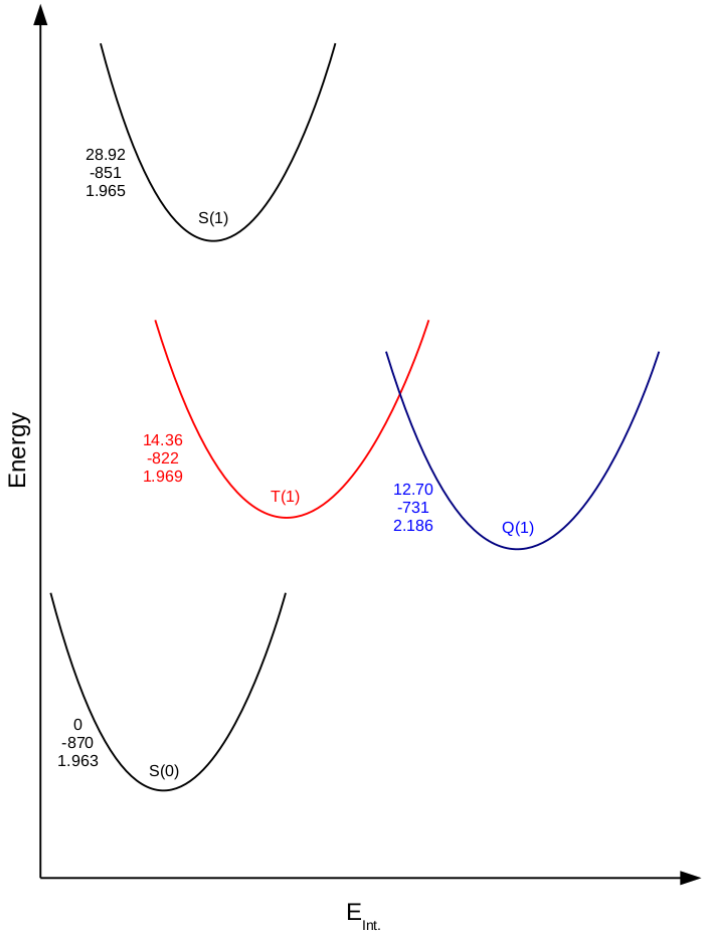

Figure 50: The scaled spin-transition pathway for the $[Fe\{7(1)\text{-}N(3)B(2)\}_2(NCS)_2]$ SCO candidate with the values being the absolute energy (top), interaction energy (middle) and average Fe-N bond length (bottom). All energies are presented in kcal mol^{-1} with bond lengths presented in Å.

The homoaromatic ligand candidate 7(1)-N(3)B(2) is the second of the candidates that include geometric isomerism, again only the cis isomer has been bound to the compound in an attempt to reduce strain on the system. Similar behaviour to 7(1)-N(4)B(5) is observed through the numerical metrics albeit with weaker associated $NICS_0$ values but stronger through-space interaction bond orders. Figure 50 shows that the addition of two of the bidentate homoaromatic ligand candidates to the test system has resulted in a low-spin compound. It also shows that there is a particularly strong interaction between the ligand sphere and Fe(II) ion at the S(0) spin-state, whilst the others are still high it is not to the same extent, this divergence

may be a factor in the large size of the HS-LS gap. An average Fe-N bond length increase of 0.247Å is far larger than would be expected of a compound exhibiting SCO behaviour.

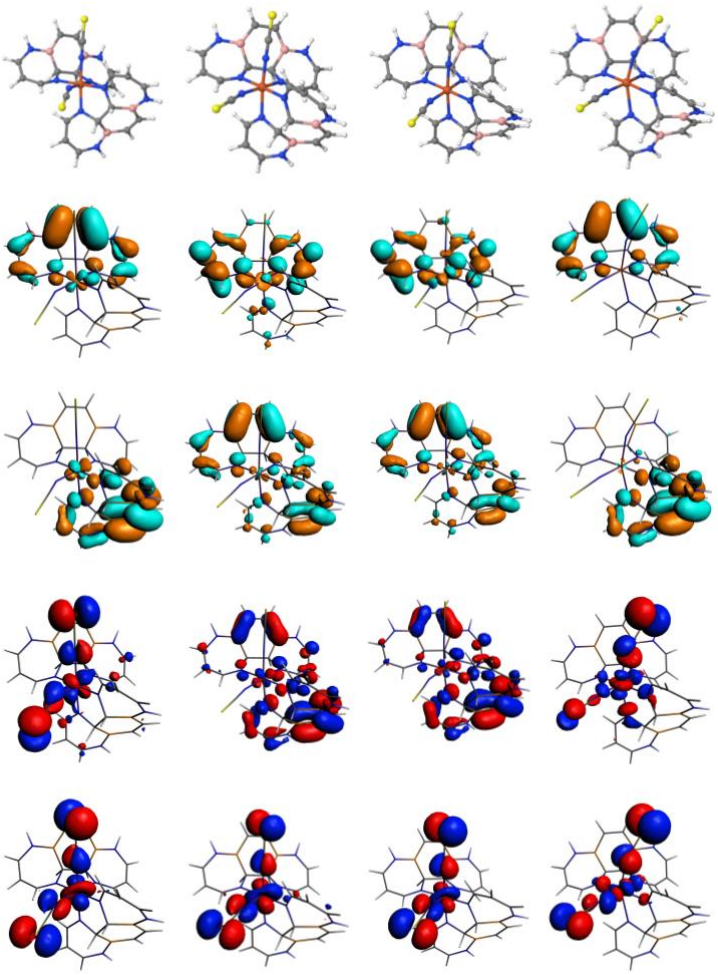

Figure 51: LUMO+1 to HOMO-1 (in descending order) for the S(0), S(1), T(1) and Q(1) states (from left to right) of the [Fe{7(1)-N(3)B(2)}$_2$(NCS)$_2$] SCO candidate.

Figure 51 shows the expected valence orbital positioning for the S(0) and Q(1) states, of note however, is the considerable amount of electron density position on B-C π-bonding orbitals in the central aryl system of both homoaromatic ligand candidates in the HOMO and LUMO of both the S(1) and T(1) states. This suggests efficient electron density acceptance from the adjacent nitrogen centre.

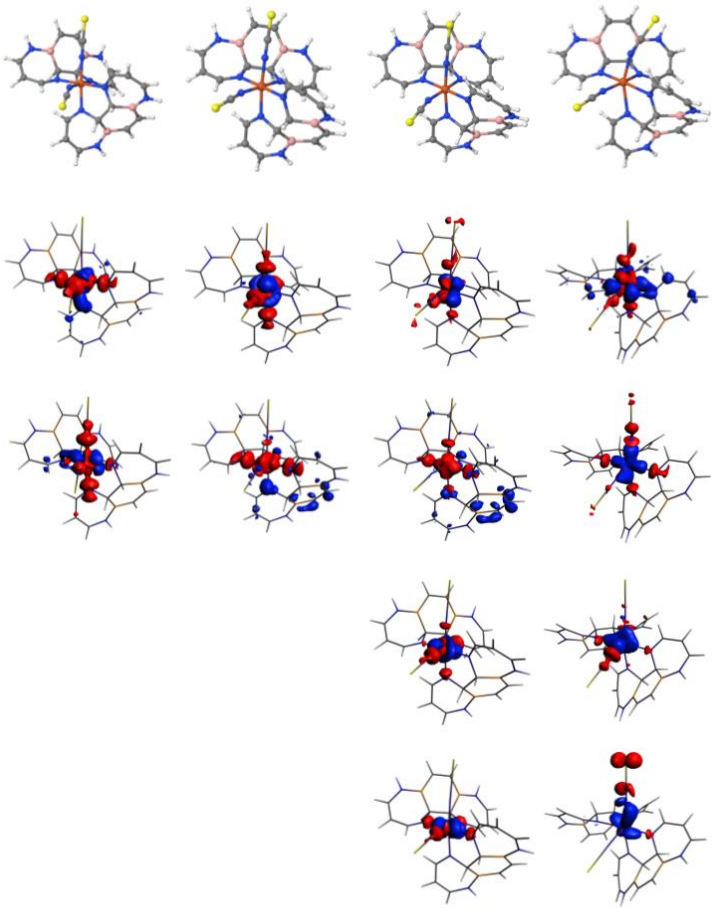

Figure 52: The deformation densities for the S(0), S(1), T(1) and Q(1) states (from left to right) of the [Fe{7(1)-N(3)B(2)}$_2$(NCS)$_2$] SCO candidate listed in descending order of magnitude of their respective eigenvalues. Charge flow is from red to blue.

The deformation densities presented in Figure 52 display evidence of DCD back-bonding into the previously mentioned B-C π-bonding orbital in the S(1) and T(1) states. There is only minimal back-bonding evident in the Q(1) state.

[Fe{7(5)-N(2)B(1)}$_2$(NCS)$_2$]

The numerical metrics of homoaromaticity as applied to 7(5)-N(2)B(1) suggest that it is likely to display a moderate homoaromatic interaction. Moreover, the SEDD shows evidence of a localisation domain and a node of electron density suggesting a moderate through-space

interaction. However, it proved impossible to optimise any state other than the ground-state singlet due to the partial dissociation of one of the bidentate homoaromatic ligand candidates confirmed by the near perfect trigonal bipyramidal symmetry around the Fe(II) metal centre. The valence orbitals of the S(0) state, the only state not to have rearranged, are shown below in Figure 53.

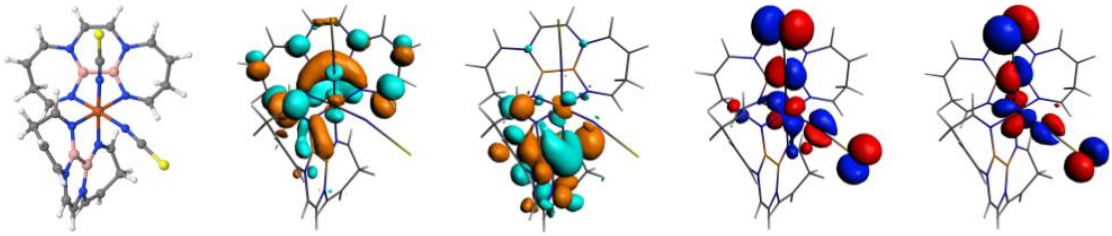

Figure 53: LUMO+1 to HOMO-1 (left to right) for the S(0) state of the [Fe{7(5)-N(2)B(1)}$_2$(NCS)$_2$] SCO candidate.

The LUMO and LUMO+1 suggest a strongly delocalised system including the vacant p_z orbitals of the boron atoms creating an empty π-bonding orbital. The population of this orbital in higher spin states could render binding to the metal centre unfavourable.

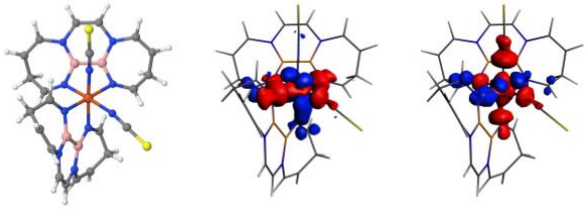

Figure 54: The deformation densities for the S(0) state of the [Fe{7(5)-N(2)B(1)}$_2$(NCS)$_2$] SCO candidate listed in descending order of magnitude of their respective eigenvalues from left to right. Charge flow is from red to blue.

The deformation densities shown in Figure 54 do not differ significantly from the majority of the other systems suggesting a stable singlet state and thus that this is likely a low-spin complex.

[Fe{7(5)-N(1)B(2)}$_2$(NCS)$_2$]

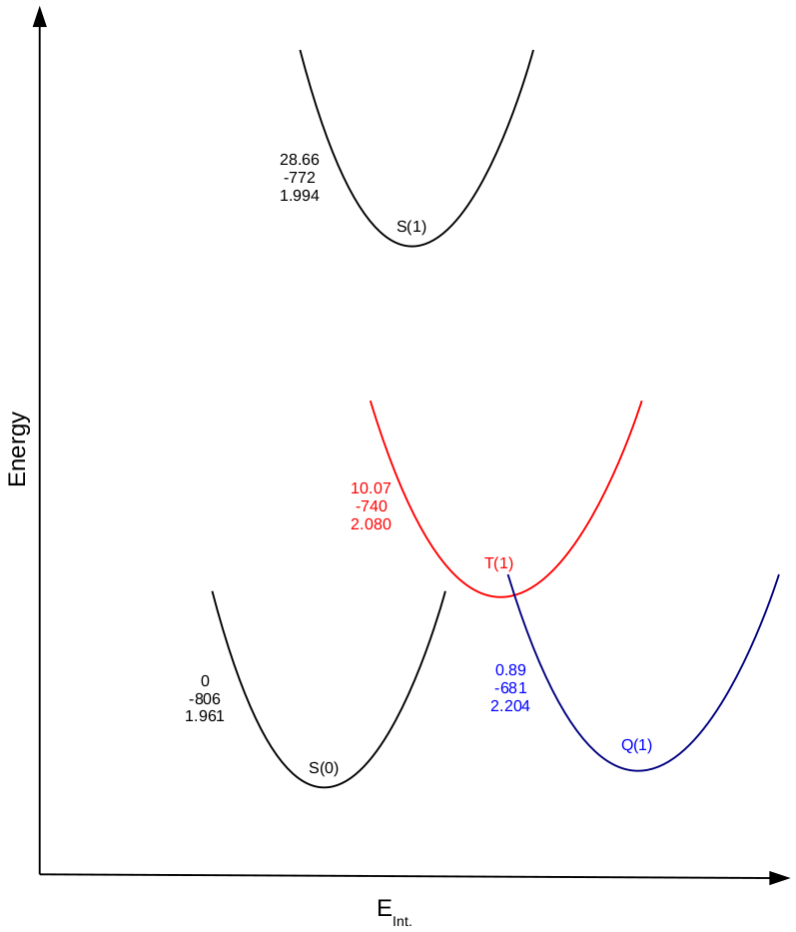

Figure 55: The scaled spin-transition pathway for the [Fe{7(5)-N(1)B(2)}$_2$(NCS)$_2$] SCO candidate with the values being the absolute energy (top), interaction energy (middle) and average Fe-N bond length (bottom). All energies are presented in kcal mol^{-1} with bond lengths presented in Å.

The numerical metrics of 7(5)-N(1)B(2) suggest that it possesses only a relatively weak homoaromatic interaction however it does possess a significant through-space bond order. The interaction energies between the ligand sphere and the Fe(II) ion as presented in Figure 55 are particularly low when compared to [Fe(Phen)$_2$(NCS)$_2$] and the other SCO candidates in this set. The average Fe-N bond length increase between S(0) and Q(1) states of 0.243Å is significantly above that which is considered indicative of SCO behaviour. Given this and the low HS-LS gap of 0.89 kcal mol^{-1}, it is likely that [Fe{7(5)-N(1)B(2)}$_2$(NCS)$_2$] will behave as a high spin compound

although to a much lesser extent than [Fe{7(5)-N(2)B(6)}$_2$(NCS)$_2$]. It is interesting to note that the S(1) state is at a far higher absolute energy than the other high spin compounds in this set.

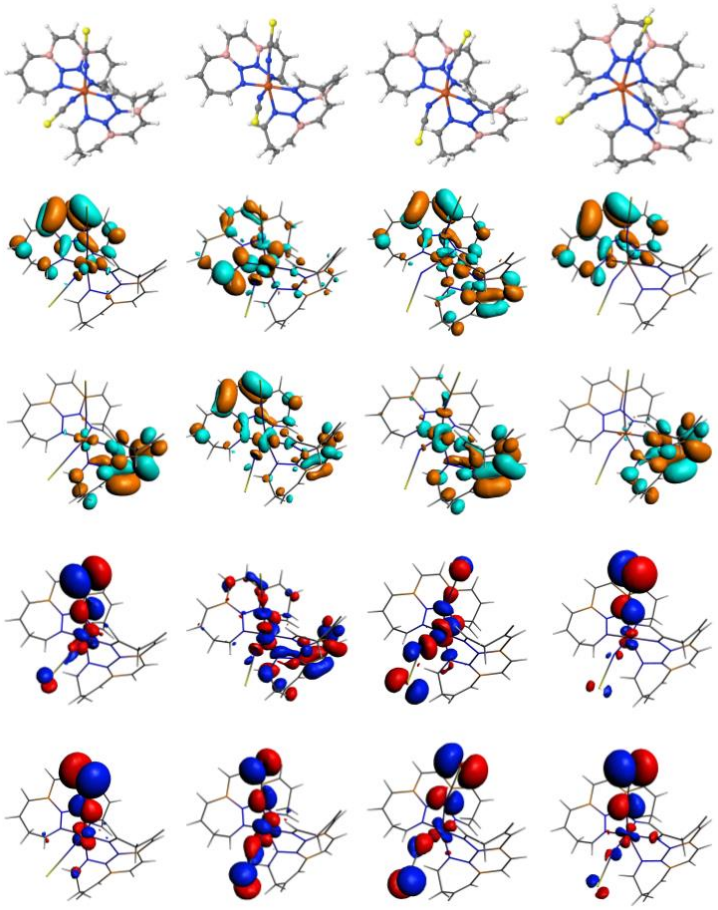

Figure 56: LUMO+1 to HOMO-1 (in descending order) for the S(0), S(1), T(1) and Q(1) states (from left to right) of the [Fe{7(5)-N(1)B(2)}$_2$(NCS)$_2$] SCO candidate.

Inspection of the valence MOs of [Fe{7(5)-N(1)B(2)}$_2$(NCS)$_2$] as shown above suggests that the relative destabilisation of the S(1) state is due to the population of a delocalised orbital over one of the homoaromatic ligand candidates. Whilst the T(1) state usually shows similar valence orbital location to the S(1) state, it is not the case here, this may well provide a rationale for the low-lying nature of this state.

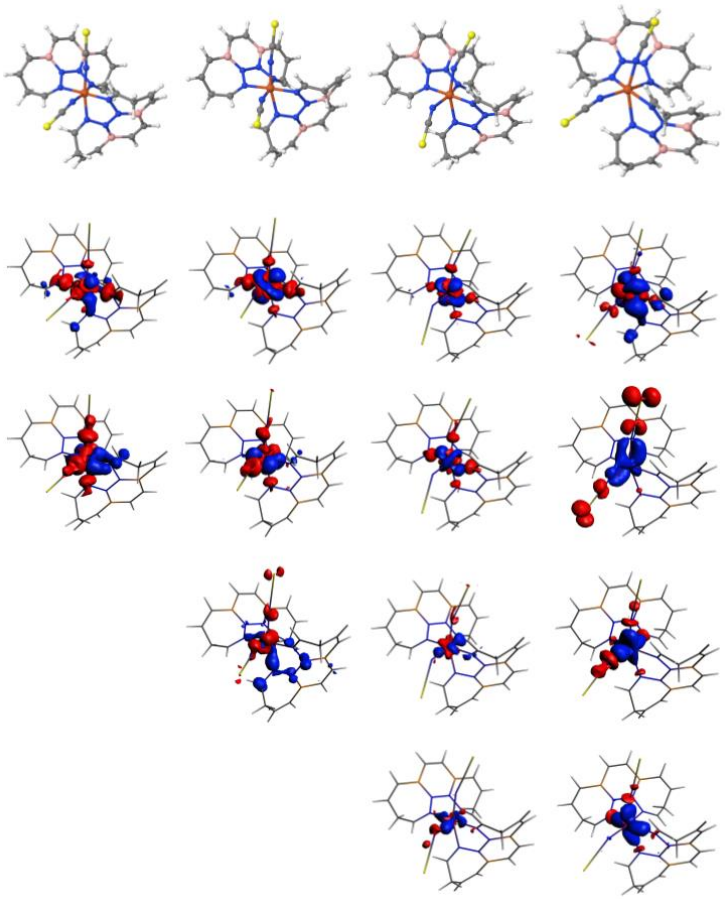

Figure 57: The deformation densities for the S(0), S(1), T(1) and Q(1) states (from left to right) of the [Fe{7(5)-N(1)B(2)}$_2$(NCS)$_2$] SCO candidate listed in descending order of magnitude of their respective eigenvalues. Charge flow is from red to blue.

The deformation densities show the expected nitrogen donation to the metal centre and d→d transitions, there is some slight evidence of back-bonding but it is limited outside of the S(1) state, this may be a further reason as to its unusual degree of stabilisation.

$[Fe\{7(6)\text{-}N(2)B(5)\}_2(NCS)_2]$

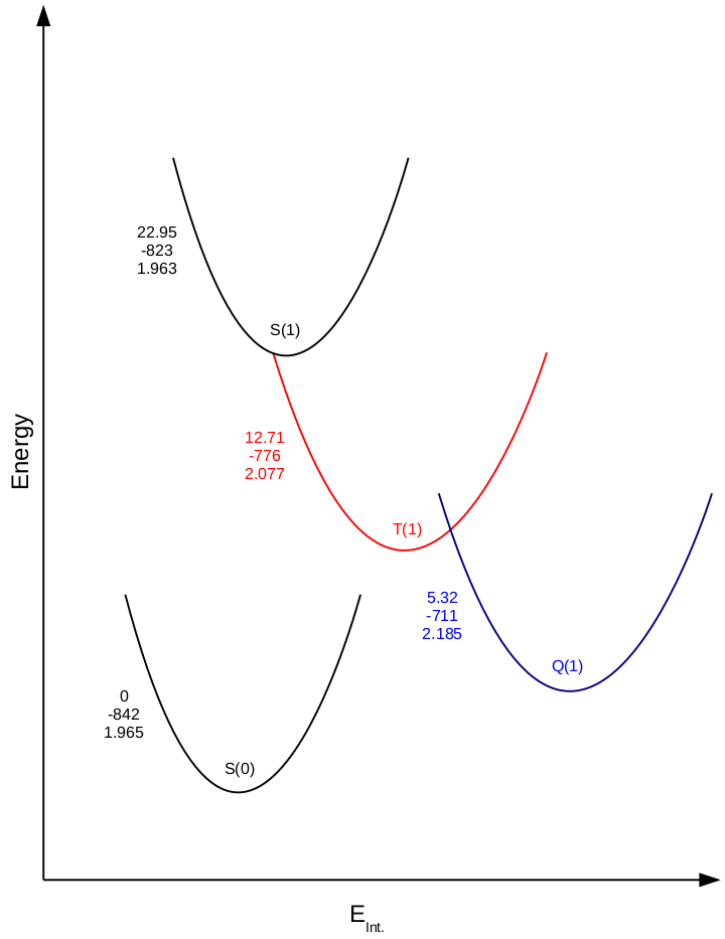

Figure 58: The scaled spin-transition pathway for the $[Fe\{7(6)\text{-}N(2)B(5)\}_2(NCS)_2]$ SCO candidate with the values being the absolute energy (top), interaction energy (middle) and average Fe-N bond length (bottom). All energies are presented in kcal mol^{-1} with bond lengths presented in Å.

The homoaromatic ligand candidate 7(6)-N(2)B(5) displays moderate through-space interaction across the homoaromatic gap both via the numerical metrics and by the presence of a localisation domain within the SEDD, although this is somewhat fragmented by the positioning of the ancillary nitrogen centre. It should be noted that the position of these ancillary nitrogen centres within the central ring without the inclusion of the vacant p_z orbital of an accompanying boron centre breaks the aromaticity of the central ring as it no longer complies with the 4n+2 rule. Comparison of the scaled spin-transition pathway documented in Figure 58 with that of $[Fe(Phen)_2(NCS)_2]$ strongly suggests that $[Fe\{7(6)\text{-}N(2)B(5)\}_2(NCS)_2]$ is likely to display SCO

behaviour. The S(1) state is slightly lower in energy suggesting it may be more accessible and the HS-LS gap is a slightly lower, 5.32 kcal mol^{-1}. Although the average Fe-N bond length increase of 0.220Å, which is slightly larger than would be expected, the majority of the spin states possess a similar interaction energy to those of $[Fe(Phen)_2(NCS)_2]$. The only exception to this is the T(1) state which is considerable lower in energy thus providing a rationale for its apparent relative stabilisation.

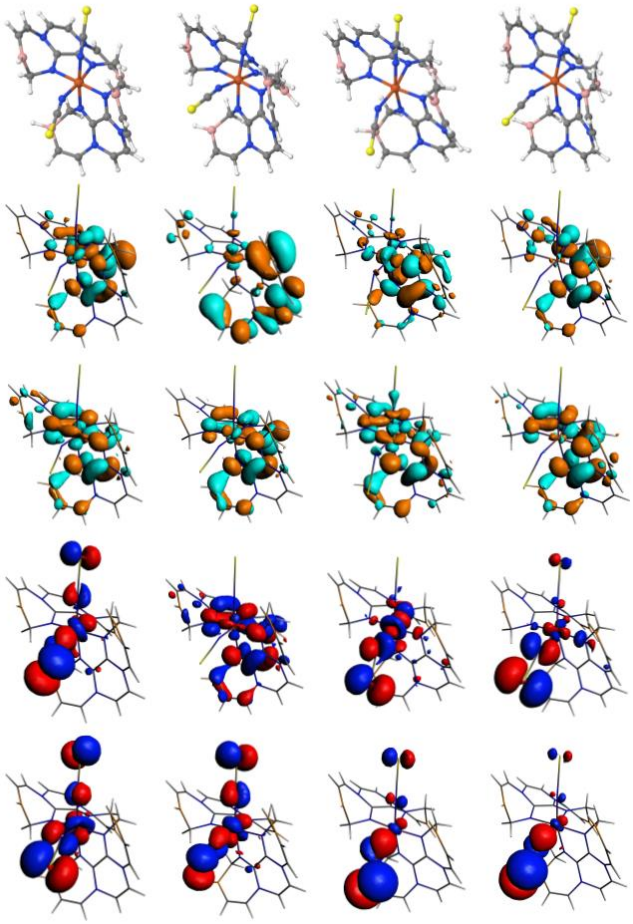

Figure 59: LUMO+1 to HOMO-1 (in descending order) for the S(0), S(1), T(1) and Q(1) states (from left to right) of the $[Fe\{7(6)\text{-}N(2)B(5)\}_2(NCS)_2]$ SCO candidate.

In a similar manner to $[Fe\{7(5)\text{-}N(1)B(2)\}_2(NCS)_2]$ above, the molecular orbitals of $[Fe\{7(6)\text{-}N(2)B(5)\}_2(NCS)_2]$ show that the HOMO of the T(1) state does not lie upon either of the

homoaromatic ligand candidates whereas the S(1) does. This again explains the large divergence in the relative energies of these states. The other valence orbitals lie in similar positions to those of $[Fe(Phen)_2(NCS)_2]$ which is unsurprising giving the similarity in the spin-state energetics.

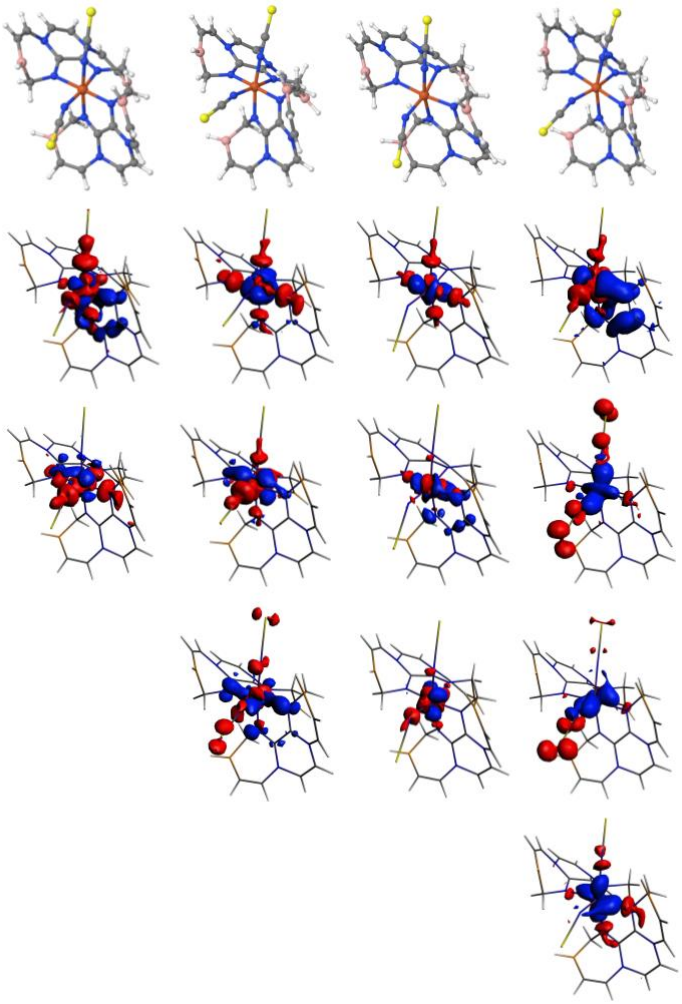

Figure 60: The deformation densities for the S(0), S(1), T(1) and Q(1) states (from left to right) of the $[Fe\{7(6)\text{-}N(2)B(5)\}_2(NCS)_2]$ SCO candidate listed in descending order of magnitude of their respective eigenvalues. Charge flow is from red to blue.

The deformation densities shown in Figure 60 show a significant amount of DCD-type back-bonding across all spin-states. The largest amount of back-bonding occurs in the Q(1) state and may account for the additional stability that enables SCO behaviour. Interestingly, the back-

bonding in the Q(1) state appears to centre upon a C-C π-bond and the donating nitrogen centre of a single homoaromatic ligand.

$[Fe\{7(5)\text{-}N(6)B(4)\}_2(NCS)_2]$

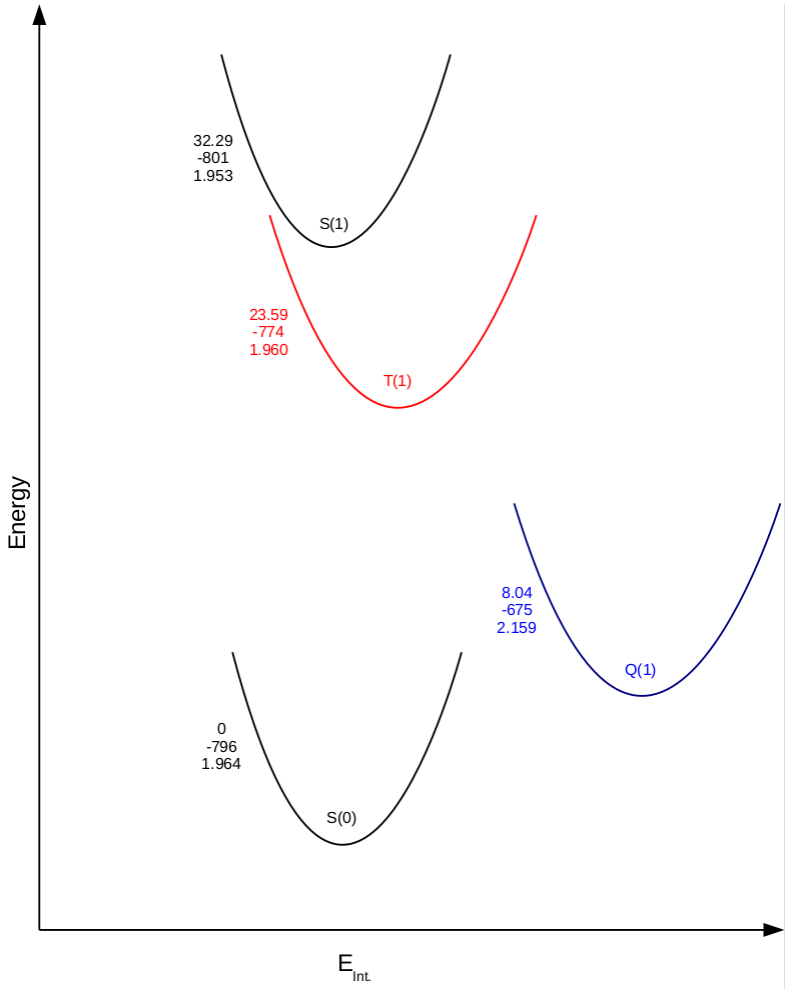

Figure 61: The scaled spin-transition pathway for the [Fe{7(5)-N(6)B(4)}$_2$(NCS)$_2$] SCO candidate with the values being the absolute energy (top), interaction energy (middle) and average Fe-N bond length (bottom). All energies are presented in kcal mol^{-1} with bond lengths presented in Å.

The bidentate homoaromatic ligand candidate 7(5)-N(6)B(4) displays the strongest homoaromatic interaction as determined by the numerical metrics. There is also a large localisation domain visible in the isosurface generated via SEDD, a through-space interaction is difficult to see however this is likely to be due to the position of the boron centre at the

bridgehead of the homoconjugative gap. This appears to have had the effect of creating a set of highly distributed spin-states, with highly energetic S(1) and T(1) spin-states. Despite this the HS-LS gap is not dissimilar from that of $[Fe(Phen)_2(NCS)_2]$ suggesting that $[Fe\{7(5)\text{-}N(6)B(4)\}_2(NCS)_2]$ may well exhibit SCO behaviour. Furthermore, the average Fe-N bond length increase is 0.195Å which is perfectly within the area expected from compounds exhibiting SCO behaviour. The increase in energy of the T(1) state may suggest that the high-spin state of this compound is trappable, an important property in spin-switchable systems. Of note is that the interaction energies associated with all of the spin-state for this system are surprisingly low.

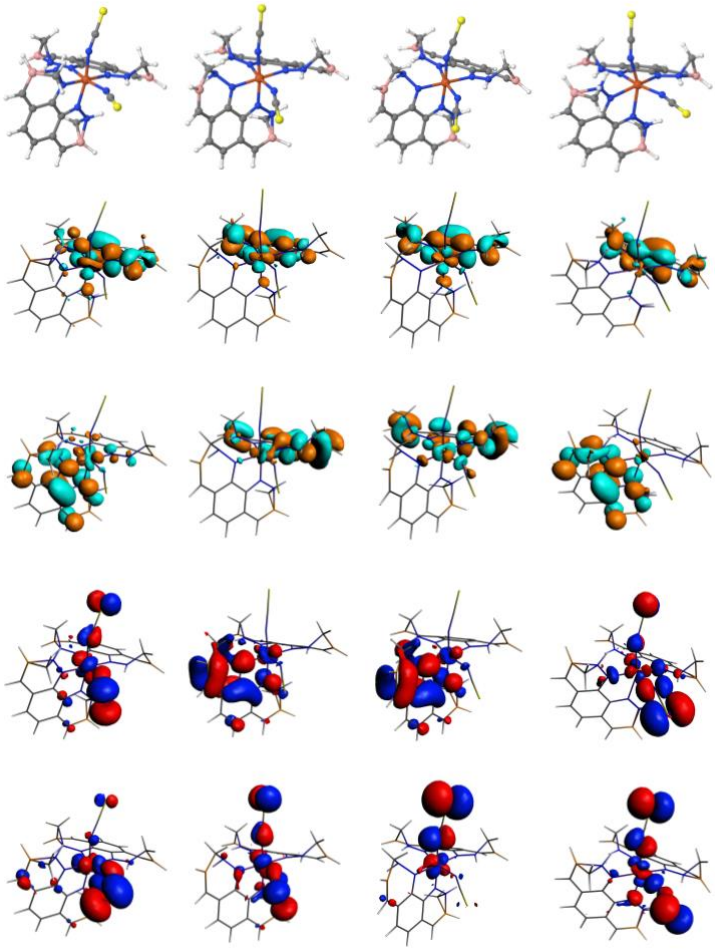

Figure 62: LUMO+1 to HOMO-1 (in descending order) for the S(0), S(1), T(1) and Q(1) states (from left to right) of the $[Fe\{7(5)\text{-}N(6)B(4)\}_2(NCS)_2]$ SCO candidate.

The HOMO of the S(1) and T(1) states lies, in large part, across the homoconjugative gap, this is likely due to the boron centre being placed on the opposite side of the gap and thus mediating charge transfer through-space. This may account for the high relative energies of these states.

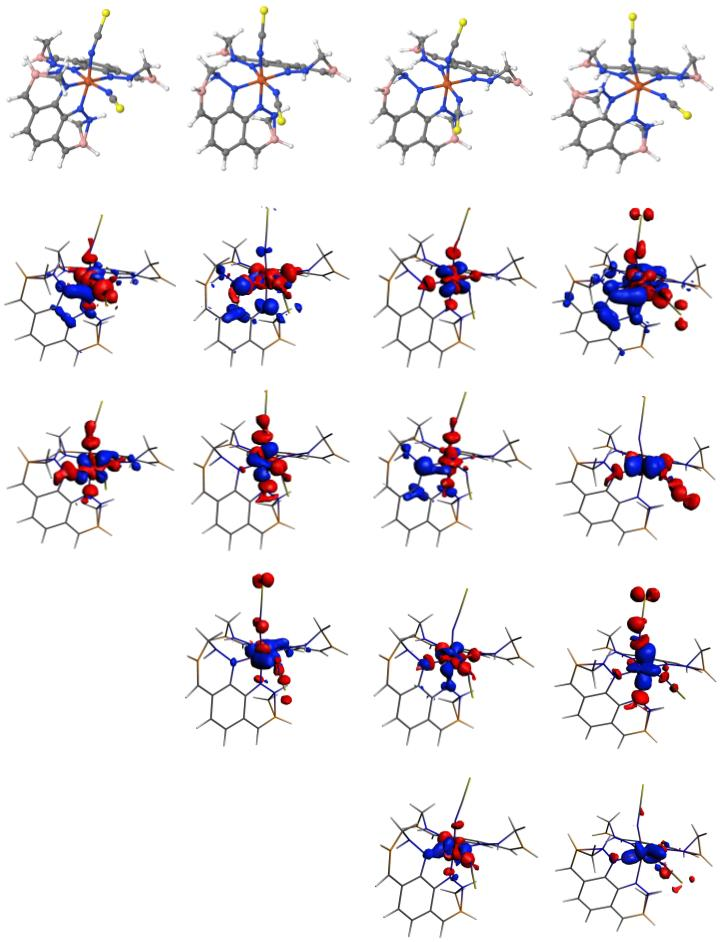

Figure 63: The deformation densities for the S(0), S(1), T(1) and Q(1) states (from left to right) of the [Fe{7(5)-N(6)B(4)}$_2$(NCS)$_2$] SCO candidate listed in descending order of magnitude of their respective eigenvalues. Charge flow is from red to blue.

The deformation densities as shown above in Figure 63 bear a striking resemblance to those of [Fe{7(6)-N(2)B(5)}$_2$(NCS)$_2$] and [Fe(Phen)$_2$(NCS)$_2$], particularly with respect to the presence of strong back-bonding in the Q(1) spin-state. This is discussed in more detail below.

$[Fe\{7(4)\text{-}N(3)B(2)\}_2(NCS)_2]$

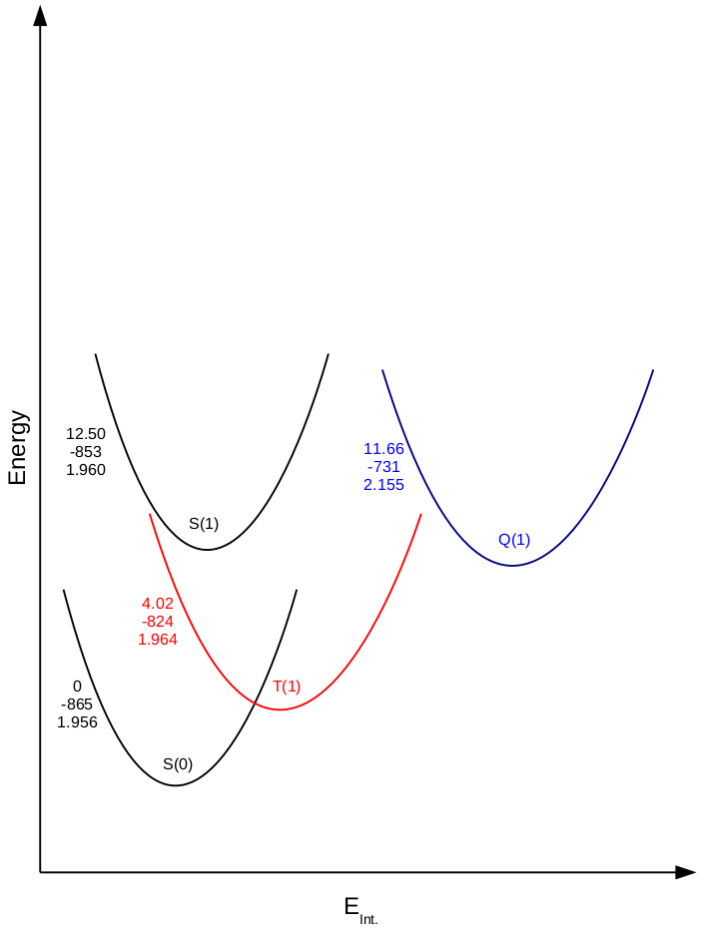

Figure 64: The scaled spin-transition pathway for the $[Fe\{7(4)\text{-}N(3)B(2)\}_2(NCS)_2]$ SCO candidate with the values being the absolute energy (top), interaction energy (middle) and average Fe-N bond length (bottom). All energies are presented in kcal mol^{-1} with bond lengths presented in Å.

It is immediately obvious from Figure 64 that $[Fe\{7(4)\text{-}N(3)B(2)\}_2(NCS)_2]$ will not display SCO behaviour. This is due to the ordering of states being inimical to a S(0)→Q(1) spin transition due to the Q(1) being significantly higher in energy than the T(1) state, therefore this candidate is highly likely to be low spin. Whilst the average bond length increase of 0.201 Å is in the SCO behaviour range this is mere coincidence. The interaction energies are at the higher end of those seen across the candidate molecules. The homoaromatic ligand candidate itself displays little to no homoaromatic behaviour via the numerical metrics and the SEDD shows only the slightest of

through-space interactions suggesting that 7(4)-N(3)B(2) shows high conjugation but only a meagre ring current.

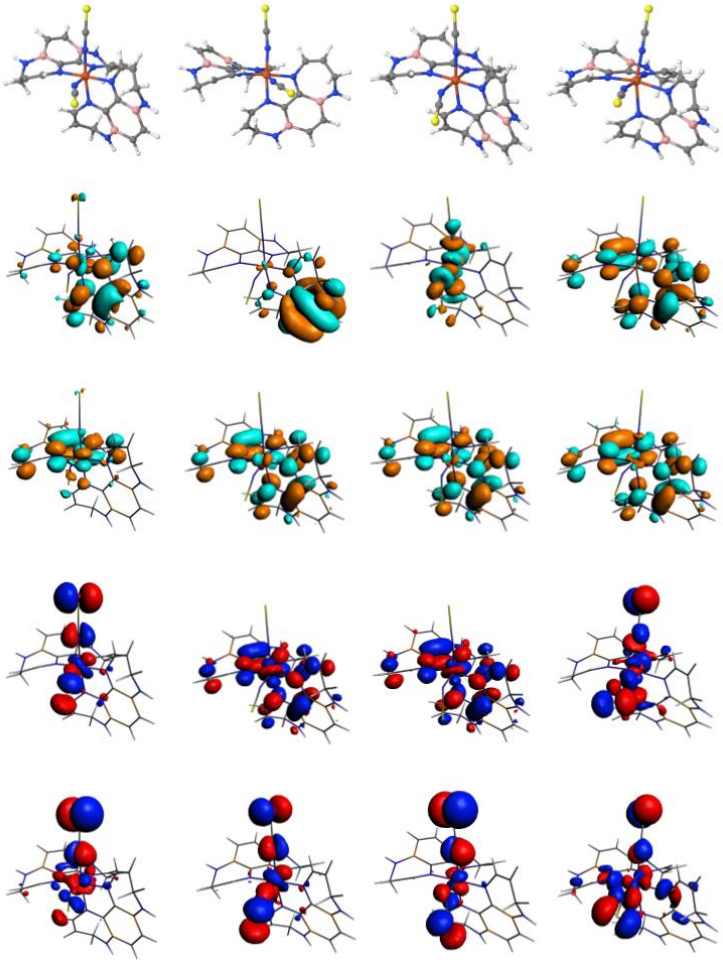

Figure 65: LUMO+1 to HOMO-1 (in descending order) for the S(0), S(1), T(1) and Q(1) states (from left to right) of the [Fe{7(4)-N(3)B(2)}$_2$(NCS)$_2$] SCO candidate.

The MOs as displayed in Figure 65 show no unusual behaviour however it is surprising that the energy of the S(1) and T(1) states is not higher given the position of the HOMO upon the homoaromatic ligand candidate.

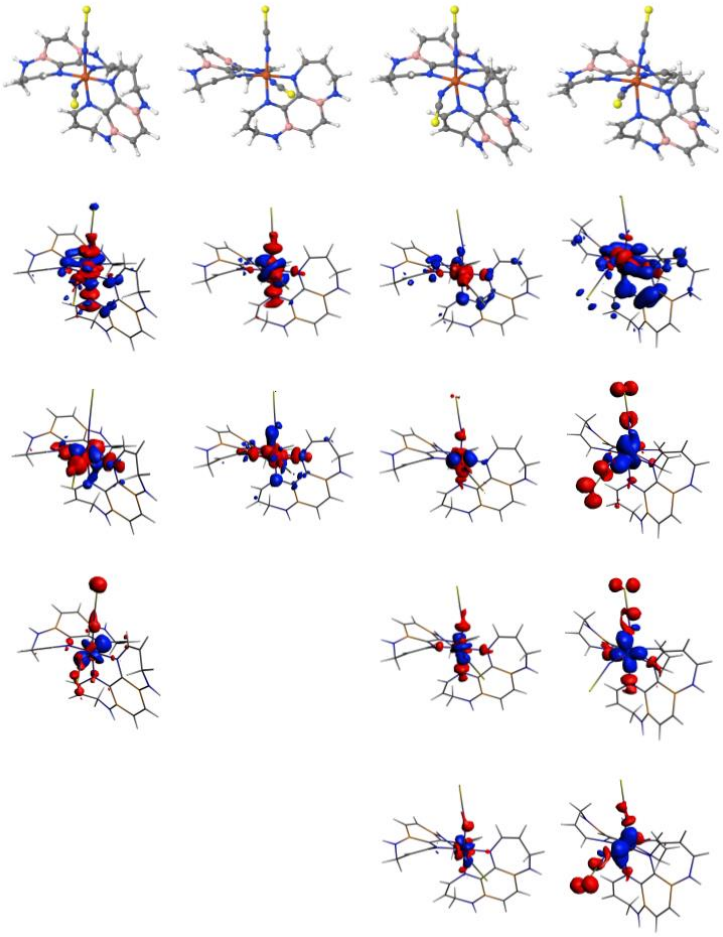

Figure 66: The deformation densities for the S(0), S(1), T(1) and Q(1) states (from left to right) of the [Fe{7(4)-N(3)B(2)}$_2$(NCS)$_2$] SCO candidate listed in descending order of magnitude of their respective eigenvalues. Charge flow is from red to blue.

The deformation densities laid out in Figure 66 are unusual in that the Q(1) state appears to show a strong degree of back-bonding that would appear to be more in line with SCO behaviour. There is also some slight signs of back-bonding is the lower spin-states.

[Fe{7(4)-N(2)B(3)}$_2$(NCS)$_2$]

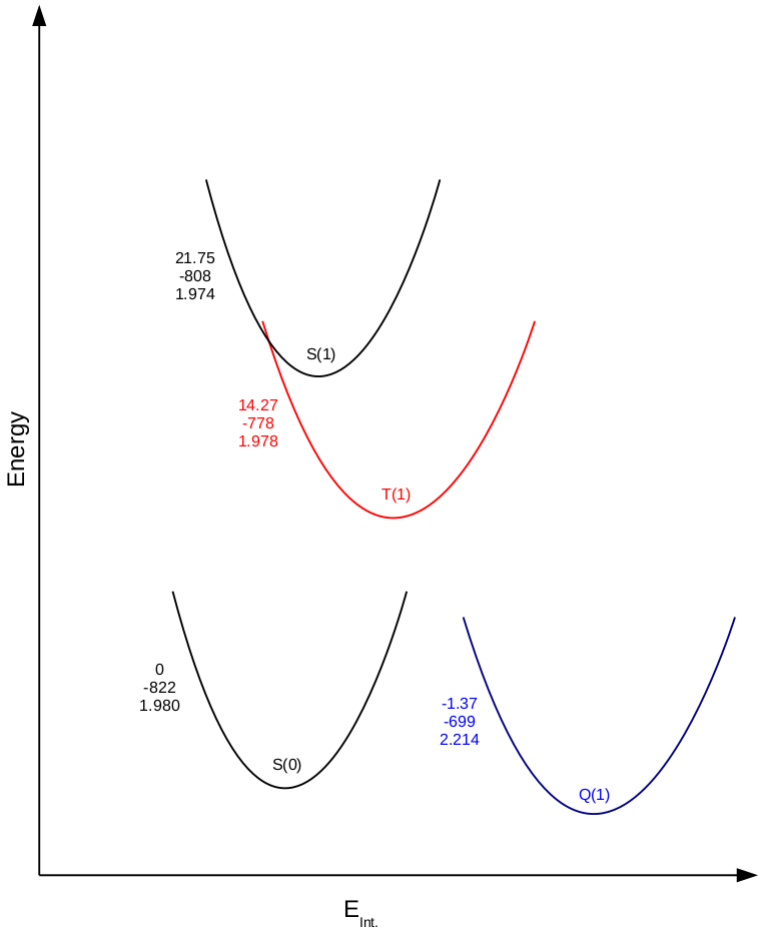

Figure 67: The scaled spin-transition pathway for the [Fe{7(4)-N(2)B(3)}$_2$(NCS)$_2$] SCO candidate with the values being the absolute energy (top), interaction energy (middle) and average Fe-N bond length (bottom). All energies are presented in kcal mol^{-1} with bond lengths presented in Å.

The numerical metrics as applied to 7(4)-N(2)B(3) suggest that it includes a strong homoaromatic interaction with a high through-space bond order, this is confirmed via SEDD which shows a localisation domain, albeit a fragmented one, and a large node of electron density in the centre of the homoconjugative gap. The results of the addition of this ligand candidate to the test compound is a high-spin compound with a relatively weak interaction energy at all spin-states. An average bond length change of 0.234 Å is larger than that expected of SCO behaviour.

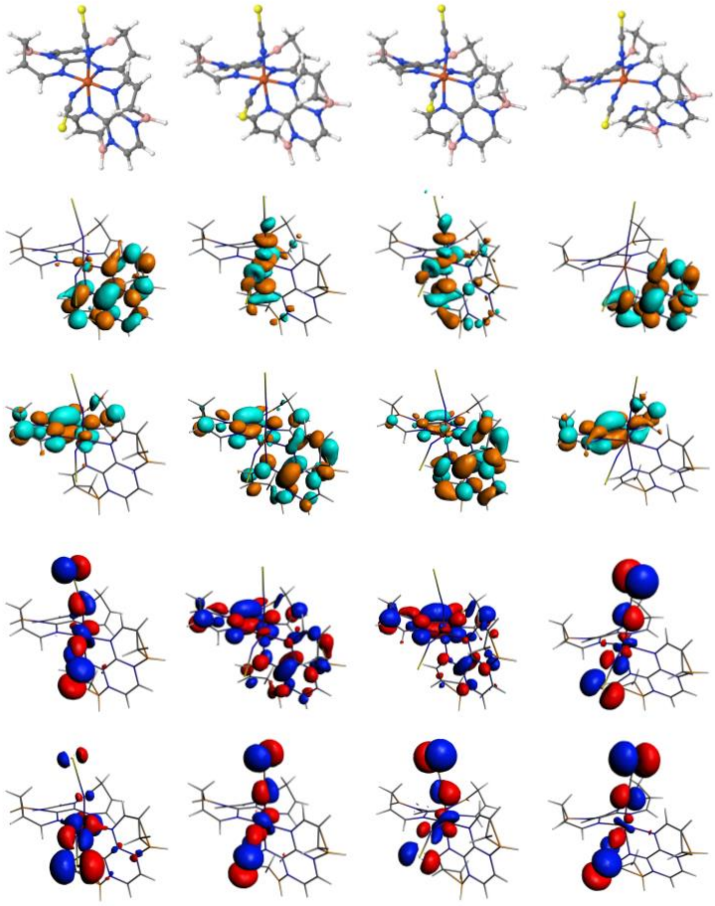

Figure 68: LUMO+1 to HOMO-1 (in descending order) for the S(0), S(1), T(1) and Q(1) states (from left to right) of the [Fe{7(4)-N(2)B(3)}$_2$(NCS)$_2$] SCO candidate.

There are no unusual characteristics in the MOs displayed in Figure 68. This suggests that the high-spin nature of [Fe{7(4)-N(2)B(3)}$_2$(NCS)$_2$] is due to the modification of the donor/acceptor properties of the homoaromatic ligand candidate.

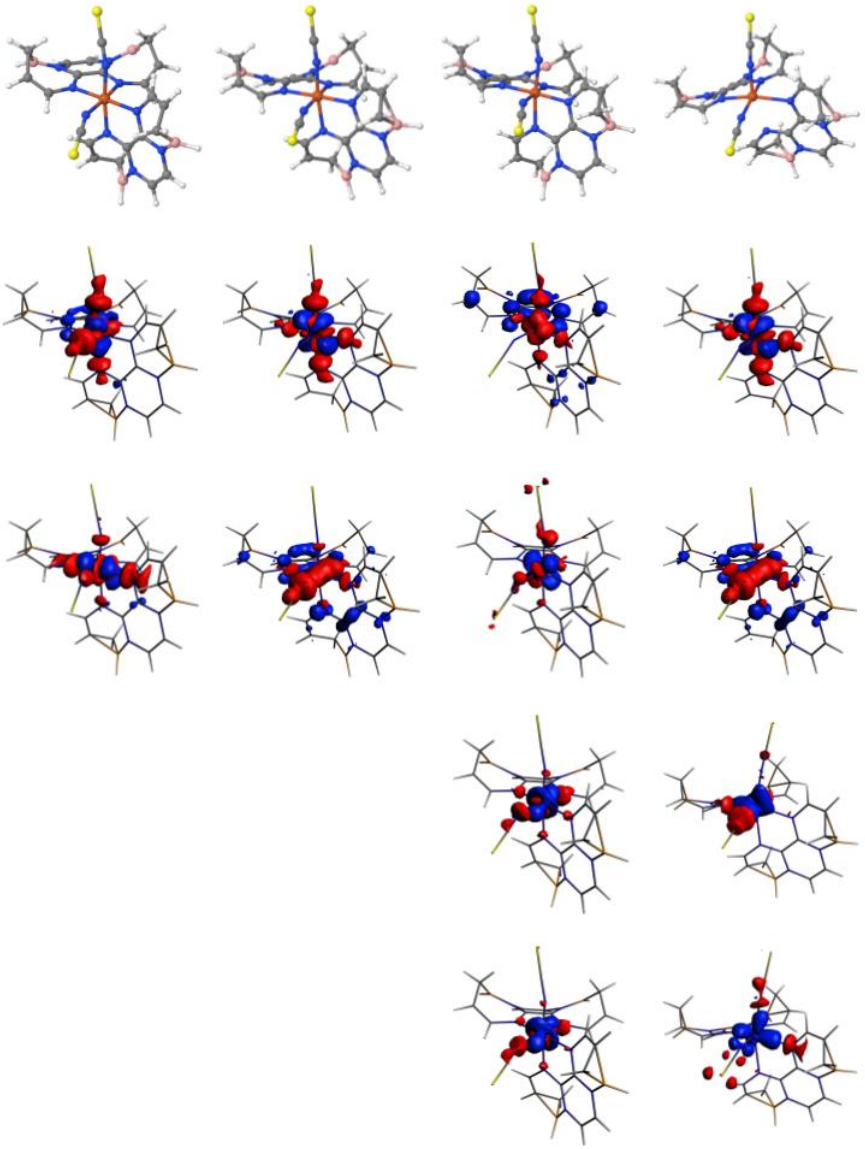

Figure 69: The deformation densities for the S(0), S(1), T(1) and Q(1) states (from left to right) of the [Fe{7(4)-N(2)B(3)}$_2$(NCS)$_2$] SCO candidate listed in descending order of magnitude of their respective eigenvalues. Charge flow is from red to blue.

The deformation densities of [Fe{7(4)-N(2)B(3)}$_2$(NCS)$_2$] given in Figure 69 show minimal back-bonding across all spin-states. This suggests that the high-spin nature of the candidate is caused by the perturbation of ligand field strength due to the structural isomerism inherent to the homoaromatic ligand candidate having a direct impact on the donating power of the nitrogen centres.

The Importance of DCD Back-Bonding

By applying a novel PAoC approach to ETS-NOCV it has been possible to elucidate upon the bonding mechanisms between the ligand sphere and the Fe(II) ion at all spin-states where previously only the S(0) state has been available. The use of this technique to analyse the bonding motifs within a set of SCO candidates based on the known SCO compound, $[Fe(Phen)_2(NCS)_2]$, and modified with the addition of structural isomers of a bidentate homoaromatic ligand candidate, has led to a surprising observation. The addition of ligands of low to moderate homoaromatic interaction led to many low-spin complexes, the deformation densities of which were predictably dominated by N→Fe electron donation and d→d transitions with only the slightest hint of the presence of DCD back-bonding. The interesting divergence from this occurs on inspection of the deformation densities of $[Fe(Phen)_2(NCS)_2]$ in Chapter 6 and of $[Fe\{7(6)\text{-}N(2)B(5)\}_2(NCS)_2]$ and $[Fe\{7(5)\text{-}N(6)B(4)\}_2(NCS)_2]$, which are the two candidate compounds most likely to show SCO behaviour. All three sets of deformation densities display strong DCD type back-bonding in the Q(1) states and suggestions of back-bonding in the S(0), T(1) and S(1) states. Interestingly the high-spin candidates also show very few signs of back-bonding. This suggests that for SCO behaviour, not only must the ligand field strength of the ligands be carefully managed to ensure a properly sized HS-LS gap to allow for a spin-transition and to create a trappable state, but there must also be an element of electron acceptance in the ligands to facilitate DCD-back-bonding. This provides a rationale for the apparent exception in the set; $[Fe\{7(4)\text{-}N(3)B(2)\}_2(NCS)_2]$, which displays strong back-bonding within the Q(1) state but does not display SCO behaviour. That is, the homoaromatic ligand candidate does not display any homoaromatic behaviour, thus is merely a highly conjugated alkyl donor and has a ligand field strength such that the compound possess the incorrect ordering of states to facilitate SCO behaviour.

Ensuring the Population of the S(1) State – TDDFT Results

It is important to ensure that the S(1) and other higher excited states can be populated by stimuli such as electromagnetic radiation, a first step to populating the low-lying Q(1) state in the systems studied above. To this end, TDDFT calculations were carried out to assess the associated oscillator strength for the vertical excitations. It will be possible to populate the S(1) state if the HOMO→LUMO transition exhibits a non-zero oscillator strength. The HOMO→LUMO transitions calculated by both ΔSCF and TDDFT are shown below in Table 35.

Candidate	HOMO-LUMO	TDDFT	Weight	Oscillator strength
$[Fe\{7(6)\text{-}N(4)B(5)\}_2(NCS)_2]$	17.619	19.106	59.52%	2.47E-03
$[Fe\{7(1)\text{-}N(4)B(5)\}_2(NCS)_2]$	20.617	21.656	59.95%	3.37E-03
$[Fe\{7(3)\text{-}N(4)B(5)\}_2(NCS)_2]$	14.090	15.430	94.56%	8.31E-03
$[Fe\{7(5)\text{-}N(2)B(6)\}_2(NCS)_2]$	15.313	-	-	-
$[Fe\{7(1)\text{-}N(3)B(2)\}_2(NCS)_2]$	15.128	18.908	48.37%	1.21E-02
$[Fe\{7(5)\text{-}N(2)B(1)\}_2(NCS)_2]$	13.675	15.633	90.65%%	9.10E-03
$[Fe\{7(5)\text{-}N(1)B(2)\}_2(NCS)_2]$	17.388	17.772	99.39%	5.30E-03
$[Fe\{7(6)\text{-}N(2)B(5)\}_2(NCS)_2]$	19.141	20.597	55.13%	2.66E-03
$[Fe\{7(5)\text{-}N(6)B(4)\}_2(NCS)_2]$	17.088	18.707	98.73%	5.57E-03
$[Fe\{7(4)\text{-}N(3)B(2)\}_2(NCS)_2]$	8.878	10.291	87.42%	7.63E-04
$[Fe\{7(4)\text{-}N(2)B(3)\}_2(NCS)_2]$	15.197	16.721	93.16%	2.79E-03

Table 35: The eigenvalue and TDDFT values for the HOMO-LUMO singlet transition from the S(0) state for the SCO candidate compounds. All energies in kcal mol^{-1}.

As can be seen in Table 35, all of the SCO candidate compounds display a non-zero oscillator strength for the HOMO→LUMO transition and thus the S(1) state of each candidate can, theoretically, be populated via excitation from the S(0) state. It should be noted that [Fe{7(5)-N(2)B(6)}$_2$(NCS)$_2$] does not possess a transition, within the lowest 10 transitions, that is dominated by HOMO→LUMO character, this is likely due to the extent by which the Q(1) state is more energetically favoured over the S(0) state. The transitions for [Fe{7(5)-N(4)B(6)}$_2$(NCS)$_2$] have not been characterised as the TDDFT did not yield a predominantly HOMO→LUMO vertical transition in the largest ten allowed transitions.

As discussed above in Chapter 6, RPBE does not accurately reproduce the energetics of the excitations either via an inspection of eigenvalues or via the use of TDDFT. A functional including exact-exchange such as the hybrid-type functional B3LYP* or even with additional long-range effects included such as the meta-hybrid functional CAM-B3LYP would better estimate the transition energies however it would require the sacrifice of the spin-state energetics which are crucial to this work. The TDDFT is used here to confirm a non-zero oscillator strength for the HOMO-LUMO transition.

Energy Decomposition Analysis

Whilst the output from the PAoC-ETS-NOCV has already been used via the use of the values of $E_{Int.}$ for the characterisation of the SCO candidate compounds above, a more intricate description of the bonding between the Fe(II) ion and the ligand sphere can be attained from the EDA. The derivation of the EDA is described above in Chapter 2. This output is displayed below separated by spin-state for clarity.

Compound	$E_{orb.\ Int.}$	$E_{elstat.}$	E_{Pauli}	$E_{int.}$
$[Fe(Phen)_2(NCS)_2]$	-598.73	-633.18	384.03	-847.89
$[Fe(BiPy)_3]^{2+}$	-571.53	-378.70	368.48	-581.75
$[Fe\{7(6)\text{-}N(4)B(5)\}_2(NCS)_2]$	-623.56	-639.79	397.12	-866.23
$[Fe\{7(1)\text{-}N(4)B(5)\}_2(NCS)_2]$	-621.84	-640.43	393.8	-868.48
$[Fe\{7(3)\text{-}N(4)B(5)\}_2(NCS)_2]$	-609.59	-623.26	382.91	-849.94
$[Fe\{7(5)\text{-}N(2)B(6)\}_2(NCS)_2]$	-578.9	-605.98	350.6	-834.28
$[Fe\{7(1)\text{-}N(3)B(2)\}_2(NCS)_2]$	-618.66	-641.82	389.98	-870.5
$[Fe\{7(5)\text{-}N(2)B(1)\}_2(NCS)_2]$	-566.48	-605.02	331.9	-839.6
$[Fe\{7(5)\text{-}N(1)B(2)\}_2(NCS)_2]$	-604.54	-586.41	384.9	-806.05
$[Fe\{7(6)\text{-}N(2)B(5)\}_2(NCS)_2]$	-611.41	-619.55	388.6	-842.36
$[Fe\{7(5)\text{-}N(6)B(4)\}_2(NCS)_2]$	-611.77	-573.6	388.83	-796.55
$[Fe\{7(4)\text{-}N(3)B(2)\}_2(NCS)_2]$	-634.49	-634.92	404.02	-865.38
$[Fe\{7(4)\text{-}N(2)B(3)\}_2(NCS)_2]$	-584.26	-604.01	366.58	-821.68

Table 36: The energy decomposition analysis for the S(0) spin-state of the benchmark systems and a set of SCO candidate compounds. All energies in kcal mol^{-1}.

Table 36 shows the EDA of the S(0) spin-state of $[Fe(Phen)_2(NCS)_2]$, $[Fe(BiPy)_3]^{2+}$ and the set of SCO candidate compounds. The known low-spin compound $[Fe(BiPy)_3]^{2+}$ has a similar $E_{Orb.\ Int.}$ to the other systems but has a significantly lower $E_{Elstat.}$ value which leads to a similarly low $E_{Int.}$ value. This is due to the difference in bonding between an ML_6 system and a ML_4X_2 system where both have 6N first spheres of coordination around an Fe(II) core, i.e. the anionic NCS ligands possess a greater coulombic attraction to the positively charged metal centre than a neutral bipy ligand. Of the remaining systems, the values of $E_{Orb.\ Int.}$ and $E_{Elstat.}$ contribute relatively equally to the value of $E_{Int.}$, the systems which are mostly likely to display SCO behaviour show a slightly dominant $E_{Elstat.}$ value, however the difference is not of a sufficient size to define this as a

characteristic of SCO behaviour. The E_{Pauli} is uniformly the smallest component, however it can vary significantly between the systems.

Compound	$E_{orb.\ Int.}$	$E_{elstat.}$	E_{Pauli}	$E_{int.}$
$[Fe(Phen)_2(NCS)_2]$	-543.08	-634.64	354.76	-822.95
$[Fe(BiPy)_3]^{2+}$	N/A			
$[Fe\{7(6)\text{-}N(4)B(5)\}_2(NCS)_2]$	-588.34	-643.01	378.04	-853.31
$[Fe\{7(1)\text{-}N(4)B(5)\}_2(NCS)_2]$	-576.73	-646.79	379.82	-843.71
$[Fe\{7(3)\text{-}N(4)B(5)\}_2(NCS)_2]$	-548.92	-619.31	338.64	-829.59
$[Fe\{7(5)\text{-}N(2)B(6)\}_2(NCS)_2]$	N/A			
$[Fe\{7(1)\text{-}N(3)B(2)\}_2(NCS)_2]$	-588.25	-651.88	389.2	-850.94
$[Fe\{7(5)\text{-}N(2)B(1)\}_2(NCS)_2]$	N/A			
$[Fe\{7(5)\text{-}N(1)B(2)\}_2(NCS)_2]$	-531.7	-580.44	340.98	-771.16
$[Fe\{7(6)\text{-}N(2)B(5)\}_2(NCS)_2]$	-549.16	-613.28	339.01	-823.42
$[Fe\{7(5)\text{-}N(6)B(4)\}_2(NCS)_2]$	-569.71	-570.59	339.3	-801
$[Fe\{7(4)\text{-}N(3)B(2)\}_2(NCS)_2]$	-612.61	-646.89	406.74	-852.75
$[Fe\{7(4)\text{-}N(2)B(3)\}_2(NCS)_2]$	-554.71	-613.41	359.61	-808.5

Table 37: The energy decomposition analysis for the S(1) spin-state of the benchmark systems and a set of SCO candidate compounds. All energies in kcal mol^{-1}.

The EDA for the S(1) state is displayed above in Table 37, this shows a reduction in magnitude across all of the stabilising interactions, this is in line with the removal of an electron from the typically non-bonding t_{2g} to the anti-bonding e_g. There is also a general increase in $E_{Pauli.}$, likely due to the proximity in d-space of two unpaired electrons.

Compound	$E_{orb.\ Int.}$	$E_{elstat.}$	E_{Pauli}	$E_{int.}$
$[Fe(Phen)_2(NCS)_2]$	-516.48	-648.62	371.56	-793.54
$[Fe(BiPy)_3]^{2+}$	-419.52	-345.58	257.25	-507.84
$[Fe\{7(6)\text{-}N(4)B(5)\}_2(NCS)_2]$	-524.66	-638.85	341.01	-822.5
$[Fe\{7(1)\text{-}N(4)B(5)\}_2(NCS)_2]$	-469.03	-614.08	287.29	-795.8
$[Fe\{7(3)\text{-}N(4)B(5)\}_2(NCS)_2]$	-482.22	-611.92	296.12	-798.01
$[Fe\{7(5)\text{-}N(2)B(6)\}_2(NCS)_2]$	N/A			
$[Fe\{7(1)\text{-}N(3)B(2)\}_2(NCS)_2]$	-518.73	-640.94	337.98	-821.68
$[Fe\{7(5)\text{-}N(2)B(1)\}_2(NCS)_2]$	N/A			
$[Fe\{7(5)\text{-}N(1)B(2)\}_2(NCS)_2]$	-441.56	-555.92	257.91	-739.56
$[Fe\{7(6)\text{-}N(2)B(5)\}_2(NCS)_2]$	-461.99	-596.78	282.2	-776.56
$[Fe\{7(5)\text{-}N(6)B(4)\}_2(NCS)_2]$	-561.25	-592.05	379.46	-773.84
$[Fe\{7(4)\text{-}N(3)B(2)\}_2(NCS)_2]$	-526.59	-630.16	333.25	-823.5
$[Fe\{7(4)\text{-}N(2)B(3)\}_2(NCS)_2]$	-477.04	-600.82	299.43	-778.43

Table 38: The energy decomposition analysis for the T(1) spin-state of the benchmark systems and a set of SCO candidate compounds. All energies in kcal mol^{-1}.

The energies presented in Table 38 pertaining to the T(1) state show an even greater reduction in stabilising interactions than the S(1) state.

Compound	$E_{orb.\ Int.}$	$E_{elstat.}$	E_{Pauli}	$E_{int.}$
$[Fe(Phen)_2(NCS)_2]$	-316.14	-565.36	162.63	-718.87
$[Fe(BiPy)_3]^{2+}$	-279.62	-297.25	150.63	-426.23
$[Fe\{7(6)\text{-}N(4)B(5)\}_2(NCS)_2]$	-347.99	-574.84	186.24	-736.59
$[Fe\{7(1)\text{-}N(4)B(5)\}_2(NCS)_2]$	-321.39	-565.92	162.52	-724.78
$[Fe\{7(3)\text{-}N(4)B(5)\}_2(NCS)_2]$	-329.95	-557.26	174.7	-712.51
$[Fe\{7(5)\text{-}N(2)B(6)\}_2(NCS)_2]$	-316.4	-542.11	150.78	-707.73
$[Fe\{7(1)\text{-}N(3)B(2)\}_2(NCS)_2]$	-324.25	-567.03	160.65	-730.64
$[Fe\{7(5)\text{-}N(2)B(1)\}_2(NCS)_2]$	N/A			
$[Fe\{7(5)\text{-}N(1)B(2)\}_2(NCS)_2]$	-321	-527.8	167.85	-680.94
$[Fe\{7(6)\text{-}N(2)B(5)\}_2(NCS)_2]$	-339.05	-558.42	186.1	-711.37
$[Fe\{7(5)\text{-}N(6)B(4)\}_2(NCS)_2]$	-339.9	-513.04	177.9	-675.05
$[Fe\{7(4)\text{-}N(3)B(2)\}_2(NCS)_2]$	-352.38	-566.02	187.35	-731.06
$[Fe\{7(4)\text{-}N(2)B(3)\}_2(NCS)_2]$	-322.71	-543.03	166.76	-698.99

Table 39: The energy decomposition analysis for the Q(1) spin-state of the benchmark systems and a set of SCO candidate compounds. All energies in kcal mol^{-1}.

The EDA associated with the Q(1) spin-state of all the systems shows a significant decrease in all stabilising interactions as is to be expected with the removal of a second electron from the non-bonding t_{2g} to the anti-bonding e_g. The $E_{Orb.\ Int.}$ value is obviously reduced to the largest extent causing the $E_{Elstat.}$ to become the dominant stabilising interaction. The $E_{Int.}$ is somewhat shielded from this reduction by a similar reduction in the E_{Pauli} but still reduces significantly.

Hirshfeld Charge Analysis

In order to elucidate a reason for the variation of electronic behaviour the Hirshfeld charges associated with the nitrogen atoms that bind in an L-type manner to the metal have been evaluated for both the bound and unbound candidate ligands. This data is displayed below in Table 40, note that the S(0) spin-state is evaluated as the bound state.

Compound	Hirshfeld Charges Upon N L-type Donors	
	Free Ligand Candidate	Bound Ligand Candidate
$[Fe\{7(6)\text{-}N(4)B(5)\}_2(NCS)_2]$	-0.139, -0.139	-0.045, -0.047, -0.045, -0.047
$[Fe\{7(1)\text{-}N(4)B(5)\}_2(NCS)_2]$	-0.131, -0.145	-0.039, -0.038, -0.040, -0.034
$[Fe\{7(3)\text{-}N(4)B(5)\}_2(NCS)_2]$	-0.136, -0.136	-0.037, -0.044, -0.044, -0.042
$[Fe\{7(5)\text{-}N(2)B(6)\}_2(NCS)_2]$	-0.219, -0.219	-0.141, -0.126, -0.138, -0.125
$[Fe\{7(1)\text{-}N(3)B(2)\}_2(NCS)_2]$	-0.152, -0.142	-0.048, -0.043, -0.045, -0.046
$[Fe\{7(5)\text{-}N(2)B(1)\}_2(NCS)_2]$	-0.216, -0.216	-0.108, -0.114, -0.114, -0.105
$[Fe\{7(5)\text{-}N(1)B(2)\}_2(NCS)_2]$	-0.107, -0.107	-0.008, -0.017, -0.012, -0.019
$[Fe\{7(6)\text{-}N(2)B(5)\}_2(NCS)_2]$	-0.133, -0.133	-0.045, -0.044, -0.056, -0.044
$[Fe\{7(5)\text{-}N(6)B(4)\}_2(NCS)_2]$	-0.085, -0.085	0.001, -0.031, -0.024, -0.018
$[Fe\{7(4)\text{-}N(3)B(2)\}_2(NCS)_2]$	-0.148, -0.148	-0.047, -0.041, -0.050, -0.042
$[Fe\{7(4)\text{-}N(2)B(3)\}_2(NCS)_2]$	-0.161, -0.161	-0.062, -0.070, -0.074, -0.069

Table 40: The Hirshfeld charges associated to the L-type N donors in the homoaromatic ligand candidates in both their free and bound states.

Table 40 does not immediately indicate a clear trend, the high-spin compounds tend to possess the higher charges whilst the low-spin compounds tend to possess lower charges however there are multiple exceptions. This would suggest that the concentration of charge upon the donor atoms is important but not the only controlling factor.

Conclusion

A range of twelve homoaromatic bidentate ligand candidates has been assessed and shown to possess a range of π-interaction strengths. The homoaromatic candidates have been shown to significantly alter the HS-LS gap of the known $[Fe(Phen)_2(NCS)_2]$ SCO complex to both reduce and increase the magnitude of the gap via structural isomerism. Of the twelve candidate compounds there are multiple examples of low-spin compounds, two examples of high spin compounds and several candidates which show properties indicative of SCO behaviour. Given this variation has been achieved merely by exploiting the electronic properties available through structural isomerism, the introduction of homoaromaticity as a technique for dedicated system design could allow for the engineering of a range of behaviours. Given the ubiquity of nitrogen donors encapsulated within aromatic rings present within the SCO field, this offers a new tool applicable to the improved design of functional materials.

Chapter 8 - Concluding Remarks and Further Work

Chapter 2 showcased initial calculations upon boron-containing systems, conducted during multiple collaborative projects. The selected projects were displayed as they allowed for an exploration of various applications of DFT to solve complex chemical problems relevant in later chapters. In addition to showing that both GGA and hybrid-type functionals could be used accurately in the calculation of a wide-range of chemical phenomena, it was also shown that the energy released in the heterolytic fission of π-bonds and thus the specific bonding contributions across the bonds could be calculated via a PAoC based method. This is important for the analysis of the compounds in Chapters 6 and 7 and would usually be impossible due to the requirement of restricted fragments. Thus, whilst the bond strengths as calculated in Chapter 2 do not clearly offer actionable trends such as to allow for the prior prediction of the strength of specific chemical bonds, it does display that the method of calculating the bonding contributions has worked for every instance of heterolytically splitting a BB π-bond thus validating the PAoC based method. It should be noted that 3-fragment calculations incurred a large degree of additional stabilisation upon bonding rendering such calculations inaccurate suggesting a limitation that could be removed in future.

Chapter 3 established a number of criteria for the rapid assessment of homoaromatic candidate compounds. Whilst more stringent criteria exist currently, they do not offer a favourable compromise between accuracy and speed. With these criteria in place a number of good homoaromatic candidates were shown resulting in several general conclusions. Firstly, using the homotropylium cation as a starting point was far more likely to result in homoaromatic behaviour than if similar steps are taken using the norbornyl cation as a starting point. Secondly, the use of NHCs as two-electron donors is likely to necessitate the use of a carbocation to

facilitate charge flow around the ring structure. Finally, the use of a carbocation removes a degree of structural control in the design as the charge will migrate to be adjacent to the carbon atom with the donor group.

These conclusions directly led to the inclusion of boron atoms with homoaromatic candidate molecules in an attempt to acquire a degree of control to allow for compound design. Given the additional structural control that boron allowed, Chapter 4 contains a large survey of the effects of structural isomerism upon the strength of the homoaromatic interaction within the compounds. It quickly became apparent that structural isomerism within such system has a significant impact on the strength, or even the presence, of a homoaromatic interaction although several overall patterns can be observed. Generally, the weakest interaction occurs when C-C π-bonds are interrupted by a two-electron donor heteroatom whereas the strongest interactions occur when the accepting boron atom is placed at the bridgehead of the homoconjugative gap and where there exists one π-cloud orbital per π-electron.

Given the large range of quantitative numerical metrics available for the assessment of aromaticity and the large number of compounds surveyed, it seemed prudent to investigate a method which would allow for the rapid, qualitative assessment of a variety of compounds to identify the presence of a homoaromatic interaction. It was shown that SEDD could be a useful analytical tool and that, whilst using a smaller basis set reduced the clarity of the output, it allowed for a less computationally expensive calculation whilst still providing the necessary data.

The difficulties inherent in calculating the behaviour of SCO compounds is well known and discussed with Chapter 6. This chapter then leads into a limited assessment of exchange-

correlation functionals on known systems to benchmark a reliable methodology. In order to allow for the geometry optimisation of the first excited states, which are difficult to attain and important to describe the spin-transition pathways, a method of optimisation was employed based upon a modified version of the PAoC calculations as introduced within Chapter 2.

Chapter 7 represents the culmination of the conclusions reached as a result of the work presented in all previous chapters. The bonding between the Fe^{2+} ions and the first sphere of coordination was investigated at all spin-states by utilising the PAoC method devised within Chapter 2. The ligands were designed following the rules and conclusions from Chapters 3 and 4. The homoaromatic nature of the ligand candidates was analysed with an SEDD method as shown to be applicable in Chapter 5. Finally the characterisation of the full spin-transition pathways was only possible due to the benchmarking presented in Chapter 6. Thus Chapter 7 contains a detailed analysis of 12 homoaromatic ligand candidates which the leads into the inspection of the spin-transition pathways of 12 candidate transition metal systems. Of these systems, four display low-spin behaviour, three display high spin-behaviour and two compounds display behaviour strongly reminiscent of spin-crossover behaviour. Upon inspection of the numerical metrics of homoaromaticity within the free ligands it becomes apparent that a weak homoaromatic interaction generally results in a low-spin complex, a particularly strong homoaromatic tends to result in a high-spin complex and a moderate to strong homoaromatic interaction is favourable for behaviour associated with SCO materials.

The range of electronic behaviour induced by mere structural isomerism within the homoaromatic ligand candidates is useful on its own merits. That said, the existence of two compounds that are likely to display SCO behaviour, $[Fe\{7(6)\text{-}N(2)B(5)\}_2(NCS)_2]$ and $[Fe\{7(5)\text{-}N(6)B(4)\}_2(NCS)_2]$ shows that there is a strong possibility that homoaromatic ligands could

support SCO behaviour with the added malleability of the properties of the system allowed by modulating the strength of the homoaromatic interaction.

Although unfortunately outside the scope of this work, the inspection of the bonding between the Fe^{2+} ions and the first sphere of coordination via a PAoC method heavily suggested the presence of DCD-type backbonding. This is both unlikely and surprising for a compound exhibiting SCO behaviour due to the non-bonding nature of the valence orbitals and thus would benefit from a more extensive and targeted investigation.

It is worth noting that due to the functionalisation of the homoaromatic systems discussed in Chapters 3 and 4 there exists the possibility of inserting a homoaromatic interaction into any system where aromaticity is present to effect a perturbation to the energetics of the system. It might be particularly interesting to insert homoaromaticity into drug precursors as a large proportion of current pharmaceuticals are already based around nitrogen heterocycles.[189]

Additionally, the structural isomers applied to the test complex in Chapter 7 represents only a small sample of the possible combinations. Given the powerful charge flux abilities of boron it may be that a wide range of electron donors could be used to modulate the strength of the current within the ring system. This would provide additional avenues to tuning the HS-LS gap of spin-switchable systems.

Bibliography

1 N. N. Greenwood, *Boron*, Pergamon Press, Oxford, 1975.

2 B. Pastina, J. Isabey and B. Hickel, *J. Nucl. Mater.*, 1999, **264**, 309–318.

3 A. Suzuki, *Angew. Chemie - Int. Ed.*, 2011, **50**, 6723–6733.

4 M. Yamashita, *Angew. Chemie - Int. Ed.*, 2010, **49**, 2474–2475.

5 E. R. Burkhardt and K. Matos, *Chem. Rev.*, 2006, **106**, 2617–2650.

6 M. Suginome, *J. Synth. Org. Chem. Jpn.*, 2007, **65**, 1048–1059.

7 N. Miyaura and A. Suzuki, *Chem. Rev.*, 1995, **95**, 2457–2483.

8 A. L. Kenward and W. E. Piers, *Angew. Chemie - Int. Ed.*, 2008, **47**, 38–41.

9 G. C. Welch, R. R. San Juan, J. D. Masuda and D. W. Stephan, *Science*, 2006, **314**, 1124–6.

10 H. Braunschweig, R. D. Dewhurst, K. Radacki, C. W. Tate and A. Vargas, *Angew. Chemie - Int. Ed.*, 2014, **53**, 6263–6266.

11 H. Braunschweig, A. Damme, R. D. Dewhurst, S. Ghosh, T. Kramer, B. Pfaffinger, K. Radacki and A. Vargas, *J. Am. Chem. Soc.*, 2013, **135**, 1903–1911.

12 W. J. Grigsby and P. P. Power, *Chem. Commun.*, 1996, **92**, 2235–2236.

13 H. Nöth, J. Knizek and W. Ponikwar, *Eur. J. Inorg. Chem.*, 1999, **1999**, 1931–1937.

14 W. J. Grigsby and P. Power, *Chem. - A Eur. J.*, 1997, **3**, 368–375.

15 H. Klusick and A. Berndt, *Angew. Chem. Int. Ed. Engl.*, 1981, **20**, 870–871.

16 C. Pluta, K.-R. Porschke, C. Kriiger and K. Hildenbrand, *Angew. Chem. Int. Ed. Eng.*, 1993, **114**, 388–390.

17 X. He, R. A. Bartlett, M. M. Olmstead, K. Ruhlandt-Senge and B. E. Sturgeon, *Angew.*

Chem. Int. Ed. Engl., 1993, **32**, 717–719.

18 A. Moezzi, R. a. Bartlett and P. P. Power, *Angew. Chemie Int. Ed. Eng.*, 1992, **31**, 1082–1083.

19 A. Moezzi, M. M. Olmstead and P. P. Power, *J. Am. Chem. Soc.*, 1992, **114**, 2715–2717.

20 P. P. Power, *Inorg. Chim. Acta*, 1992, **198-200**, 443–447.

21 Y. Wang, B. Quillian, P. Wei, C. S. Wannere, Y. Xie, R. B. King, H. F. Schaefer, P. V. R. Schleyer and G. H. Robinson, *J. Am. Chem. Soc.*, 2007, **129**, 12412–12413.

22 H. Braunschweig, R. D. Dewhurst, K. Hammond, J. Mies, K. Radacki and A. Vargas, *Science*, 2012, **336**, 1420–1422.

23 H. Braunschweig and R. D. Dewhurst, *Angew. Chemie - Int. Ed.*, 2013, **52**, 3574–3583.

24 H. Braunschweig and R. D. Dewhurst, *Organometallics*, 2014, **33**, 6271–6277.

25 H. Braunschweig, V. Dyakonov, J. O. C. Jimenez-Halla, K. Kraft, I. Krummenacher, K. Radacki, A. Sperlich and J. Wahler, *Angew. Chemie - Int. Ed.*, 2012, **51**, 2977–2980.

26 R. Bertermann, H. Braunschweig, R. D. Dewhurst, C. Hörl, T. Kramer and I. Krummenacher, *Angew. Chemie - Int. Ed.*, 2014, **53**, 5453–5457.

27 P. Bissinger, H. Braunschweig, A. Damme, I. Krummenacher, A. K. Phukan, K. Radacki and S. Sugawara, *Angew. Chemie - Int. Ed.*, 2014, **53**, 7360–7363.

28 H. Braunschweig, A. Damme, R. D. Dewhurst, T. Kramer, S. Östreicher, K. Radacki and A. Vargas, *J. Am. Chem. Soc.*, 2013, **135**, 2313–2320.

29 H. Braunschweig, P. Brenner, R. D. Dewhurst, I. Krummenacher, B. Pfaffinger and A. Vargas, *Nat. Commun.*, DOI:10.1038/ncomms1884.

30 H. Braunschweig, Q. Ye, A. Vargas, K. Radacki and A. Damme, *Angew. Chemie - Int. Ed.*,

2013, **52**, 10657–10660.

31 H. Braunschweig, R. D. Dewhurst, F. Hupp, M. Nutz, K. Radacki, C. W. Tate, A. Vargas and Q. Ye, *Nature*, 2015, **522**, 327–330.

32 H. Braunschweig, T. Dellermann, R. D. Dewhurst, W. C. Ewing, K. Hammond, J. O. C. Jimenez-Halla, T. Kramer, I. Krummenacher, J. Mies, A. K. Phukan and A. Vargas, *Nat. Chem.*, 2013, **5**, 1025–1028.

33 B. Su and R. Kinjo, *Synth.*, 2017, **49**, 2985–3034.

34 A. Stock and E. Pohland, *Ber. Dtsch. Chem. Ges.*, 1926, **59**, 2210–2215.

35 A. Soncini, C. Domene, J. J. Engelberts, P. W. Fowler, A. Rassat, J. H. Van Lenthe, R. W. A. Havenith and L. W. Jenneskens, *Chem. - A Eur. J.*, 2005, **11**, 1257–1266.

36 R. Islas, E. Chamorro, J. Robles, T. Heine, J. C. Santos and G. Merino, *Struct. Chem.*, 2007, **18**, 833–839.

37 A. K. Phukan, A. K. Guha and B. Silvi, *Dalt. Trans.*, 2010, **39**, 4126.

38 D. E. Bean and P. W. Fowler, *J. Phys. Chem. A*, 2011, **115**, 13649–13656.

39 B. Kiran, A. K. Phukan and E. D. Jemmis, *Inorg. Chem.*, 2001, **40**, 3615–3618.

40 P. G. Campbell, A. J. V. Marwitz and S. Y. Liu, *Angew. Chemie - Int. Ed.*, 2012, **51**, 6074–6092.

41 M. J. . Bosdet and W. E. Piers, *Can. J. Chem.*, 2009, **87**, 8–29.

42 L. Weber, *Coord. Chem. Rev.*, 2001, **215**, 39–77.

43 E. R. Abbey and S.-Y. Liu, *Org. Biomol. Chem.*, 2013, **11**, 2060.

44 J. Pan, J. W. Kampf and A. J. Ashe, *Organometallics*, 2004, **23**, 5626–5629.

45 J. Pan, J. W. Kampf and A. J. Ashe, *Organometallics*, 2008, **27**, 1345–1347.

46 H. Braunschweig, R. D. Dewhurst and V. H. Gessner, *Chem. Soc. Rev.*, 2013, **42**, 3197.

47 H. Braunschweig and M. Colling, *Eur. J. Inorg. Chem.*, 2003, **2003**, 393–403.

48 M. A. Halcrow, *Coord. Chem. Rev.*, 2009, **253**, 2493–2514.

49 M. A. Halcrow, *Chem. Soc. Rev.*, 2011, **40**, 4119.

50 A. Bousseksou, G. Molnár, L. Salmon and W. Nicolazzi, *Chem. Soc. Rev.*, 2011, **40**, 3313.

51 H. A. Goodwin, *Coord. Chem. Rev.*, 1976, **18**, 293–325.

52 P. Gütlich, *Struct. Bond.*, 1981, **44**, 83–195.

53 P. Gutlich, A. Hauser and H. Spiering, *Angew. Chem. Int. Ed.*, 1994, **33**, 2024–2054.

54 P. Gütlich, Y. Garcia and H. A. Goodwin, *Chem. Soc. Rev.*, 2000, **29**, 419–427.

55 H. Li and H. Peng, *Curr. Opin. Colloid Interface Sci.*, 2018, **35**, 9–16.

56 G. Molnár, L. Salmon, W. Nicolazzi, F. Terki and A. Bousseksou, *J. Mater. Chem. C*, 2014, **2**, 1360–1366.

57 L. Cambi and L. Szego, *Ber. Dtsch. Chem. Ges. Tl. B*, 1931, **64**, 2591–2598.

58 A. H. Ewald, R. L. Martin, I. G. Ross and A. H. White, *Proc. R. Soc. London Ser. A*, 1964, **280**, 235–257.

59 B. N. Figgis and G. E. Toogood, *J. Chem. Soc. Dalt. Trans.*, 1972, 2177–2182.

60 E. Konig and K. Madeja, *Inorg. Chem.*, 1967, **6**, 48–55.

61 S. K. Kulshreshtha and S. R., *Chem. Phys. Lett.*, 1986, **123**, 215–217.

62 R. Claude, J.-A. Real, J. Zarembowitch, O. Kahn, L. Ouahab, D. Grandjean, K. Boukheddaden, F. Varret and A. Dworkin, *Inorg. Chem.*, 1990, **29**, 4442–4448.

63 G. S. Matouzenko, A. Bousseksou, S. Lecoq, P. J. van Koningsbruggen, M. Perrin, O. Kahn

and A. Collet, *Inorg. Chem.*, 1997, **36**, 2975–2981.

64 A. B. Gaspar, G. Agusti, V. Martinez, M. C. Munoz, G. Levchenko and J.-A. Real, *Inorg. Chem. Acta*, 2005, **358**, 4089–4094.

65 J. P. Jesson, S. Trofimenko and D. R. Eaton, *J. Am. Chem. Soc.*, 1967, **89**, 3148–3158.

66 J. Olguín and S. Brooker, *Coord. Chem. Rev.*, 2011, **255**, 203–240.

67 J. J. McGarvey, H. Toftlund, A. H. R. Al-Obaidi, K. P. Taylor and S. E. J. Bell, *Inorg. Chem.1*, 1993, **32**, 2469–2472.

68 P. A. Anderson, T. Astley, M. A. Hitchman, F. R. Keene, B. Moubaraki, K. S. Murray, B. W. Skelton, E. R. T. Tiekink, H. Toftlund and A. H. White, *J. Chem. Soc. Dalt. Trans.2*, 2000, 3505–3512.

69 J.-A. Real, J. Zarembowitch, O. Kahn and X. Solans, *Inorg. Chem.*, 1987, **26**, 2939–2943.

70 K. S. Murray and C. J. Kepert, *Top. Curr. Chem.*, 2004, **233**, 195–228.

71 J.-F. Letard, P. Guionneau and L. Goux-Capes, *Top. Curr. Chem.*, 2004, **235**, 221.

72 T. Forestier, S. Momet, N. Daro, T. Nishihara, S.-I. Mouri, K. Tanaka, O. Fouche, E. Freysz and J.-F. Letard, *Chem. Comm.*, 2008, 4327.

73 M. Reiher, *Inorg. Chem.*, 2002, **41**, 6928–6935.

74 M. Swart, *J. Chem. Theor. Comput.*, 2008, **4**, 2057–2066.

75 H. Paulsen, L. Duelund, H. Winkler, H. Toftlund and A. X. Trautwein, *Inorg. Chem.*, 2001, **40**, 2201–2204.

76 L. M. Lawson-Daku, A. Vargas, A. Hauser, A. Fouqueau and M. E. Casida, *ChemPhysChem*, 2005, **6**, 1393–1410.

77 K. P. Jensen and J. Cirera, *J. Phys. Chem. A*, 2009, **113**, 10033–10039.

78 T. F. Hughes and R. A. Friesner, *J. Chem. Theor. Comput.*, 2011, **7**, 19–32.

79 G. Baranovich, *Chem. Phys. Lett.*, 2003, **369**, 668–672.

80 F. Neese, *J. Biol. Inorg. Chem.*, 2006, **11**, 702–711.

81 S. Zein, S. A. Bohrsch, P. Fleuret-Lessard, M. E. Casida and H. Chermette, *J. Chem. Phys.*, 2007, **126**, 14105.

82 H. Paulsen, V. Schunemann and J. A. Wolny, *Eur. J. Inorg. Chem.*, 2013, 628–641.

83 K. Pierloot and S. Vancoillie, *J. Chem. Phys.*, 2008, **128**, 34104.

84 E. I. Ioannidis and H. J. Kulika, *J. Chem. Phys.*, 2015, **143**, 34104.

85 K. P. Kepp, *J. Inorg. Biochem.*, 2011, **105**, 1286–1292.

86 S. R. Mortensen and K. P. Kepp, *J. Phys. Chem. A*, 2015, **119**, 4041–4050.

87 K. P. Kepp, *Inorg. Chem.*, 2016, **55**, 2717–2727.

88 R. C. Raffenetti, *J. Chem.Phys.*, 1973, **59**, 5936.

89 L. Fan and T. Ziegler, *J. Chem. Phys.*, 1991, **95**, 7401–7408.

90 L. Versluis and T. Ziegler, *J. Chem. Phys.*, 1988, **88**, 322–328.

91 W. Kohn and L. J. Sham, *Phys. Rev.*, 1965, **140**, A1133–A1138.

92 W. Koch and M. C. Holthausen, *A Chemist's Guide to Density Funtional Theory*, Wiley-VCH, 2008, p. 45.

93 M. Seth, G. Mazur and T. Ziegler, *Theor. Chem. Acc.*, 2011, **129**, 331–342.

94 H. A. Bethe, *Ann. Phys.*, 1929, **3**, 133–206.

95 J. H. Van Vleck, *Phys. Rev.*, 1932, **41**, 208–215.

96 J. S. Griffith and L. E. Orgel, *Q. Rev. Chem. Soc.*, 1957, **11**, 381–393.

97 C. A. Daul, *J. Phys. Conf. Ser.*, , DOI:10.1088/1742-6596/428/1/012023.

98 B. N. Figgis, *Compr. Coord. Chem. Theory Backgr.*, 1987, 213–279.

99 H. Eyring, J. Walter and G. E. Kimball, *Quantum Chemistry*, Wiley, New York, 1950.

100 C. E. Schäffer and C. K. Jørgensen, *J. Inorg. Nucl. Chem.*, 1958, **8**, 143–148.

101 C. F. Guerra, J. G. Snijders, G. te Velde and E. J. Baerends, *Theor. Chem. Acc.*, 1998, **99**, 391–403.

102 B. Hammer, L. B. Hansen and J. K. Norskov, *Phys. Rev.*, 1999, **B 59**, 7413.

103 H. Braunschweig, W. C. Ewing, T. Kramer, J. D. Mattock, A. Vargas and C. Werner, *Chem. - A Eur. J.*, 2015, **21**, 12347–12356.

104 H. Braunschweig, W. C. Ewing, S. Ghosh, T. Kramer, J. D. Mattock, S. Östreicher, A. Vargas and C. Werner, *Chem. Sci.*, 2016, **7**, 109–116.

105 H. Braunschweig, I. Krummenacher, C. Lichtenberg, J. D. Mattock, M. Schäfer, U. Schmidt, C. Schneider, T. Steffenhagen, S. Ullrich and A. Vargas, *Angew. Chemie - Int. Ed.*, 2017, **56**, 889–892.

106 H. Braunschweig, T. Dellermann, R. D. Dewhurst, B. Hupp, T. Kramer, J. D. Mattock, J. Mies, A. K. Phukan, A. Steffen and A. Vargas, *J. Am. Chem. Soc.*, 2017, **139**, 4887–4893.

107 S. R. Wang, M. Arrowsmith, J. Böhnke, H. Braunschweig, T. Dellermann, R. D. Dewhurst, H. Kelch, I. Krummenacher, J. D. Mattock, J. H. Müssig, T. Thiess, A. Vargas and J. Zhang, *Angew. Chemie - Int. Ed.*, 2017, **56**, 8009–8013.

108 S. R. Wang, M. Arrowsmith, H. Braunschweig, R. D. Dewhurst, M. Dömling, J. D. Mattock, C. Pranckevicius and A. Vargas, *J. Am. Chem. Soc.*, 2017, **139**, 10661–10664.

109 I. Mayer, *Chem. Phys. Lett.*, 1983, **97**, 270–274.

110 M. Mitoraj, M. A and T. Ziegler, *Organometallics*, 2009, **28**, 3727.

111 M. Mitoraj, M. A and T. Ziegler, *J. Chem. Theo. Comp.*, 2009, **5**, 962.

112 R. Patchett, R. C. Knighton, J. D. Mattock, A. Vargas and A. B. Chaplin, *Inorg. Chem.*, 2017, **56**, 14345–14350.

113 K. Griffiths, P. Kumar, J. D. Mattock, A. Abdul-Sada, M. B. Pitak, S. J. Coles, O. Navarro, A. Vargas and G. E. Kostakis, *Inorg. Chem.*, 2016, **55**, 6988–6994.

114 P. Politzer, P. R. Laurence and K. Jayasuriya, *Environ. Heal. Perspect.*, 1985, **61**, 191–202.

115 K. Griffiths, V. N. Dokorou, J. Spencer, A. Abdul-Sada, A. Vargas and G. E. Kostakis, *CrystEngComm*, 2016, **18**, 704–713.

116 J. D. Mattock, A. Vargas and R. D. Dewhurst, *Chem. - A Eur. J.*, 2015, **21**, 16968–16974.

117 R. V Williams, *Chem. Rev.*, 2001, **101**, 1185–1204.

118 H. E. Zimmerman, G. L. Grunewald, *J. Am. Chem. Soc.*, 1966, **88**, 183–184.

119 H. E. Zimmerman, R. W. Brinkley, R. S. Givens, M. A. Sherwin, *J. Am. Chem. Soc.*, 1967, **89**, 3932–3933.

120 R. E. Factor, N. J. Turro, J.-M. Liu, H. E. Zimmerman and R. E. Factor, *J. Org. Chem.*, 1980, **45**, 3511–3512.

121 A. Ault, *J. Chem. Educ.*, 2001, **78**, 924–927.

122 G. Li, Z. Wang, S. Zhang, Z. Xi, C. Wang, J. Yuan, G. Li, Z. Wang, S. Zhang and Z. Xi, *J. Am. Chem. Soc.*, 2006, **128**, 4564–4565.

123 G. Dixit, T. Bredtmann, M. Ivanov and G. Dixit, *Nat. Commun.*, 2014, **5**, 5589.

124 M. Alcarazo, C. W. Lehmann, A. Anoop, W. Thiel and A. Furstner, *Nat. Chem.*, 2009, **1**, 295–301.

125 D. Martin, M. Soleilhavoup and G. Bertrand, *Chem. Sci.*, 2011, **2**, 389–399.

126 D. Martin, M. Melaimi, M. Soleilhavoup and G. Bertrand, *Organometallics*, 2011, **30**, 5304–5313.

127 D. P. Curran, A. Solovyev, M. M. Brahmi, L. Fensterbank, M. Malacria and E. Lacote, *Angew. Chem. Int. Ed.*, 2011, **50**, 10294–10317.

128 Y. Wang and G. H. Robinson, *Dalton Trans.*, 2012, **41**, 337–345.

129 S. Khan, S. S. Sen and H. W. Roesky, *Chem. Commun.*, 2012, **48**, 2169–2179.

130 C. D. Martin, M. Soleilhavoup and G. Bertrand, *Chem. Sci.*, 2013, **4**, 3020–3030.

131 H. Schmidbaur and A. Schier, *Angew. Chem. Int. Ed.*, 2013, **52**, 176–186.

132 H. Braunschweig and R. D. Dewhurst, *Organometallics*, 2014, **33**, 6271–6277.

133 M. Soleilhavoup and G. Bertrand, *Acc. Chem. Res.*, 2015, **48**, 256–266.

134 D. Himmel, I. Krossing and A. Schnepf, *Angew. Chem. Int. Ed.*, 2014, **53**, 370–374.

135 G. Frenking, *Angew. Chem. Int. Ed.*, 2014, **53**, 6040–6046.

136 D. Himmel, I. Krossing and A. Schnepf, *Angew. Chem. Int. Ed.*, 2014, **53**, 6047–6048.

137 M. J. Frisch, G. W. Trucks, H. B. Schlegel, G. E. Scuseria, M. A. Robb, J. R. Cheeseman, G. Scalmani, V. Barone, B. Mennucci, G. A. Petersson, H. Nakatsuji, M. Caricato, X. Li, H. P. Hratchian, A. F. Izmaylov, J. Bloino, G. Zheng, J. L. Sonnenberg, M. Hada, M. Ehara, K. Toyota, R. Fukuda, J. Hasegawa, M. Ishida, T. Nakajima, Y. Honda, O. Kitao, H. Nakai, T. Vreven, J. A. Montgomery, Jr., J. E. Peralta, F. Ogliaro, M. Bearpark, J. J. Heyd, E. Brothers, K. N. Kudin, V. N. Staroverov, T. Keith, R. Kobayashi, J. Normand, K. Raghavachari, A. Rendell, J. C. Burant, S. S. Iyengar, J. Tomasi, M. Cossi, N. Rega, J. M. Millam, M. Klene, J. E. Knox, J. B. Cross, V. Bakken, C. Adamo, J. Jaramillo, R. Gomperts, R. E. Stratmann, O.

Yazyev, A. J. Austin, R. Cammi, C. Pomelli, J. W. Ochterski, R. L. Martin, K. Morokuma, V. G. Zakrzewski, G. A. Voth, P. Salvador, J. J. Dannenberg, S. Dapprich, A. D. Daniels, O. Farkas, J. B. Foresman, J. V Ortiz, J. Cioslowski and D. J. Fox, 2013.

138 A. D. Becke, *J. Chem. Phys.*, 1993, **98**, 1372–1377.

139 A. D. McLean and G. S. Chandler, *J. Chem. Phys.*, 1980, **72**, 5639–5648.

140 R. Krishnan, J. S. Binkley, R. Seeger and J. A. Pople, *J. Chem. Phys.*, 1980, **72**, 650–654.

141 A. J. H. Wachters, *J. Chem. Phys.*, 1970, **52**, 1033–1036.

142 P. J. Hay, *J. Chem. Phys.*, 1977, **66**, 4377–4384.

143 K. Raghavachari and G. W. Trucks, *J. Chem. Phys.*, 1989, **91**, 1062–1065.

144 M. J. Frisch, J. A. Pople and J. S. Binkley, *J. Chem. Phys.*, 1984, **80**, 3265–3269.

145 K. Wiberg, *Tetrahedron*, 1968, **24**, 1083.

146 F. Weinhold and C. R. Landis, *Valency and Bonding: A Natural Bond Orbital Donor-Acceptor Perspective*, Cambridge University Press, Cambridge, U.K., 2005.

147 A. E. Reed, L. A. Curtiss and F. Weinhold, *Chem. Rev.*, 1988, **88**, 899–926.

148 P. v. R. Schleyer, C. Maerker, A. Dransfield, H. Jiao and N. J. E. Hommes, *J. Am. Chem. Soc.*, 1996, **118**, 6317–6318.

149 C. Corminboeuf, T. Heine, G. Seifert, P. v. R. Schleyer and J. Weber, *Phys. Chem. Chem. Phys.*, 2001, **6**, 273–278.

150 J. R. Cheeseman, G. W. Trucks, T. A. Keith and M. J. Frisch, *J. Chem. Phys.*, 1996, **104**, 5497–5509.

151 K. Wolinski, J. F. Hilton and P. Pulay, *J. Am. Chem. Soc.*, 1990, **112**, 8251–8260.

152 Jmol: an open-source Java viewer for chemical structures in 3D. http://www.jmol.org/.

153 S. Grimme, J. Antony, S. Ehrlich and H. Kreig, *J. Chem. Phys.*, 2010, **132**, 154104.

154 S. Grimme, S. Ehrlich and L. Goerigk, *J. Comp. Chem.*, 2011, **32**, 1456–1465.

155 T. Clark, J. Chandrasekhar, G. W. Spitznagel and P. v. R. Schleyer, *J. Comp. Chem.*, 1983, **4**, 294–301.

156 P. K. Freeman, *J. Org. Chem.*, 2005, **70**, 1998–2001.

157 D. Kunz, E. O. Johnsen, B. Monsler and F. Rominger, *Chem. Eur. J.*, 2008, **14**, 10909–10914.

158 B. Donnadieu, G. Bertrand, C. A. Dyker and V. Lavallo, *Angew. Chem. Int. Ed.*, 2008, **47**, 3206–3209.

159 V. Lavallo, C. A. Dyker, B. Donnadieu and G. Bertrand, *Angew. Chem. Int. Ed.*, 2008, **47**, 5411–5414.

160 M. Melaimi, P. Parameswaran, B. Donnadieu, G. Frenking, G. Bertrand, *Angew. Chem. Int. Ed.*, 2009, **48**, 4792–4795.

161 I. Fernandez, C. A. Dyker, A. DeHope, B. Donnadieu, G. Frenking, G. Bertrand, *J. Am. Chem. Soc.*, 2009, **131**, 11875–11881.

162 P. Hohenberg and W. Kohn, *Phys. Rev.*, 1964, **136**, B864–B871.

163 J. D. Mattock, A. Vargas and R. D. Dewhurst, *Chem. Eur. J.*, 2015, **21**, 16968–16974.

164 J. M. Schulman, R. L. Disch, P. v. R. Schleyer, M. Buhl, M. Bremer and W. Koch, *J. Am. Chem. Soc.*, 1992, **114**, 7897–7901.

165 H. J. Choi, D. Roundy, H. Sun, M. L. Cohen and S. G. Louie, *Nature*, 2002, **418**, 758–760.

166 C. E. Webster, Y. B. Fan, M. B. Hall, D. Kunz and J. F. Hartwig, *J. Am. Chem. Soc.*, 2003, **125**, 858–859.

167 C. Foroutan-Nejad, S. Hahbazian and P. Rashidi-Ranjbar, *Phys. Chem. Chem. Phys.*, 2010, **12**, 12630–12637.

168 A. Stanger, *Phys. Chem. Chem. Phys.*, 2011, **13**, 12652–12654.

169 C. Foroutan-Nejad, S. Hahbazian and P. Rashidi-Ranjbar, *Phys. Chem. Chem. Phys.*, 2011, **13**, 12655–12658.

170 G. Acke, S. V. Damme, R. W. A. Havenith and P. Bultinck, *J. Comp. Chem.*, 2018, **39**, 511–519.

171 A. C. Tsipis, *Phys. Chem. Chem. Phys.*, 2009, **11**, 8244–8261.

172 C. Foroutan-Nejad, Z. Badri, S. Hahbazian and P. Rashidi-Ranjbar, *J. Chem. Phys. A*, 2011, **115**, 12708–12714.

173 C. Foroutan-Nejad, S. Hahbazian, F. Feixas, P. Rashidi-Ranjbar and M. Sola, *J. Comp. Chem.*, 2011, **32**, 2422–2431.

174 A. D. Becke and K. E. Edgecombe, *J. Chem. Phys.*, 1990, **92**, 5397.

175 M. Kohout and A. Savin, *J. Comp. Chem*, 1997, **18**, 1431.

176 P. de Silva, J. Korchowiec and T. A. Wesolowski, *Chem. Phys. Phys. Chem.*, 2012, **13**, 3462–3465.

177 P. de Silva, J. Korchowiec and T. A. Wesolowski, *J. Chem. Phys.*, 2014, **140**, 164301–164309.

178 P. de Silva, J. Korchowiec, N. R. J. S. and T. A. Wesolowski, *Chimia (Aarau).*, 2013, **67**, 253–256.

179 P. J. Stephens, F. J. Devlin, C. F. Chabalowski and M. J. Frisch, *J. Phys. Chem.*, 1994, **98**, 11623.

180 D. P. Chong, E. van Lenthe, S. J. A. van Gisbergen and E. J. Baerends, *J. Comp. Chem.*, 2004, **25**, 1030.

181 E. van Lenthe and E. J. Baerends, *J. Comp. Chem.*, 2003, **24**, 1142.

182 D. P. Chong, *Mol. Phys.*, 2005, **103**, 749.

183 A. Berces, R. M. Dickson, L. Fan, H. Jacobsen, D. Swerhone and T. Ziegler, *Comp. Phys. Comm.*, 1997, **100**, 247–262.

184 H. Jacobsen, A. Berces, D. Swerhone and T. Ziegler, *Comp. Phys. Comm.*, 1997, **100**, 263–276.

185 S. K. Wolff, *Int. J. Quantum Chem.*, 2005, **104**, 645–659.

186 E. van Lenthe, E. J. Baerends and J. G. Snijders, *J. Chem. Phys.*, 1994, **101**, 9783–9792.

187 R. Bouten, E. J. Baerends, E. van Lenthe, L. Visscher, G. Schreckenbach and T. Ziegler, *J. Phys. Chem. A*, 2000, **104**, 5600–5611.

188 S. J. A. van Gisbergen, J. G. Snijders and E. J. Baerends, *Comp. Phys. Comm.*, 1999, **118**, 119–138.

189 E. Vitaku, D. T. Smith and J. T. Njardarson, *J. Med. Chem.*, 2014, **57**, 10257–10274.

190 M. Arrowsmith, H. Braunschweig and T. E. Stennett, *Angew. Chem. Int. Ed.*, 2017, **56**, 96-115.

Appendix

Figures Corresponding to Characterising the B-B Bond in Chapter 2

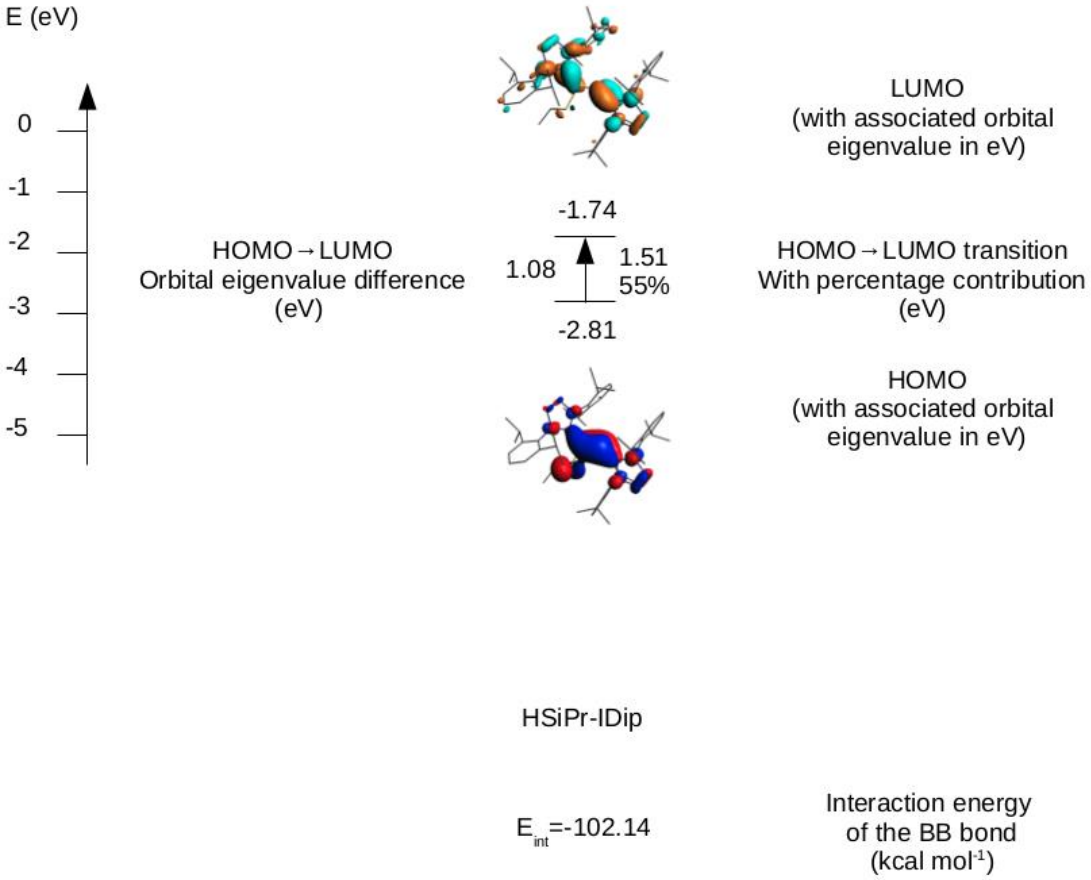

Figure 70: A key describing the values presented pertaining to the HOMO-LUMO gap of a set of diborenes for Figures 71-80.

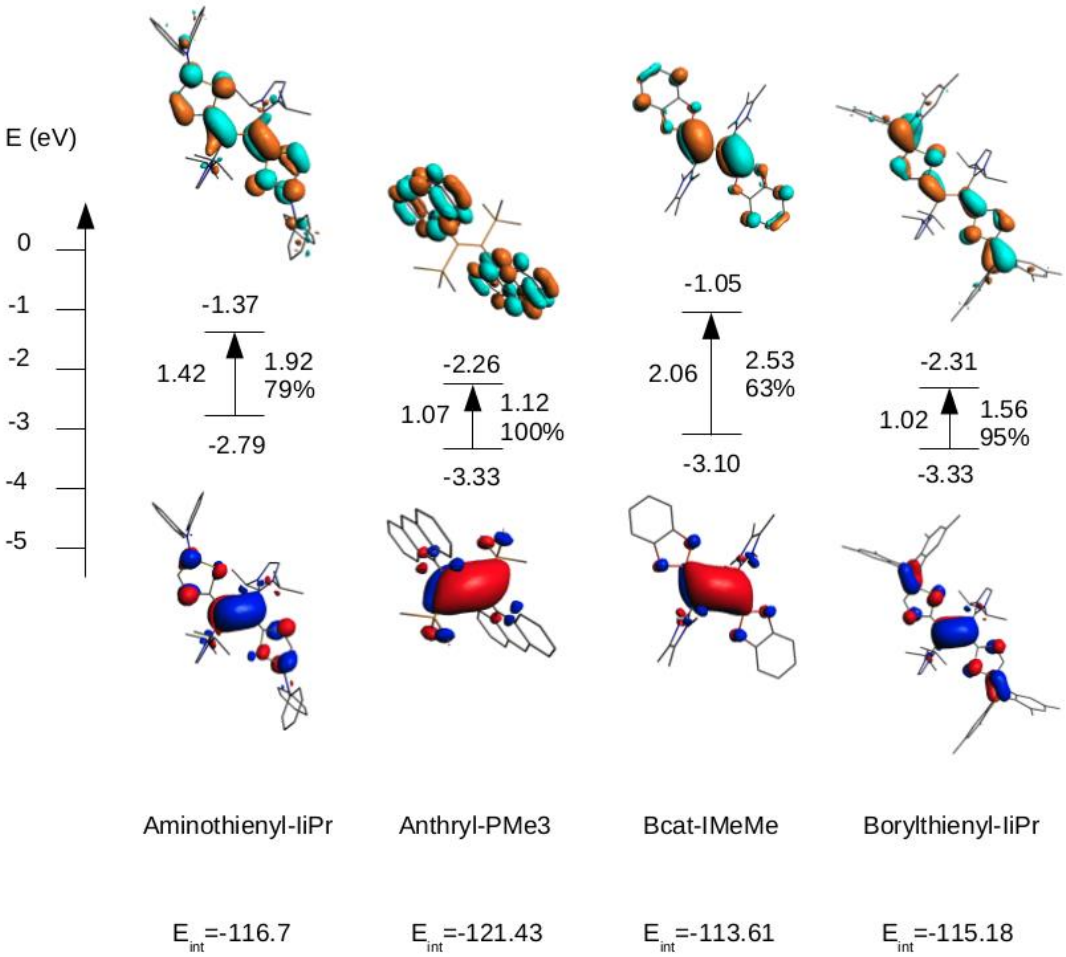

Figure 71: The characterisation of the HOMO-LUMO gaps of BB(aminothienyl)$_2$(IiPr)$_2$, BB(anthryl)$_2$(PMe$_3$)$_2$, BB(BCat)$_2$(IMeMe)$_2$, and BB(borylthienyl)$_2$(IiPr)$_2$ (from left to right).

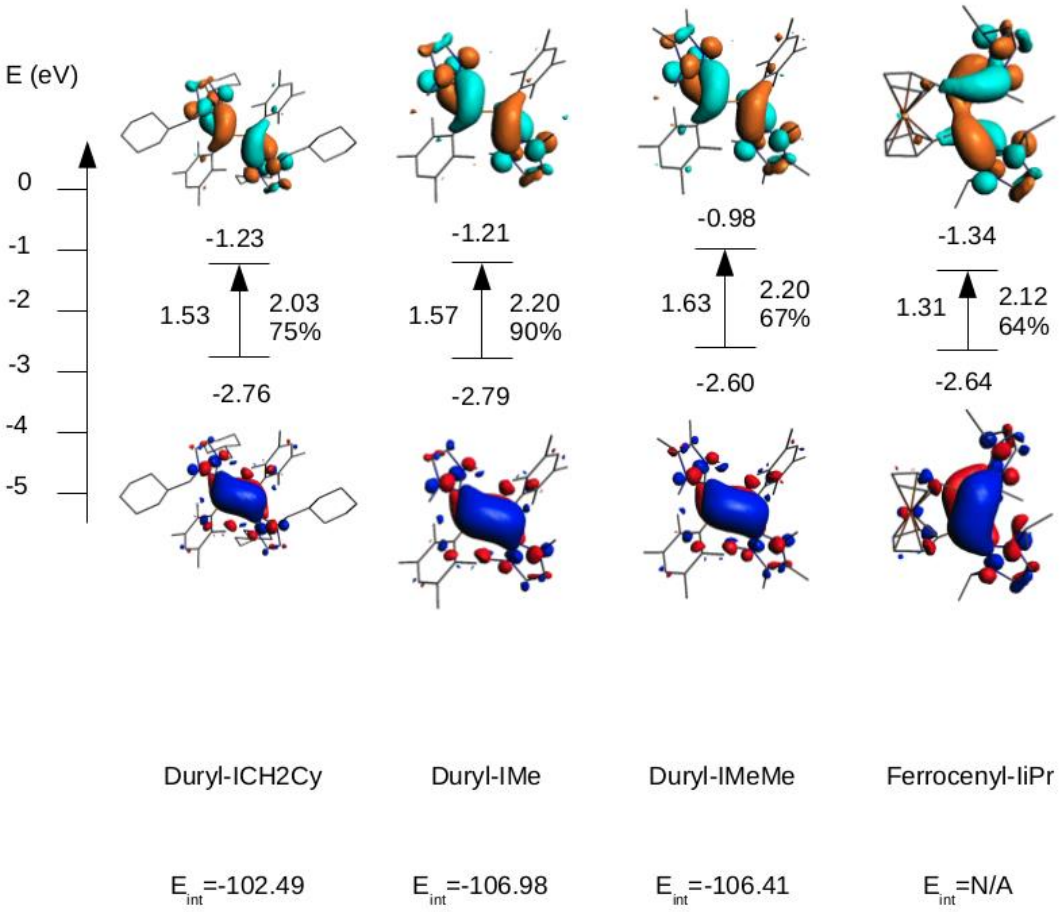

Figure 72: The characterisation of the HOMO-LUMO gaps of BB(duryl)$_2$(ICH2Cy)$_2$, BB(duryl)$_2$(IMe)$_2$, BB(duryl)$_2$(IMeMe)$_2$, and BB(ferrocenyl)(IiPr)$_2$ (from left to right).

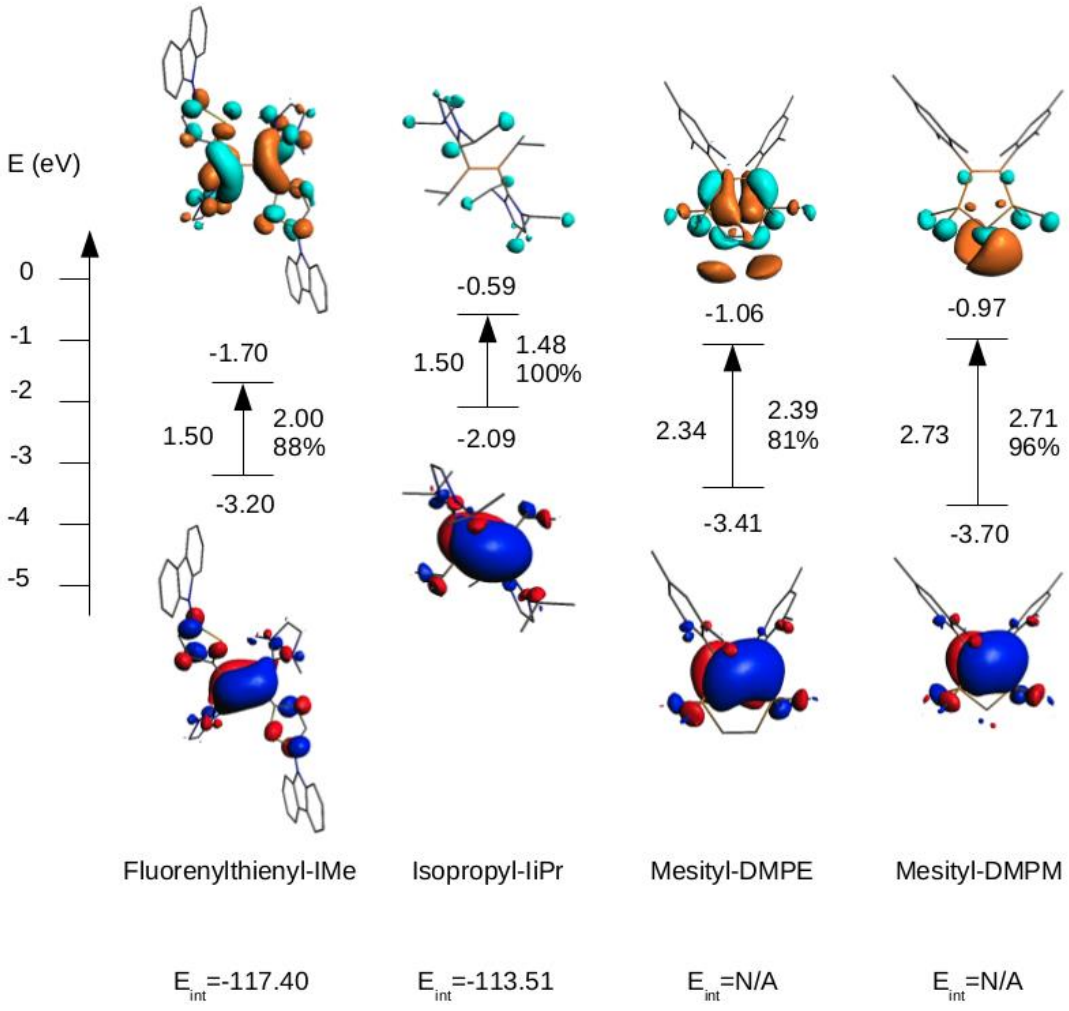

Figure 73: The characterisation of the HOMO-LUMO gaps of BB(fluorenylthienyl)$_2$(IMe)$_2$, BB(isopropyl)$_2$(IiPr)$_2$, BB(mesityl)$_2$(DMPE), and BB(mesityl)$_2$(DMPM) (from left to right).

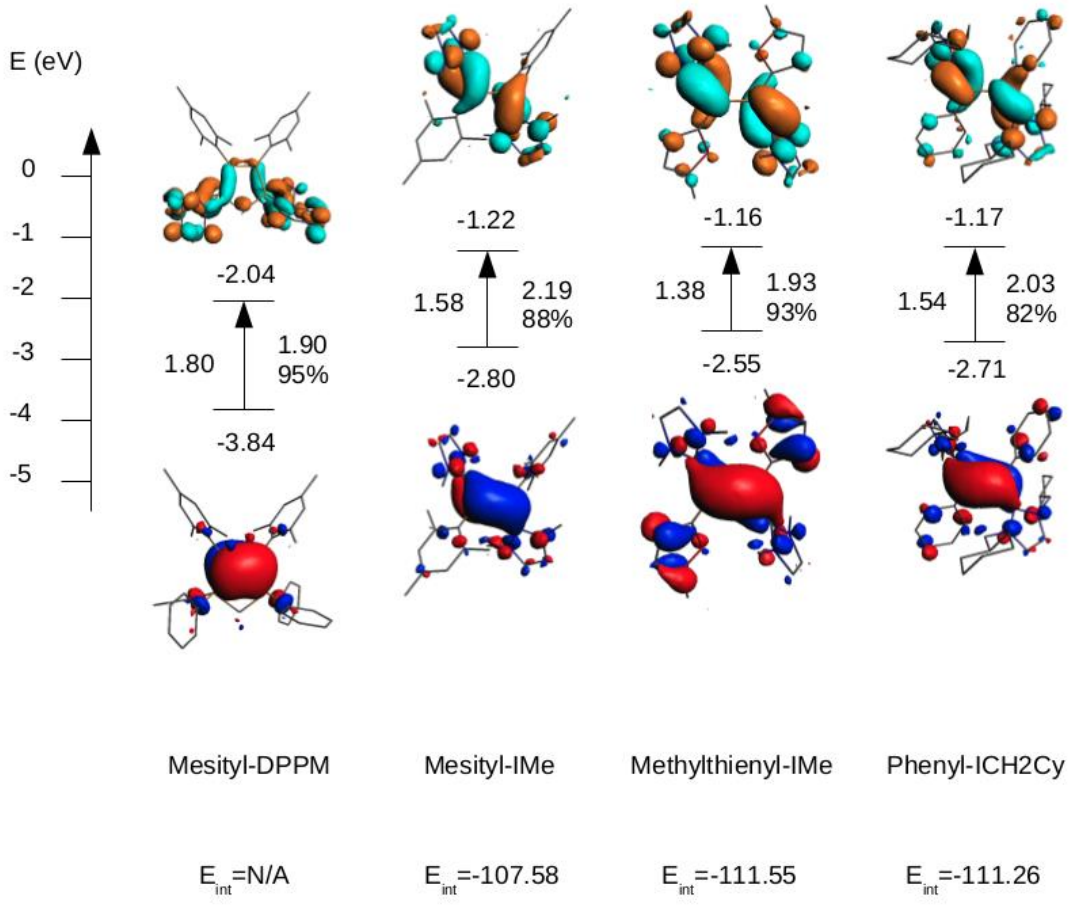

Figure 74: The characterisation of the HOMO-LUMO gaps of $BB(mesityl)_2(DPPM)$, $BB(mesityl)_2(IMe)_2$, $BB(methylthienyl)_2(IMe)_2$, and $BB(phenyl)_2(ICH_2Cy)_2$ (from left to right).

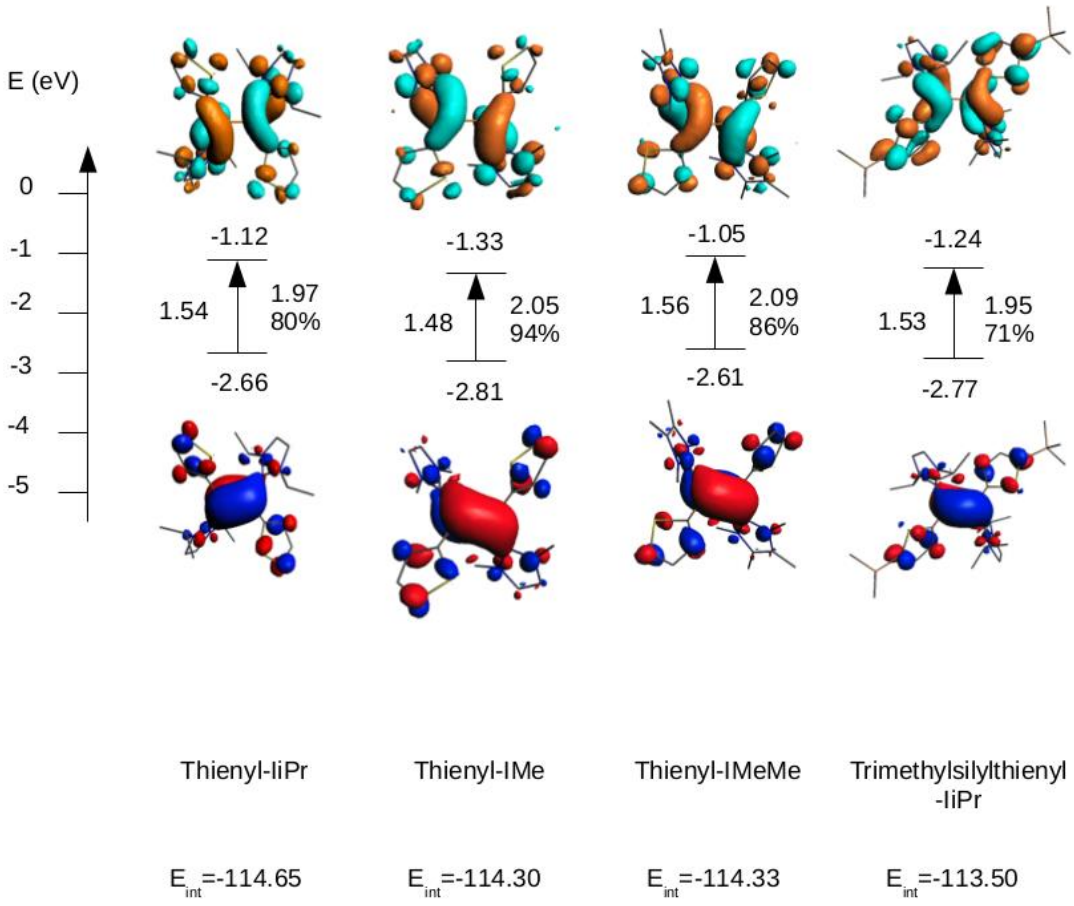

Figure 75: The characterisation of the HOMO-LUMO gaps of BB(thienyl)$_2$(IiPr)$_2$, BB(thienyl)$_2$(IMe)2, BB(thienyl)$_2$(IMeMe)$_2$, and BB(trimethylsilylthienyl)$_2$(IiPr)$_2$ (from left to right).

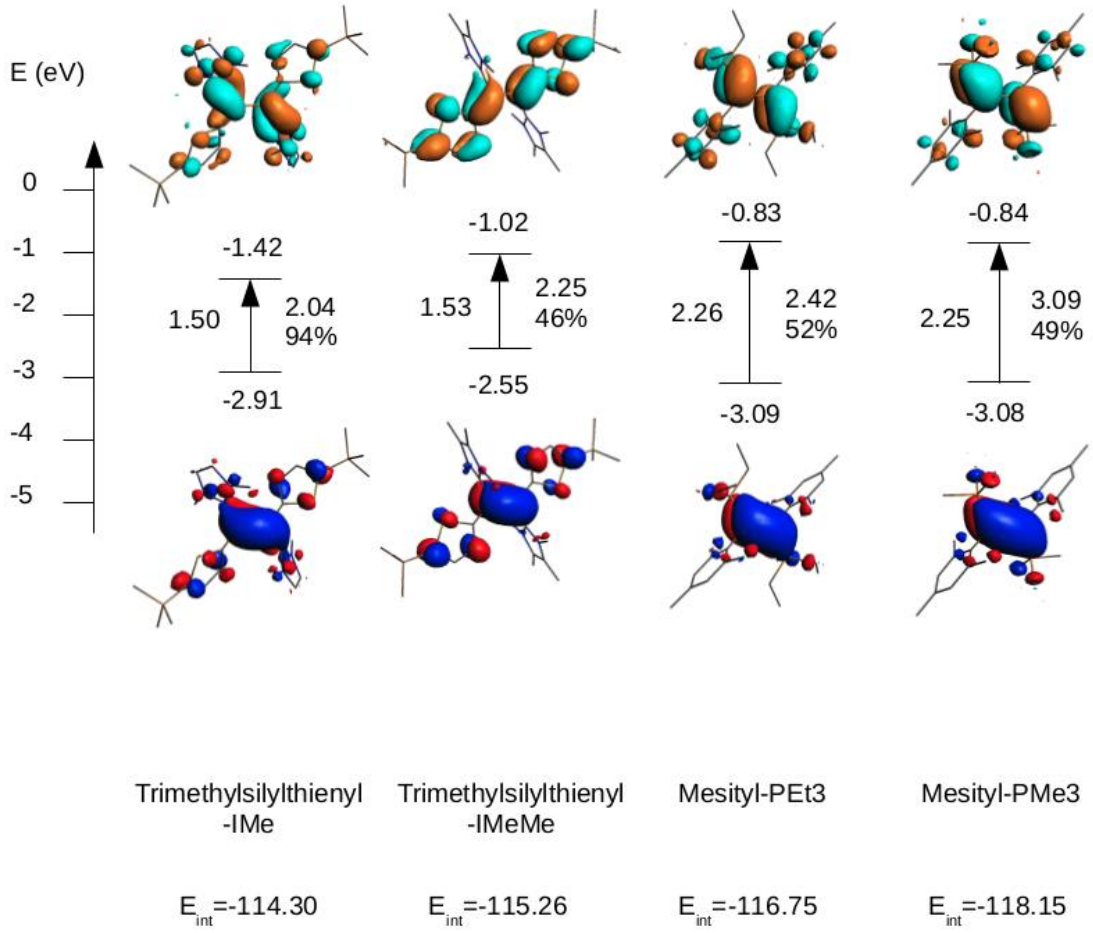

Figure 76: The characterisation of the HOMO-LUMO gaps of BB(trimethylsilylthienyl)$_2$(IMe)$_2$, BB(trimethylsilylthienyl)$_2$(IMeMe)$_2$, BB(mesityl)$_2$(PEt$_3$)$_2$, and BB(mesityl)$_2$(PMe$_3$)$_2$ (from left to right).

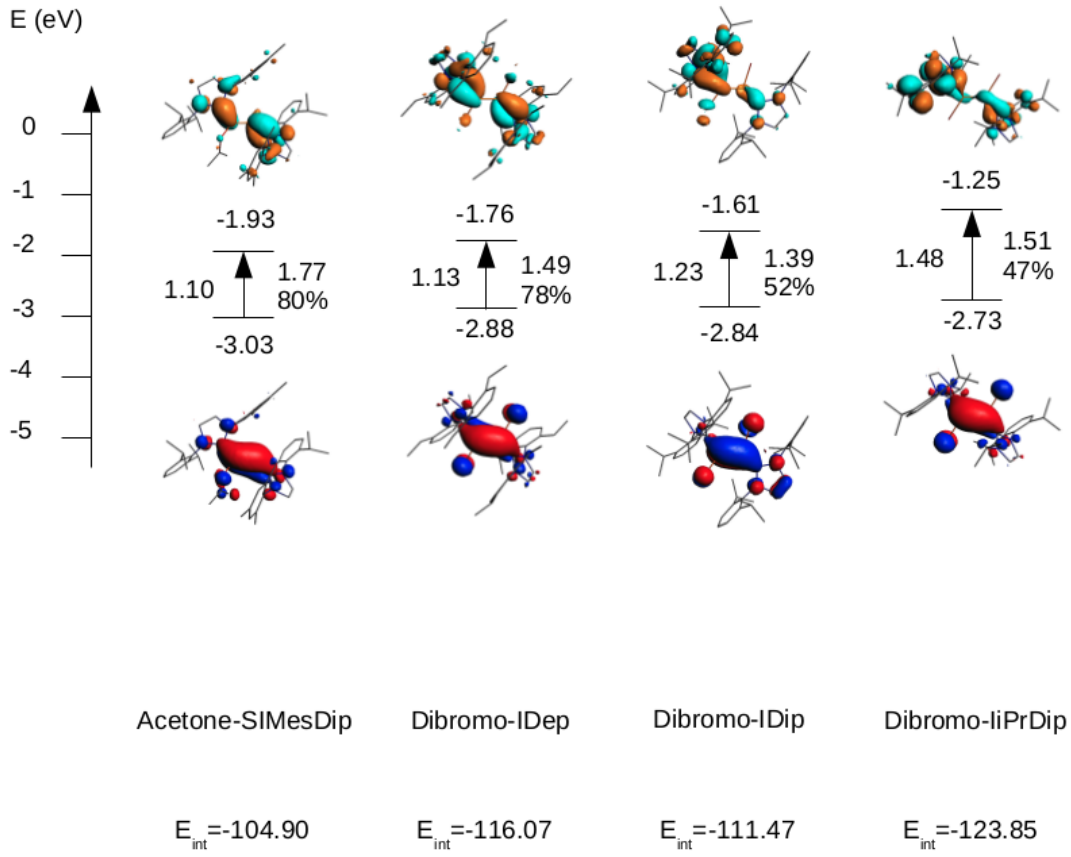

Figure 77: The characterisation of the HOMO-LUMO gaps of BB(propanone)$_2$(SIMesDip)$_2$, BB(Br)$_2$(IDep)$_2$, BB(Br)$_2$(IDip)$_2$, and BB(Br)$_2$(IiPrDip)$_2$ (from left to right).

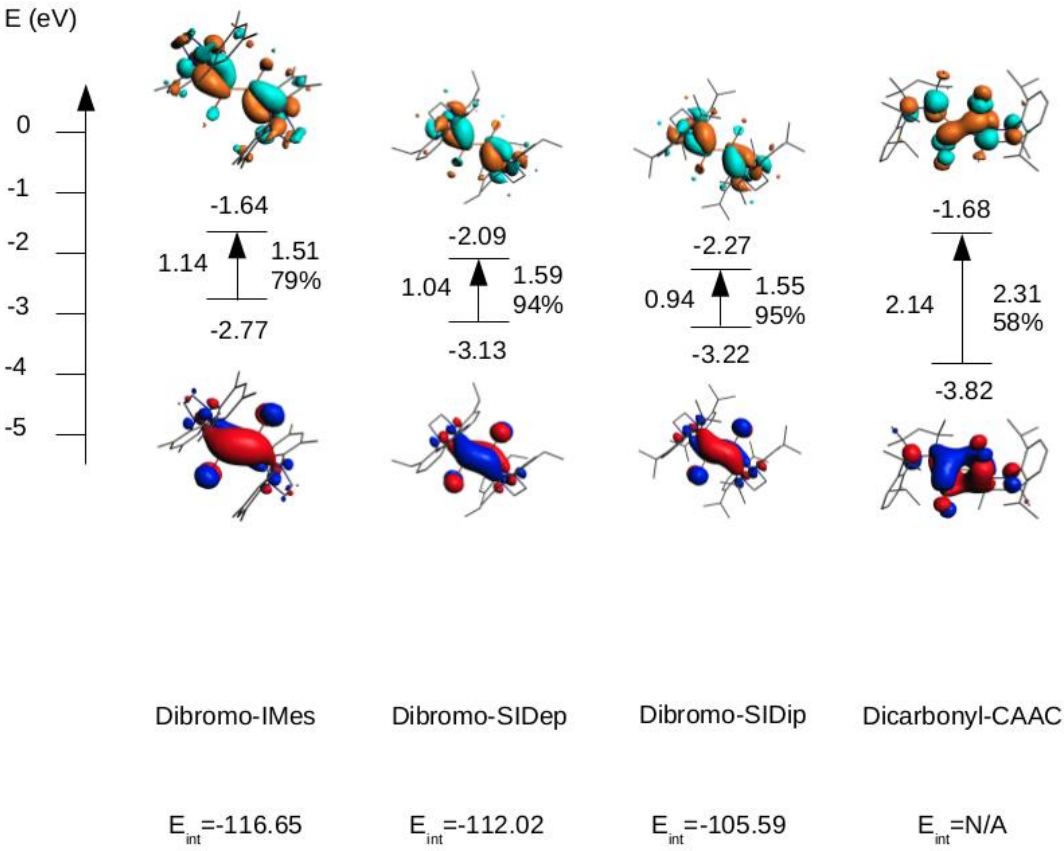

Figure 78: The characterisation of the HOMO-LUMO gaps of $BB(Br)_2(IMes)_2$, $BB(Br)_2(SIDep)_2$, $BB(Br)_2(SIDip)_2$, and $BB(CO)_2(CAAC)_2$ (from left to right).

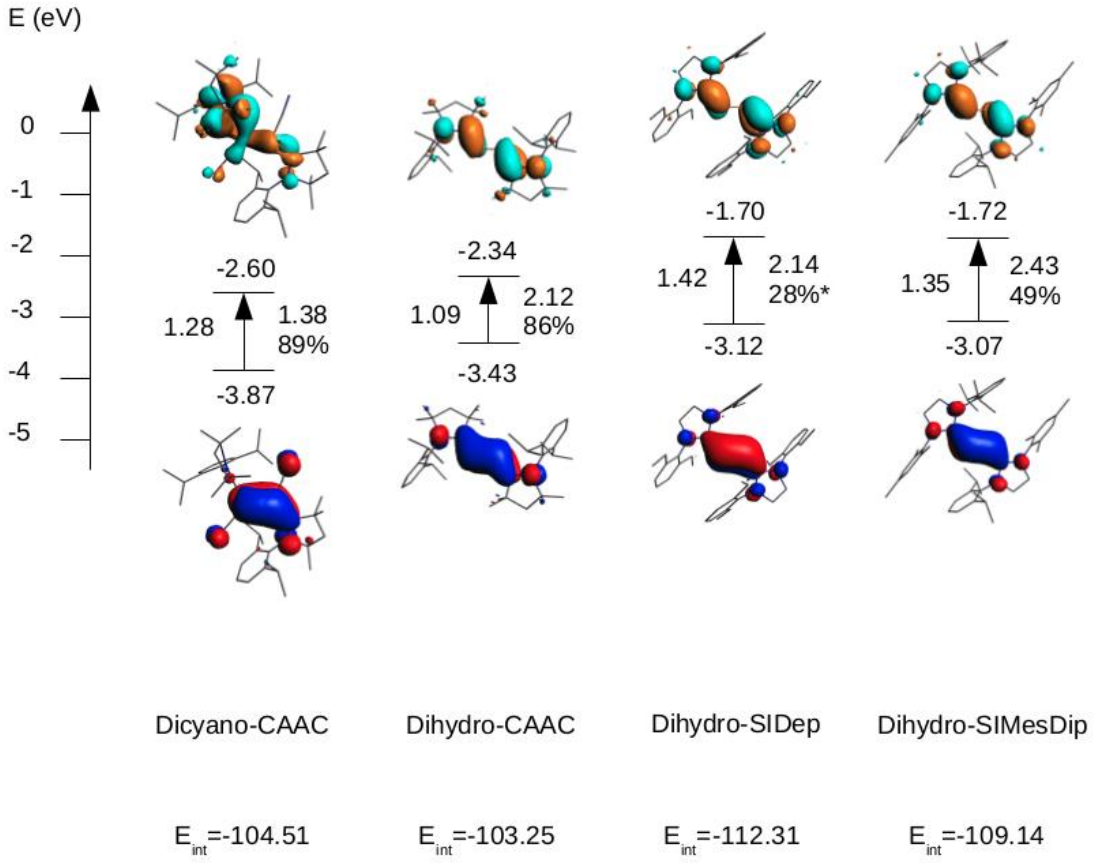

Figure 79: The characterisation of the HOMO-LUMO gaps of $BB(CN)_2(CAAC)_2$, $BB(H_2O)_2(CAAC)_2$, $BB(H_2O)_2(SIDep)_2$, and $BB(H_2O)_2(SIMesDip)_2$ (from left to right).

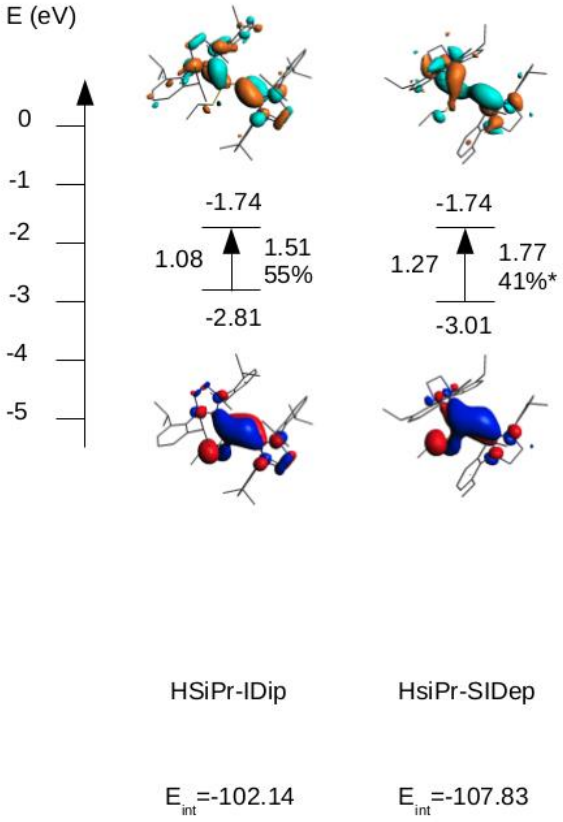

Figure 80: The characterisation of the HOMO-LUMO gaps of $BB(HSiPr)_2(IDip)_2$ (left) and $BB(HSiPr)_2(SIDep)_2$ (right).

Compound	Calculated B-B bond length (Å)	Experimental B-B bond length (Å)
$BB(duryl)_2(IMe)_2$	1.6391	1.590
$BB(isopropyl)_2(IiPr)_2$	1.6155	1.578
$BB(mesityl)_2(DMPE)$	1.6087	1.583
$BB(mesityl)_2(DPPM)$	1.6234	1.593
$BB(mesityl)_2(IMe)_2$	1.6387	1.593
$BB(mesityl)_2(PEt_3)_2$	1.6113	1.579
$BB(mesityl)_2(PMe_3)_2$	1.6052	1.573
$BB(Br)_2(IDip)_2$	1.6149	1.546
$BBH_2(SIDep)_2$	1.6154	1.589
$BBH_2(CAAC)_2$	1.6411	1.625

Table A1: A comparison of a selection of calculated B=B bond lengths with the appropriate experimental values taken from a review by Arrowsmith *et al.*.[190]

Note that the calculated bond lengths are generally slightly longer than the experimentally attained bond lengths. As they tend to follow similar trends it is likely that the divergence is caused by crystal packing forces.

List of Publications

Controllable Modulation of the High Spin-Low Spin Energy Difference in Transition Metal Complexes Using Boron-Based Homoaromatic Ligands

James D. Mattock and Alfredo Vargas

In preparation

Characterisation of the Boron-Boron Bond and Determination of the HOMO-LUMO Gap in a Series of Diborenes

James D. Mattock, Rian D. Dewhurst, Tom E. Stennett, Holger Braunschweig and Alfredo Vargas

In preparation

Boron Centres Allow Design, Control and Systematic Tuning of Neutral Homoaromatics for Functionalization Purposes

James D. Mattock and Alfredo Vargas

ChemPhysChem 06/2018; DOI:10.1002/cphc.201800453

Diboryldiborenes pi-Conjugated B4 Chains Isoelectronic to the Butadiene Dication

Alexander Hermann, Jessica Cid, James D. Mattock, Rian D. Dewhurst, Ivo Krummenacher, Alfredo Vargas, Michael J. Ingleson, Holger Braunschweig

Angewandte Chemie International Edition 06/2018; DOI:10.1002/anie.201805394

Direct Access to a cAAC-Supported Dihydrodiborene and its Dianion.

Merle Arrowsmith, James Mattock, Julian Böhnke, Ivo Krummenacher, Alfredo Vargas, Holger Braunschweig

Chemical Communications 03/2018; DOI:10.1039/C8CC01580

Bottleable Neutral Analogues of $[B_2H_5]^-$ as Versatile and Strongly Binding η^2 Donor Ligands

Sunewang Rixin Wang, Dominic Prieschl, James D. Mattock, Merle Arrowsmith, Conor Pranckevicius, Tom E. Stennett, Rian D. Dewhurst, Alfredo Vargas, Holger Braunschweig

Angewandte Chemie International Edition 03/2018; DOI:10.1002/anie.201801722

Unsymmetrical, Cyclic Diborenes and Thermal Rearrangement to a Borylborylene.

Tom E Stennett, James D Mattock, Ivonne Vollert, Alfredo Vargas, Holger Braunschweig

Angewandte Chemie International Edition 02/2018; DOI:10.1002/anie.201800671

Unusual Heterobimetallic Adducts of a Calix[4]arene-Based Thione Ligand.

Ruth Patchett, Richard C. Knighton, James D. Mattock, Alfredo Vargas, Adrian B. Chaplin: Potassium Binding Adjacent to Cationic Transition-Metal Fragments

Inorganic Chemistry 11/2017 56(22)., DOI:10.1021/acs.inorgchem.7b02441

Monomeric 16-Electron π-Diborene Complexes of Zn(II) and Cd(II)

Sunewang Rixin Wang, Merle Arrowsmith, Holger Braunschweig, Rian D. Dewhurst, Michael Dömling, James D. Mattock, Conor Pranckevicius, Alfredo Vargas

Journal of the American Chemical Society 07/2017; 139(31). DOI:10.1021/jacs.7b06644

Engineering a Small HOMO-LUMO Gap and Intramolecular C-H Borylation by Diborene/Anthracene Orbital Intercalation

Sunewang R. Wang, Merle Arrowsmith, Julian Böhnke, Holger Braunschweig, Theresa Dellermann, Rian D. Dewhurst, Hauke Kelch, Ivo Krummenacher, James D. Mattock, Jonas H. Müssig, Torsten Thiess, Alfredo Vargas, Jiji Zhang

Angewandte Chemie International Edition 05/2017; DOI:10.1002/anie.201704063

Strongly Phosphorescent Transition Metal π Complexes of Boron-Boron Triple Bonds

Holger Braunschweig, Theresa Dellermann, Rian D Dewhurst, Benjamin Hupp, Thomas Kramer, James D Mattock, Jan Mies, Ashwini K Phukan, Andreas Steffen, Alfredo Vargas

Journal of the American Chemical Society 02/2017; 139(13). DOI:10.1021/jacs.7b00766

Dibora[2]ferrocenophane: A Carbene-Stabilized Diborene in a Strained cis -Configuration

Holger Braunschweig, Ivo Krummenacher, Crispin Lichtenberg, James D. Mattock, Marius Schäfer, Uwe Schmidt, Christoph Schneider, Thomas Steffenhagen, Stefan Ullrich, Alfredo Vargas

Angewandte Chemie International Edition 12/2016; 56(3). DOI:10.1002/anie.201609601

Efficient NiII2LnIII2 Electrocyclization Catalysts for the Synthesis of trans-4,5-Diaminocyclopent-2-enones from 2-Furaldehyde and Primary or Secondary Amines

Kieran Griffiths, Prashant Kumar, James D Mattock, Alaa Abdul-Sada, Mateusz B Pitak, Simon J Coles, Oscar Navarro, Alfredo Vargas, George E Kostakis

Inorganic Chemistry 06/2016; 55(14). DOI:10.1021/acs.inorgchem.6b00720

A Binuclear 1,1'-Bis(boratabenzene) Complex: Unprecedented Intramolecular Metal-Metal Communication through a B-B Bond

Holger Braunschweig, Serhiy Demeshko, William C Ewing, Ivo Krummenacher, Bret B Macha, James D Mattock, Franc Meyer, Jan Mies, Marius Schäfer, Alfredo Vargas

Angewandte Chemie International Edition 05/2016; 55(27). DOI:10.1002/anie.201603437

Trimetallaborides as Starting Points for the Syntheses of Large Metal-Rich Molecular Borides and Clusters

Holger Braunschweig, William C. Ewing, Sundargopal Ghosh, Thomas Kramer, James D. Mattock, Sebastian Östreicher, Alfredo Vargas, Christine Werner

Chemical Science 12/2015; 7(1). DOI:10.1039/C5SC03206G

Identification of a Lead Candidate in the Search for Carbene-Stabilised Homoaromatics

James D. Mattock, Alfredo Vargas, Rian D. Dewhurst

Chemistry - A European Journal 10/2015; 21(47). DOI:10.1002/chem.201501948

Organometallic Probe for the Electronics of Base-Stabilized Group 11 Metal Cations

Holger Braunschweig, William C Ewing, Thomas Kramer, James D Mattock, Alfredo Vargas, Christine Werner

Chemistry - A European Journal 07/2015; 21(35). DOI:10.1002/chem.201500788\